AD NUMBER
AD815009
LIMITATION CHANGES

TO:

Approved for public release; distribution is unlimited.

FROM:

Distribution authorized to U.S. Gov't. agencies and their contractors; Critical Technology; MAY 1967. Other requests shall be referred to Rome Air Development Center, Attn: EMLI, Griffiss AFB, NY 13441-5700. This document contains export-controlled technical data.

AUTHORITY

RADC ltr, 17 Sep 1971

AD815003

Technical Report...

CONTINUED STUDIES ON ADVANCED FERRIMAGNETIC MATERIALS APPLIED TO DIGITAL PHASE SHIFTERS

FINAL REPORT

28 February 1966 to 28 February 1967

ARPA ORDER No. 550 - PROGRAM CODE No. 6E30

RADC Contract No. AF30(602)4122

Air Force Systems Command
Research and Technology Division
Rome Air Development Center
Griffiss Air Force Base, New York

Project Defender
Advanced Research Projects Agency (ARPA)
Department of Defense
Washington, D.C.

D D C
JUN 9 1967
RECEIVED
B

(SPERRY) MICROWAVE ELECTRONICS COMPANY

CLEARWATER, FLORIDA

TECHNICAL REPORT

CONTINUED STUDIES ON ADVANCED FERRIMAGNETIC MATERIALS APPLIED TO DIGITAL PHASE SHIFTERS

FINAL REPORT

28 February 1966 to 28 February 1967

ARPA ORDER No. 550 - PROGRAM CODE No. 6E30
RADC CONTRACT No. AF30(602)4122
STATEMENT #2 UNCLASSIFIED

This document is subject to special export controls and each
transmittal to foreign governments or foreign nationals may be *AFB, N.Y.*
made only with prior approval of *RADC (EMLI), Griffiss AFB, N.Y.*
1344 8

Air Force Systems Command
Research and Technology Division
Rome Air Development Center
Griffiss Air Force Base, New York

Project Defender
Advanced Research Projects Agency (ARPA)
Department of Defense
Washington, D.C.

Title of Work:

Continued investigations directed toward the improve-
ment and evaluation of ferrimagnetic materials for use
in microwave digital phase shifters at L-, S-, C-, and
X-bands.

May 1967

SPERRY MICROWAVE ELECTRONICS COMPANY
DIVISION OF SPERRY RAND CORPORATION
CLEARWATER, FLORIDA

SJ-220-4002-6

Copy No _14_

TABLE OF CONTENTS

TABLE OF CONTENTS (Cont'd)

LIST OF ILLUSTRATIONS ...

LIST OF ILLUSTRATIONS (Cont'd)

iv

LIST OF ILLUSTRATIONS (Cont'd)

LIST OF ILLUSTRATIONS (Cont'd)

LIST OF ILLUSTRATIONS (Cont'd)

LIST OF ILLUSTRATIONS (Cont'd)

LIST OF TABLES

1 SUMMARY

This report describes the results of work performed by Sperry Microwave Electronics Company for the Rome Air Development Center and the Advanced Research Projects Agency during the course of Contract No. AF30(602)-4122(ARPA Order No. 550).

The objectives of this program were:

1. To determine the limitations imposed by intrinsic material parameters on the peak power handling capacity of ferrite digital phase shifters,

2. To develop ferrimagnetic materials with improved properties for use in high peak power digital phase shifters, and

3. To develop techniques for predicting performance characteristics of ferrite digital phase shifters from a knowledge of intrinsic material parameters and structural dimensions, and

4. To evaluate both the improved materials and various existing materials in appropriate rf structures at frequencies in L, S, C and X bands.

The principal results and conclusions of this program are:

1. (a) The peak power capacity of ferrite materials increases with decreasing ratio of $\gamma 4\pi M_s$ to operating frequency (i.e., $m_s = \dfrac{\gamma 4\pi M_s}{\omega}$) and with increasing spinwave linewidth ΔH_k.

   (b) At a given frequency, peak power capacity can thus be controlled by utilizing rare earth doping to increase the spinwave linewidth, ΔH_k, of the material and/or aluminum doping to decrease its $4\pi M_s$.

2. Increasing ΔH_k or decreasing $4\pi M_s$ to improve peak power capacity at a given frequency generally increases the low power insertion loss. Ferrimagnetic materials have been developed to achieve an optimum compromise between peak power capacity and low power insertion loss for L, S, C and X bands.

3. A model accounting for the rf properties of partially magnetized (or remanent state) magnetic materials and computational techniques utilizing that model have been developed. These techniques, with the aid of a digital computer, permit the accurate prediction of the loss and phase characteristics of remanent

state phasers from a knowledge of structural dimensions and
the intrinsic material parameters $4\pi M_s$, ΔH_i (intimately re-
lated to ΔH_k), remanence ratio, dielectric constant and
dielectric loss tangent. The magnetic material parameters
involved in predicting low power characteristics are the same
ones required for predicting peak power capacity. Thus, a
single set of intrinsic parameter measurements suffices for
the prediction of both high and low power material performance
characteristics.

4. The materials developed have been evaluated in appropriate
rf test structures. The results of these evaluations indicate
that waveguide nonreciprocal digital phase shifters operating
at peak power levels of 700 kw, 500 kw, 300 kw and 150 kw
in L, S, C and X bands, respectively, with less than 1 db
per 360° of differential phase shift are feasible.

A brief description of the contents of each section of this report follows.
Throughout this program, emphasis has been placed on attaining high peak power
capacity even at the possible expense of some degradation of other performance
characteristics. To permit an assessment of the cost of attaining a specified peak
power capacity in terms of possible degradation of other performance characteristics,
the interrelationships between peak power capacity, insertion loss, phase shift,
temperature stability, etc., are examined. The relationships between these per-
formance characteristics arise from their dependence on intrinsic material para-
meters. The results of these studies highlight the "tradeoffs" that might be made to
obtain the optimum digital phase shifter for a given high peak power application.

Section 2

Background information and a statement of the program objectives are pre-
sented.

Section 3

This section presents both a qualitative and an analytical discussion on how
the intrinsic material parameters of remanent state ferrimagnetic materials in-
fluence the operating characteristics of ferrite digital phase shifters (FDPS).
Emphasis is placed on clearly describing the limitations imposed by intrinsic
material parameters on high peak power operation.

The section begins with a qualitative description of the operating principles
of a waveguide nonreciprocal digital phase shifter. Following the introductory
comments is a discussion of a physical model for remanent state ferrites which

1-2

appears to account quite well for the experimentally observed properties of these materials:

> The central concept used in the development of the physical model is that a remanent state material is made up of a substantial number of magnetic domains. Each domain is a magnetically saturated region whose properties can be described by conventional theory of saturated media. The behavior of the domains differs because each may have a different shape, and the magnetization of the various domains points in different directions. Each of these domains then experiences an "effective" bias field whose magnitude is related to intrinsic material parameters and to the shape of the domain. For a remanent state material with a reasonable remanence ratio, there will be a major zone of domains with nearly parallel moments which will occupy most of the volume of the sample. From the physical model a mathematical model for remanent state ferrites is developed based on averaging the properties of the individual saturated regions to obtain a set of effective properties for the bulk remanent state material. The mathematical characterization thus takes the form of a complex "average" tensor permeability which includes the effects of intrinsic linewidth, magnetocrystalline anisotropy, remanent magnetization and an average demagnetizing field appropriate to the major zone of domains. The distribution and shape of the magnetic domains, and hence the value of the average demagnetizing field, are determined to a large extent by sample shape and the remanence ratio of the material.

The discussion of physical and mathematical models of remanent state ferrites is followed by a description of analysis techniques which can be used to obtain numerical relationships between the transfer characteristics of a phase shifter (i.e., loss and phase) and the dimensional and material parameters of the structure. As an example of these techniques, the propagation constant equation is derived for a typical digital phase shifter model.

An analysis of peak power effects in remanent state ferrites is next presented:

> The analysis is based on the multidomain model of remanent materials mentioned previously. Since each domain is a magnetically saturated region, the peak power effects on a domain by domain basis may be interpreted in terms of the spinwave interactions of the well-known Suhl-Schloemann theory of nonlinear effects in saturated media. Each domain may experience a different effective bias field and hence may have a different threshold power level from all other domains. The threshold level observed experimentally by comparing power levels at the output and input of a phase shifter is the threshold level of the "worst" or most unfavorably biased domain. In the usual FDPS, the occurrence of the first order nonlinear process is the factor which limits peak power performance. In the first order process energy

1-3

from the uniform precession is scattered and lost to half-frequency spinwave modes. For this process the threshold field h_{crit} is proportional to the spinwave linewidth ΔH_k and inversely proportional to the normalized saturation magnetization m_s. Since ΔH_k is a function of the wave number k ($\Delta H_k \approx A + Bk$), h_{crit} depends upon the availability of low to medium k number half-frequency spinwaves. In remanent state ferrites the availability of half-frequency spinwaves with low to medium k values in turn depends upon m_s through the dependence of each domain's effective bias field on demagnetizing terms.

For even the most unfavorably biased domains (Polder-Smit type domains), low k spinwaves are no longer available when m_s drops below about 0.3. As a result of the k dependence of ΔH_k, these domains, will exhibit an increase in ΔH_k, and hence h_{crit} for $m_s \approx 0.3$. For other types of domains the restriction of scattering to high k states (and an increase in h_{crit}) will occur at larger values of m_s. Thus, the rate of change of h_{crit} with m_s will vary with the type of domains present in the toroid. In any event, however, h_{crit} must increase in the vicinity of 0.3.

Thus, the threshold field, and hence the peak power handling capacity can be controlled by changes in the ΔH_k of low k spinwaves (e.g., by rare earth doping of garnets) or by changing m_s (e.g., by aluminum doping of garnets).

The final portion of this section deals with the ferrite square loop properties of interest in FDPS. The dependence of remanence ratio (R_r), coercive force (H_c), and switching time T_s are related to the intrinsic and ceramic properties of the ferrite.

Section 4

This section presents a discussion and comparison of the results of the analytical and experimental phases of the program. The results presented include

1. Numerical predictions of phase shifter performance characteristics obtained from a computer-aided solution of the exact boundary value problem, including the effects of losses, for the waveguide digital phase shifter configuration on which most of the experimental measurements were performed,

2. Extensive experimental data depicting the effect of material and dimensional parameters on low and high peak power digital phase shifter characteristics,

3. Experimental data depicting the dependence of the microwave and square loop material properties on preparation techniques, composition, and ambient temperature.

Principal conclusions based on these data are:

1. High peak power digital phasers can be constructed. Non-reciprocal waveguide digital phasers operating at peak power levels of 700 kw, 500 kw, 300 kw, and 150 kw in L, S, C and X Bands, respectively, with an insertion loss of less than 1 db per 360° of differential phase shift are feasible.

2. Peak power capacity of ferrimagnetic materials can be predicted from a knowledge of $4\pi M_s$, ΔH_k and operating frequency.

3. At a given operating frequency, peak power capacity can be increased by increasing ΔH_k (e.g., by rare earth doping in garnets) and/or decreasing $4\pi M_s$ (e.g., by aluminum doping).

4. Accurate (5 percent or better) analytical prediction of both loss and phase characteristics of ferrite digital phasers from a knowledge of intrinsic material parameters and structural dimension has been demonstrated. The unique features of the analytical treatment are: (a) representation of magnetic losses via the intrinsic linewidth ΔH_i; (b) representation of remanent state magnetic properties by an "averaged" complex tensor permeability; (c) inclusion of both magnetic and dielectric losses exactly in the solution as opposed to the usual perturbation techniques.

5. Material parameters and structural dimensions can be selected to optimize phase shifter performance in terms of

    *   Loss per 360° of differential phase shift,
    *   Peak power handling capacity,
    *   Phase shift per unit length, or
    *   Stability of performance over a large frequency range, or
    *   Stability of performance over a large temperature range, etc.,

    but if more than one of these capabilities is required simultaneously then compromise, rather than ultimate, characteristics must be accepted,

6. Peak power capacity and low power insertion loss are intimately related. In general, modifying a material to achieve higher peak power capability will lead to some increase in low power insertion loss.

7. Low power insertion loss increases linearly with increasing intrinsic linewidth. The usual polycrystalline linewidth is not generally significant in determining low power loss.

8. Operation of waveguide digital phasers in the normal above resonance mode have been demonstrated at operating frequencies as low as L band. At L band frequencies, as in X, C, and S bands, the measured differential phase shift and loss are in very good agreement with analytical predictions. Figures of merit of the order of 650°/db have been realized.

9. Below resonance (in frequency) operation has been achieved in a helical line digital phase shifter. The shape of the resonance loss curve for the remanent state material is very much like the resonance curve of a saturated sample, only broader. A figure of merit of about 25 degrees/db has been achieved at 1 GHz but further investigation has not indicated that a practical level of performance is feasible.

10. High density materials appear to have the best overall properties for use in remanent state phase shifters. Considerable premium should be placed on materials having highest possible density and homogeneity.

11. Remanence magnetization appears to vary with temperature in approximately the same manner as the saturation magnetization, indicating that the remanence ratio, R_r, is approximately independent of temperature. Exceptions to this general rule occur in cases where the anisotropy field of the material changes significantly with temperature, and for sufficient driving fields, increased anisotropy fields produce small increases in remanence ratio.

12. Coercive fields, H_c, vary directly with anisotropy fields.

Section 5

This section lists publications and lectures related to this program.

Section 6

This section presents a summary of the conclusions deduced from the results of this study. Typical tradeoffs between peak power, insertion loss, and phase shift per unit length are illustrated in Table IX.

2 INTRODUCTION

2.1 BACKGROUND OF PROGRAM

Research and development efforts on ferrite digital phase shifters (FDPS) have established certain guidelines useful in the selection of materials and structures for these devices. These efforts have established that materials from the magnesium-manganese ferrite and the rare earth substituted yttrium aluminum iron garnet families are the chief materials of interest. The structures of principal interest for high power applications are dielectrically loaded rectangular ferrite toroid configurations in reduced width waveguide. Within these basic guidelines, certain refinements of the material and structural parameters will serve to optimize the performance characteristics of digital phase shifters. For example, rare earth doping may be utilized to increase the peak power handling capacity of the ferrite, and gadolinium substitutions can stabilize the magnetization of the ferrite, and hence the phase shift of the devices over wide ranges of temperature and average power. The limitations of these and other such techniques and the interrelation of the various device properties have not been clear.

It was the purpose of this program to determine these limitations, develop the necessary improvements in the materials, and establish quantitative information which will clearly define the tradeoffs involved in obtaining satisfactory peak power performance with minimum sacrifice of insertion loss, switching characteristics, etc. To this end, a combined theoretical and experimental program was initiated. The theoretical and experimental efforts were closely coordinated. It is felt that a more complete understanding of the physical processes involved in remanent state devices has been obtained, and that the analytical techniques developed can permit the prediction of the intrinsic material parameters required to yield prescribed phase shifter characteristics. In addition, an investigation was performed on the effects of material preparation techniques on the material parameters which are found to be important in determining phase shifter performance.

2.2 PROGRAM OBJECTIVES

The basic program objectives were as follows:

- Improvement and evaluation of ferrite and garnet materials for use in digital phase shifters at L, S, C and X bands with increased effort at the lower frequency bands. Emphasis was placed on development of peak power capability of the order of 100 kilowatts while generating insertion losses of 1 db or less and phase stability with temperature variation over the military range.

- A study of microwave digital phase shift structures with special emphasis on materials derived in this program combined with the requirements for high switching speed, low switching power, low loss, low holding power, compact configuration, low unit cost, and high peak and average power handling capability.

3   OPERATING DYNAMICS OF FERRITE* DIGITAL PHASE SHIFTERS

3.1   BASIC CONCEPT OF FERRITE DIGITAL PHASE SHIFTERS (FDPS)

Ferrite loaded transmission structures have been used for a number of years to obtain electrically-controllable reciprocal and nonreciprocal phase shift.[1]   The operation of early ferrite phase shifters was based on changes in the propagation constant of the ferrite loaded structure which occur when the rf permeability of the ferrite is varied by controlling the ferrite's dc magnetic bias field.   These variable-bias-field phase shifters were rather bulky in size and slow in switching from one phase shift value to another, due to the substantial electromagnet required.   In addition, dc power consumption was high because of the holding current required to maintain a given phase shift.   Such characteristics are unacceptable in many applications.   Beam steering in a rapid scanning array, for example, requires high performance, variable phase shifters capable of fast switching, requiring low switching and holding power, and producible in large numbers at low cost.

The ferrite "digital"[2] or "latching" phase shifter concept represents a significant and promising advance in phase shifters for rapid scanning array application.   The innovation that distinguishes the digital phase shifter from its predecessors is the utilization, as the phase shift element, of a "square hysteresis loop" ferrite physically arranged to form a closed magnetic path.   Operation is then based on the change in propagation constant which occurs when the rf permeability of the ferrite is varied by changing the remanent magnetization of the ferrite.   The remanent magnetization is varied by switching from one remanent state to another around major or minor hysteresis loops.   Digital phase shifters can be realized in rectangular and cylindrical waveguide, coaxial, stripline, helical, meander and other transmission structures.

A cutaway view of a particularly useful nonreciprocal ferrite digital phase shifter is shown in Figure 1.   In this structure, the phase shifting element is a rectangular toroid of "square loop" ferrite positioned along the axis of the rectangular waveguide.   A single turn of wire coaxial to the ferrite toroid provides a path for the current pulses which magnetize the ferrite to either of two remanent magnetization states

---

* The word "ferrite" is used in this report to represent any ferrimagnetic material.

[1]   B. Lax and K. J. Button, Microwave Ferrites and Ferrimagnetics, McGraw-Hill Book Company, Inc., 1962. pp. 589-609.

[2]   M. A. Treuhaft and L. M. Silber, "Use of Microwave Ferrite Toroids to Eliminate External Magnets and Reduce Switching Power," Proc. IRE, vol. 46, p. 8, 1958.

$(+M_r$ or $-M_r)$ as shown in Figure 2. Bias power is thus required only in switching from one state to the other, i.e., no holding current is required. Corresponding to these states, there are phase shifts $+\phi_r$ and $-\phi_r$ and their difference, $\Delta\phi_r$, is the nonreciprocal, differential phase shift of the ferrite "bit." In the device several bits of different values are used in cascade to achieve step-wise variable, or digital, phase shift by activating (charging to $+M_r$) the appropriate combinations of bits, with the remaining bits left in the reference $(-M_r)$ state. The dielectric load of the toroid helps to concentrate the rf energy in the ferrite. If a total adjustable phase shift of 360° is required, for example, the lengths of the toroid segments might be selected so that phase shifts of 180°, 90°, 45°, 22.5^O, 11.25^O, and 5.625^O are obtained. The result is a phase shifter capable of exhibiting any differential phase shift from 0° to 360° in 5.625^O steps. Common terminology is to call such a device a six-digit or six-bit phase shifter.

As implied above, the FDPS may be devised in a variety of transmission structures and may be nonreciprocal or reciprocal, depending upon the manner in which the rf fields couple to the magnetic moments of the ferrite. All of the ferrite toroid may be immersed in the rf field or, alternatively, to aid in temperature stabilization, only a portion of the ferrite may be immersed in the rf field with the magnetic path completed by external ferrite segments.[3] However, in all the varieties of ferrite digital phase shifters, the properties of the ferrite itself have the dominant role in determining the "quality" of the device.

The sections that follow discuss and analyze the role of the ferrite properties in determining the operating characteristics of ferrite digital phase shifters. Material requirements for reciprocal and nonreciprocal phase shifters are very similar. Emphasis in the analysis and experiments reported here is placed on the nonreciprocal variety which, thus far, appears to be most promising for phased array application.

---

[3] E. Stern and W. J. Ince, "Temperature Stabilization of Unsaturated Microwave Ferrite Devices," 11th Annual Conf. on Magnetism and Magnetic Materials, San Francisco (November 1965); J. Appl. Phys. **37**, 1075 (1 March 1966).
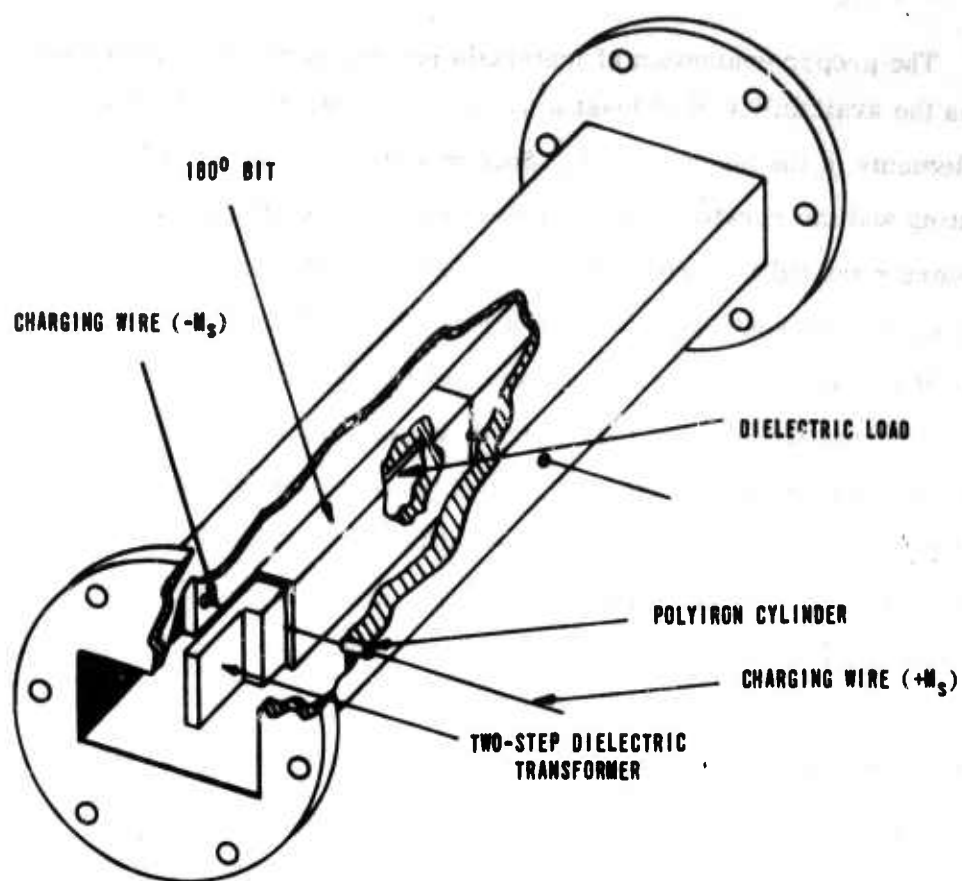
Figure 1. Cutaway View of a Waveguide Latching Phase Shifter
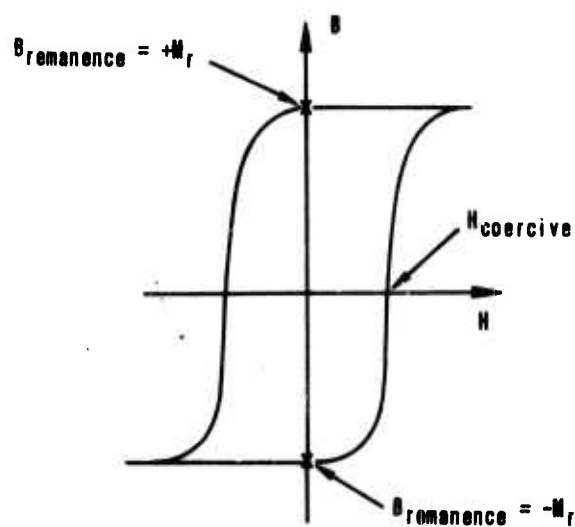
Figure 2. Hysteresis Loop of a High Remanence
(i.e., "Square-Loop") Ferrite

3.2 ANALYTICAL MODELS OF FERRITE DIGITAL PHASE SHIFTERS

The proper evaluation of materials for use in ferrite digital phase shifters requires the availability of at least a qualitative physical model for the materials and other elements of the phase shifter. Such models serve as an indispensable aid in correlating and interpreting experimental data. To be able to predict the material parameters required for producing a phase shifter with specified performance characteristics or, alternatively, to predict how a given material will perform in a phase shifter without actually carrying out an experimental test, it is necessary to have an accurate mathematical model for the material and other elements of the phase shifter. In addition to the mathematical models, analysis techniques are required which enable the transfer characteristics of the phase shifter to be related mathematically to the intrinsic material and dimensional parameters of the device structure. The validity of the mathematical models and analysis techniques must then be carefully evaluated by comparison of analytical predictions with the results of experiments performed on laboratory models of the phase shifter. With such models and analysis techniques available, the performance of ferrite in different frequency bands and with different geometries can be evaluated without having to resort to an actual laboratory measurement for each geometry and frequency.

A major difficulty in generating analytical models for ferrite devices is in the representation of the ferrite itself. If the ferrite is magnetically saturated, then its microwave magnetic properties, including magnetic losses, can be represented by the Landau - Lifshitz permeability tensor.[4] However, for a partially magnetized or remanent state material, such as those used in ferrite digital phase shifters, the Landau - Lifshitz permeability tensor is not an accurate representation of its magnetic properties and a more general representation, based on a generalized physical model of the ferrite, must be derived.

---

[4] B. Lax and K. J. Button, Ibid, P 154.

3.2.1 Microwave Magnetic Properties of Partially Magnetized Ferrites

The representation of the microwave magnetic properties, particularly of magnetic losses, in partially magnetized ferrites is complicated by the existence of a multiplicity of magnetic domains of various shapes and orientations. It has been suggested by Ince and Stern[5] and others that the remanent state ferrites in digital phase shifters can be treated as though the ferrite is magnetically saturated with an equivalent saturation magnetization equal to the actual remanence magnetization, so far as phase shift is concerned, and totally unmagnetized so far as losses are concerned. Magnetic losses are then represented by the artifice of a magnetic loss tangent ($\tan\delta = \frac{\mu''}{\mu'}$) in analogy with the lossy initial permeability of unmagnetized samples. This characterization suffers from the fact that it obscures the relation of the magnetic losses to the intrinsic parameters of the ferrite. Magnetic loss tangents of remanent state ferrite toroids are not intrinsic parameters of the material. The measured value of loss tangent varies with the manner in which it is measured, the frequency of the measurement, and so forth. Thus, in order for a magnetic loss tangent characterization of the losses in a device to be truly meaningful, the measurement frequency and the geometry of the test configuration (i.e., the manner in which the rf field couples to the magnetic moments of the ferrite) must be the same as those of the operational device.

Another issue arising in the characterization of remanent state ferrite toroids is the question of the value of the effective internal bias field H_i of the material. Because there is no externally applied bias field, a possible starting point is to assume that H_i is zero. This is in fact the procedure followed by most other investigators. However, inasmuch as a resonance type of loss has been experimentally observed in remanent state toroids,[6] it appears that the effective internal bias field is not zero, and this fact must be taken into account in any accurate model for partially magnetized materials.

---

[5] W.J. Ince and E. Stern, "Non-Reciprocal Remanence Phase Shifters in Rectangular Waveguide," IEEE International Convention Record, Part 5, p. 33, 1966.

[6] Final Report on "Advanced Ferrimagnetic Materials Applied To Digital Phase Shifters," Sperry Microwave Electronics Company, Report on ARPA Order No 550, Program Code No 4730, RADC Contract No AF-30(602)3490, January 1966, PP 130-160.

Because of the inherent disavantages of available characterizations of the microwave magnetic properties cf remanent state ferrites, a strong effort has been made to develop a model which accounts for observed phenomena and which can be used for accurate prediction of phase and loss characteristics in ferrite devices such as the digital phase shifter. In the "new" model for remanent state or partially magnetized ferrites, magnetic losses are accounted for via an intrinsic resonance linewidth, and the effects of a nonzero effective internal field are included. This model, to be described below, appears to account rather completely for the observed loss and phase properties of remanent state ferrite toroids.

The physical "picture" on which the new model is based is as follows. A saturated ferrite sample is composed of a single magnetic domain, i.e., all the microscopic moments in the material are aligned. However, in a remanent state or partially magnetized material, the microscopic magnetic moments are no longer all aligned. Instead, the sample will be composed of a number of magnetic domains, each of which is completely saturated (i.e. the moments are all aligned), but with the moments in various domains oriented in different directions. Each domain has associated with it an effective bias field which arises from magnetocrystalline anisotropy effects and from demagnetizing fields that result from the rf demagnetizing factors associated with the particular domain shape and environment (i.e. similar to the Polder – Smit argument).[7] The effective field of each domain may be different, and as a consequence in each domain the magnetization will exhibit precessional resonance at a characteristic frequency determined by the anisotropy field and the particular demagnetizing field of the domain. In general then, a spatial averaging process must be carried out to mathematically relate the net rf magnetization to the rf magnetic field, and it is apparent that the domain structure will exert an appreciable influence on the macroscopic properties of the material.

The permeability tensor for partially magnetized ferrites can be obtained by an extension of a concept suggested by Rado,[8] who made an extensive qualitative examination of arbitrarily magnetized ferrite media. In such media the intrinsic tensor relationship may be written in the form

[7] D. Polder and J. Smit, "Resonance Phenomena in Ferrites," Rev. Modern Physics, 25, 89(1953).

[8] G. T. Rado, "On the Electromagnetic Characterization of Ferromagnetic Media: Permeability Tensors and Spin Wave Equations, "IRE Trans. on Ant. and Prop., vol. AP-4, p. 512 (1956).

$$
\begin{bmatrix} <b_x> \\ <b_y> \\ <b_z> \end{bmatrix} = \mu_o \begin{bmatrix} <\mu_{11}> & <\mu_{12}> & <\mu_{13}> \\ <\mu_{21}> & <\mu_{22}> & <\mu_{23}> \\ <\mu_{31}> & <\mu_{32}> & <\mu_{33}> \end{bmatrix} \begin{bmatrix} <h_x> \\ <h_y> \\ <h_z> \end{bmatrix} \qquad (1)
$$

where $<b>$ and $<h>$ are the spatial averages of the time-varying components of the magnetic induction and the magnetic field intensity. The $<\mu_{j\kappa}>$ are effective permeability components averaged over several domains and, as such, are directly measurable quantities. Under the assumptions of Rado's theory, the relation between the macroscopic "point" field quantities $\vec{b}$ and $\vec{h}$ (not average) is given by a spin wave equation at points within the domain walls and by a tensor inside the domains, but the experimentally important relation between the average quantities $<\vec{b}>$ and $<\vec{h}>$ is given by a tensor everywhere. Relating $<\mu_{j\kappa}>$ to the measurable intrinsic magnetic properties of the ferrite is, in general, exceedingly difficult.

As suggested by Rado, the relation $<\mu_{j\kappa}>$ between the effective rf fields $<\vec{b}>$ and $<\vec{h}>$ can sometimes be obtained by performing spatial averages on the relation $\mu_{j\kappa}$ between the "point" rf fields $\vec{b}$ and $\vec{h}$ of an appropriate saturated media problem. With this in mind the relationships between $\vec{b}$ and $\vec{h}$ for a ferrite sample consisting of a single domain magnetized by an applied magnetic field will now be considered.[*] The saturation magnetization $\vec{M}_s$ of the domain and the net effective magnetic field $\vec{H}_i'$ are assumed to be oriented in different directions as shown in Figure 3.

---

[*] The following derivation closely follows that of J. L. Allen as given in "The Analysis of Ferrite Phase Shifters Including the Effects of Losses," Ph.D. Dissertation, Georgia Institute of Technology, May, 1966.
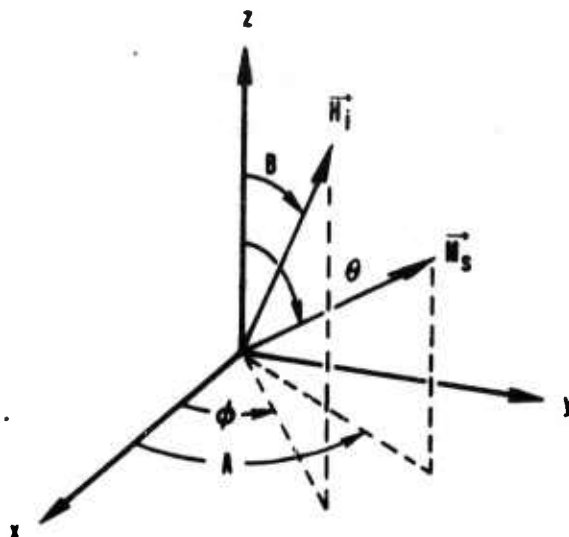
Figure 3. Relative Directions of the Saturation Magnetization
$\vec{M}_s$ and of the Net Effective Static Magnetic Field
Acting on a Single Domain

The equation of motion for the macroscopic magnetization, including losses
via the Landau-Lifshitz damping term, is

$$\frac{d\vec{M}}{dt} = \gamma_e (\vec{M} \times \vec{H}) - \frac{\alpha}{M} \vec{M} \times \frac{d\vec{M}}{dt} \qquad (2)$$

where $\quad \vec{M} = \vec{M}_s + \vec{m}e^{j\omega t} \quad \vec{H} = \vec{H}_i + \vec{h}e^{j\omega t}$

$$\vec{M}_s = \left|\vec{M}_s\right| \left|\vec{i} \sin\theta\cos\phi + \vec{j} \sin\theta\sin\phi + \vec{\kappa} \cos\theta\right| = \text{saturation magnetization}$$

$$\vec{h} = \vec{i}h_x + \vec{j}h_y + \vec{\kappa}h_z = \text{rf magnetic field}$$

$$\vec{m} = \vec{i}m_x + \vec{j}m_y + \vec{\kappa}m_z = \text{rf magnetization}$$

$$\gamma_e = \gamma(1 + \alpha^2), \ \alpha = \frac{1}{\omega\tau}, \ \tau = \text{damping time-constant}$$

$$\vec{H}_i = \vec{i}H_x + \vec{j}H_y + \vec{\kappa}H_z = \text{net effective field acting on a single domain}$$

$$= \left|\vec{H}_i\right| \left|\vec{i} \sin B \cos A + \vec{j} \sin B \sin A + \vec{\kappa} \cos B\right|$$

Expanding Equation 2, equating coefficients of $e^{j\omega t}$, and after considerable algebra the following small signal permeability is obtained.

$$
\vec{\mu} = \mu_0 \begin{bmatrix} \mu_{11} & \mu_{12} & \mu_{13} \\ \mu_{21} & \mu_{22} & \mu_{23} \\ \mu_{31} & \mu_{32} & \mu_{33} \end{bmatrix} \tag{3}
$$

$$
\mu_{11} = 1 + \frac{\gamma_e |\vec{M}_s|}{\Delta} \left\{ \left[\gamma_e H_z (\cos\theta - \alpha \sin^2\theta \sin\phi\cos\phi) + \gamma_e H_y (\sin\theta\sin\phi \right.\right.
$$
$$
\left. + \alpha\sin\theta\cos\theta\cos\phi) \right] + j \left[\omega\alpha(\cos^2\theta + \sin^2\phi\sin^2\theta) \right.
$$
$$
\left.\left. + \frac{1}{\omega}(\gamma_e H_z \gamma_e H_x \sin\theta\sin\phi - \gamma_e H_x \gamma_e H_y \cos\theta) \right] \right\}
$$

$$
\mu_{12} = \frac{-j\gamma_e |\vec{M}_s|}{\Delta} \left\{ \omega\cos\theta + \alpha\sin^2\theta\cos\phi \left(\omega\sin\phi + j\gamma_e H_z \cos\phi \right) \right. \tag{4}
$$
$$
- \frac{1}{\omega}(\gamma_e H_x)(\gamma_e H_x \cos\theta + \gamma_e H_z \sin\theta\cos\phi) + j(\alpha\gamma_e H_x \cos\theta
$$
$$
\left. - \gamma_e H_y)\sin\theta\cos\phi \right\}
$$

$$
\mu_{13} = \frac{-j\gamma_e |\vec{M}_s|}{\Delta} \left\{ -\omega\sin\theta\sin\phi + \omega\alpha\cos\theta\sin\vartheta\sin\phi + \frac{1}{\omega}\cdot \gamma_e H_x \sin\theta(\gamma_e H_x \sin\phi \right.
$$
$$
- \gamma_e H_y \cos\phi) + j\alpha\sin^2\theta\cos\phi(2\gamma_e H_x \sin\phi - \gamma_e H_y \cos\phi)
$$
$$
\left. -j\gamma_e H_z \sin\theta\cos\phi \right\}
$$

$$
\mu_{21} = \frac{-j\gamma_e |\vec{M}_s|}{\Delta} \left\{ -\omega\cos\theta + \omega\alpha\sin^2\theta\sin\phi\cos\phi + \frac{1}{\omega}\gamma_e H_y(\gamma_e H_y \cos\theta \right.
$$
$$
\left. - \gamma_e H_z \sin\theta\sin\phi) + j\sin\theta\sin\phi(\alpha\gamma_e H_y \cos\theta - \alpha\gamma_e H_z \sin\theta\sin\phi - \gamma_e H_x) \right\}
$$

$$\mu_{22} = 1 + \frac{\gamma_e |\vec{M}_s|}{\Delta} \left\{ \gamma_e H_z (\cos\theta + \alpha \sin^2\theta \sin\phi\cos\phi) \right.$$

$$+ \gamma_e H_z \sin\theta(\cos\phi - \alpha\cos\theta\sin\phi) + j\omega\alpha(\cos^2\theta + \cos^2\phi \sin^2\theta)$$

$$\left. + \frac{1}{\omega} \gamma_e H_y (\gamma_e H_x \cos\theta - \gamma_e H_z \sin\theta\cos\phi) \right\}$$

$$\mu_{23} = \frac{-j\gamma_e |\vec{M}_s|}{\Delta} \left\{ \omega\sin\theta\cos\phi + \omega\alpha\cos\theta\sin\theta\sin\phi \right.$$

$$+ \frac{1}{\omega} \gamma_e H_y (\gamma_e H_x \sin\theta\sin\phi - \gamma_e H_y \sin\theta\cos\phi)$$

$$\left. + j\alpha\gamma_e H_x \sin^2\theta \sin^2\phi - j\gamma_e H_z \sin\theta\sin\phi - j\alpha\gamma_e H_y \sin^2\theta \sin\phi\cos\phi \right\}$$

$$\mu_{31} = \frac{-j\gamma_e |\vec{M}_s|}{\Delta} \left\{ \omega\sin\theta\sin\phi + \omega\alpha\sin\theta\cos\theta\cos\phi \right.$$

$$+ \frac{1}{\omega} \gamma_e H_z (\gamma_e H_y \cos\theta - \gamma_e H_z \sin\theta\sin\phi)$$

$$\left. + j\alpha\gamma_e H_y \cos^2\theta - j\gamma_e H_x \cos\theta - j\alpha\gamma_e H_z \sin\theta\cos\theta\sin\phi \right\}$$

$$\mu_{32} = \frac{-j\gamma_e |\vec{M}_s|}{\Delta} \left\{ -\omega\sin\theta\cos\phi + \omega\alpha\sin\theta\cos\theta\sin\phi \right.$$

$$+ \frac{1}{\omega} \gamma_e H_z (\gamma_e H_z \sin\theta\cos\phi - \gamma_e H_x \cos\theta)$$

$$\left. - j\alpha\gamma_e H_x \cos^2\theta - j\gamma_e H_y \cos\theta + j\alpha\gamma_e H_z \cos\theta\sin\theta\cos\phi \right\}$$

$$\mu_{33} = 1 + \frac{\gamma_e |\vec{M}_s|}{\Delta} \left\{ \alpha\gamma_e H_x \sin\theta\cos\theta\sin\phi + \gamma_e H_y \sin\theta\sin\phi \right.$$

$$- \alpha\gamma_e H_y \sin\theta\cos\theta\cos\phi + \gamma_e H_x \sin\theta\cos\phi$$

$$\left. - j\frac{1}{\omega} \gamma_e H_z (\gamma_e H_x \sin\theta\sin\phi + \gamma_e H_y \sin\theta\cos\phi) + j\omega\alpha\sin^2\theta \right\}$$

where

$$\Delta = \left[-\omega^2 - (\omega\alpha)^2 + (\gamma_e|\vec{H}_i|)^2\right] + j\left[2\omega\alpha\gamma_e H_x \sin\theta\cos\phi \right.$$
$$\left. + 2\omega\alpha\gamma_e H_y \sin\theta\sin\phi + 2\omega\alpha\gamma_e H_z \cos\theta\right]$$

$$H_x = |\vec{H}_i|\sin B \cos A$$

$$H_y = |\vec{H}_i|\sin B \sin A$$

$$H_z = |\vec{H}_i|\cos B$$

If θ and B are both zero, corresponding to a saturated media with saturation magnetization and bias field oriented in the same direction, the permeability given in Equation 4 reduces to the familar Landau-Lifshitz form.

As previously noted, an unsaturated material is composed of many domains with the magnetizations of the individual domains oriented at different angles (θ-B, ϕ-A) relative to the effective internal magnetic field $\vec{H}_i$. The result of Equation 4 can be extended so that it applies in unsaturated media if spatial averages which extend over several domains can be performed. Since the distributions of the magnetizations of the domains as functions of ϕ and θ and of the $\vec{H}_i$'s as functions of B and A are not always known, the averaging cannot, in general, be carried out explicitly. However, observing that, in most cases of practical interest, there exists a physically preferred direction for the magnetization and the effective static magnetic field often permits the averaging with respect to angles in the plane perpendicular to the preferred direction to be performed explicitly. The physically preferred direction of magnetization may arise in various ways. For instance, if we apply even a very small dc bias field to the sample, a preferred direction of magnetization is established in the direction of the applied field. Alternatively, if we arrange the ferrite so that it forms a closed magnetic path, such as the toroids in the latching phase shifters, the geometry of the sample establishes preferred magnetization directions. Assume, then, that the preferred magnetization direction is the +z direction and that this is also the preferred direction for the $\vec{H}_i$'s. For this

3-11

situation, all values of ϕ and of A between 0 and 2π are equally likely. If it is assumed that $\left|\vec{M}_s\right|$ and $\left|\vec{H}_i\right|$ have the same value for all of the "several domains" over which the spatial averaging is to be performed and that the angles between the $\vec{H}_i$'s and the z-axis are small, the tensor permeability of Equation 3 after averaging with respect to ϕ and A becomes

$$\langle \vec{\mu} \rangle_{\phi, A} = \mu_o \begin{bmatrix} \langle \mu_{11} \rangle_{\phi, A} & \langle \mu_{12} \rangle_{\phi, A} & 0 \\ \langle \mu_{21} \rangle_{\phi, A} & \langle \mu_{22} \rangle_{\phi, A} & 0 \\ 0 & 0 & \langle \mu_{33} \rangle_{\phi, A} \end{bmatrix} \tag{5}$$

$$\langle \mu_{11} \rangle_{\phi, A} = \langle \mu_{22} \rangle_{\phi, A} = 1 + \frac{\gamma_e \left|\vec{M}_s\right| \left| \gamma_e \left|\vec{H}_i\right| \cos\theta + j\omega\alpha \left(\cos^2\theta + \frac{1}{2}\sin^2\theta\right) \right|}{\Delta} \tag{6}$$

$$\langle \mu_{12} \rangle_{\phi, A} = -\langle \mu_{21} \rangle_{\phi, A} = \frac{-j \, \gamma_e \left|\vec{M}_s\right| \left| \omega\cos\theta + j \frac{\alpha \gamma_e \left|\vec{H}_i\right| \sin^2\theta}{2} \right|}{\Delta}$$

$$\langle \mu_{33} \rangle_{\phi, A} = 1 + \frac{\left| j\omega\alpha \sin^2\theta \right|}{\Delta}$$

$$\langle \mu_{13} \rangle_{\phi, A} = \langle \mu_{31} \rangle_{\phi, A} = \langle \mu_{23} \rangle_{\phi, A} = \langle \mu_{32} \rangle_{\phi, A} = 0$$

where $\Delta = \left[\left(\gamma_e \left|\vec{H}_i\right|\right)^2 - \omega^2 - (\omega\alpha)^2 \right] + j \left[2 \gamma_e \left|\vec{H}_i\right| \omega\alpha\cos\theta \right]$

It is now convenient to change notation and write

$$\langle \mu \rangle_{\phi, A} = \langle \mu_{11} \rangle_{\phi, A} = \langle \mu_{22} \rangle_{\phi, A}$$

$$-j\langle k \rangle_{\phi, A} = \langle \mu_{12} \rangle_{\phi, A} = -\langle \mu_{21} \rangle_{\phi, A}$$

$$\langle \mu_z \rangle_{\phi, A} = \langle \mu_{33} \rangle_{\phi, A}$$

Separating $\langle \mu \rangle_{\phi,A}$, $\langle \kappa \rangle_{\phi,A}$, and $\langle \mu_z \rangle_{\phi,A}$ into real and imaginary parts yields after some simplifying algebra

$$\langle \mu' \rangle_{\phi,A} = 1 + \frac{\gamma_e |\vec{M}_s| \, \gamma_e |\vec{H}_1| \cos\theta \left\{ \left[\gamma_e |\vec{H}_1| \right]^2 - \omega^2 - [\omega\alpha]^2 \cos^2\theta \right\}}{\Delta} \qquad (7)$$

$$\langle \mu'' \rangle_{\phi,A} = \frac{\gamma_e |\vec{M}_s| \omega\alpha \cos^2\theta \left\{ -\frac{3}{2} (\gamma_e |\vec{H}_1|)^2 + \frac{1}{2}\omega^2 + \frac{1}{2}(\omega\alpha)^2 \right.}{\Delta}$$
$$\left. - \frac{1}{2} \left[(\gamma_e |\vec{H}_1|)^2 - \omega^2 - (\omega\alpha)^2 \right] \right\}$$

$$\langle \kappa' \rangle_{\phi,A} = \frac{\gamma_e |\vec{M}_s| \omega \cos\theta \left\{ (\gamma_e |\vec{H}_1|)^2 \alpha^2 \sin^2\theta + \left[(\gamma_e |\vec{H}_1|)^2 - \omega^2 - (\omega\alpha)^2 \right] \right\}}{\Delta}$$

$$\langle \kappa'' \rangle_{\phi,A} = \frac{\gamma_e |\vec{M}_s| \omega\alpha \gamma_e |\vec{H}_1| \left\{ 2\omega - \frac{\sin^2\theta}{\omega} \left[\frac{1}{2}(\gamma_e |\vec{H}_1|)^2 \right. \right.}{\Delta}$$
$$\left. \left. + \frac{3}{2}\omega^2 - \frac{1}{2}(\omega\alpha)^2 \right] \right\}$$

$$\langle \mu_z' \rangle_{\phi,A} = 1 + \frac{\gamma_e |\vec{M}_s| \left\{ (\omega\alpha)^2 (\gamma_e |\vec{H}_1|) (2\sin^2\theta \cos\theta) \right\}}{\Delta}$$

$$\langle \mu_z'' \rangle_{\phi,A} = \frac{\gamma_e |\vec{M}_s| \left\{ \omega\alpha \sin^2\theta \left[\omega^2 + (\omega\alpha)^2 - (\gamma_e |\vec{H}_1|)^2 \right] \right\}}{\Delta}$$

where $\Delta = \left[(\gamma_e |\vec{H}_1|)^2 - \omega^2 - (\omega\alpha)^2 \right]^2 + \left[2\gamma_e |\vec{H}_1| \omega\alpha \cos\theta \right]^2$

If the angle between $\vec{H}_1$ and the z-axis is large, the expressions for the components of the permeability tensor are somewhat more complicated. In this more general situation the permeability components, after averaging with respect to angles in the xy-plane, are functions of both θ and B. To perform the averages

with respect to θ and B, it is necessary to know the distribution of these angles as functions of the other parameters of the problem (e.g., as a function of the applied bias field).

For the case in which the angle between $\vec{H}_1$ and the z-axis is small, the permeability components, as given in Equation 7, are functions of θ alone. Even in this case, the average with respect to θ cannot be performed explicitly without making specific assumptions about the distributions of θ as a function of the applied bias field. However, because the average with respect to θ is intimately related to measurable physical quantities, a very useful form of the permeability tensor for unsaturated media can be obtained as follows. Write the average of the permeability components given in Equation 7 with the operator $\langle \ \rangle_\theta$ denoting spatial average with respect to θ. Collecting terms and recognizing their physical significance leads to the desired permeability components. Writing out the average with respect to θ, the following expressions are obtained

$$\langle \mu' \rangle_{\phi, A, \theta} = 1 + \frac{1}{\Delta}\left\{ \gamma_e|\vec{H}_1|\left[(\gamma_e|\vec{H}_1|)^2 - \omega^2\right]\gamma_e|\vec{M}_s| \langle \cos\theta \rangle_\theta \right. \tag{8}$$
$$\left. + \gamma_e|\vec{H}_1|(\omega\alpha)^2 \gamma_e|\vec{M}_s|\langle \cos^3\theta \rangle_\theta \right\}$$

$$\langle \mu'' \rangle_{\phi, A, \theta} = \frac{\omega\alpha}{\Delta}\left\{\left[\frac{3}{2}(\gamma_e|\vec{H}_1|)^2 + \frac{1}{2}\omega^2 + \frac{1}{2}(\omega\alpha)^2\right]\gamma_e|\vec{M}_s|\langle\cos^2\theta\rangle_\theta \right.$$
$$\left. - \frac{\gamma_e|\vec{M}_s|}{2}\left[(\gamma_e|\vec{H}_1|)^2 - \omega^2 - (\omega\alpha)^2\right]\right\}$$

$$\langle \kappa' \rangle_{\phi, A, \theta} = \frac{1}{\Delta}\left\{(\gamma_e|\vec{H}_1|)^2\alpha^2 \gamma_e|\vec{M}_s|(\langle\cos\theta\rangle_\theta - \langle\cos^3\theta\rangle_\theta) \right.$$
$$\left. + \left[(\gamma_e|\vec{H}_1|)^2 - \omega^2 - (\omega\alpha)^2\right]\gamma_e|\vec{M}_s|\langle\cos\theta\rangle_\theta\right\}$$

3-14

$$\langle \kappa'' \rangle_{\phi, A, \theta} = \frac{\omega \alpha \gamma_e |\vec{H}_1|}{\Delta} \left\{ 2\omega \gamma_e |\vec{M}_s| - \frac{1}{\omega} \left[\frac{1}{2}(\gamma_e |\vec{H}_1|)^2 + \frac{3}{2}\omega^2 \right. \right.$$
$$\left. \left. - \frac{1}{2}(\omega\alpha)^2 \right] \gamma_e |\vec{M}_s| (1 - \langle \cos^2\theta \rangle_\theta) \right\}$$

$$\langle \mu_z' \rangle_{\phi, A, \theta} = 1 + \frac{1}{\Delta} \left| (\omega\alpha)^2 (\gamma_e |\vec{H}_1|)(2\gamma_e|\vec{M}_s|)(\langle\cos\theta\rangle_\theta - \langle\cos^3\theta\rangle_\theta) \right|$$

$$\langle \mu_z'' \rangle_{\phi, A, \theta} = \frac{\omega\alpha}{\Delta} \left| \left[\omega^2 + (\omega\alpha)^2 - (\gamma_e|\vec{H}_1|)^2 \right] \left| \gamma_e|\vec{M}_s| \right| \left[1 - \langle\cos^2\theta\rangle_\theta \right] \right|$$

Where it has been recognized that the second term of Δ is very small compared to the first term for parameter values corresponding to the normal operating range of phase shifters so that $\Delta \approx \left[-\omega^2 + (\gamma_e|\vec{H}_1|)^2 - (\omega\alpha)^2 \right]^2$.

In the permeability components of Equation 8, terms of the form $|\vec{M}_s| \langle\cos\theta\rangle_\theta$, $|\vec{M}_s| \langle\cos^2\theta\rangle_\theta$, and $|\vec{M}_s| \langle\cos^3\theta\rangle_\theta$ are observed to occur. The first term, $|\vec{M}_s| \langle\cos\theta\rangle_\theta$, is physically just the remanent magnetization, M_r, in the z-direction. The second and third terms can be related to the remanence ratio, R_r, which is defined by

$$R_r = \frac{M_r}{|\vec{M}_s|} = \langle\cos\theta\rangle_\theta .$$ If M_r is to be greater than zero, the distribution of the magnetizations of the domains with respect to θ must be "peaked" in the first quadrant so that $\langle\cos\theta\rangle_\theta > 0$. If this is true, it is easily shown that

$$|\vec{M}_s| \langle\cos^2\theta\rangle_\theta \geq |\vec{M}_s| \left| \langle\cos\theta\rangle_\theta \right|^2 = |\vec{M}_s| R_r^2$$

and

$$|\vec{M}_s| \langle\cos^3\theta\rangle_\theta \leq |\vec{M}_s| \cdot \langle\cos\theta\rangle_\theta = |\vec{M}_s| R_r.$$

The saturation magnetization $|\vec{M}_s|$ and the remanent magnetization can be measured by independent methods. The damping constant α (or ΔH) can be determined from other measurements. The quantities $\langle\cos^2\theta\rangle_\theta$ and $\langle\cos^3\theta\rangle_\theta$ can be approximated by R_r^2 and R_r^3, respectively, where R_r

3-15

is the measured ratio of remanence magnetization to saturation magnetization. Since ω the microwave radian frequency, will be known, this leaves only $\left|\vec{H}_i\right|$ as an unknown factor in Equation 8. $\left|\vec{H}_i\right|$ can often be estimated by using Kittels equation to compute an effective field for an "average" or "major" domain. The demagnetizing factors for the "average" domain can often be estimated from the geometry of the sample.

It is significant that the real and imaginary parts of the permeability components depend in different ways upon $<\cos\theta>_\theta$, $<\cos^2\theta>_\theta$, and $<\cos^3\theta>_\theta$. The following special case vividly displays these differences. Suppose that $\left|\vec{H}_i\right| = 0$ in Equation 8. The permeability components then become

$$<\mu'>_{\phi,\,A,\,\theta} \approx 1$$

$$<\kappa'>_{\phi,\,A,\,\theta} \approx \frac{-\omega\gamma_e\left|\vec{M}_s\right|<\cos\theta>_\theta}{\left[\omega^2 + (\omega\alpha)^2\right]}$$

$$<\mu_z'>_{\phi,\,A,\,\theta} \approx 1$$

$$<\mu''>_{\phi,\,A,\,\theta} \approx \frac{\omega\alpha\left[\dfrac{\gamma_e\left|\vec{M}_s\right|}{2}(1 + <\cos^2\theta>_\theta)\right]}{\left[\omega^2 + (\omega\alpha)^2\right]}$$

$$<\kappa''>_{\phi,\,A,\,\theta} \approx 0$$

$$<\mu_z''>_{\phi,\,A,\,\theta} \approx \frac{\omega\alpha\gamma_e\left|\vec{M}_s\right|}{\left[\omega^2 + (\omega\alpha)^2\right]}(1 - <\cos^2\theta>_\theta)$$

where

$$\left|\vec{M}_s\right|<\cos\theta>_\theta = \text{remanent magnetization} = M_r$$

$$<\cos\theta>_\theta = \text{remanent ratio} = R_r$$

Then $\dfrac{1}{2}\left|\vec{M}_s\right|<1 + \cos^2\theta>_\theta = \dfrac{1}{2}\left|\vec{M}_s\right|\left\{1 + <\cos^2\theta>_\theta\right\}$

$$\geq \dfrac{1}{2}\left|\vec{M}_s\right|\left(1 + \left[<\cos\theta>_\theta\right]^2\right).$$

3-16

Therefore, $\frac{1}{2}\left|\vec{M}_s\right| < 1 + \cos^2\theta >_\theta \overset{d}{=} M_{L_{xy}} \geq \frac{1}{2}\left|\vec{M}_s\right|(1 + R_r^2)$.

Similarly, $\left|\vec{M}_s\right| < 1 - \cos^2\theta >_\theta = \left|\vec{M}_s\right|\left\{1 - <\cos^2\theta>\right\}$

$$\leq \left|\vec{M}_s\right|\left(1 - \left[<\cos\theta>_\theta\right]^2\right) \text{ or } \left|\vec{M}_s\right| < 1 - \cos^2\theta >_\theta \overset{d}{=} M_{L_z}$$

$\leq \left|\vec{M}_s\right|(1 - R_r^2)$. Thus the magnetization enters the real and imaginary parts of the permeability components in different manners. The appropriate effective magnetization to use in the real (phase shift) part is the remanent magnetization, M_r, while the proper effective magnetization to use in the imaginary (loss) parts is $M_{L_{xy}}$ for the xy-components and M_{L_z} for the z-component. The bounds on the M_L's are

$$\frac{1}{2}\left|\vec{M}_s\right|(1 + R_r^2) \leq M_{L_{xy}} \leq \left|\vec{M}_s\right|$$

$$0 \leq M_{L_z} \leq \left|\vec{M}_s\right|(1 - R_r^2)$$

The magnetic losses represented by the imaginary parts of the permeability components of Equation 8 physically represent the spatial averages of losses due to damping of the precessional motion of the magnetization within the individual domains. The effective static magnetic field H_i is to be interpreted as an effective internal field which includes anisotropy and demagnetizing effects. With this interpretation, the high-frequency portion of the "low-field" losses[9] are accounted for directly by the model. The model does not include domain-wall losses. However, in high-density, unstressed ferrites domain-wall losses are usually confined to the frequency region below 100 Mc[10] and will, therefore, not be important in predicting losses at microwave frequencies.

[9] Ibid, P446
[10] Ibid, P541

The mathematical model, which has been described above, for the proper-
ties of remanent state or partially magnetized ferrites has been utilized in the solution
of the boundary value problems for several FDPS configurations. The results of these
computations, together with comparison with experimental data, are given in Section
4.5. Very good correlation of experimental and analytical results is obtained leading
to considerable confidence in the above model.

3.2.2 High Power Characteristics of Partially Magnetized Ferrites

Performance characteristics of ferrite phase shifters normally deteriorate
as either the rf average power or peak power level is increased to high values. De-
gradation of performance characteristics at high average power levels is due pri-
marily to heating effects and may be controlled to some extent by designing the device
structures to promote efficient removal of heat from the ferrite and/or utilizing
ferrites having temperature stable properties.

As the peak rf input power to a ferrite device is increased, a threshold power
level will be reached beyond which the insertion loss will increase appreciably due to
inherent nonlinearities of the system of precessing dipole moments. The peak power
capacity of FDPS depends both on the intrinsic threshold or critical field (h_{crit}) of the
ferrite and on the dimensional and electromagnetic parameters of the device structure
through their influence on the actual rf magnetic field intensity that will exist in the
ferrite for a given input power level. The nonlinear or high power effects in saturated
ferrites has been reasonably well explained in terms of spinwave interactions.[11] There
has, however, been some question as to the role of spinwave interactions in nonlinear
phenomena in remanent state materials.

The domain model, which was used in Section 3.2.1 to obtain a mathematical
representation of the low power properties of partially magnetized materials, offers
a means by which high power phenomena in remanent state materials can be interpreted
in terms of the theory developed for saturated materials. A partially magnetized
ferrite sample, such as the "latched" toroid in a FDPS, is made up of a number of
domains of various shapes, sizes, and orientations. The magnetic moments within
each domain are all, of course, aligned (i.e., a domain is, by definition, a saturated
region). When an rf field is applied to a partially magnetized sample, the magnetic

[11] Ibid, page 206

3-18

moments of each domain "see" an effective field determined by magnetocrystalline anisotropy and the rf demagnetizing factors of the domain. Each saturated region or domain may thus experience an effective bias field different from that of all other domains. The rf magnetic field intensity (h_{crit}), for which the precession of the magnetic spin system first becomes unstable, is a function of intrinsic ferrite properties (saturation magnetization, spinwave linewidth, etc.), operating frequency (ω) and the effective internal bias field (H_i). When the maximum rf magnetic field intensity in a domain exceeds h_{crit} for that domain, the spin system becomes unstable and nonlinear effects contribute to the losses. Therefore, for a given ferrite at a specified frequency, the domain or domains biased most unfavorably will go unstable first.

From the nonlinear theory for saturated samples, it is well known that high power effects in ferrites arise from the unstable buildup of oscillations of pairs of spinwaves whose frequencies are either degenerate with the microwave signal frequency or equal to one-half the operating frequency. The half-frequency spinwaves are more closely coupled to the uniform precession of the magnetization than are the degenerate spinwaves. Thus, the diversion of energy from the uniform precession to half-frequency spinwaves is known as a first order process, while the coupling to degenerate spinwaves is referred to as second order.

The second order nonlinear process, when it takes place, results in a saturation of the main resonance absorption line. The minimum threshold field for the second order process occurs when the material is biased to resonance. For lower or higher bias fields, the threshold field for this process is quite high.

The first order nonlinear process may occur when the material is biased to resonance, or it may be observed as an anomalous absorption at bias field values below that required for resonance. Effective bias field values in the remanent state toroids used in FDPS are normally well below the field required for resonance. For this case, the threshold field for the first order process is appreciably lower than that for the second order process. Therefore, the first order process, in which energy is transferred from the uniform precession to half-frequency spinwaves, is the nonlinear process that limits the high peak power performance of digital phase shifters.

3-19

Since the occurance of the first order nonlinear process depends upon the availability of half-frequency spinwaves, considerable insight into the magnitude of the threshold field h_{crit} can be obtained from an examination of the spinwave dispersion relationship. Figure 4 illustrates the spinwave dispersion curve in traditional manner. The abscissa is the spinwave number, $k = 2\pi/\lambda$, where λ is the spinwave wavelength. The ordinate is frequency. The upper curve is for spinwaves propagating perpendicular to the magnetization and the lower curve for spin waves propagating parallel to the static magnetization. The position of the spinwave manifold relative to the microwave signal frequency ω can be adjusted by varying the saturation magnetization of the ferrite or its effective bias field. If the position of the spinwave manifold is such that $\omega/2$ is greater than ω_b, then half-frequency spinwave states are available and the first order process will take place at sufficiently high power levels. If the spin wave manifold is positioned such that $\omega/2$ is less than ω_b, half-frequency spinwaves are not available* and the first order process is forbidden. In remanent state toroids $\omega/2$ is normally greater than ω_b, and the first order process is allowed. The damping of the
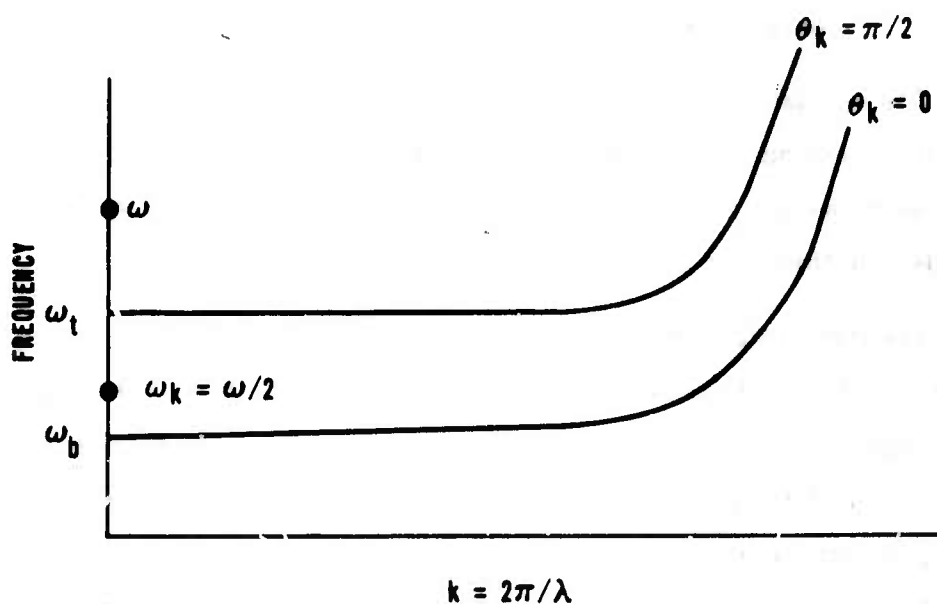
Figure 4. Conventional Spinwave Manifold Showing the Dependence of Availability Spinwave Numbers (k) on Operating Frequency (ω)

---

* There are, however, discrete "Walker" modes[10] with very low k numbers which have frequencies somewhat less than ω_b.

uniform precession by the various spinwaves depends upon the wave number k of the spinwaves to which energy is being transformed. Thus, the spinwave linewidth is a function of k.

It appears that the dependence of ΔH_k on k is $\Delta H_k = A + B k$ where A and B are intrinsic material parameters.[12] The parameter A is the spinwave linewidth for k = 0 modes. The magnitude of A depends heavily upon material composition. For polycrystalline YIG, A is of the order of five oersteds. Materials doped with fast re-laxing ions, such as the rare earths Dy, Ho, Yb, etc., have much larger A's. Four percent Dy doped YIG for example, has an A value of about 150 oersteds. The Bk term in the ΔH_k expression does not appear to depend upon composition. That is, Bk for YIG seems to be about the same as Bk for a heavily rare earth doped material. Therefore, the Bk factor is much more important in determining the magnitude of ΔH_k for materials such as YIG than for rare earth doped materials. In fact, for heavy rare earth doping, A may well be so large that it "swamps" the Bk term to such an extent that ΔH_k appears to be independent of k.

The first order nonlinear process can occur both for the normal pumping arrangement in which the rf magnetic field lies in a plane perpendicular to the direction of the static magnetization and for the parallel pumping scheme in which the rf magnetic field is parallel to the static magnetization direction. Perpendicular and parallel pumping occur simultaneously in the usual internal toroid FDPS. The threshold fields for normal and parallel pumping are somewhat different, and Stern[13] has expressed the threshold for pumping at some oblique angle, ϕ, in terms of normal and parallel thresholds as:

$$\frac{1}{h_{th_o}} = \frac{1 + \sin \phi}{h_{crit_n}} + \frac{\cos \phi}{h_{crit_p}}$$

where subscript o, n, and p refer to oblique, normal, and perpendicular pumping and ϕ is the angle between the rf field and dc magnetization. Both h_{crit_n} and h_{crit_p}

[12] Comstock App. Physics Jnl., 6, 29 (1955)

[13] E. Stern, Nonlinear Threshold in Remanent Ferrite, Presented at the G-MTT 1967 at the International Microwave Symposium, 9 May 1967

are directly proportional to the spinwave linewidth ΔH_k and inversely proportional to the ratio of the saturation magnetization and frequency ω_m/ω, thus the threshold for the general case will be of the form

$$h_{crit} = \left[\Delta H_k \Big/ (\omega_m/\omega)\right] \left[F(H_1, \theta_k)\right] \tag{9}$$

where $\omega_m = \gamma 4\pi M_s$ and $F(H_1, \theta_k)$ is a function of bias field H_1 and spinwave propagation direction θ_k as appropriate for the pumping arrangement under consideration. Direct control of h_{crit} for both normal and parallel pumping at a given frequency can thus be obtained by variation of ΔH_k (such as by rare earth doping of garnets) or by variation of ω_m/ω (for example, by aluminum doping of garnets). The damping of the various spinwaves depends upon their wave numbers k with the shorter wavelength modes being more heavily damped.

An abrupt change in the threshold field for both normal and parallel pumping should occur when the spinwave manifold is positioned so that $\omega_k = \omega/2$ is greater than ω_t. In this situation the only half-frequency spinwaves available are those with very large k values. Thus, since $\Delta H_k = A + Bk$, ΔH_k, and hence h_{crit}, increases abruptly as low k half-frequency spinwaves become unavailable. This effect will be most marked for materials having low A values (e.g., pure YIG) and will be less important as rare earth doping is increased to provide very large values of $\Delta H_k\big|_{k=0}$.

From the above discussion some interesting observations can be made about the values to be expected from measurements of the apparent critical field, h_{crit} for FDPS. A variety of domains, each having a different effective bias field, exist in a remanent state toroid (or any other partially magnetized sample). The measurement of the high power threshold for a phase shifter consists simply of detecting the rf peak power level at which the device insertion loss first increases from its low power level. This effect will take place at the power level for which the precession of the magnetic moments in the most <u>unfavorably biased domain</u> first goes unstable. To obtain higher threshold powers in FDPS, it is therefore necessary to increase the threshold field of the most unfavorable domains. Doping with rare earths accomplishes this feat by increasing the ΔH_k of all domains, including the most unfavorable, and the observed

threshold power level naturally increases. Decreasing ω_m/ω likewise increases the h_{crit} of each domain somewhat. As ω_m/ω is decreased, the effective bias field (arising from demagnetization effects) for each domain also decreases. The most dramatic influence on the threshold field from variation in ω_m/ω occurs when ω_m/ω is decreased to the point where the effective bias field of every domain is such that there are no low k, $\omega/2$ spinwaves available, i.e., where the relative position of the spinwave manifold is such that $\omega/2 > \omega_t$. At this value of ω_m/ω an abrupt increase in h_{crit} occurs. The value of ω_m/ω for which all domains are biased so that $\omega/2 > \omega_t$ can be estimated as follows.

At low values of ω_m/ω the most unfavorable biasing of a domain possible occurs for the Polder-Smit (anti-parallel) domains. For these domains H_i is approximately $(4/3\ K_1/M_s + 4\pi M_s)$, or if K_1/M_s is negligible with respect to $4\pi M_s$, then $H_i \approx 4\pi M_s$. Inserting this value of H_i into the equation for the upper frequency limit of the spinwave manifold and equating that frequency to $\omega/2$, it is easily shown that when $\omega_m/\omega > 0.345$, H_i is sufficiently small to guarantee that only high k, $\omega/2$ spinwaves will be available. This situation is illustrated in the normalized spinwave dispersion plot for Polder-Smit domains shown in Figure 5.
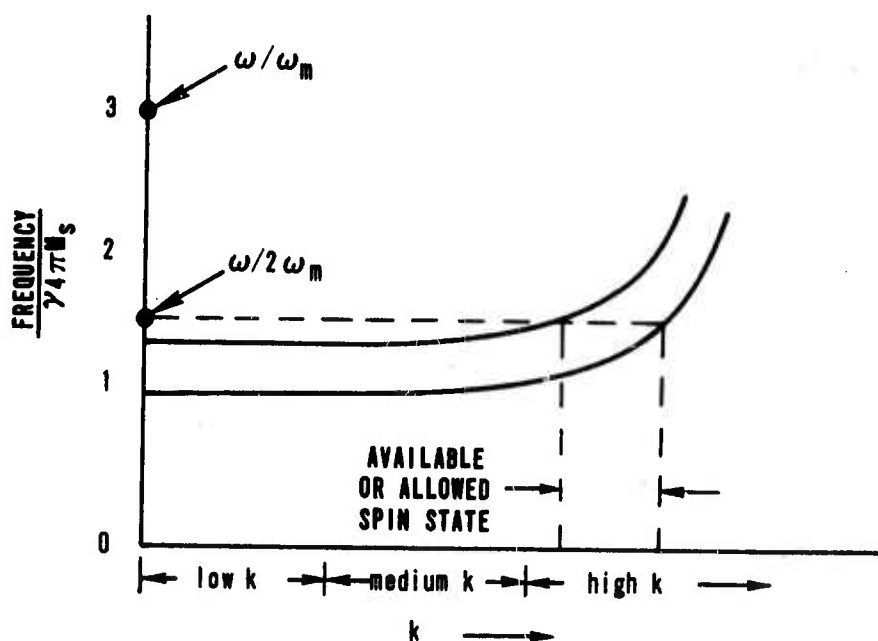
Figure 5. Normalized Spinwave Dispersion Curve Assuming $H_i = 4\pi M_s$ (Polder-Smit Domains)

The spinwave manifold position for any value of ω_m/ω will vary from one domain to the next in accordance with the variation in effective internal field in the various domains. For a fixed value of ω_m/ω, domains with largest demagnetizing fields will have spinwave manifolds positioned highest with respect to the frequency axis. Polder-Smit type domains will always have their spinwave manifolds positioned higher than those of other domains. Thus, one cannot draw a single spinwave manifold for the remanent state ferrite as a whole but must consider instead the integrated result of the spinwave manifolds for each of the various domains.

High power "effects" will be observed when the most susceptible domain goes unstable and exhibits an increase in loss. The relative increase in loss on such an occurrence will be dependent on the total volume contained in the most susceptible domains. Thus, the increase in loss seen when a large domain (or a large volume of the toroid) exhibits nonlinearities will be bigger than that observed when a smaller domain becomes unstable. Since the instability threshold is lowest for spinwaves with $\theta = \pi/2$, the most susceptible domains will be those with $\omega/2 = \omega_k$. At different ω_m/ω values, this condition will be satisfied by different types of domains. At high ω_m values, larger or major domains may be most susceptible while at low ω_m values, smaller domains with large transverse demagnetizing factors may be the only ones satisfying the necessary conditions for low threshold. As a result of these considerations, one might expect that as the limiting case of the Polder-Smit domains is approached the relative increase in loss at the onset of nonlinearity will become smaller and the slope of loss as a function of power then would decrease as this limiting domain configuration is approached (or as ω_m/ω decreases). At higher ω_m/ω values, larger volumes of the toroid go unstable and a substantial slope of loss as a function of power would be observed.

The spinwave manifold curve sketched in Figure 5 is drawn for a uniformly magnetized ellipsoid in a field arising from external sources. In the case of a domain in a remanent ferrite, the internal field value is determined by the anisotropy and transverse demagnetizing factors. As a result of the finite dimensions of the domain, the influence of the dipolar portion of the effective field may vary to some extent with wavelength of spinwaves involved. For example, as the wavelength of these spinwaves becomes shorter, the influence of the transverse demagnetizing factors becomes less important. When the spinwave wavelength is very short compared to the sample dimensions, then the effects of the boundary are relatively unimportant and, for the

short wavelength spinwaves with λ_k less than approximately one-tenth the domain size, the dipolar fields arising at the boundary are unimportant. In this region, of course, the exchange fields become the dominant term. For the usual grain size of 1 to 10 microns, dipolar fields would not contribute significantly to the effective field of spinwaves of wavelength less than one-tenth micron or k values of greater than approximately $5 \times 10^{+5}$. However, it appears that for medium to low k spinwaves, the demagnetizing fields would be relevant since the wavelengths are then of the order of the grain dimensions. These low ΔH_k spinwaves will participate in the initial onset of nonlinearities.

If one considers the Polder-Smith domains alone, i.e., the domains with the highest and therefore most unfavorable biasing condition for low ω_m/ω values, one would find a very abrupt break in the curve of h_{crit} as a function of ω_m/ω. However, since these domains probably occupy a very small volume of the total sample and since at the higher ω_m/ω values other domain geometries would be more susceptible to non-linearities, the threshold as a function of ω_m/ω observed for the total sample will not be as abrupt as that predicted for the limiting case of Polder-Smith domains. Figure 6 shows the dependence of h_{crit} in the limiting Polder-Smith domain and also h_{crit} dependence in the form of $(\omega_m/\omega)^{-1}$ and $(\omega_m/\omega)^{-2}$. A physical interpretation of the $(\omega_m/\omega)^{-2}$ type of dependence might be found in the fact that as frequency is increased the intrinsic linewidth ΔH_k also increases since intrinsic linewidth is directly proportional to frequency. Thus as ω_m/ω is decreased, ΔH_k actually increases with decreasing frequency. For data taken at fixed frequency and as a function of different magnetization values in a series of materials, such as yttrium aluminum garnet, one again finds that the intrinsic linewidth increases and therefore ΔH_k increases with decreasing $4\pi M_s$ value presumably due to a weakening of dipolar and exchange forces which tend to hold the magnetization aligned.

3.2.3 Dielectric and Geometrical Characteristics of FDPS

The macroscopic electromagnetic properties, including the effects of losses, of dielectric materials in the phase shifters are accounted for in the usual manner by a complex permittivity $\epsilon_d = \epsilon_o(\epsilon_d' - j\epsilon_d'')$ and by a permeability $\mu_d = \mu_o$ where ϵ_o and μ_o are the permittivity and permeability of free space. Similarly, the dielectric properties of the ferrite are accounted for by the complex permittivity $\epsilon_f = \epsilon_o(\epsilon_f' - j\epsilon_f'')$.
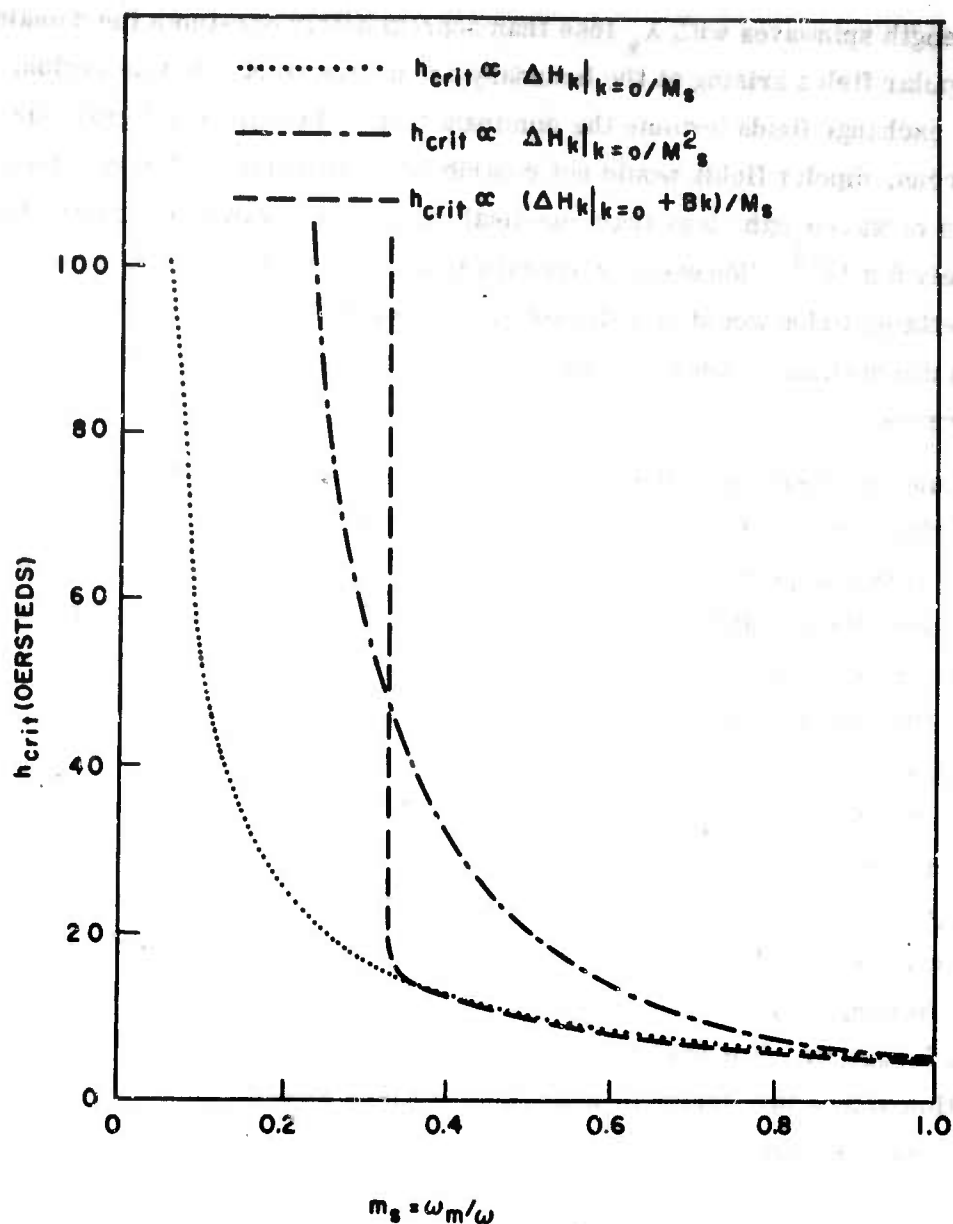
Figure 6. Comparison of Three Methods of Computing the Critical Field Dependence on ω_m/ω

For the purpose of analysis, it is usually convenient and often necessary to consider a model which is geometrically less complicated than the physical device. As an example, refer to Figure 7 which illustrates a cross section of the single-toroid FDPS shown in Figure 2. In the normal operational mode of this phase shifter (i.e., the fundamental TE mode), the rf magnetic field is entirely in the xy-plane. The magnetization in the top and bottom "crossbars" of the toroids is principally in the
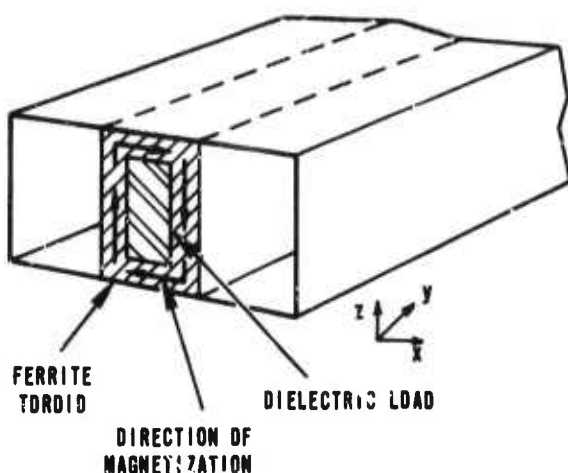
Figure 7. A Waveguide Nonreciprocal Latching Phase Shifter

FERRITE TOROID

DIELECTRIC LOAD

DIRECTION OF MAGNETIZATION

± x direction, while in the vertical legs the magnetization tends to be in the ± z direction. To first order, when the incident rf magnetic field and the direction of magnetization of a sample are mutually parallel, there is no interaction between the field and the magnetization. Therefore, the crossbars of the toroid "look" approximately like pieces of dielectric to the incident rf field. In the vertical legs the magnetization is normal to the rf magnetic field and a strong interaction takes place.

From the above observations, it is apparent that the single-toroid latching phase shifter can be represented by the twin slab model shown in Figure 8. When the dielectric core and the ferrite toroid of the practical device have the same dielectric constant, that value is, of course, used for the dielectric constant of the dielectric load of the model. If the dielectric constants of the dielectric core and the ferrite are different, an "effective" dielectric constant computed on a volume basis (see paragraph 4.5.1) is used for the dielectric load of the model. Geometrical models for other configurations are obtained in a similar fashion.
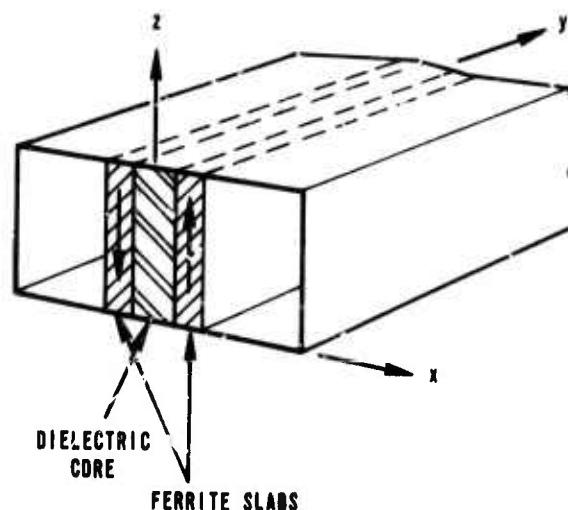
Figure 8. Twin-Slab Model for "Single-Toroid" Ferrite Latching Phase Shifter

DIELECTRIC CORE

FERRITE SLABS

3.3 ANALYSIS TECHNIQUES

To establish quantitative relationships between the transfer characteristics of a ferrite device and its material and dimensional parameters, it is necessary to solve the boundary value problem for the device structure. The general procedure is to solve Maxwell's equations in an appropriate coordinate system and apply the pertinent boundary conditions. The resulting equations can be manipulated to yield an equation which can be numerically solved for the propagation constant. For many transmission structures it is possible to derive the characteristic equation for the propagation constant by a simpler procedure which was suggested by Seidel[14] and is referred to as the "transverse operator" method. Seidel's procedure is closely related to the familiar ABCD matrix formulation for transmission line circuits. The transverse operator technique is based on the fact that in a TE mode waveguide where the rf field components have no variation in the direction of the E field, the electromagnetic field is completely specified by the E field and the longitudinal h component alone. For example, the electromagnetic field in the structure of Figure 9 has components E_z, h_x, and h_y but is completely specified by E_z and h_y since h_x is linearly related to h_y through the divergence condition on the induction field. Both E_z and h_y are continuous at the interfaces of the strata of the waveguide cross section. Hence, in analogy with the ABCD matrix representation of cascaded transmission lines, a transverse transfer matrix is defined which "transfers" the quantities E_z and h_y from one point along a transverse axis to another.

$$\begin{bmatrix} E_{za} \\ h_{ya} \end{bmatrix} = \begin{bmatrix} A & B \\ C & D \end{bmatrix} \begin{bmatrix} E_{zb} \\ h_{yb} \end{bmatrix} \tag{10}$$

The overall transverse operator matrix relating the fields at point a to the fields at point b is the matrix product of the transfer operators of the individual regions separating the point. If points a and b are taken to be the walls of the waveguide, then $E_{za} = E_{zb} = 0$ and

$$\begin{bmatrix} 0 \\ h_{ya} \end{bmatrix} = \begin{bmatrix} A & B \\ C & D \end{bmatrix} \begin{bmatrix} 0 \\ h_{yb} \end{bmatrix} \tag{11}$$

---

[14]H. Seidel, "Ferrite Slabs in Transverse Electric Mode Wave Guide," J. Appl. Phys., 28, February 1957.

or

$$0 = B\, h_{yb} \tag{12}$$

$$h_{ya} = D\, h_{yb}$$
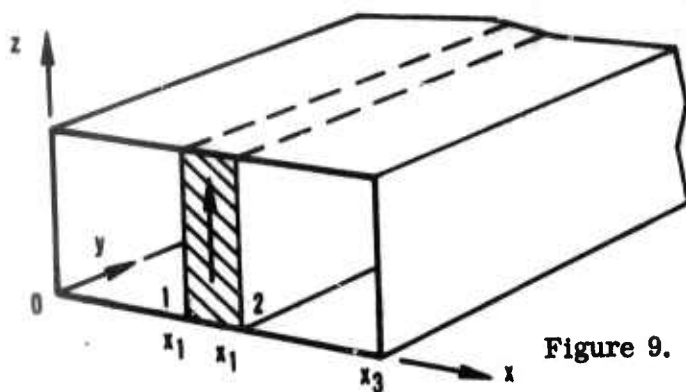
Figure 9. A Ferrite Loaded Rectangular Waveguide

For a nontrivial solution h_{yb} must be nonzero. Therefore, B must be zero. From this condition the equation for the propagation constant is easily determined. If the structure analyzed has electromagnetic symmetry about some point, for example, point o is such a point in the structure of Figure 10 ; the y-component of the h field must be zero about that point and a simplification in the computations is necessary to obtain the propagation equation results. The operator relating the fields at point o to those at the wall can be written as

$$\begin{bmatrix} 0 \\ h_{ya} \end{bmatrix} = \begin{bmatrix} A & B \\ C & D \end{bmatrix} \begin{bmatrix} E_{zo} \\ 0 \end{bmatrix} \tag{13}$$

or

$$0 = A\, E_{zo} \tag{14}$$

$$h_{ya} = C\, E_{zo}$$

For a nontrivial solution E_{zo} must be different from zero, and A must, therefore, be identically zero. This condition leads to the equation for the propagation constant of symmetrical structures.

3-29
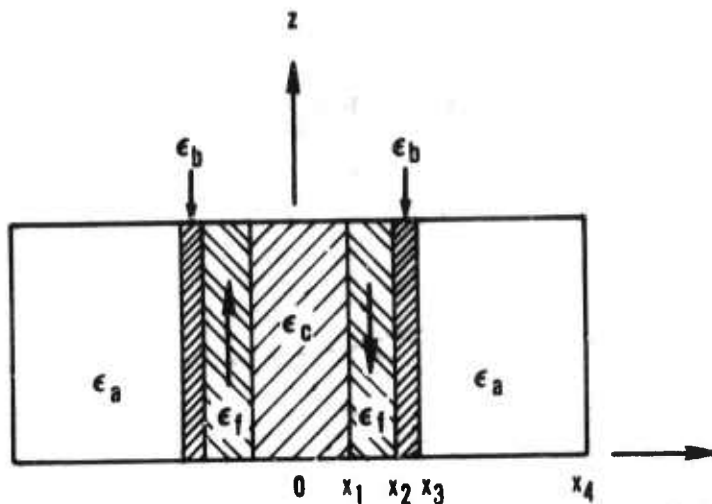
Figure 10. A Structure with Electromagnetic Symmetry about 0

The ABCD parameters for ferrite and dielectric regions are easily obtained from Maxwell's equations. The following derivation for these parameters is modeled after that of Seidel, but the notation is somewhat different.

Consider a TE mode waveguide structure such as that shown in Figure 9. The ferrite slab is of width δ and is assumed to be infinitely long in the y direction. The preferred direction for the effective internal static magnetic field H_i and the saturation magnetization $\vec{M}_s$ is assumed to be in the +z direction. The intrinsic permeability tensor then has the general form

$$\langle \vec{\mu} \rangle_{avg} = \mu_0 \begin{bmatrix} \langle \mu \rangle_{avg} & -j\langle \kappa \rangle_{avg} & 0 \\ j\langle \kappa \rangle_{avg} & \langle \mu \rangle_{avg} & 0 \\ 0 & 0 & \langle \mu_z \rangle_{avg} \end{bmatrix} \qquad (15)$$

where
$$\langle \mu \rangle_{avg} = \langle \mu' \rangle_{avg} - j\langle \mu'' \rangle_{avg}$$

$$\langle \kappa \rangle_{avg} = \langle \kappa' \rangle_{avg} - j\langle \kappa''' \rangle_{avg}$$

$$\langle \mu_z \rangle_{avg} = \langle \mu_z' \rangle_{avg} - j\langle \mu_z'' \rangle_{avg}$$

and $\langle \mu' \rangle_{avg}$, $\langle \mu'' \rangle_{avg}$, $\langle \kappa' \rangle_{avg}$, $\langle \kappa'' \rangle_{avg}$, $\langle \mu_z' \rangle_{avg}$, and $\langle \mu_z'' \rangle_{avg}$ are given by Equation 8 of Section 3.2.1.

3-30

Assume a general form for the electric field inside the ferrite, say

$$E_z = \left[Be^{jk_m x} + Ce^{-jk_m x} \right] e^{-\gamma y} e^{j\omega t} \qquad (16)$$

where

$$k_m^2 = \gamma^2 + \frac{\omega^2 \mu_o \epsilon_o \epsilon_f}{\rho} = \text{square of the wave number in the ferrite}$$

$$\rho = \frac{<\mu>_{avg}}{\left[<\mu>_{avg} \right]^2 - \left[<\kappa>_{avg} \right]^2}$$

$$\gamma = \text{propagation constant}$$

The magnetic field itensity in the y direction is

$$h_y = \frac{\rho}{j\omega\mu_o} \left[\left(jk_m + \frac{\gamma}{\theta} \right) Be^{jk_m x} + \left(-jk_m + \frac{\gamma}{\theta} \right) Ce^{-jk_m x} \right] e^{-\gamma y} e^{j\omega t} \qquad (17)$$

where

$$\theta = \frac{-<\mu>_{avg}}{j<\kappa>_{avg}}$$

Using Equations 16 and 17, the fields at point one ($x = x_1$) and at point two ($x = x_1 + \delta$) can be written as

$$E_{z1} = \left[Be^{jk_m x_1} + Ce^{-jk_m x_1} \right] e^{-\gamma y} e^{j\omega t} \qquad (18)$$

$$E_{z2} = \left[Be^{jk_m(x_1 + \delta)} + Ce^{-jk_m(x_1 + \delta)} \right] e^{-\gamma y} e^{j\omega t} \qquad (19)$$

$$h_{y1} = \frac{\rho}{j\omega\mu_o} \left[\left(jk_m + \frac{\gamma}{\theta} \right) Be^{jk_m x_1} + \left(-jk_m + \frac{\gamma}{\theta} \right) Ce^{-jk_m x_1} \right] e^{-\gamma y} e^{j\omega t} \qquad (20)$$

$$h_{y2} = \frac{\rho}{j\omega\mu_o}\left[\left(jk_m + \frac{\gamma}{\theta}\right)Be^{jk_m(x_1 + \delta)}\right.$$

$$\left. + \left(-jk_m + \frac{\gamma}{\theta}\right)Ce^{-jk_m(x_1 + \delta)}\right]e^{-\gamma y}e^{j\omega t} \qquad (21)$$

Referring to Figure 9, the electric field in the z-direction and the magnetic field in the y-direction at point one can be related to the corresponding fields at point two by the transverse operator equation

$$\begin{bmatrix} E_{z1} \\ h_{y1} \end{bmatrix} = \begin{bmatrix} A & B \\ C & D \end{bmatrix} \begin{bmatrix} E_{z2} \\ h_{y2} \end{bmatrix} \qquad (22)$$

Expanding Equation 22 yields the following two equations.

$$E_{z1} = AE_{z2} + Bh_{y2} \qquad (23)$$

$$h_{y1} = CE_{z2} + Dh_{y2} \qquad (24)$$

Substituting Equations 18 through 21 into Equations 23 and 24 allows the parameters ABCD to be evaluated. These parameters for a ferrite region of width δ are

$$A = \cos k_m \delta + \frac{\gamma}{k_m \theta}\sin k_m \delta$$

$$B = \frac{-j\omega\mu_o}{\rho k_m}\sin k_m \delta \qquad (25)$$

$$C = \frac{j\rho}{\omega\mu_o k_m}\left(\frac{-\gamma^2}{\theta} - k_m^2\right)\sin k_m \delta$$

$$D = \cos k_m \delta - \frac{\gamma}{k_m \theta}\sin k_m \delta$$

If the internal effective static magnetic field and the magnetization reverse in direction, the only change necessary is to reverse the sign of θ.

3-32

For a dielectric region $\rho \rightarrow 1$ and $\theta \rightarrow \infty$, so that the parameters for a dielectric region of width W can be written as

$$A = \cos k_d W$$

$$B = \frac{-j \omega \mu_o}{k_d} \sin k_d W$$

$$C = \frac{-j k_d}{\omega \mu_o} \sin k_d W \tag{26}$$

$$D = \cos k_d W$$

As an example of the application of this method, consider the structure shown in Figure 11 which is a twin-slab model of the single internal toroid FDPS. This structure has electromagnetic symmetry about o. The overall transfer matrix is

$$\begin{bmatrix} A & B \\ C & D \end{bmatrix} = \begin{bmatrix} A_1 & B_1 \\ C_1 & D_1 \end{bmatrix} \begin{bmatrix} A_2 & B_2 \\ C_2 & D_2 \end{bmatrix} \begin{bmatrix} A_3 & B_3 \\ C_3 & D_3 \end{bmatrix}$$
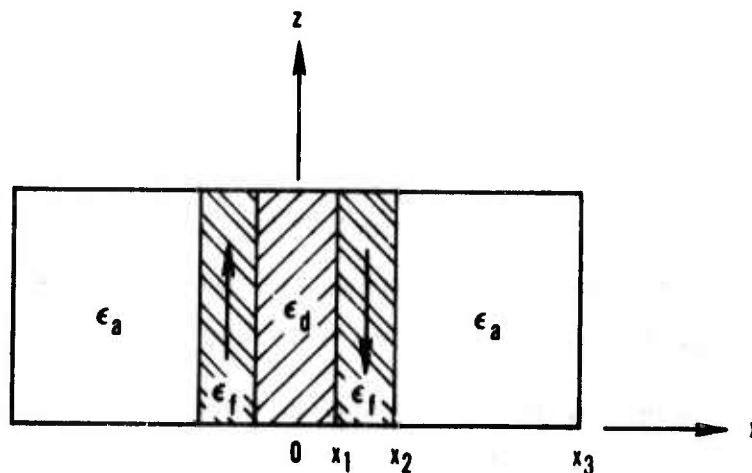
Figure 11. Dielectric Loaded Twin-Slab Structure

Carrying out this multiplication and setting A = o yields

$$A = A_1 (A_2 A_3 + B_2 C_3) + B_1 (C_2 A_3 + D_2 C_3) = o$$

Substituting for the A's B's, C's, and D's from Equations 25 and 26, the following equation for the propagation constant is obtained

$$
\left[\frac{k_m}{\rho} (k_a - k_d) \cot k_m (x_2 - x_1) - \frac{\gamma}{\rho \theta} (k_a + k_d) \right] \cos \left\{ k_d x_1 - k_a (x_3 - x_2) \right\}
$$

$$
+ \left[\frac{k_m}{\rho} (k_a + k_d) \cot k_m (x_2 - x_1) - \frac{\gamma}{\rho \theta} (k_a - k_d) \right] \cos \left\{ k_d x_1 + k_a (x_3 - x_2) \right\}
$$

$$
+ \left[k_m^2 + \frac{\gamma^2}{\theta^2} - \frac{k_a k_d}{\rho^2} \right] \sin \left\{ k_d x_1 - k_a (x_3 - x_2) \right\} \tag{27}
$$

$$
- \left[k_m^2 + \frac{\gamma^2}{\theta^2} + \frac{k_a k_d}{\rho^2} \right] \sin \left\{ k_d x_1 + k_a (x_3 - x_2) \right\} = 0
$$

where

$$k_m^2 = \frac{\omega^2 \mu_o \epsilon_o \epsilon_f}{\rho} + \gamma^2 \qquad k_d^2 = \omega^2 \mu_o \epsilon_o \epsilon_d + \gamma^2$$

$$k_a^2 = \omega^2 \mu_o \epsilon_o \epsilon_a + \gamma^2 \qquad \rho = \frac{\mu}{\mu^2 - \kappa^2}$$

$$\theta = j \frac{\mu}{\kappa} \qquad \gamma = \alpha + j\beta$$

$$\mu = \mu' - j\mu'' \qquad \kappa = \kappa' - j\kappa''$$

$$\epsilon_d = \epsilon'_d - j\epsilon''_d \qquad \epsilon_f = \epsilon'_f - j\epsilon''_f$$

$$\epsilon_a = \epsilon'_a - j\epsilon''_a$$

If the dimensional and material parameters of the structure are specified, this equation can be solved numerically for the propagation constant γ. With γ known, the rf electric and magnetic fields are easily obtained from Maxwell's equations.

A presentation and discussion of the solutions of the propagation constant equation for a number of FDPS configurations are given in Section 4.5. Good correlation is found between experimental and calculated results, leading to considerable confidence in the mathematical models and techniques presented in the above sections.

3.4 INFLUENCE OF INTRINSIC AND CERAMIC PROPERTIES ON SQUARE LOOP CHARACTERISTICS

The relative desirability of a ferrite material for use in a digital phase shifter depends strongly on the materials' ratio of remanent magnetization to saturation magnetization, its coercive field, and time required for switching it from one remanent state to the other. In general, a "good" ferrite for digital phase shifter applications will have a high remanence ratio, a low coercive field, and a small switching time. Each of these properties is discussed below.

3.4.1 Remanence Ratio

The remanence ratio is probably the single most important square loop property as far as microwave applications of ferrite toroids is concerned. Ideally, the remanent magnetization should equal the saturation magnetization, i.e., the remanence ratio R_r should be 1.0. This ideal situation is unlikely to be attained in practice. Remanence ratios of 0.6 to 0.7 are more normally encountered.

In a polycrystalline ferrite or garnet material, the magnetization in the individual crystallites will, due to crystalline anisotropy, prefer to be aligned along the easy (111) directions of the crystallites. If magnetocrystalline anisotropy were the only factor influencing the magnetization in individual crystallites, the remanence ratio for a cubic material would be approximately 0.87. This result assumes that in the saturated state the magnetization in all crystals is parallel to the applied field and relaxes to the nearest easy direction, or body diagonal, when the field is removed. This ideal value is difficult to realize in practice because of unfavorable contributions from other anisotropies (stress anisotropy or magnetostriction) and shape anisotropy. The existence in polycrystalline materials of pores, or voids, in the material also gives rise to local demagnetizing fields which will lower the resultant remanence ratio. Thus, magnetocrystalline anisotropy will tend to favor a high remanence ratio while porosity and other anisotropies tend to decrease remanence ratio. If the magnetocrystalline anisotropy is large compared to other anisotropies and demagnetizing fields arising at magnetic discontinuities in the materials, the remanence ratio can approach the theoretical limit of 0.87. Thus, highest remanence ratios will be realized in materials having low magnetostriction, low unfavorable internal stresses, and a dense, homogenous magnetic structure with a high magnetocrystalline anisotropy. The same ceramic qualities that lead to high remanence ratio also tend to lead to low resonance linewidths.

A unidirectional anisotropy favoring high remanence ratio can sometimes be built into a material by controlling its shape and internal stresses. Quenching, lattice

3-35

deformations, applied pressure, etc., are techniques sometimes used. Such techniques, however, do not seem very practical for microwave materials because of their unfavorable effects on microwave properties.

In actual device applications, most microwave materials are not driven into saturation with the available drive fields (approximately 25 oersteds maximum). The hysteresis loop on which operation is based is then not the saturated loop, but rather some minor loop. To classify and optimize materials, it is necessary to measure the absolute value of the remanent magnetization at the drive fields normally used in digital phase shifters in order that such measurements have practical meaning. It is desirable that these drive fields be as low as possible consistent with a realization of nearly maximum values of remanence ratio, R_r.

The following procedures are used to measure the remanent magnetization.

1) The $4\pi M_s$ of the material is measured by some independent means, such as a vibrating sample magnetometer, in applied fields of the order of 5,000 oersteds.

2) The hysteresis loop is measured on a hysteresograph. The drive fields used are, whenever possible, 10 times the coercive field of the material. For most materials the remanent magnetization is observed to change very little between drive fields of 8 to 10 times the coercive field of the material. From this hysteresis loop, the "squareness" and coercive field can be measured. The squareness is defined as $S_D = \dfrac{4\pi M_{RD}}{4\pi M_D}$, where S_D is the "squareness," $4\pi M_{RD}$ is the remanent magnetization for the drive field used and $4\pi M_D$ is the magnetization at the peak of the drive field. The measurement of $4\pi M_D$ is described below.

If the core reverses an amount of flux $\Delta\phi$ in a time Δt, the average voltage V produced during switching is

$$<V> = N \frac{\Delta\phi}{\Delta t} \tag{28}$$

where N is the number of turns threading the core. If A is the cross-sectional area of the legs of the core and B_D is the change in flux density at the drive field used

$$\Delta\phi = A\,\Delta B_D \tag{29}$$

and

$$\Delta B_D = \Delta(4\pi M_D) \tag{30}$$

3-36

for the low drive fields used for toroidal geometries. Therefore

$$\Delta\phi = A\Delta(4\pi M_D) \tag{31}$$

and

$$(4\pi M_D) = \frac{\langle V\rangle \Delta t}{A N} \tag{32}$$

Using proper integrating circuits and known values of A and N, $\Delta(4\pi M_D)$ can be measured (see Figure 12 for interpretation of $\Delta(4\pi M_D)$. It is recommended that calibration samples be used for ease in the measurement and use of $\langle V\rangle \Delta t$.

With the measured value of "squareness" and $4\pi M_D$, the $4\pi M_{RD}$ can be computed. For drive fields of eight to ten times the coercive field of the material

$$4\pi M_{RD} = 4\pi M_R \tag{33}$$

for most materials. The remanence ratio of the material is then computed as

$$R_R = \frac{4\pi M_R}{4\pi M_S} \tag{34}$$
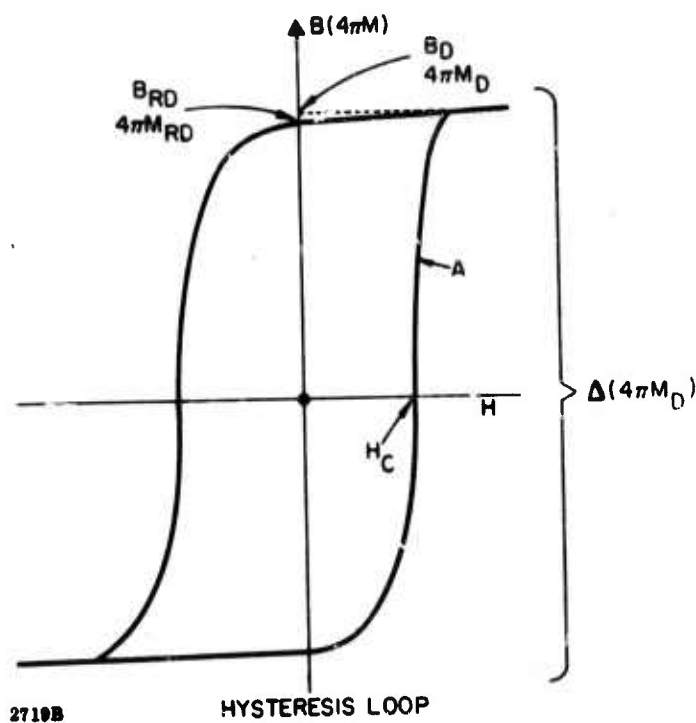
Figure 12. Hysteresis Loop of Ferrimagnetic Materials

3.4.2 Coercive Force

The coercive force of ferrite materials used in digital phase shifters is determined principally by the ease with which domain walls can move through the polycrystalline material. At the drive fields encountered in digital phase shifters, the switching action is due almost entirely to domain wall motion, and thus it is the ease with which domain walls can be nucleated and moved through the material that determines the coercive field.

The motion of a domain wall through a magnetic material is determined by a combination of both intrinsic and ceramic properties. The coercive field for domain wall motion can be described by the empirical relation

$$H_c = \frac{2 K_1 (\Delta v)}{\pi M_s} \left[0.386 + \log \sqrt{\frac{2\pi M_s^2}{K_1}} \right] \qquad (35)$$

where (Δv) is the fractional volume of nonmagnetic inclusions, and H_c is the coercive field in oersteds. $\frac{2 K_1}{M_s}$ is the conventional magnetocrystalline anisotropy field. Experimental results are generally found to be in reasonable agreement with this expression.

Thus, we see that the coercive field varies with the anisotropy field, $\frac{2 K_1}{M_s}$, and the volume of nonmagnetic inclusions (pores, impurities, etc.). For minimum coercive field, a maximum density and a minimum anisotropy field are desirable. Clearly, optimum square loop properties (minimum H_c and maximum R_r) place conflicting demands on the magnetocrystalline anistropy. A minimum anisotropy field is desirable for a small coercive field, while a large anisotropy field is desirable for a large remanence ratio. This set of opposing demands normally leads to an observed decrease in remanence ratio when very small coercive fields are encountered. However, coercive fields of less than one oersted are easily obtainable in combination with remanence ratios of approximately 0.7.

3.4.3 Switching Time

The switching time of a ferrite toroid is essentially the sum of the time required to nucleate a domain wall and the time required for the domain wall to propagate across the width of the toroid. The switching and dynamic behavior of ferrimagnetic oxides have been treated in detail in two summary articles on this subject. These articles are as follows:

(1) J. B. Birks and J. Hart, Progress in Dielectrics, Volume 5, Academic Press, Inc., Publishers, New York, 1963, (H. P. Peloschek; "Square Loop Ferrites and their Applications," pp 37-93).

(2) Harvey Rubinstein, "Switching Properties of Ferrites and Garnets," Scientific Report No. 6 (Series 2), Gordon McKay Laboratory of Applied Science, Harvard University, Cambridge, Mass. (Nov. 30, 1962) Cont. No. AF19(604)5487, AFCRL.

These articles deal with all of the possible switching mechanisms and analytical expressions which describe the behavior of flux reversal in ferrimagnetic oxides. The highlights of these articles, as they pertain particularly to switching aspects of materials used in ferrite digital phase shifters, have been discussed in considerable detail in the Final Report on RADC Contract No. AF30(602)3490.

Perhaps it can suffice here to mention that three possible mechanisms for switching are possible. One is called pure wall displacement, the second, incoherent rotations, and the third, coherent rotations. These various mechanisms have switching times which vary between the longest time for pure wall displacement and the shortest time for coherent rotations. The switching fields involved vary also, being smallest for pure wall displacement and largest for coherent rotations. In any case, the switching time can be given by the expression $t_s(H - H_o) = S$, where S is a constant for the material at a given temperature and is called the switching coefficient. $(H - H_o)$ is the effective drive field where H is the applied field and H_o is a function of the material and approximately equal to the coercive field.

The switching coefficient of the material is expressed in oersteds-microseconds and varies with the type of switching mechanism used. The switching constants for the three different modes of flux reversal in ferrites may differ by as much as a factor of 20. That is, the switching coefficient for pure wall displacement may be 20 times the switching coefficient for coherent rotations. In view of the drive fields normally used in FDPS, however, the domain wall motion mechanism is the principal switching mechanism operative, and its switching constant is the one to be considered in calculations of switching time. This switching coefficient for domain wall motion can be shown to be given by

$$S_w = \frac{6.4 \, d \, \lambda \times 10^{-2}}{\delta g^2 M_s} = \frac{\beta d}{2M_s} \tag{36}$$

where d = distance moved by domain wall

$$\beta = \frac{12.8\,\psi\,\text{X}10^{-2}}{\delta g^2}$$

δ = domain wall thickness = $\sqrt{\dfrac{kT_c}{K_1 a}}$

k = Boltzman's constant,

ψ = intrinsic damping parameter = $\dfrac{\gamma M_s \Delta H}{2H_r}$

ΔH = intrinsic linewidth

H_r = field (oe) required for ferrimagnetic resonance at the linewidth measurement frequency.

Typical switching constants S_w for domain wall motion are of the order of 0.1 to 1 oersted microseconds. Thus, for a drive field of approximately 5 times the coercive field, we find that the switching time, t_s, is of the order of 0.02 to 0.2 microseconds. These switching times are sufficiently rapid for most microwave applications so that other flux reversal processes involving domain rotation need not be considered. The application of other flux reversal processes would lead to very high drive field requirements which would be intolerable for most phased array applications.

4 SUMMARY AND DISCUSSION OF RESULTS

4.1 INTRODUCTION

This section presents and discusses results of the analytical and experimental work carried out to determine the effect of intrinsic ferrite parameters on the performance characteristics of FDPS. The overall goal of this work was to develop theoretical and experimental techniques which would determine the limitations on performance of ferrite phasers and would permit the pinpoint specification of the intrinsic material parameter values required to obtain optimum FDPS performance characteristics under a specified set of constraints (i.e., constraints such as average and peak power handling requirements, permissible insertion loss, stability of phase and loss with temperature, etc.).

Physical and mathematical models for remanent state ferrites were presented in Section 3. These models were developed to enable the prediction and evaluation of the performance characteristics of ferrites in different frequency bands and with different geometries without having to resort to an actual measurement of loss and phase shift for each frequency and geometry employed. Moreover, the models permit the prediction and evaluation of the effects of variations in intrinsic material parameters on loss, phase shift, and high power threshold. In attempting to verify the material models proposed, a computer-aided analysis has been carried out to find the exact solutions to the boundary value problems for various device configurations. Differential phase shift, insertion loss, and rf field intensities for each configuration are obtained from the solution to its boundary value problem. This analysis has been supported and guided by an extensive set of experimental measurements on a variety of FDPS configurations and a wide array of material parameters. The combined theoretical and experimental effort has been aimed towards substantiating and improving the physical model proposed for remanent state ferrites, so that a more complete understanding of the operation and limitations on FDPS could be obtained.

4.2 MEASUREMENT EQUIPMENT AND TECHNIQUES

Equipment and techniques are described for performing measurements of the following material parameters: density, saturation magnetization, g-factor, linewidth, Curie temperature, dielectric constant, dielectric loss tangent, remanence ratio, and coercive field. In addition, equipment and techniques for measuring device phase shift, insertion loss, VSWR, high power threshold, switching time, and switching energy are described.

4.2.1 Measurement of Material Properties

(a) Measurement of $4\pi M_s$. The measurement of $4\pi M_s$ was made with the vibrating sample magnetometer shown in Figure 13. This measurement is based on the detection of the ac magnetic field set up by the vibrating magnetic sample. A small sphere of the unknown material is placed in a strong saturating dc magnetic field. The sample is vibrated at a low audio frequency (100 cps) and the oscillating dipole field thus generated is detected by two coils so positioned as to minimize stray pickup. The magnitude of this dipole field is compared to the signal detected by two similar coils from a known calibrated sample attached to the same vibrating rod. This system, first proposed by Foner,[15] is capable of accurate, continuous readout and lends itself well to the measurement of saturation magnetization as a function of temperature. The magnetometer can also be used to measure coercive force on spherical samples.
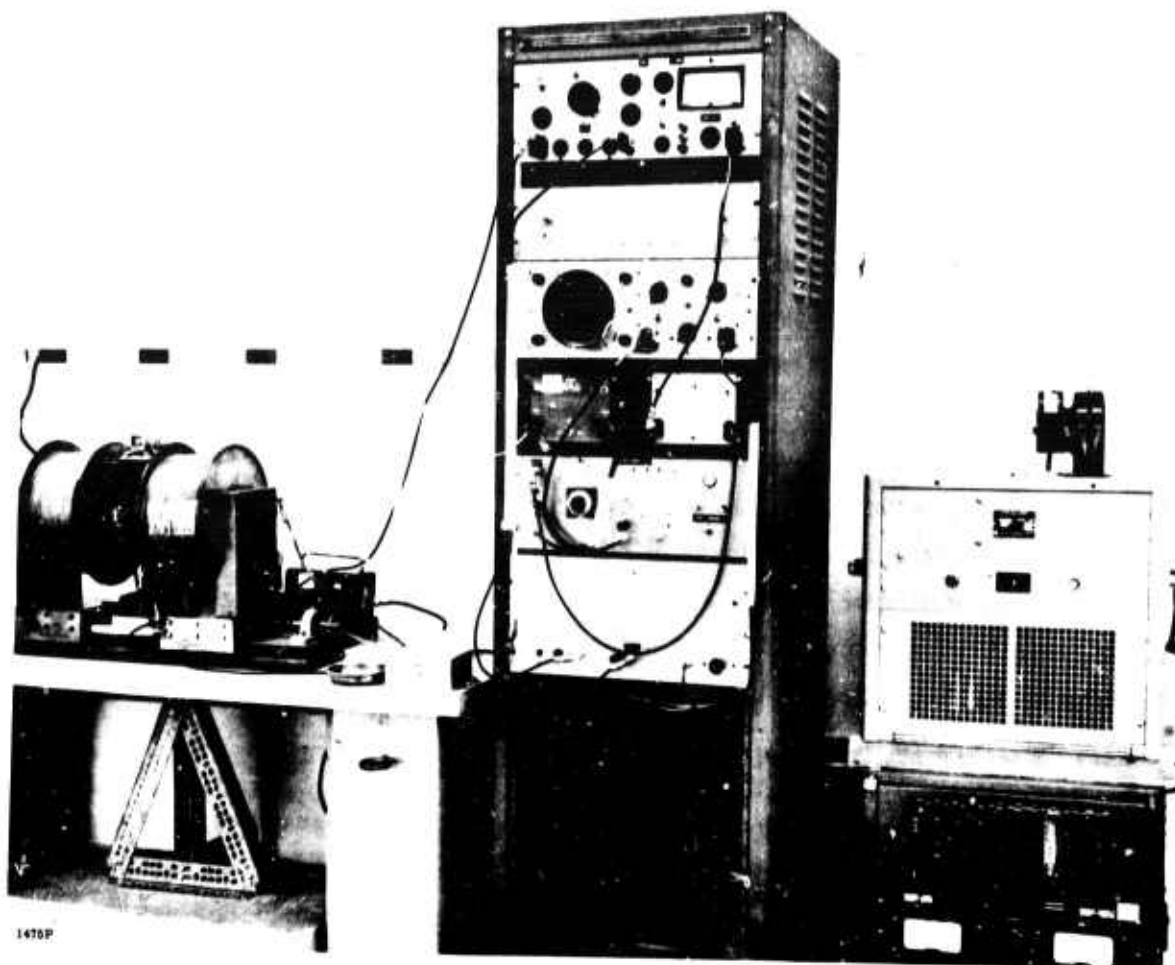
Figure 13. Vibrating Sample Magnetometer

[15] Foner, "Versatile and Sensitive Vibrating Sample Magnetometer," Rev. of Scientific Instrument 30, 549 (1959)

(b) Measurement of ΔH, g_{eff}-factor, magnetic susceptibility and anisotropy field. Reflection type resonance spectrometers were used for measurements of line-widths. The samples measured were generally in the form of spheres 20 ±2 mils in diameter. The spheres were made by forcing a roughly cubical shaped sample of the material with compressed air around the inner periphery of a wheel coated with an abrasive powder. A 4/0 finish can easily be obtained using this method.

The effective g-factor is obtained simultaneously with the linewidth data by simply noting the field at which maximum absorption occurs and substituting this into Kittel's resonance equation. Figure 14a shows the X band resonance spectrometer and Figure 14b shows the C band resonance spectrometer in Sperry's Materials Measurements Laboratory.

This same equipment can be used for the measurement of anisotropy field in aligned single crystal samples.

By monitoring the reflected signal from the cavity or shorted coaxial line as the field is varied, it is possible to obtain a plot of resonance line profile or imaginary part of the magnetic susceptibility as a function of applied field.

(c) Measurement of T_c. Curie temperature measurements are done most rapidly with the simple furnance arrangement sketched in Figure 15. The test procedure is based on the balancing of gravitational and magnetic forces. As the temperature is raised and the Curie temperature is approached, the magnetization of a ferromagnetic body approaches zero. The Curie temperature can then be defined, in this measurement, as the temperature at which the force of gravity overcomes the magnetic force. The temperature at which the sample (S) drops from the magnet (P) can be determined by using two strips of foil (F) to close an electrical circuit and ring a bell when the sample forces the strips to touch. The temperature can then be read on a thermocouple. More precise determinations are made by measuring the temperature at which the magnetization falls to zero on the vibrating sample magnetometer of Figure 13. Curie temperature data are obtained directly when the saturation magnetization is measured as a function of temperature.
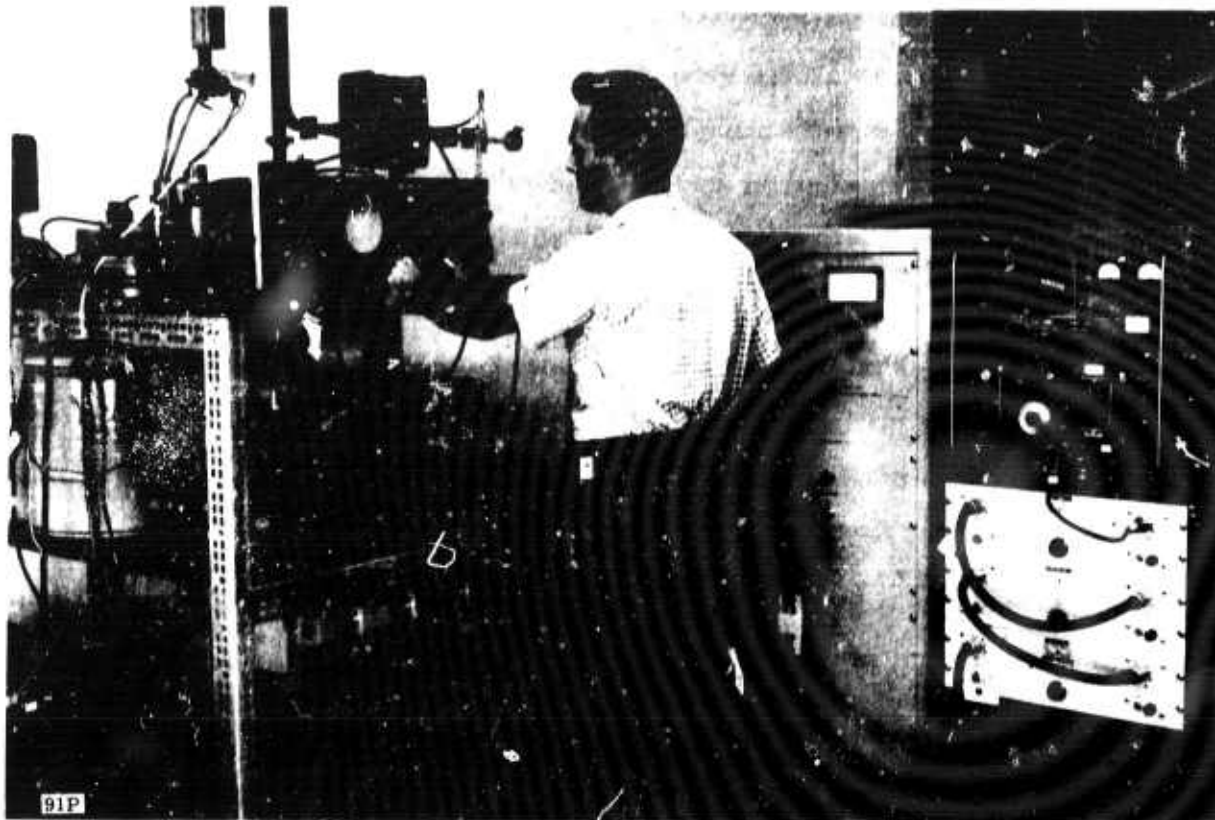
Figure 14 A. X Band Resonance Spectrometer
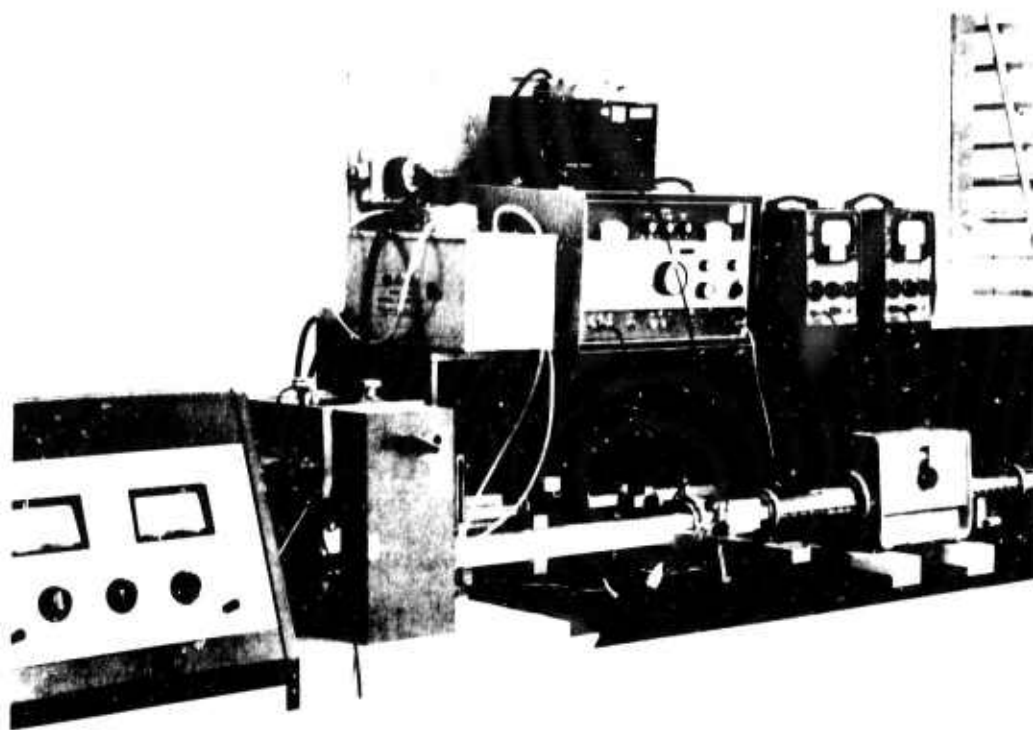
Figure 14 B. C Band Resonance Spectrometer
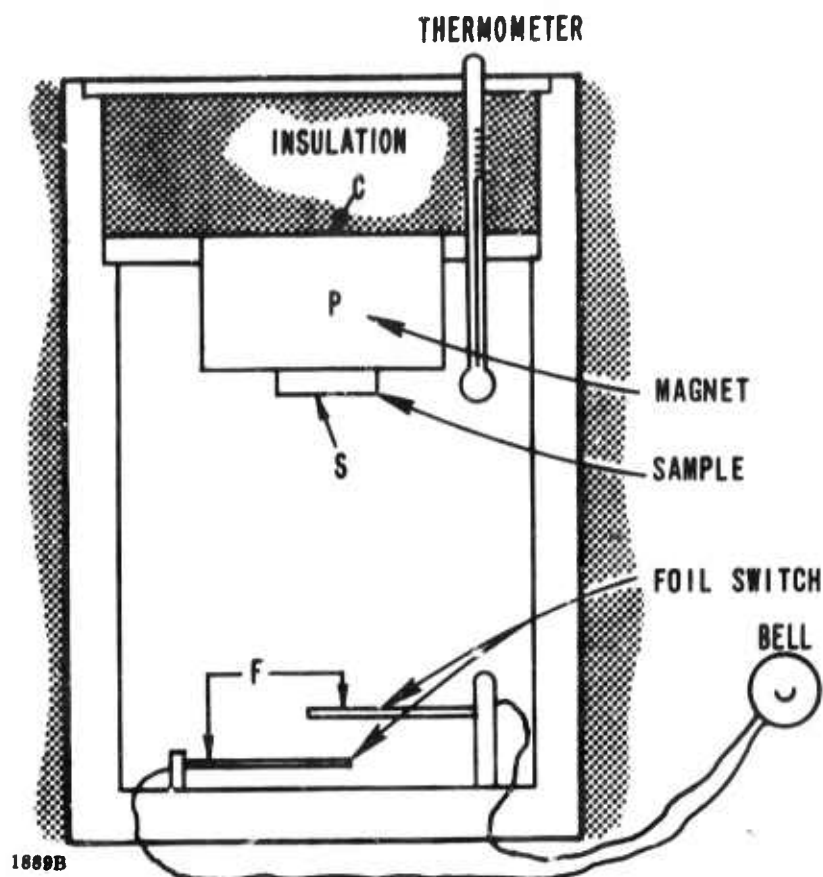
Figure 15. Furnace Arrangement for Simple Measurement of Curie Temperature. Explanatory Comments are in the Text.

(d) Measurement of Dielectric Constant and Dielectric Loss Tangent. Measurements of dielectric loss tangent and dielectric constant were made at X band. A small cylindrical sample of the material to be measured is inserted into a transmission cavity at a point of a maximum electric field and minimum magnetic field. In the case of samples with large saturation magnetizations a magnetic field is applied to essentially eliminate domain wall magnetic losses at the test frequency. If the Q and the resonant frequency of the cavity are known before and after a sample is inserted, $\tan \delta$ and ϵ' can be calculated. $\tan \delta$ can be measured down to 0.0001 and ϵ' values are accurate to about 5 percent. This equipment is shown in Figure 16.

(e) Lattice Constants and X Ray Density. The lattice constants of various garnet and ferrite compounds vary from compound to compound. For a garnet of the series $5\,Fe_2O_3 \cdot 3\,(Y_{2-x}Gd_xO_3)$, if the lattice constants of the end points (in this case YIG and GdIG) were known, the variation of lattice constant with x can be calculated by Vegards's rule. The lattice constant of these materials was determined from X-ray

4-5
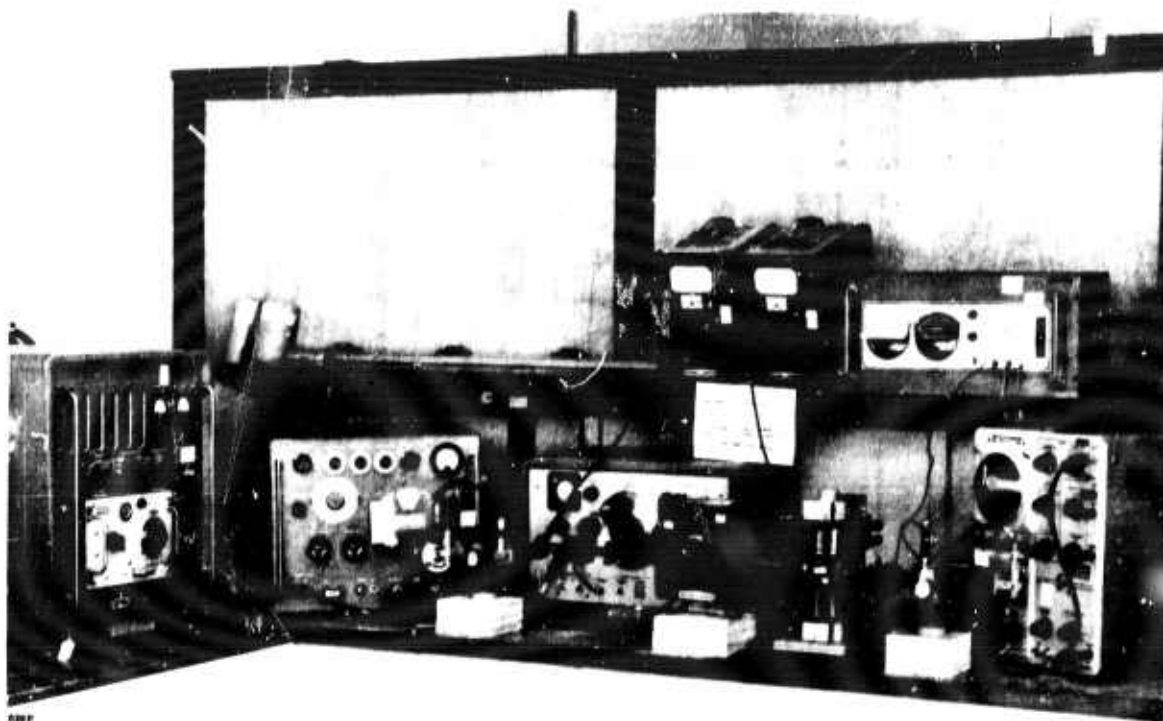
Figure 16. Dielectric Constant and Dielectric Loss Tangent Measurement
Equipment (X Band)

diffractometer of Figure 17 Model(General Electric XRD-5). The theoretical density
of the materials can be computed once the lattice constants and chemical composition
are known. X-ray diffraction data collected on this apparatus was also used to study
the phase purity of materials.

(f) Measurement of Density. Density was measured in this laboratory by
weighing accurately on chemical balances a sample of regular, measured dimensions,
and by computing the ratio of weight to volume. For irregular samples, a mercury
volumeter was used; this device works by measurement of the buoyancy of the sample
when immersed in mercury.

(g) Measurement of Remanence Ratio and Coercive Field. A hysteresograph,
or square loop tester, has been built for the evaluation and measurement of the hyster-
esis properties of ferrimagnetic oxides. The equipment operates at 60 cps and consists
of a coaxial drive probe, integrator, function generator, peak reading voltmeter and
scope display. Squareness ratio ($S_D = 4\pi M_{RD}/4\pi M_D$) and the ratio of the coercive
field to the drive field (H_C/H_D) are read directly from digital potentiometers.

4-6
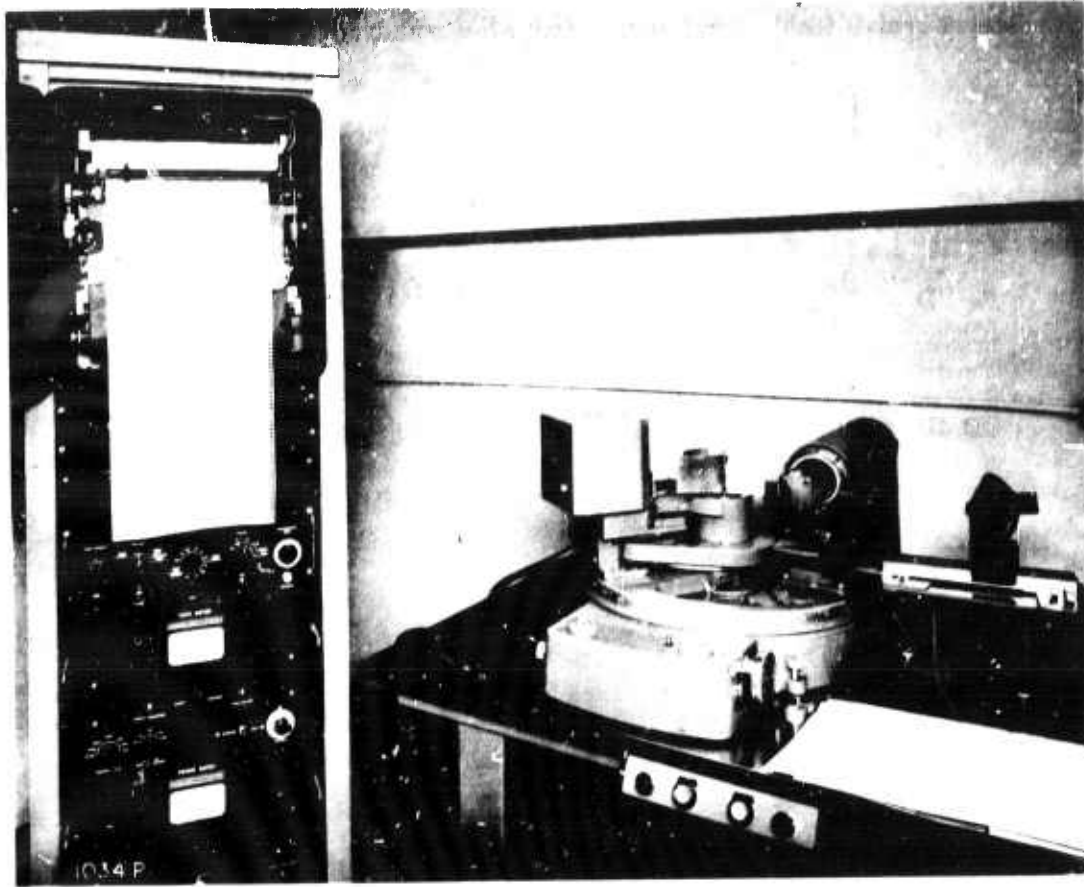
Figure 17.   General Electric XRD-5 X ray Diffractometer in Sperry Micro-
wave Electronics Company Laboratory

The square loop tester is depicted in Figure 18 and Figure 19 is a brief schematic of
the apparatus.

The flux change involved in switching from $(-4\pi M_D)$ to $(+4\pi M_D)$, namely $\Delta\phi$,
is calculated from the voltage read on the peak-reading voltmeter using a reference
toroid sample supplied by Mr. D. H. Temme of M.I.T. Lincoln Laboratories.   The
remanent flux density $(4\pi M_{RD})$ is then the product of this flux and the squareness
ratio divided by the cross sectional area of the toroid legs: $4\pi M_{RD} = S_D(\Delta\phi)/A$

where
$$A = \ell W_4$$

ℓ = length of the toroid

W_4 = width of the toroid legs

The coercive field is calculated from the equation

$$H_C = \left(H_C / H_D\right)\left(\frac{0.445\, I_D}{OD + ID}\right) \text{ oersteds}$$

where

I_D = the RMS current (amperes) used to magnetize the toroid to $\pm 4\pi M_D$

and

OD, ID = the mean toroid outer and inner diameters respectively, in inches.
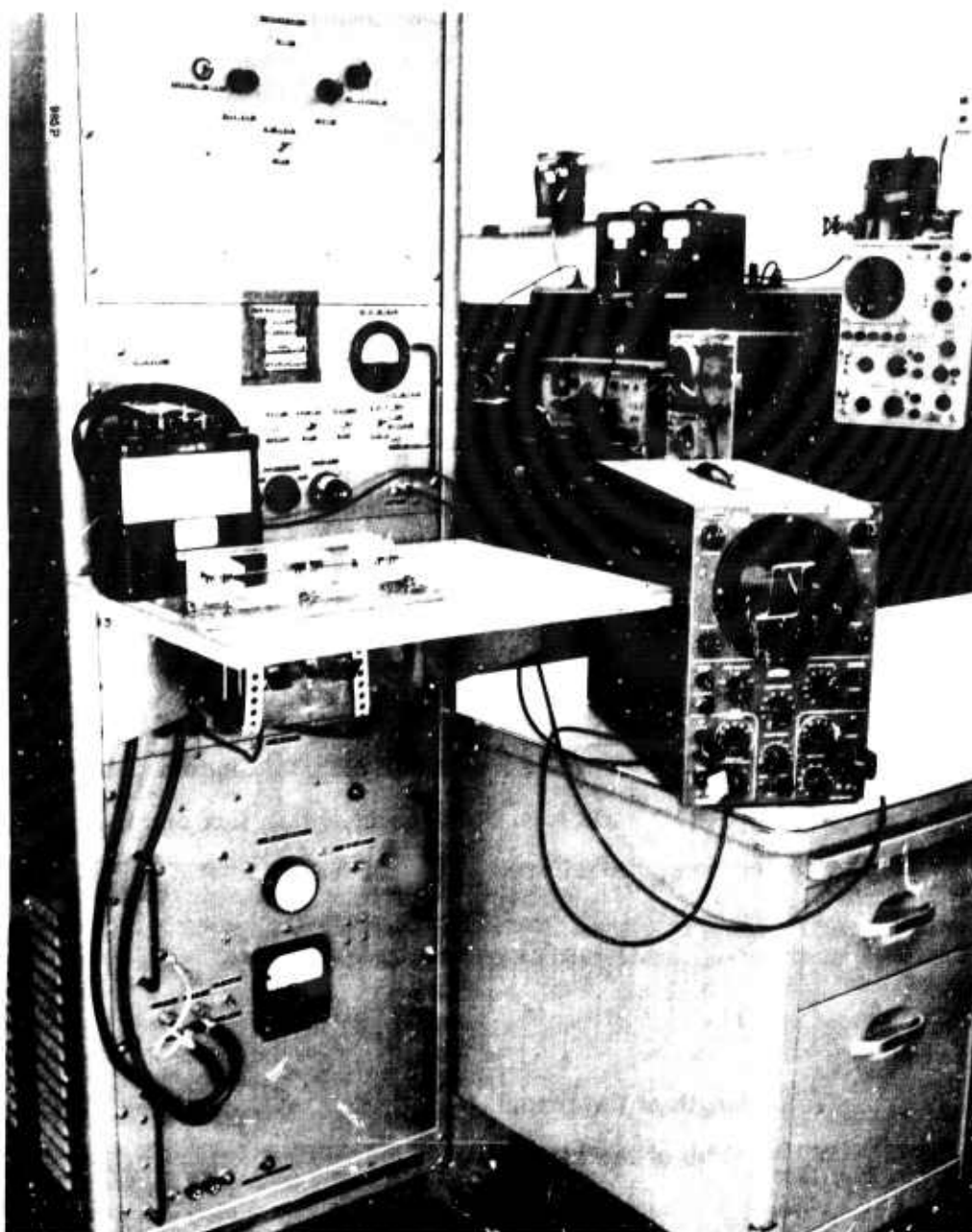
Figure 18. Square Loop Tester
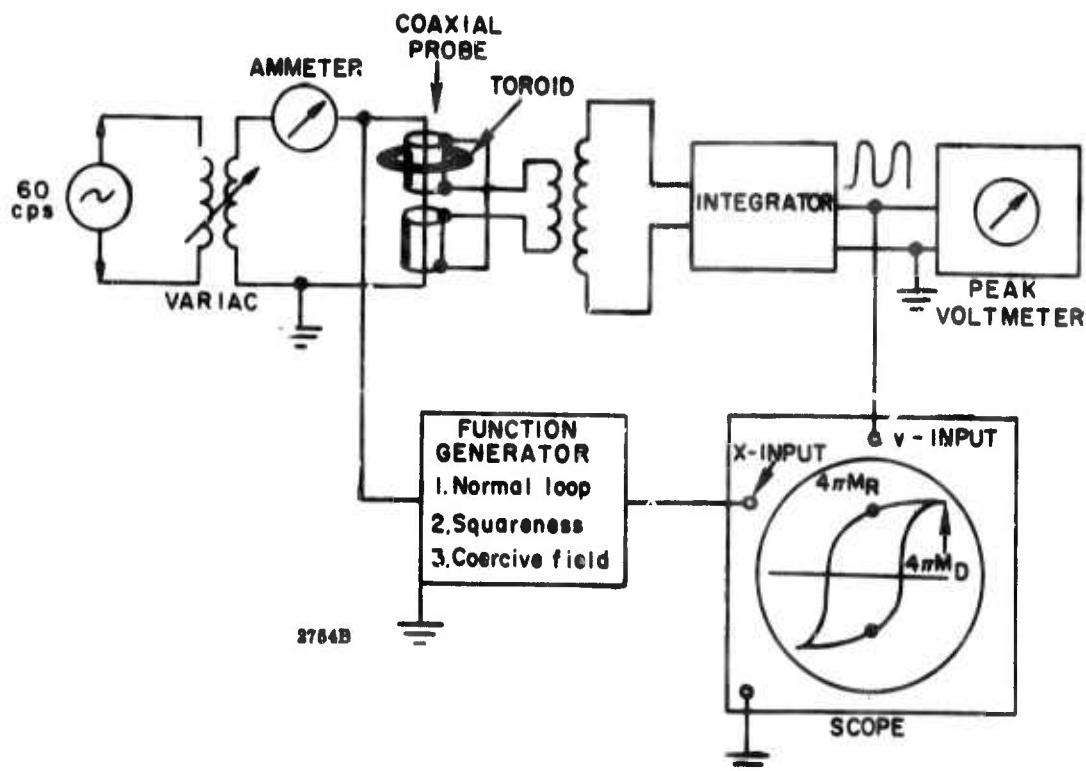
Figure 19. Schematic of Square Loop Tester Modified for Measuring the
Remanent Magnetization

(h) Grain Size and Shape. A Richert metallograph was used in the measurement
of grain size and shape.   The instrument is capable of magnifications up to 2300 and
is equipped with photographic attachments.   The metallograph is shown in Figure 20.

The toroid sample which was used for measuring remanence ratio and coercive
field was sliced in half with a diamond cutoff wheel.   The newly exposed surface of the
sample was then polished using 9 micron, 1 micron and 0. 05 micron aluminum oxide
polishing powders on a lapping wheel.   After the proper polished surface was obtained,
the sample was thermal etched for 1 hour at 200°C below the sintering temperature.

Photomicrographs, 500 magnification, were taken of the etched surface of the
sample using the metallograph.   Transparent material printed with hexagonal shapes
were prepared as overlays for the photomicrographs.   The distance between parallel
sides of the hexagonal shapes were made to correspond to 5, 7, 11, 13, 16, 20, 22, 25 or
29 microns at 500 magnification.   The particle size of the sample was then determined
by comparison of the overlays with the photomicrograph.

(i) Average Powder Particle Size. The average particle size of each material batch was measured just before the pressing and sintering operations. The apparatus shown in Figure 21 is a Fisher Sub-Sieve Sizer. The powder samples were first heated to 500°C to drive off the wax binder, then weighed to obtain 1 cm^{3} portions based on the theoretical material density. This method of measurement is supposed to have an accuracy of ± 0.05 microns.

4.2.2 Preparation Procedure

The square loop properties of these materials are strongly related to the process by which they are prepared and to the mechanical properties of the microstructure of the fired ceramic. Therefore, the preparation procedure was given special attention and studies of the structure were made at various points in the fabrication procedure.

From the raw oxide stage to the final (rf testing) stage, the following procedure was used. The particle sizes of the raw oxides were first measured in a Fisher Sub-Sieve Sizer. They were then measured out and placed in stainless steel ball jars. Batch sizes varied from 1500 to 3000 grams for the ferrites and from 1400 to 4000 grams for the garnets. The oxides were mixed by ball milling with water and one-half inch diameter stainless steel balls for 8 hours. (Mixing times of 8, 16 and 24 hours were compared in 30 and 60 percent gadolinium substituted YIG). The water was then removed by vacuum filtering, the oxides dried, screened and presintered in MgO boats from 900°C to 1150°C (for 8 hours) for the ferrites and $120)^{o}$C (for 8 hours) for the garnets. Average particle sizes of some of the compositions were measured at this point with the Fisher Sub-Sieve Sizer.

A second ball milling operation (with water) was performed to achieve a good distribution of small average size particles and to introduce a binder. The ball milling time was 4 hours for the ferrites and varied from 16 to 24 hours for the garnets. The mixture was then filtered and dried and samples of the dried powders were checked for average particle sizes.

The dried powders were then pressed into hollow cylinders (for measuring square loop and switching properties), bars (to be machined into toroids for rf measurements in the 1250 MHz to 1450 MHz frequency range), and toroids (for rf measurements in C and X bands). The samples were then fired in electric furnaces at 1250°C

4-10
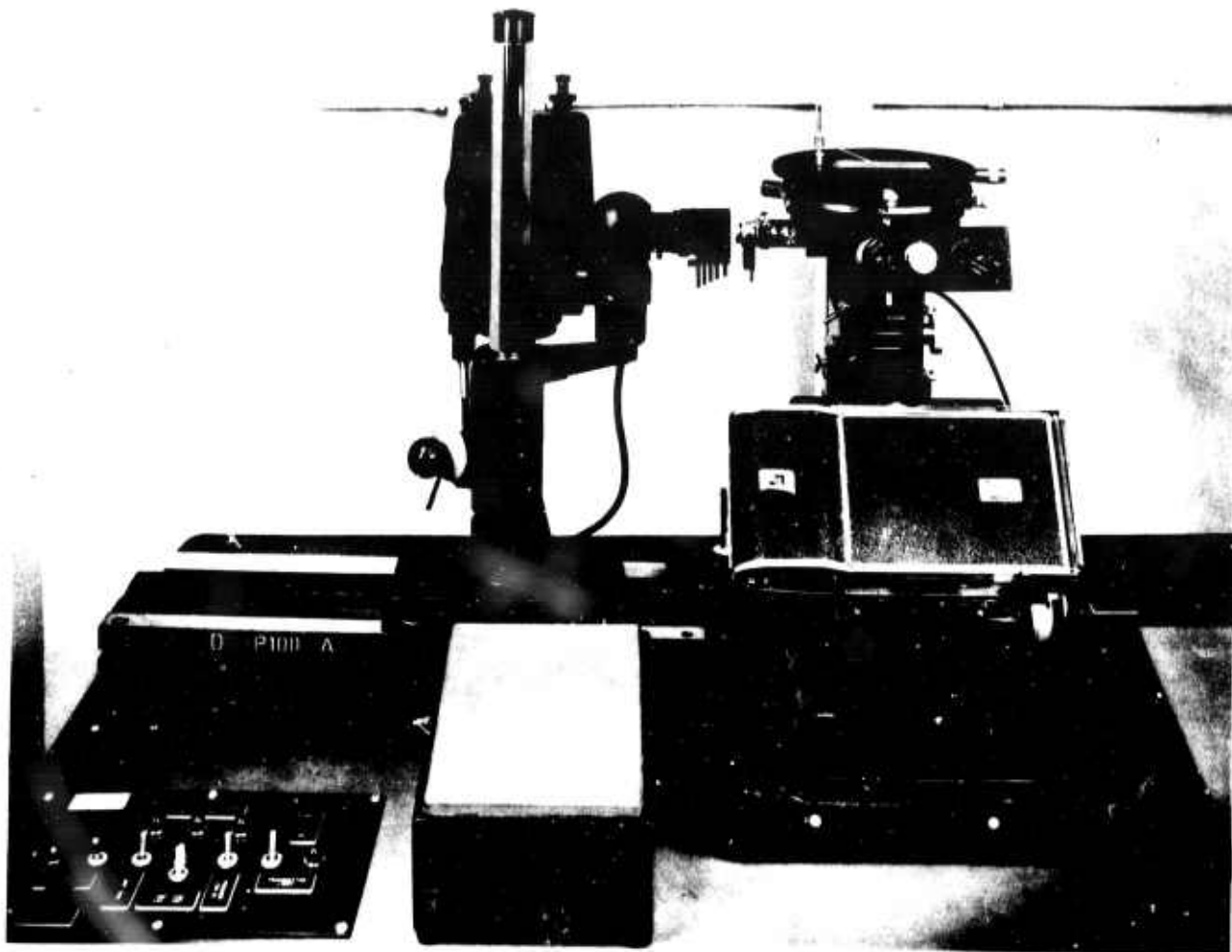
Figure 20. Reichert Metallograph Used for Material Evaluation

to $1400^{\circ}C$ for the ferrites and $1475^{\circ}C$ to $1500^{\circ}C$ for the garnets (except that some cylindrical samples of YIG were prepared using varying firing temperatures so as to check remanence ratio versus density). Minute samples were removed from the rf samples for measuring loss tangent, linewidth, magnetization, etc.

4.2.3 Measurement of Device Characteristics

(a) Measurement of Attenuation and VSWR. Measurement of attenuation and VSWR was done in the so-called ratio-detector setup depicted in Figure 22a. This method, described by Hunton et al,[16] yields a continuous display of the loss and VSWR across the frequency band and, assuming 30 db directivity, is accurate to 7 percent. This method was used only at milliwatt power levels. At high power levels the attenuation was measured by a slightly different technique as shown in Figure 23.

---

[16] J. K. Hunton and E. Lorence, "Improved Sweep Frequency Techniques for Boardband Microwave Test," Hewlett-Packard Journal, Vol. 12, No. 4, December 1960.
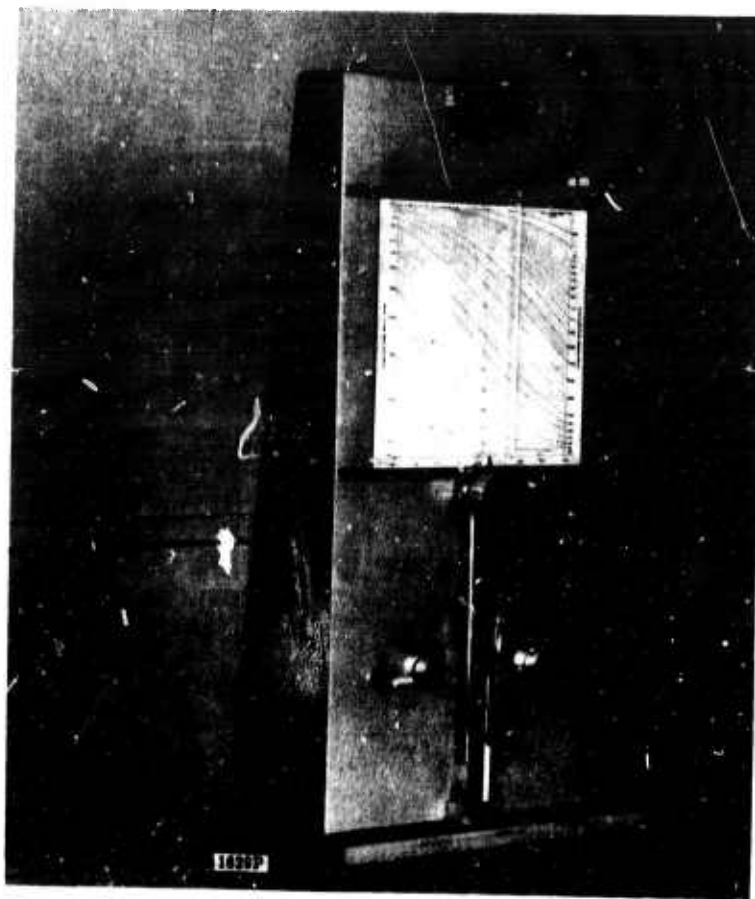
Figure 21. Fisher Sub-Sieve Sizer

(b) <u>Measurement of Differential Phase Shift</u>. Differential phase shift was measured in the phase bridge setup shown in Figure 22b. At the power splitter the rf energy divides with half the energy going into each arm. The losses of the test piece (digital phase shifter) in the lower arm are balanced and monitored by the calibrated attenuator in the upper arm. The ferrite is magnetized to the state corresponding to β+ and the calibrated phase shifter is adjusted to provide a null readout at the detector. The reading on the calibrated phase shifter is noted. The ferrite is then magnetized to β- and the calibrated phase shifter is again adjusted for a null. The second reading can now be subtracted from the first, the difference representing the differential phase shift. This method has an accuracy of better than 5 percent.

4-12
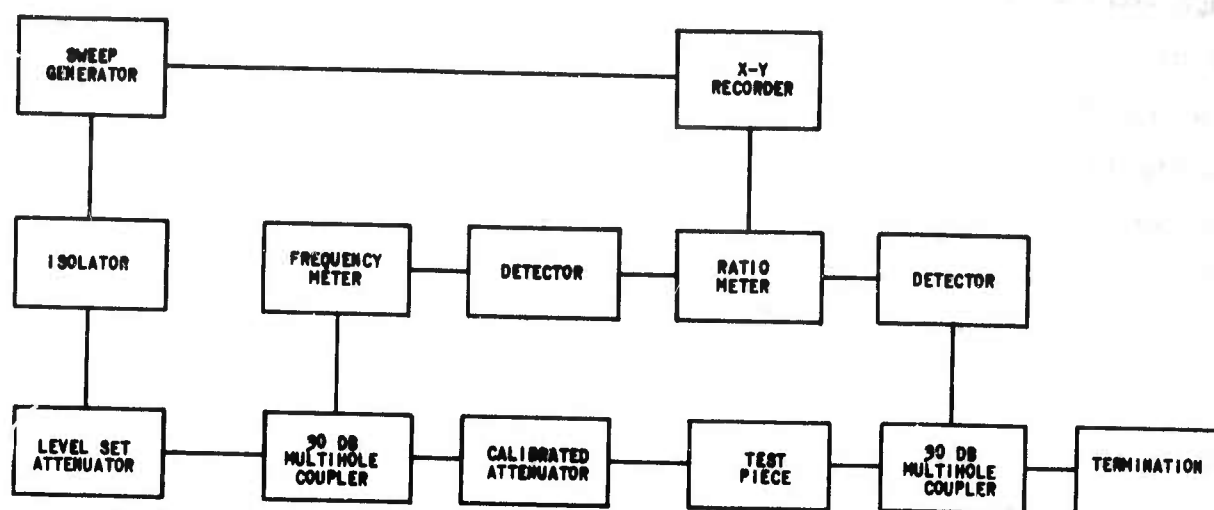
A. RATIO DETECTOR SETUP FOR MEASURING ATTENUATION AND VSWR

2706B
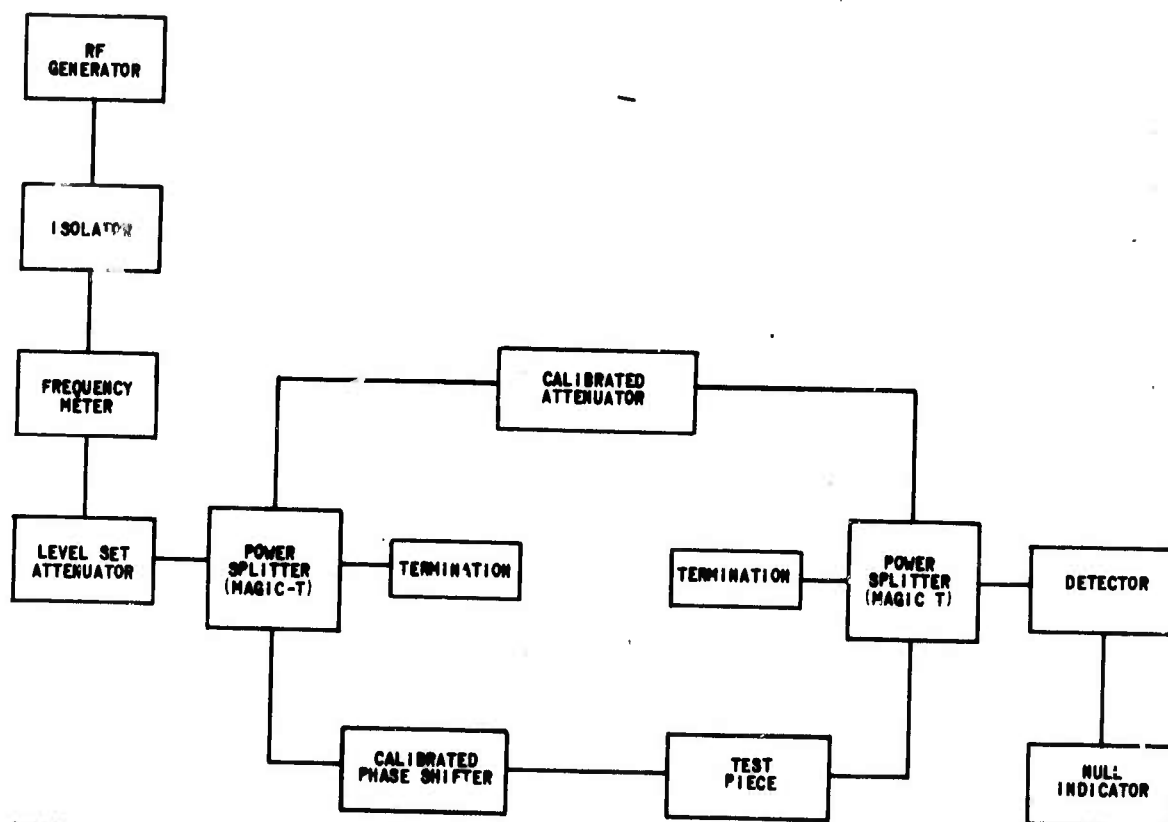
B PHASE BRIDGE SETUP FOR MEASURING PHASE SHIFT

Figure 22. Laboratory Setups for Measurement of Attenuation and Phase Shift at Low Power Levels

-4-13

This method of measuring phase shift is easily adapted to measurements at high power levels. The calibrated phase shifter is then used in the upper arm which is strongly decoupled from the main (high power) line containing the FDPS through the use of a multihole or crossguide coupler instead of the first magic-tee. A similar coupler is placed in the main line just after the test piece. The down-arm energy of this second coupler is combined by a magic-tee with the energy flowing through the calibrated phase shifter. Providing the main-line arm of this second coupler is well terminated, the accuracy should be 5 percent or better.

(c) Measurement of Attenuation at High Power Levels. The conventional means of measuring attenuation at high power levels are generally quite inaccurate because of drift problems associated with the high power source and the nulling of the detector-bridge apparatus. This problem has been largely solved by using the power-ratio scheme depicted in Figure 23.

This method involves the use of two 30 db multihole couplers, two attenuators, two thermistors, two average power meters and an x-y recorder. The line is first calibrated by butting the couplers and adjusting the attenuators so that, at all anticipated power levels, the recorder tracks a previously recorded zero-db line when the output from meter #1 is used to form the x-axis and the output from meter #2 forms the y-axis. Grid lines representing other attenuation levels can then be traced by appropriately setting attenuator #2. When the device is inserted in the line, its attenuation vs input power level is recorded as a continuous function of power in a matter of seconds.

This method has the following advantages over conventional methods:

1. Since power level ratios only are recorded, any fluctuations in source output cancel.

2. Because of the speed with which the measurement is made, null drift is minimized.

3. The attenuation display is continuous with increasing input power so that the onset of peak power instabilities can be detected at early levels.
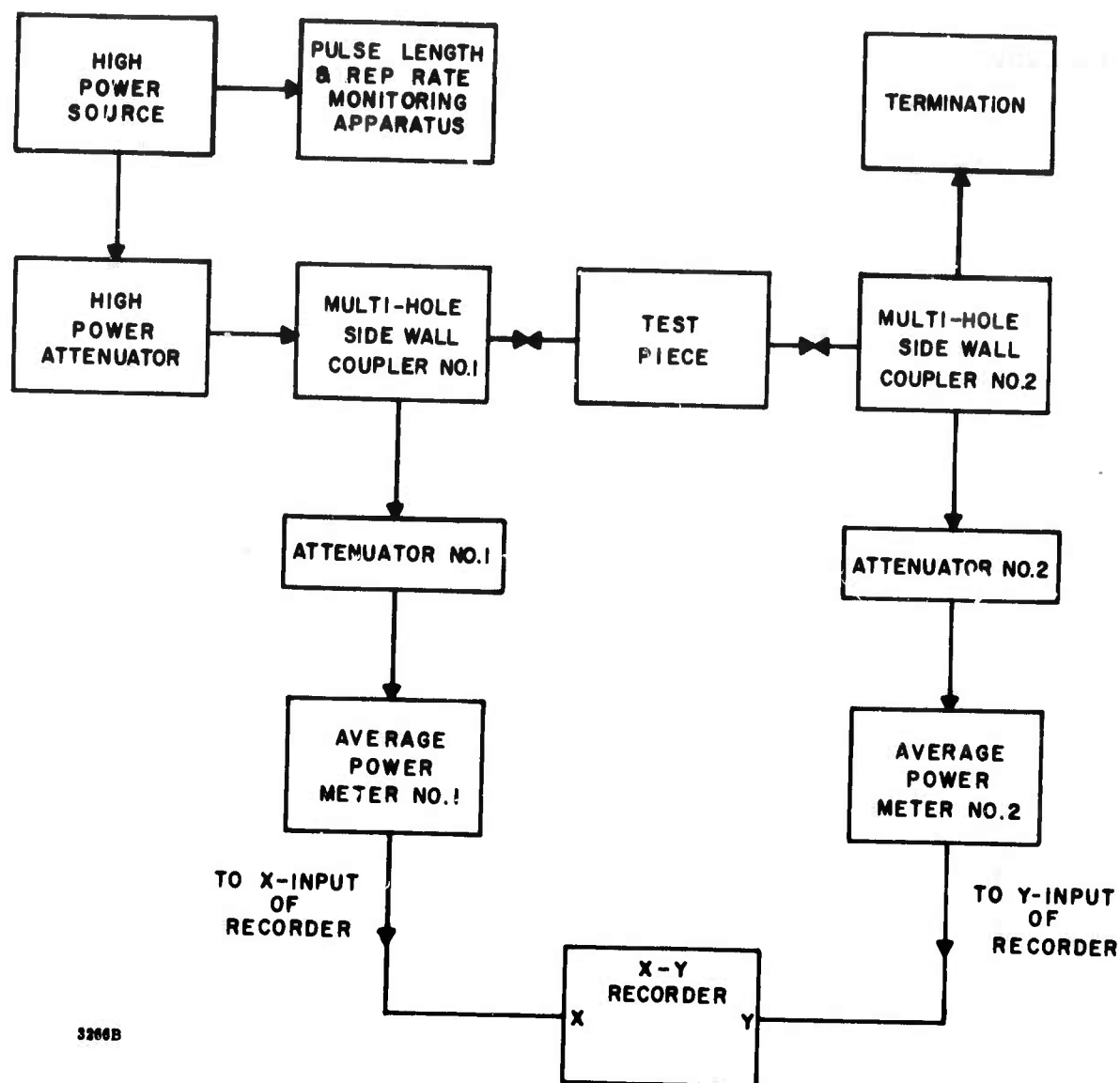
Figure 23. Power-Ratio Setup for Measuring Attenuation at High Power Levels

(d) **Measurement of Switching Energy and Switching Time.** The switching energy cannot be measured directly. There are several methods by which it can be measured indirectly and two are described below.

The solid traces in the graphs of Figure 24 show the voltage pulse across and the current pulse through the charging wire of the toroid. These traces are typical of the oscillograms obtained using fast-responding current and voltages probes. The dashed lines are intended to enclose a geometrical area roughly equivalent to the irregular area actually obtained. The switching energy is then

$$U_s = V_o I_o (\Delta t) \quad \text{(Joules)}. \tag{37}$$

4-15

Typically

$$V_o = 35 \text{ volts}$$

$$I_o = 10 \text{ amps}$$

$$\Delta t = 1 \text{ microsecond}$$

so

$$U_s = 35 \times 10 \times 10^{-6} = 350 \text{ microjoules.}$$

The second method is that of measuring the rms voltage and current required for continuous switching at a rate R. Using this method

$$U_s = \frac{I_{rms} \times V_{rms}}{2R} \text{ joules} \qquad (38)$$

where the factor 2 is used because R is given in cycles/second and therefore represents switching from a given state to another and back again.

2700B
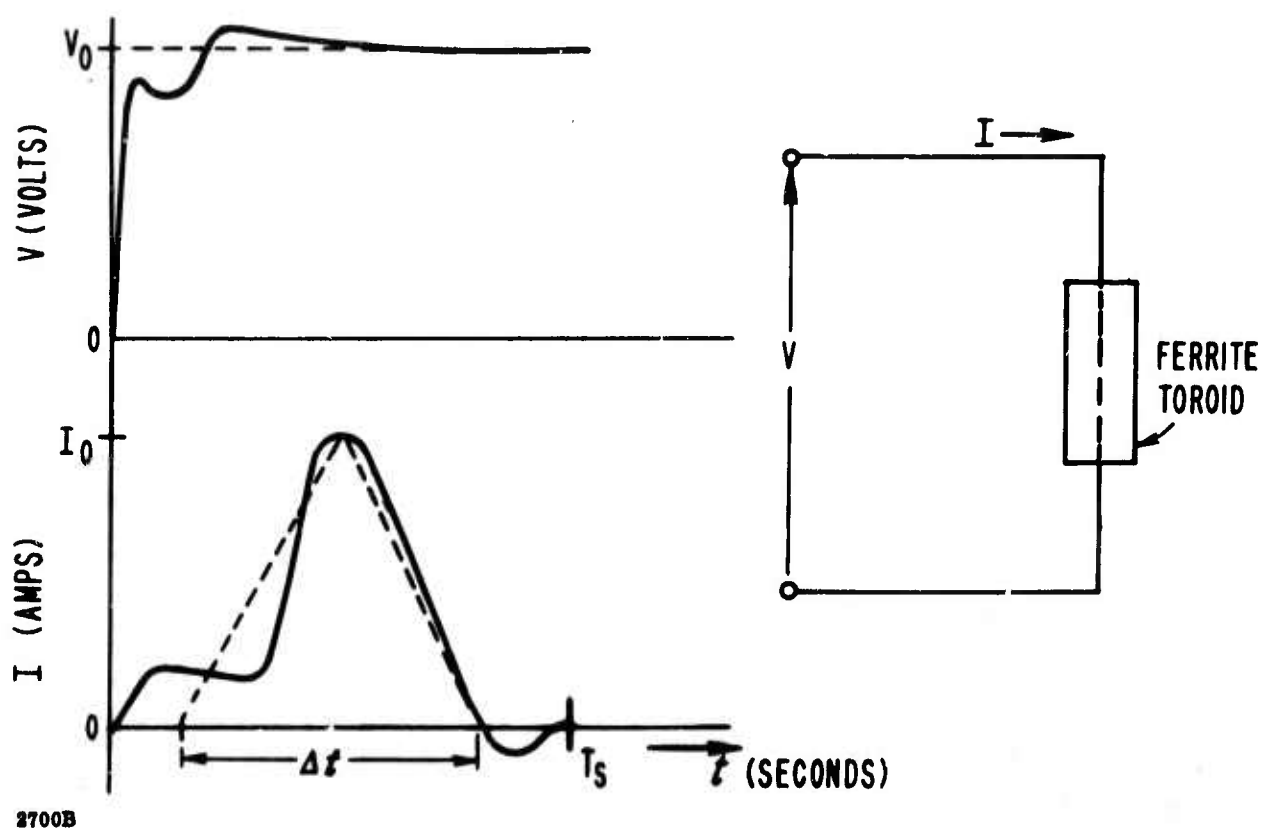
Figure 24. Typical Voltage and Current Waveforms Observed During Fast Switching of the Ferrite Toroids. The Switching Time T_s is also Shown.

4-16

4.3 MATERIALS FOR EVALUATION (COMPOSITIONS AND REASONS FOR SELECTION)

A comprehensive list of the material compositions which have been fabricated and evaluated is provided by Tables I and II of Section 4.4 and Tables V, VI and VII of Section 4.5. It is, perhaps, worthwhile noting that the materials listed in the referenced tables have been selected a few at a time throughout the program. These materials thus reflect a continuous feedback of the information obtained from the evaluation studies discussed in Section 4.4 and 4.5.

The suitability of a given ferrimagnetic material for use in a phase shifter ultimately depends on the performance requirements imposed on the phase shifter. Certain features, however, are desired of all good phase shifter materials. Among these are low dielectric and magnetic losses, high remanence ratio, low coercive field, high reproducibility of all properties, temperature stability of microwave and square loop properties, and low cost. Low cost is particularly important in large array applications. The relative costs of nonoriented ferrimagnetic materials can be compared by simply examining the cost of the raw oxides used in fabricating each material, since the preparation cost is reasonably constant from one material to the next. The raw oxide costs for the spinel ferrites is considerably less than that for the garnets, and when cost is the overriding factor, ferrites certainly are preferred over garnets.

In a given application tradeoffs must normally be made among the various desired properties to obtain a material that is satisfactory from all points of view. The material studies carried out on this program have been selected to determine and highlight possible trade-off areas. Particular emphasis has been placed on obtaining optimum materials for use in high peak power phase shifters in X, C, S, and L bands.

The materials listed in Tables I, II, V, VI, VII and VIII have been carefully selected to provide the basis for a thorough study of square loop and microwave properties of ferrimagnetic materials and their influence on the performance characteristics of FDPS. A brief summary of these investigations is as follows:

Three aluminum dysprosium doped YIG materials, three aluminum gadolinium doped YIG materials, and one aluminum gadolinium dysprosium doped material were selected for rf evaluation at low frequencies (L band). The aluminum doping is used to lower the saturation magnetization. Gadolinium doping imparts some measure of temperature (and average power) stability to the magnetization, and dysprosium doping is used to enhance the high peak power handling capacity of these materials.

Five gadolinium doped YIG materials were chosen for further studies of the dependence of loss and threshold power level on magnetization in materials with increasing anisotropy.

Four dysprosium doped YIG materials were selected to study the dependence of loss and threshold power level as a function of both magnetization and intrinsic linewidth.

Five ferrites from the nickel-zinc family were chosen for investigations of loss and threshold power level versus magnetization of these materials with larger intrinsic linewidths and widely varying anisotropy.

Four materials from the magnesium manganese aluminum ferrite family were selected to evaluate loss and threshold power level variation with magnetization for small intrinsic linewidths and varying anisotropy.

Three materials from the nickel cobalt ferrite family were selected for investigation of loss and threshold power variation with magnetization in the presence of low anisotropy and rather high intrinsic linewidths.

A single sample of lithium ferrite was also prepared for general rf evaluation in the 5 to 10 GHz frequency range.

Six compositions, namely three Al doped YIGs, two NiZn ferrites and one MgMn ferrite were evaluated in below resonance ($f < f_r$) operation in L band.

While some of these materials would not necessarily be selected as "good" digital phase shifter materials, they are nonetheless of considerable interest because their properties represent a wide range of intrinsic material parameters which can be used as an aid in testing and understanding the dependence of phase shifter performance on ferrite characteristics. The investigation of the dependence of magnetic loss on

linewidth through the evaluation of the series of dysprosium doped garnets illustrates this point.

4.4 MATERIAL PROPERTIES

Tables I and II list data accumulated on 14 garnet and 13 ferrite materials, respectively. Large batches of each composition were prepared for this second phase of the RADC/ARPA program so that extensive materials and device studies could be made on the same material batch. This eliminates the possibility of introducing batch-to-batch variations.

Measured properties of the compositions shown in Tables I and II are discussed in this section.

The sample nomenclature used on this program is as follows:

Example: G-251 - 15 C

Designates a particular
composition

Designates the batch
number of this parti-
cular composition

Designates the parti-
cular sample pressed
from this composition
and batch
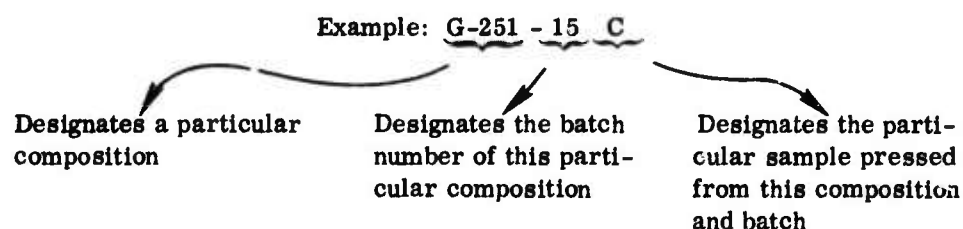
The average powder particle sizes were obtained using a Fisher Sub-Sieve Sizer according to the method outlined in Section 4.2.1. In general, the ferrite powders were found to have smaller average particle sizes than the garnets.

The grain size and square loop values listed were obtained from half-inch long, relatively thin walled (0.060") toroids fired in the same furnace with the device toroids. Photomicrographed surfaces were prepared in accordance with the method given in Section 4.2.1. The average grain sizes were estimated by comparing the photomicrographs with plastic overlays. Little correlation of static and microwave properties with grain size was found.

4-19

Some materials for these tables have been subjected to special investigations. Table III shows the effects of mixing time in 30% gadolinium substituted yttrium iron garnet and 60% gadolinium substituted yttrium iron garnet. Three batches of each material were made with mixing times of 8, 16 and 24 hours each. The usual mixing time is 8 hours. The purpose of this study was to determine if the square loop properties could be improved without degrading such microwave properties as the dielectric loss tangent. A waxing time of 24 hours was used throughout.

Powder particle size measurements made just after the mixing of the raw oxides showed a decrease in particle size with increasing mixing time as might be expected. However, there seems to be no correlation to the average particle sizes measured after the waxing time which are also shown. Furthermore, increasing the mixing time has no apparent effect on the measured densities or the measured grain sizes. The measured density for all three 30% gadolinium substituted yttrium iron garnet samples was approximately 5.50, while that for the 60% gadolinium substituted yttrium iron garnet was approximately 5.84. The grain sizes of the two compositions were approximately 12 and 16 microns for the 30% and 60% gadolinium substituted yttrium iron garnets, respectively. On the other hand, improvements in linewidth, coercive force and remanence ratio, taken on the whole, might indicate that the 24 hours mixing time is to be preferred (the observed small changes in loss tangent could very well be explained by experimental error).

Figure 25 shows photomicrographs of three samples each from the 30% and 60% gadolinium substituted yttrium iron garnets listed in Table III. It is seen from the remanence ratio and coercive force values that a reasonably good correlation exists between porosity, as evidenced by the holes, and square loop properties.

Dependence of Square Loop Properties on Composition. While composition does not, in general, appear to be a limiting factor in the achievement of good square loop properties, both remanence ratio and coercive field are influenced by factors which are dependent on composition. In particular, the coercive field varies with anisotropy field $\left[\text{as can be seen from Eq. (35)}\right]$ which in turn is largely determined by composition.
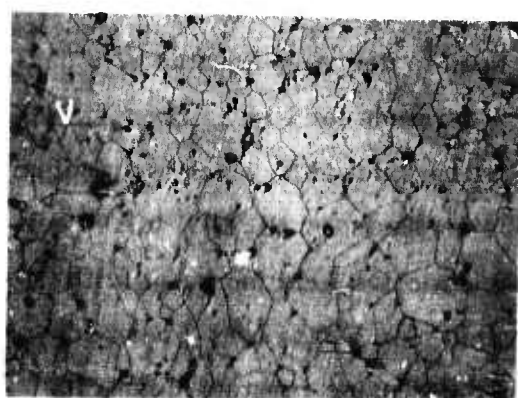
D80A2-4-10C   Mix Time=8 hours
Average Grain Size=15 microns
Density=5.85 gm/Cm^3,
R_r=.34 H_c=2.25 oe.
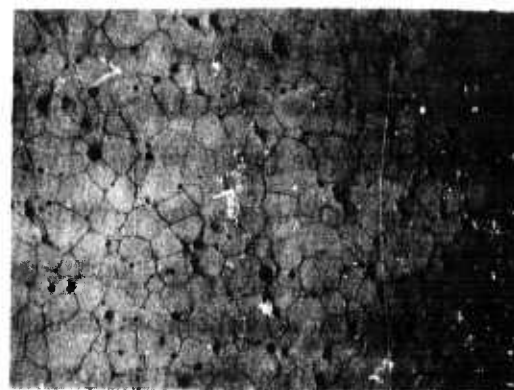
D80A2-2-10C Mix Time=8 hours
Average Grain Size=13 microns
Density=5.50 gm/Cm^3
R_r=.20 H_c=.90 oe.
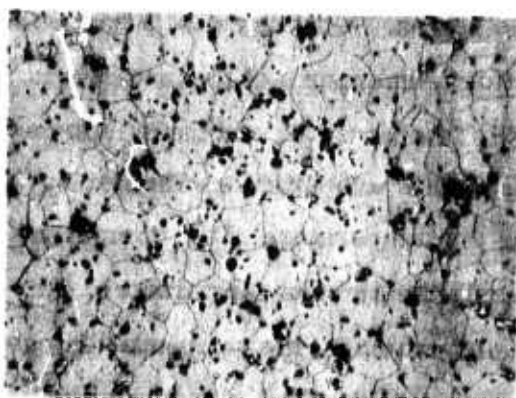
D80A2-4-11C   Mix Time=16 hours
Average Grain Size=16 microns
Density=5.82 gm/Cm^3
R_r=.38 H_c=2.10 oe.
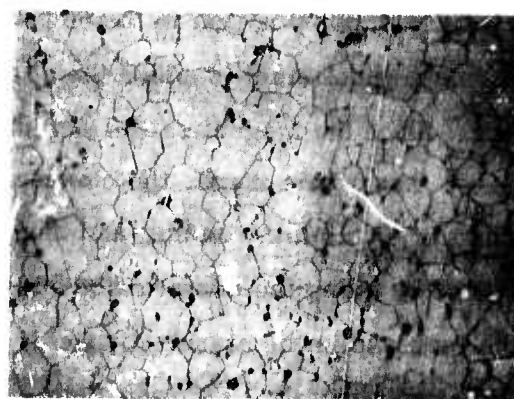
D80A2-2-11C   Mix Time=16 hours
Average Grain Size=12 microns
Density=5.48 gm/Cm^3
R_r=.63 H_c=1.00 oe.
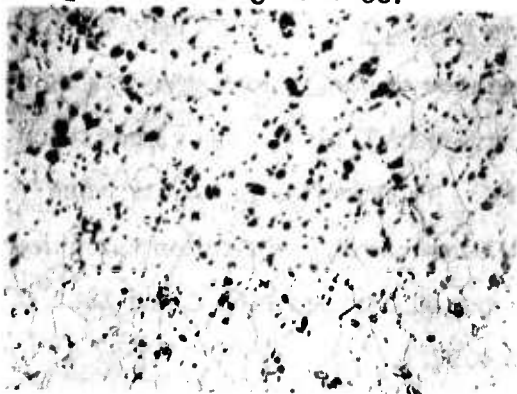
D80A2-4-12C   Mix Time=24 hours
Average Grain Size=16 microns
Density=5.88 gm/Cm^3
R_r=.37 H_c=2.05 oe.
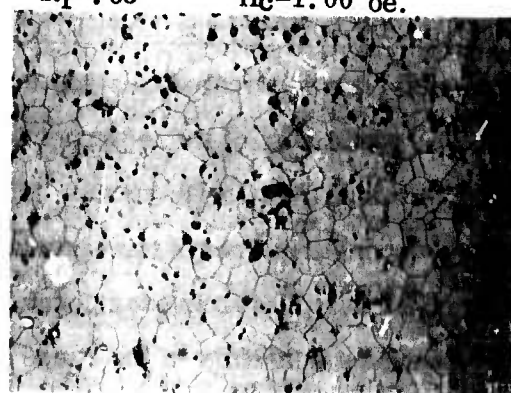
D80A2-2-12C Mix Time=24 hours
Average Grain Size=12 microns
Density=5.49 gm/Cm^3
R_r=.72 H_c=.95 oe.

Figure 25.   Photomicrographs of 60% Gadolinium Substituted YIG
and 30% Gadolinium Substituted YIG

Two examples of the variation of H_c with composition (taken from Tables I and II) are shown in Figure 25A (nickel zinc ferrite) and Figure 25B (gadolinium substituted YIG). In Figure 25A the coercive field is seen to decrease from about 6 oersteds for pure nickel ferrite ($NiFe_2O_4$) to about 0.4 oersteds for $Ni_{0.325}Zn_{0.675}Fe_2O_4$. Over this same compositional range, the polycrystalline linewidth, which is principally determined by the anisotropy field, varies from 530 oersteds for $NiFe_2O_4$ to 100 oersteds for $Ni_{0.325}Zn_{0.675}Fe_2O_4$. In Figure 25B the coercive field increases with increasing gadolinium content from about 0.75 oersted for YIG to over 2 oersteds for 60 percent gadolinium substituted YIG while over this same range the linewidth varies from 40 oersteds for YIG to over 200 oersteds for the 60 percent Gd substituted material. It is to be noted also that coercive field, like linewidth, is increasing much more rapidly with composition in the 60 percent Gd region. What is actually happening is that as more gadolinium is added the compensation temperature of the material is increasing. Since the magnetization vanishes at this temperature, and the anisotropy field $\left(\dfrac{K_1}{m_s}\right)$ has a pole there, the closer one gets to this temperature, whether by increasing the gadolinium content (and thus raising the temperature of the compensation point) or by fixing the composition and decreasing the ambient temperature, the faster the increase in the anisotropy field. Thus, for example, the compensation point of GdIG is approximately $15^\circ C$ (see Figure 31) and one would expect to measure an exceedingly large coercive field for this material at room temperature.

Dependence of Square Loop Properties on Porosity. Table IV lists the properties of materials fabricated to study the dependence of square loop properties on density. The remainder of these properties are listed in Table I. The composition chosen for this investigation is yttrium iron garnet. The changes in density were obtained by varying the firing temperature while the remaining fabrication variables were held constant. The firing temperature was varied between $1400^\circ C$ and $1500^\circ C$ with corresponding densities in the range 4.71 to 4.97.
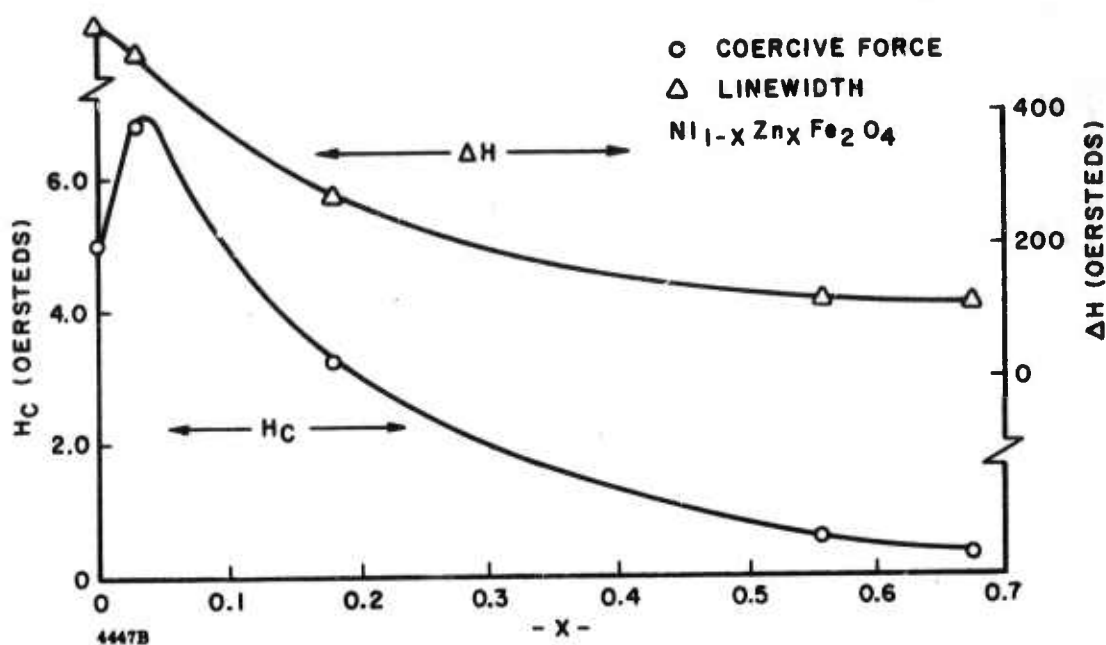
Figure 25A. Variation of Coercive Force and Linewidth with Zinc Content in Nickel-Zinc Ferrite
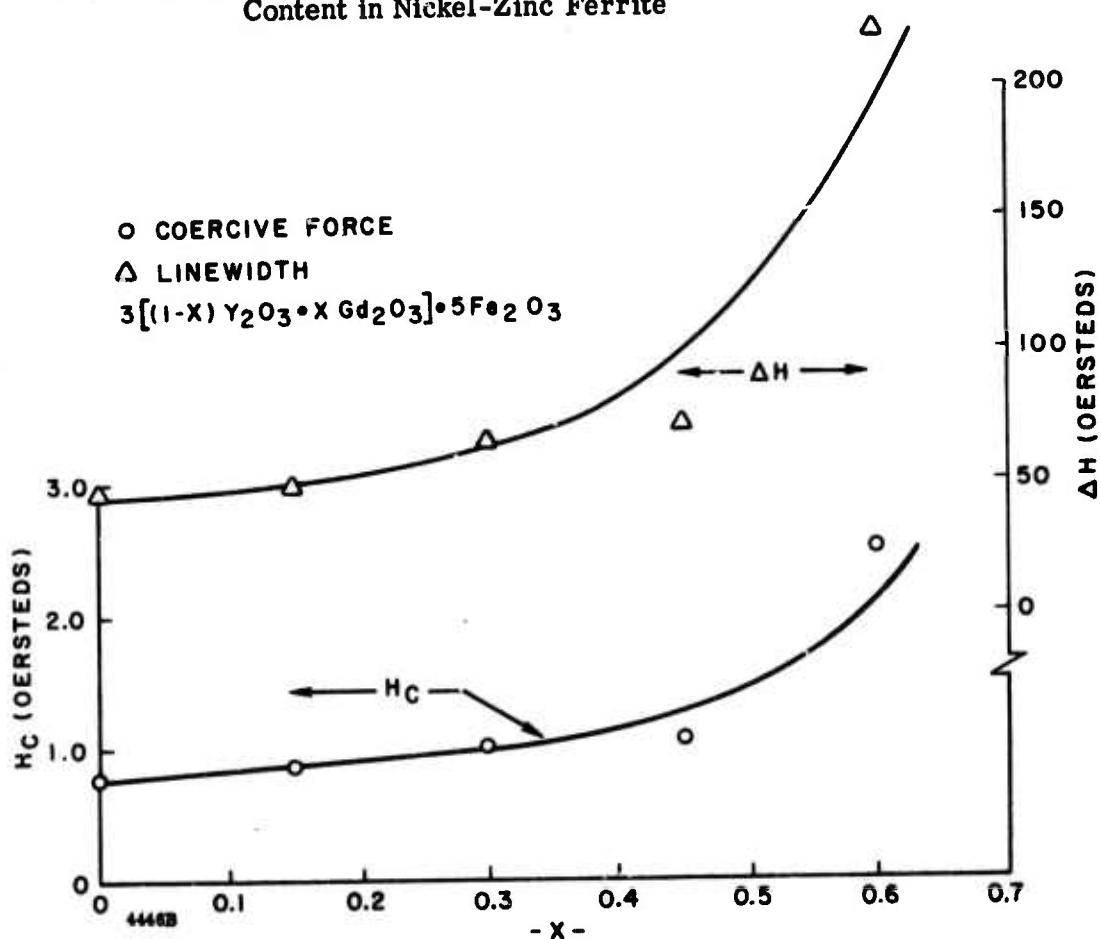
Figure 25B. Variation of Coercive Force and Linewidth with Gadolinium Content in Gadolinium-Doped YIG

TABLE I. GARNET MATER
EVALUATION FR

$$3\left[(1.0\text{-}x)\,Y_2O_3 \cdot xRE_2O_3\right]\cdot 5$$
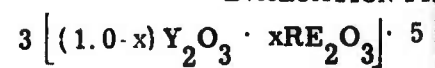
SMEC NO.	COMPOSITION x	w	BATCH SIZE	WAXING TIME (HRS)	FIRING SCHEDULE (°C/HR)	ρ_m/ρ_x gms/cm³	PARTICLE SIZE (MICRONS)	TANδ/ε' X BAND	G FACTOR
D80A1-108	0	0	3600	24	1475 / 5	5.08 / 5.17	2.50	0.0004 / 15.8	2.02
G238-6	0	0.20	2800	24	1500 / 5	4.98 / 5.04	NM	0.0024 / 14.9	2.02
G250-6	0	0.25	2750	24	1500 / 5	4.98 / 5.01	NM	0.0019 / 14.2	2.03
D80A2-1-14	0.15 Gd	0	3950	24	1475 / 5	5.30 / 5.38	2.15	0.0005 / 16.0	2.02
D80A2-2-10	0.30 Gd	0	3950	24	1475 / 5	5.50 / 5.56	1.75	0.0005 / 16.2	2.02
D80A2-3-7	0.45 Gd	0	4100	24	1475 / 5	5.69 / 5.76	1.90	0.0001 / 16.5	2.02
D80A2-4-10	0.60 Gd	0	4200	24	1475 / 5	5.85 / 5.95	2.35	0.0006 / 16.3	2.05
G129-4	0.02 Dy	0	2950	24	1475 / 5	5.14 / 5.20	1.90	0.0004 / 16.0	1.99
G351-4	0.05 Dy	0	2950	24	1475 / 5	5.18 / 5.32	1.85	0.0016 / 16.0	1.96
G131-3	0.10 Dy	0	3000	24	1475 / 5	5.26 / 5.25	1.90	0.0010 / 16.1	1.88
G490-1	0.02 Dy	0.20	2800	24	1500 / 5	5.04 / 5.10	NM	0.0091 / 15.0	1.96
G491-1	0.05 Dy	0.20	2850	24	1500 / 5	5.07 / 5.16	NM	0.004 / 15.2	1.86
G431-3	0.15 Gd	0.20	2900	24	1500 / 5	5.20 / 5.24	NM	0.0016 / 14.5	2.05
G493-1	0.15 Gd 0.02 Dy	0.20	2950	24	1500 / 5	5.19 / 5.31	NM	0.0040 / 14.8	1.95

* ρ_m = measured density

ρ_x = x-ray density

NM – Not measured

$$\text{[}_2\text{O}_3] \cdot 5\left[(1.0-w)\text{Fe}_{1.925}\text{O}_3 \cdot w\text{A}\ell_{1.925}\text{O}_3\right]$$
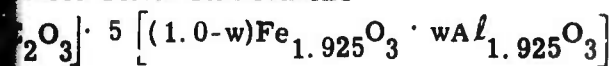
g FACTOR	LINE WIDTH ΔH (oe) X BAND	$4\pi M_S$ (GAUSS)	DRIVE CURRENT I_D (AMPS RMS)	COERCIVE FIELD H_c (OE) (60~)	COERCIVE FIELD (H_D/H_c)	SQUARENESS S_D	$4\pi M_{RD}$ (GAUSS)	REMANENCE RATIO R_R	SAMPLE* SHAPE	w/w
2.02	47	1730	10.0	0.76	8.95	0.74	1165	0.68	b	0.385 / 0.265
2.02	35	510	10.0	0.71	10.0b	0.65	250	0.49	b	0.385 / 0.265
2.03	38	290	9.7	0.68	10.0b	0.52	100	0.35	b	0.385 / 0.265
2.02	47	1525	11.8	0.86	10.0b	0.79	1057	0.69	b	0.385 / 0.265
2.02	66	1285	15.0	1.00	10.0	0.76	817	0.64	b	0.385 / 0.265
2.02	69	1625	14.3	1.04	10.0	0.67	660	0.64	b	0.385 / 0.265
2.05	220	716	20.0	2.50	5.80	0.59	290	0.41	b	0.385 / 0.265
1.99	91	1780	10.0	0.75	10.0	0.88	1340	0.76	b	0.385 / 0.265
1.96	168	1730	10.0	0.77	9.0	0.87	1256	0.73	b	0.385 / 0.265
1.88	295	1755	10.0	0.90	8.0	0.88	1170	0.67	b	0.385 / 0.265
1.96	123	515	9.25	0.65	10.0	0.59	220	0.44	b	0.385 / 0.265
1.86	274	500	9.90	0.72	10.0	0.44	160	0.32	b	0.385 / 0.265
2.05	110	370	17.1	1.20	10.0	0.58	130	0.35	b	0.385 / 0.265
1.95	230	300	15.9	1.09	10.0	0.59	120	0.49	b	0.385 / 0.265

*SAMPLE SHAPE

(a)   (b)

TABLE II. FER

SMEC NO.	COMPOSITION	BATCH SIZE	WAXING TIME (hours)	FIRING SCHEDULE (°C/HR)	ρ_m/ρ_x gms/cm³	POWDER PARTICLE SIZE (microns)	TANδ/ε X BAND
16-20	$Ni_{1.0} Mn_{0.02} Fe_{1.9} O_4$	1700	4	1400 / 7	4.86 / 5.35	1.40	0.010
78-4	$Ni_{0.97} Zn_{0.03} Mn_{0.02} Fe_{1.9} O_4$	1700	4	1275 / 7	4.92 / 5.35	1.35	0.006
77-3	$Ni_{0.824} Zn_{0.176} Mn_{0.02} Fe_{1.9} O_4$	1750	4	1275 / 7	5.02 / 5.35	1.35	0.015
91-3	$Ni_{0.44} Zn_{0.56} Mn_{0.02} Fe_{1.9} O_4$	2800	4	1250 / 7	5.04 / 5.35	1.45	0.001
61-4	$Ni_{0.325} Zn_{0.675} Mn_{0.02} Fe_{1.9} O_4$	1750	4	1250 / 7	5.13 / 5.35	1.40	0.001
83-8	$0.58MgO \cdot 0.06MnO \cdot 0.36Fe_2O_3$	1750	4	1320 / 7	4.20 / 4.39	1.50	0.001
121-3	$0.87Mg \cdot 0.04Mn \cdot 0.10Cu \cdot 0.03Co \cdot 0.27Al \cdot 1.48Fe \cdot 4O$	1850	4	1400 / 7	4.29 / 4.50	NM	0.002
65-28	$0.516MgO \cdot 0.057MnCO_3 \cdot 0.091Al_2O_3 \cdot 0.366Fe_2O_3$	1800	4	1400 / 7	4.05 / 4.40	NM	0.001
115-2	$0.565MgO \cdot 0.063MnCO_3 \cdot 0.112Al_2O_3 \cdot 0.261Fe_2O_3$	1700	4	1400 / 7	3.95 / 4.30	NM	0.001
18-8	$Ni_{0.975} Co_{0.025} Mn_{0.02} Fe_{1.9} O_4$	2800	4	1275 / 7	4.80 / 5.30	NM	NM
50-2	$Ni_{0.965} Co_{0.035} Mn_{0.02} Fe_{1.9} O_4$	1800	4	1250 / 7	4.86 / 5.30	NM	NM
G147-1	$Ni_{0.950} Co_{0.050} Mn_{0.02} Fe_{1.9} O_4$	2750	4	1250 / 7	4.87 / 5.30	NM	0.009
64-4	$Li_{1.0} Fe_5 O_8$	1750	4	1250 / 7	4.34 / 4.75	NM	>0.01 N

* ρ_m = measured density

ρ_x = x-ray density

NM - Not measured

POWDER PARTICLE SIZE (MICRON)	TAN δ'd X BAND	G FACTOR	LINE WIDTH ΔH (oe) X BAND	$4\pi\mu_S$ (GAUSS)	DRIVE CURRENT I_0 (AMPS RMS)	COERCIVE FIELD H_c (OE) (60~)	COERCIVE FIELD (H_D/H_c)	SQUARENESS S_D	$4\pi M_{RD}$ (GAUSS)	REMANENCE RATIO R_R	SAMPLE SHAPE	w/a
.40	0.010 / 12.6	2.44	520	2815	20.0	5.00	2.60	0.71	998	0.36	b	0.385 / 0.265
.35	0.006 / 12.7	2.38	485	2965	20.0	6.80	2.15	0.80	1220	0.41	b	0.385 / 0.265
.35	0.015 / 13.2	2.27	270	3820	20.0	3.25	4.50	0.76	1854	0.49	b	0.385 / 0.265
.45	0.0016 / 13.7	2.13	115	3770	5.0	0.55	10.0	0.95	2445	0.65	b	0.385 / 0.265
.40	0.001 / 14.9	2.07	197	2770	2.53	0.35	10.0	0.34	539	0.20	b	0.385 / 0.265
.50	0.001 / 12.9	2.13	512	2065	20.0	2.35	6.20	0.81	1175	0.57	b	0.385 / 0.265
NM	0.002 / 12.7	2.05	266	1440	20.0	2.22	10.0	0.49	505	0.35	b	0.385 / 0.265
NM	0.001 / 11.7	2.02	140	1190	10.0	1.11	10.0	0.69	678	0.57	b	0.385 / 0.265
NM	0.001 / 11.2	2.01	176	615	6.4	0.71	10.0	0.48	172	0.28	b	0.385 / 0.265
NM	NM / NM	2.23	375	2865	20.0	11.5	2.0	0.74	1170	0.41	b	0.385 / 0.265
NM	NM / NM	2.37	349	2970	20.0	10.3	2.2	0.69	1160	0.39	b	0.385 / 0.265
NM	0.009 / 12.5	2.35	625	NM	NM	NM	NM	NM	NM	NM	b	0.385 / 0.265
NM	>0.01 / NM	2.23	595	3365	20.0	2.94	4.50	0.85	2176	0.65	b	0.385 / 0.265

...sured density

...ay density

...measured

*SAMPLE SHAPE
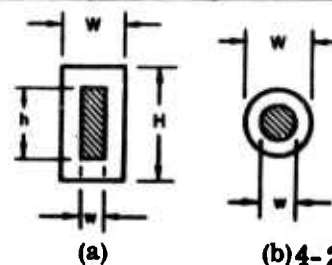
(a)   (b)   4-27/4-28

TABLE III. THE EFFECTS OF N
COMPOSITIONS FR

$$3 \left[(1.0\text{-}x)\, Y_2O_3 \cdot xRE_2O_3 \right] \cdot$$
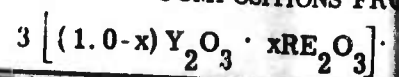
SMEC NO.	COMPOSITION	BATCH SIZE	MIXING TIME (HOURS)	PARTICLE SIZE (MICRONS)	WAXING TIME (HOURS)	PARTICLE SIZE (MICRONS)	FIRING SCHEDULE (°C/HR)	DENSITY (gm/cm³)	GRAIN SIZE (MICRONS)
D80A2-2-10B	0.30 Gd	3950	8	1.70	24	1.75	1475 / 5	5.50	13
D80A2-2-10C	0.30 Gd	3950	8		24	1.75	1475 / 5	5.50	NM
D80A2-2-11B	0.30 Gd	3950	16	1.60	24	1.75	1475 / 5	5.48	NM
D80A2-2-11C	0.30 Gd	3950	16		24	1.75	1475 / 5	5.48	12
D80A2-2-12B	0.30 Gd	3950	24	1.50	24	1.80	1475 / 5	5.49	NM
D80A2-2-12C	0.30 Gd	3950	24		24	1.80	1475 / 5	5.49	12
D80A2-4-10B	0.60 Gd	4200	8	2.25	24	2.45	1475 / 5	5.85	NM
D80A2-4-10C	0.60 Gd	4200	8		24	2.45	1475 / 5	5.85	15
D80A2-4-11B	0.60 Gd	4200	16	2.10	24	2.40	1475 / 5	5.82	NM
D80A2-4-11C	0.60 Gd	4200	16		24	2.40	1475 / 5	5.82	16
D80A2-4-12B	0.60 Gd	4200	24	1.85	24	2.00	1475 / 5	5.85	NM
D80A2-4-12C	0.60 Gd	4200	24		24	2.00	1475 / 5	5.85	16

NM - Not measured

HE EFFECTS OF MIXING TIME IN TWO
OMPOSITIONS FROM THE FAMILY

$$[Y_2O_3 \cdot xRE_2O_3] \cdot 5 [Fe_{1.925}O_3]$$
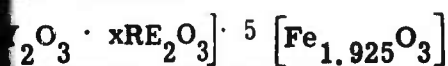
DENSITY (gm/cm³)	GRAIN SIZE (MICRONS)	G FACTOR	LINE WIDTH ΔH (oe) X BAND	$4\pi\mu_S$ (GAUSS)	TANδ/ε' X BAND	COERCIVE FIELD H_c (OE) (60~)	SQUARENESS S_D	$4\pi M_{RD}$ (GAUSS)	REMANENCE RATIO R_R	SAMPLE* SHAPE	w/w
5.50	13	2.02	65	1200	0.0011 / 16.2	0.90	0.837	1005	0.70	b	0.385 / 0.265
5.50	NM	NM	NM	NM	NM	0.90	0.837	1005	0.70	b	0.385 / 0.265
5.48	NM	2.02	75	NM	0.0008 / 16.2	1.00	0.791	950	0.64	b	0.385 / 0.265
5.48	12	NM	NM	NM	NM	1.05	0.788	945	0.63	b	0.385 / 0.265
5.49	NM	2.02	59	NM	0.0016 / 16.0	0.95	0.836	1003	0.71	b	0.385 / 0.265
5.49	12	NM	NM	NM	NM	0.95	0.844	1013	0.72	b	0.385 / 0.265
5.85	NM	2.05	235	716	0.0021 / 16.2	2.20	0.539	386	0.33	b	0.385 / 0.265
5.85	15	NM	NM	NM	NM	2.25	0.550	394	0.34	b	0.385 / 0.265
5.82	NM	2.05	225	NM	0.0037 / 16.5	2.10	0.569	407	0.38	b	0.385 / 0.265
5.82	16	NM	NM	NM	NM	2.10	0.576	412	0.38	b	0.385 / 0.265
5.85	NM	2.03	220	NM	0.0013 / 16.5	2.05	0.574	411	0.37	b	0.385 / 0.265
5.85	16	NM	NM	NM	NM	2.05	0.571	409	0.37	b	0.385 / 0.265

*SAMPLE SHAPE
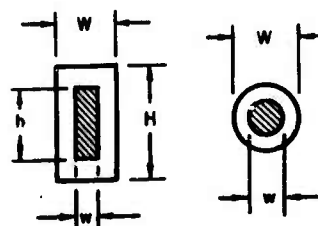
TABLE IV. PROPERTIES OF MATERIALS FABRICATED TO STUDY
THE DEPENDENCE OF SQUARE LOOP PROPERTIES ON DENSITY

SMEC No.	Firing Temp/ Time ($^{\circ}C$/hr)	Density (gm/Cm^3)	ρ_m/ρ_x*	$4\pi M_s$ (Gauss)	$4\pi M_r$ (Gauss)	Remanence Ratio	Coercive Force (Oersteds)
D80A1-108J	1400/5	4.76	0.9207	1639	972	0.546	1.12
D80A1-108K	1400/5	4.71	0.9110	1622	972	0.546	1.12
D80A1-108G	1425/5	4.75	0.9188	1635	990	0.556	1.05
D80A1-108H	1425/5	4.83	0.9342	1663	1013	0.569	1.01
D80A1-108E	1450/5	4.80	0.9284	1653	1013	0.569	0.94
D80A1-108F	1450/5	4.92	0.9517	1694	1100	0.618	0.78
D80A1-108	1475	4.94	0.9555	1700	1152	0.647	0.63
D80A1-108	1475	4.92	0.9517	1694	1062	0.597	0.59
D80A1-108	1500	4.97	0.9613	1711	1098	0.617	0.41

* ρ_m = Measured density
ρ_x = X-ray density

In general, the remanence ratio increased with increasing density while the coercive force decreased with increasing density. These data are shown graphically in Figure 26, plotted as a function of the percent theoretical density. In these calculations the theoretical density of this yttrium iron garnet material was taken as 5.17. This number is calculated from the measured x-ray lattice constant. In Figure 26 it is seen that the remanence ratio increases from 0.50, corresponding to 91% theoretical density, to 0.605 corresponding to 96% density. The coercive force decreases from approximately 1.20 oersteds at 91% to about 0.60 oersteds at 95.5% theoretical density. Thus, a general improvement in square loop properties of these yttrium iron garnet samples is obtained by increasing the density, as one would expect.

Temperature Dependence of Square Loop Properties. Figure 27 shows the remanence ratio and coercive force dependence on temperature in a round, thin walled toroid of 2% dysprosium substituted yttrium iron garnet. Also shown is the variation of the magnetization of yttrium iron garnet with temperature over this temperature range of -100°C to $+100^{o}$C. The coercive force is seen to decrease quite linearly from 1.18 oersteds at -100°C to 0.55 oersteds at $+100^{o}$C. This is a result which is felt to reflect the temperature dependence of the anisotropy field. The remanence magnetization also decreases rather linearly over this range from about 1560 gauss at -100°C to about 1080 gauss at $+100^{o}$C. The rate of decrease of the remanent magnetization is not as rapid as the decrease in saturation magnetization of the yttrium iron garnet. The reason for this decreased dependence on temperature in the remanence magnetization is probably connected to the concurrent decrease in coercive force. When a constant current drive is used, the net effect is that of driving the sample harder at the higher temperatures. This is shown graphically in Figures 28 and 29.

Figures 28 and 29 also show the remanent magnetization dependence on temperature in two nearly identical garnet materials measured in the one case with H_d/H_c constant and in the other case with the driving current constant. A marked difference is observed in the rate of decrease of the remanent magnetization with increasing temperature as determined by the two methods of measurement. Using a constant current drive, the remanence ratio is found to remain very nearly constant over this temperature range, while with the constant ratio of drive field to coercive field the remanence ratio continually decreases with increasing temperature. This may evidence

4-32
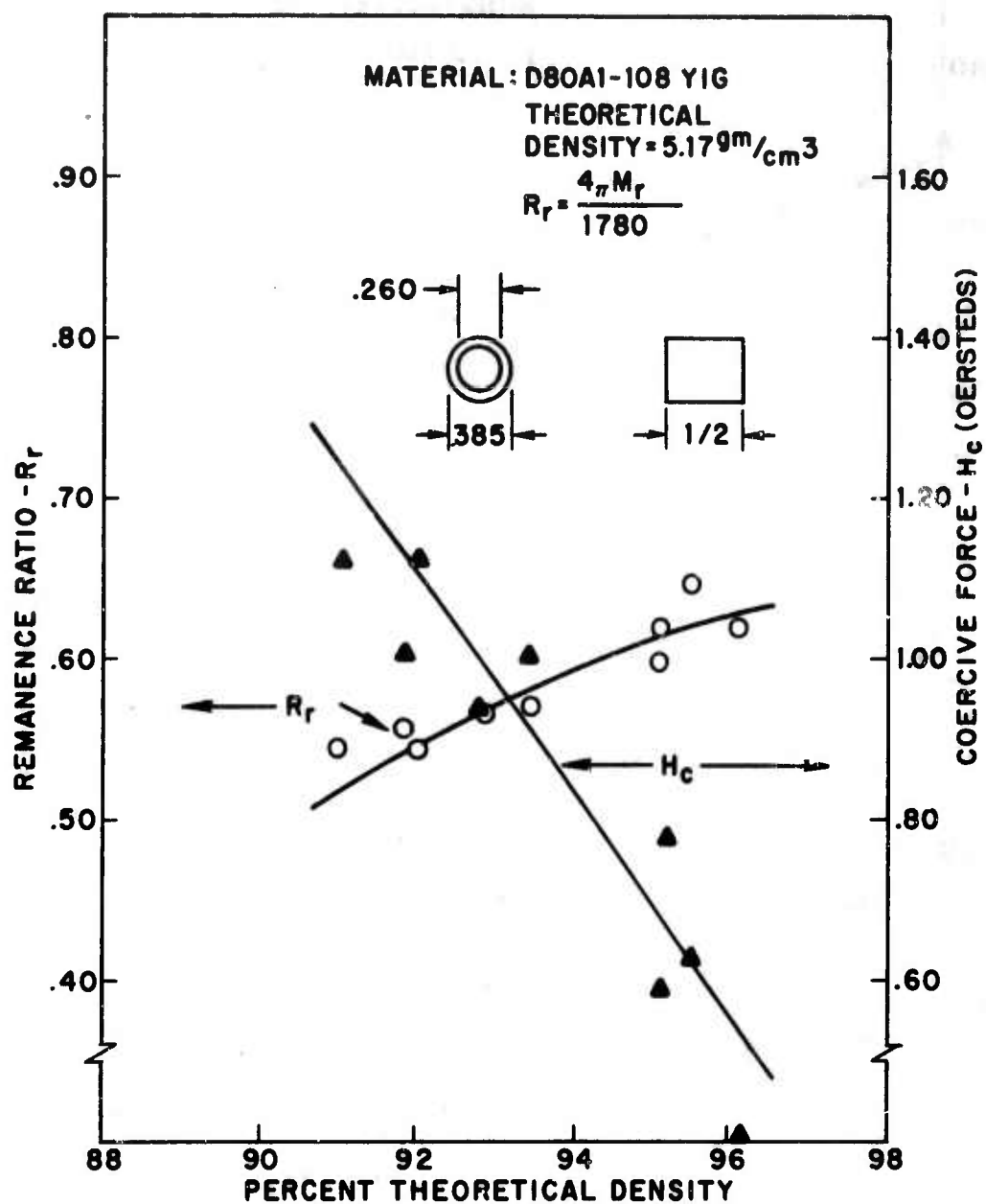
Figure 26. Remanent Magnetization and Coercive Force Dependence on Temperature with Drive Current (I_D) Constant
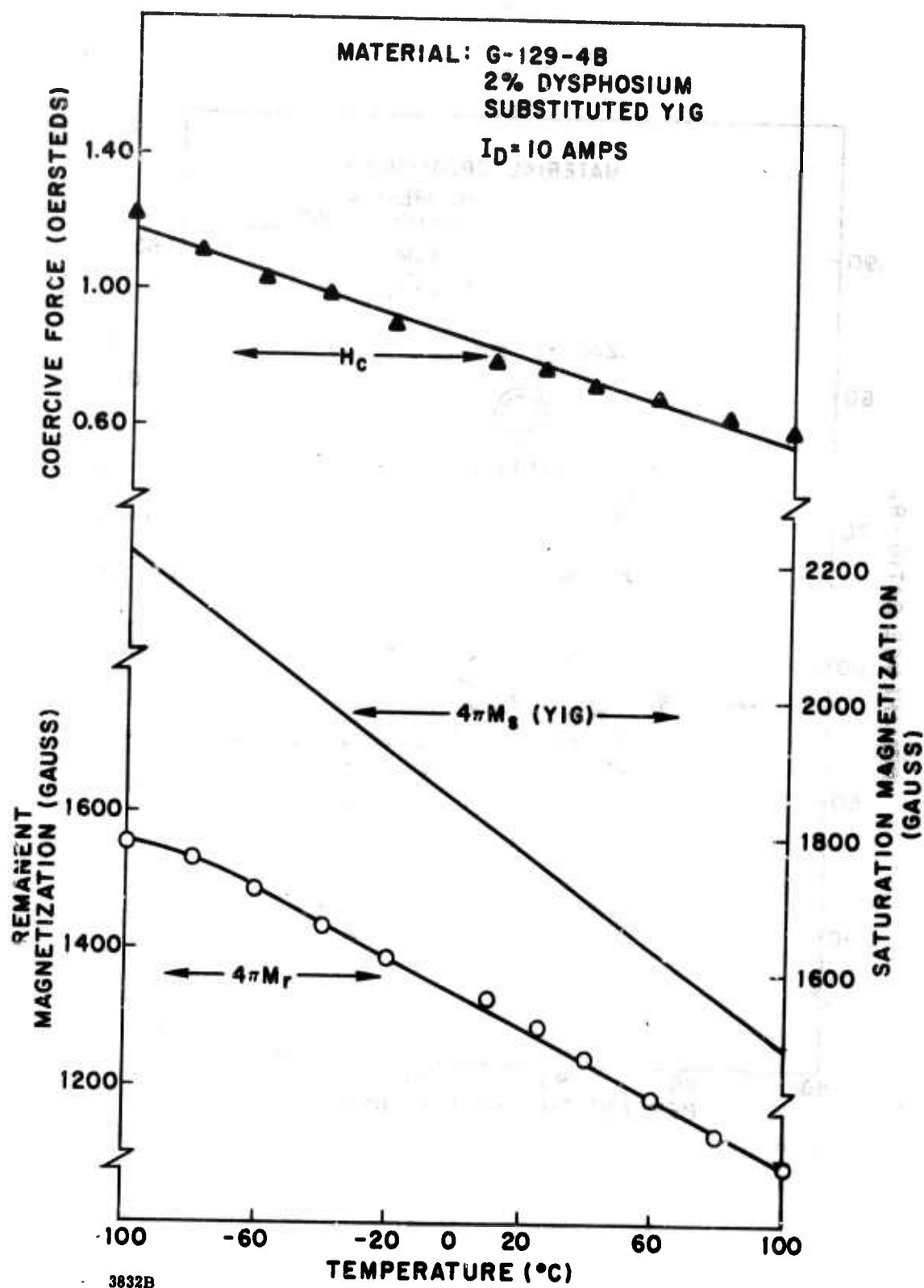
Figure 27. Remanence Ratio and Coercive Force Versus Temperature
with Constant Drive Current I_D

MATERIAL: G-302C
15% GD, 10% Al
SUBSTITUTED YIG
$H_D/H_C = 9.0$

3829B
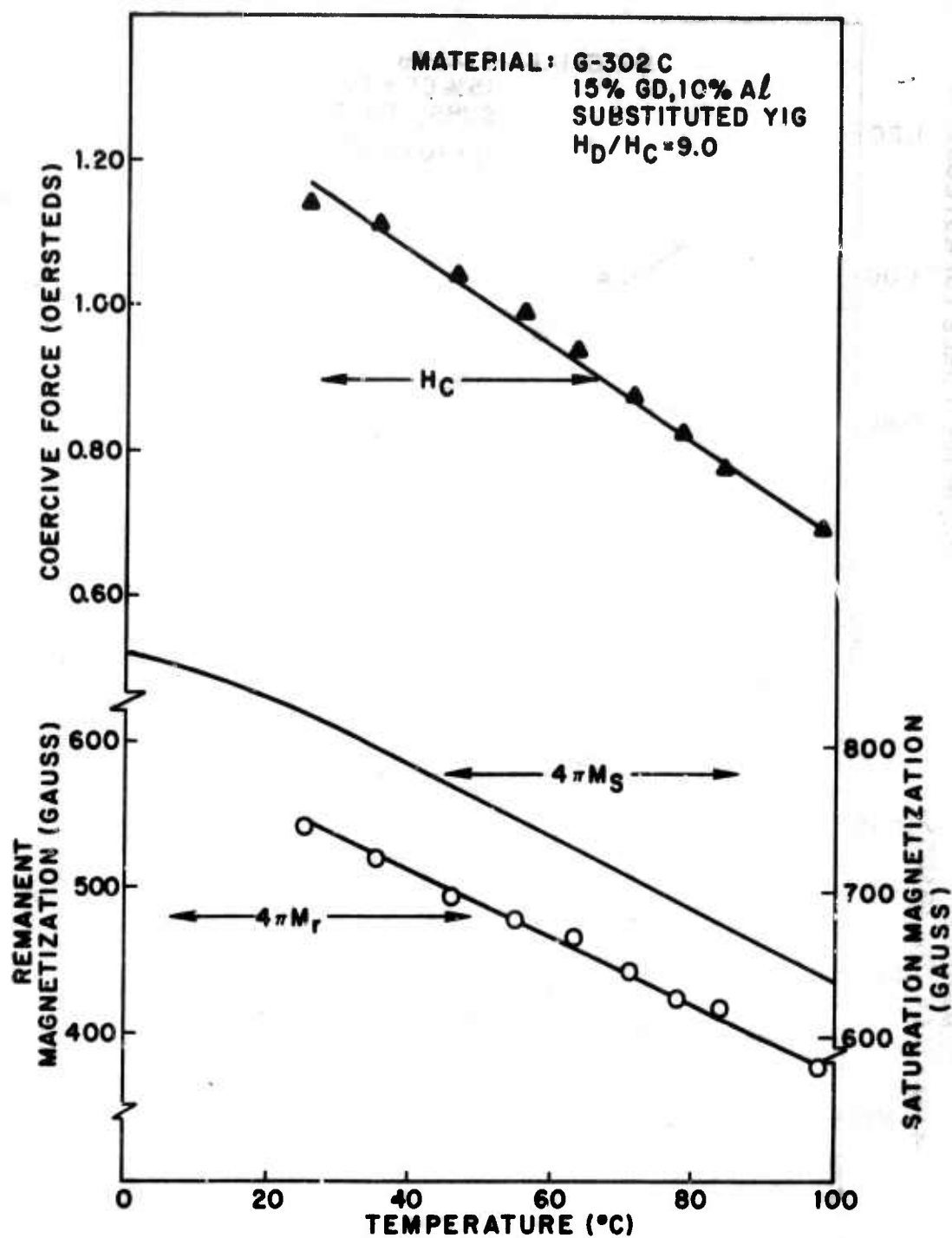
Figure 28. Remanent Magnetization and Coercive Force Dependence
on Temperature with H_d/H_c Constant
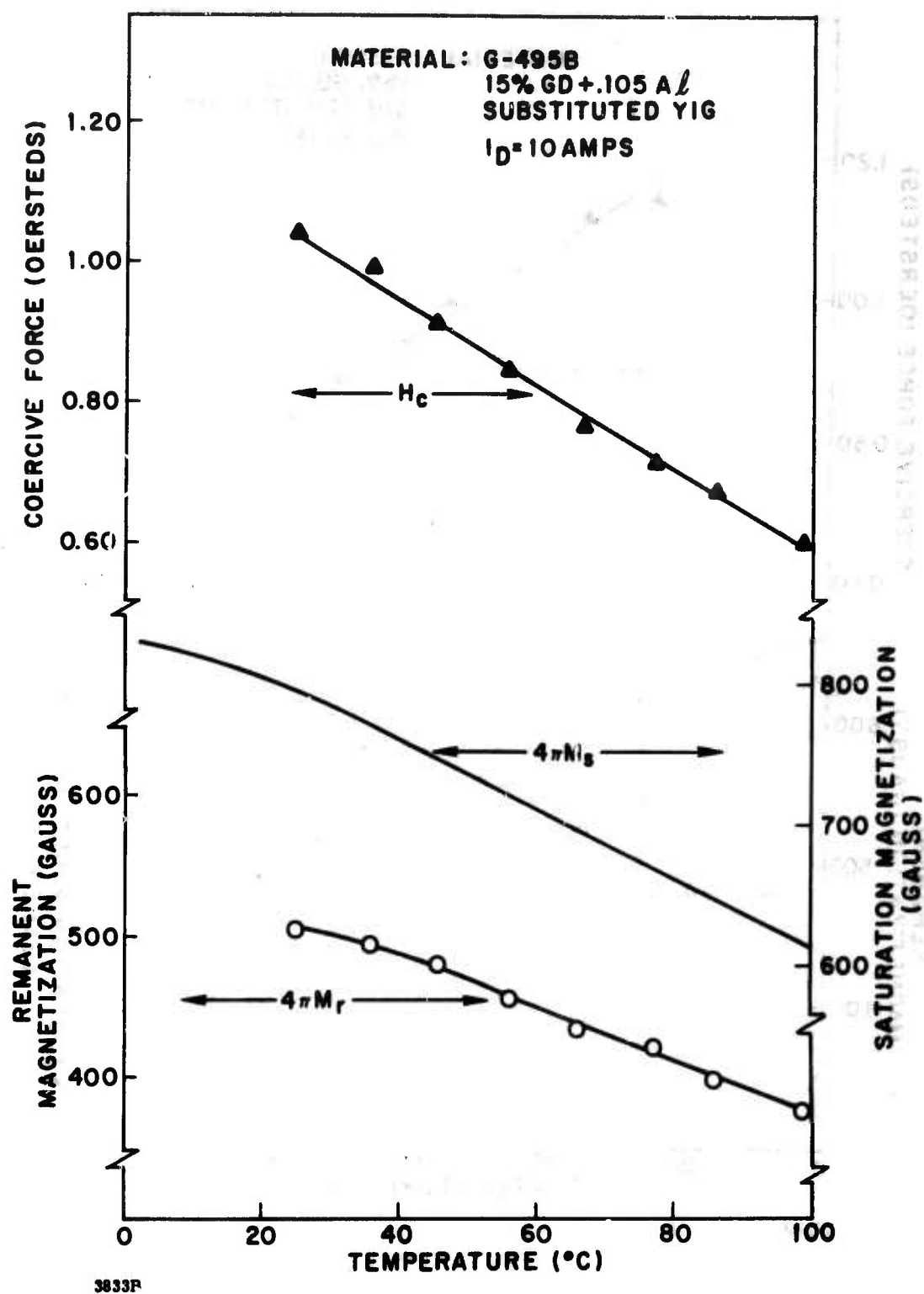
Figure 29. Remanent Magnetization and Coercive Force Dependence on Temperature with Drive Current (I_D) Constant

an inherent increase in remanence ratio with increasing anisotropy field. As stated earlier in Section 3.4, a very large anisotropy field should cause the remanence ratio to approach 0.87 in cubic materials.

Figure 30 shows the remanent magnetization and coercive force dependence on temperature in a round, thin walled toroid of 30% gadolinium substituted YIG. Also shown is the typical variation in saturation magnetization of this type material with temperature. The coercive field is again seen to decrease approximately linearly over the temperature range -100°C to $+100^{\circ}$C from 1.19 oersteds to about 0.76 oersteds. The remanence magnetization varies approximately as the saturation magnetization over this temperature range, except that at the lower temperature extreme it is seen to flatten out. This flattening may be explained by the increased coercive force which has the effect of holding the remanence magnetization at a higher level. That is to say, the sample is less prone to demagnetize after the driving pulse by virtue of the increased anisotropy field which can help offset the effects of porosity, etc.

During these measurements, the ratio of H_d/H_c (the ratio of the driving field to the coercive field) has been allowed to vary and the driving current was held constant. This is approximately the situation found in an actual working device. If the current is varied so as to hold the ratio H_d/H_c constant, the remanent magnetization is again found to decrease more rapidly with increasing temperature.

The temperature characteristics of many materials from the yttrium-gadolinium-iron and the yttrium-gadolinium-aluminum-iron garnet families are presented in Figures 31, 32, 33, 34, 35 and 36. These results show the degree of temperature compensation possible and illustrate that materials possessing almost any value of magnetization up to a value of approximately 1200 can be prepared and temperature compensated.
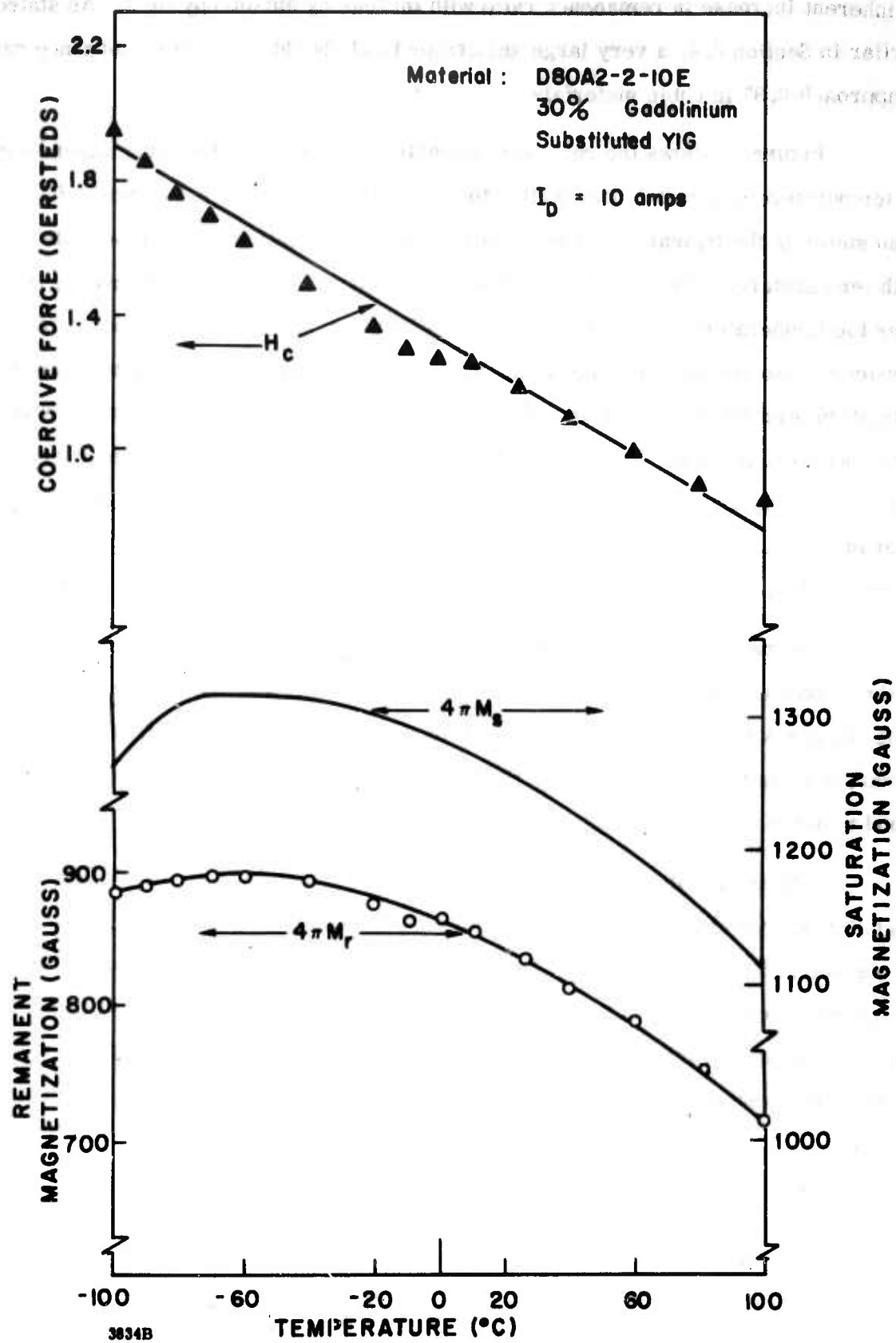
Figure 30. Remanent Magnetization and Coercive Force Versus
Temperature with Constant Drive Current I_D
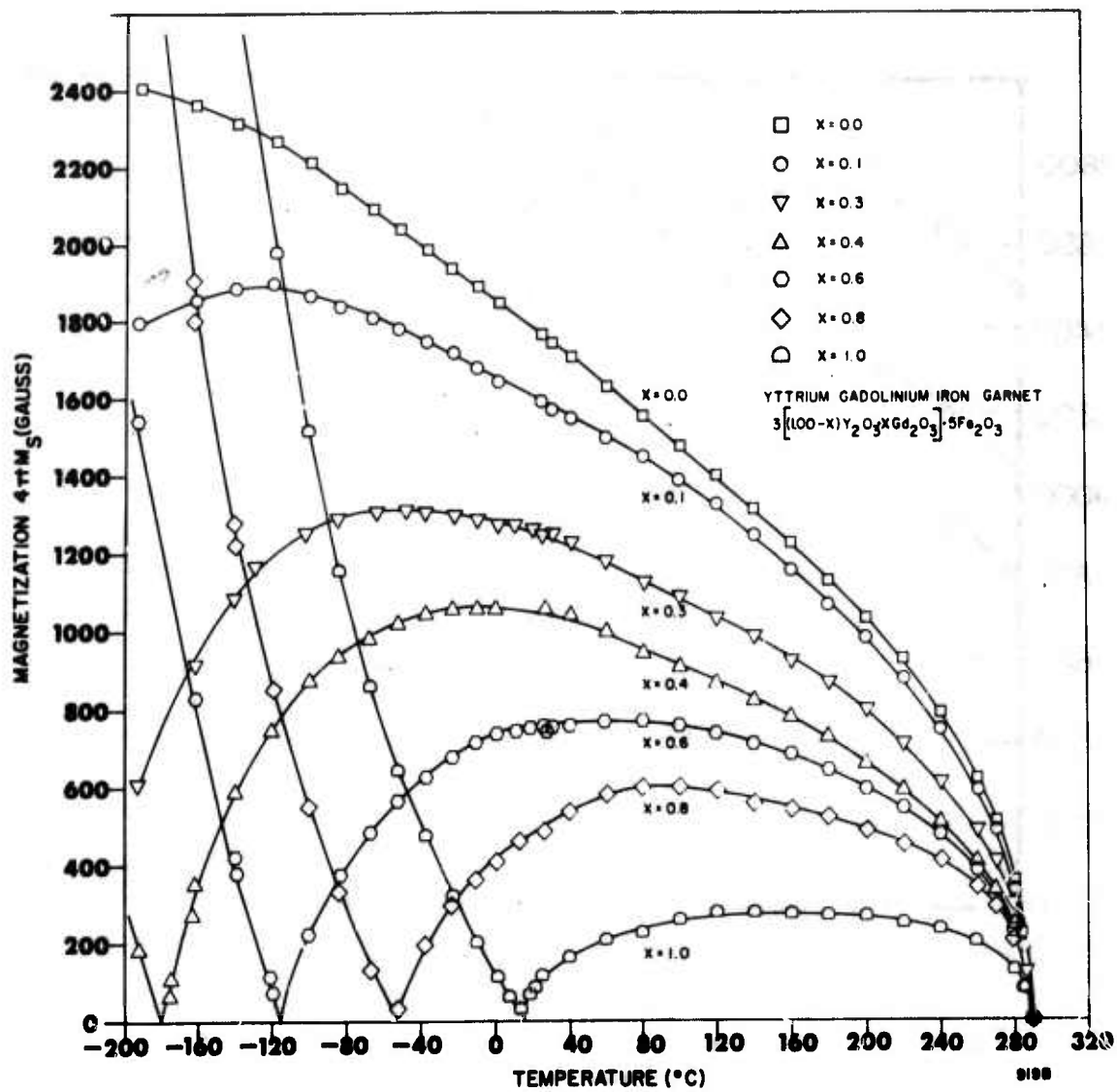
Figure 31. Variation of the Saturation Magnetization with Temperature for Yttrium Gadolinium Iron Garnet
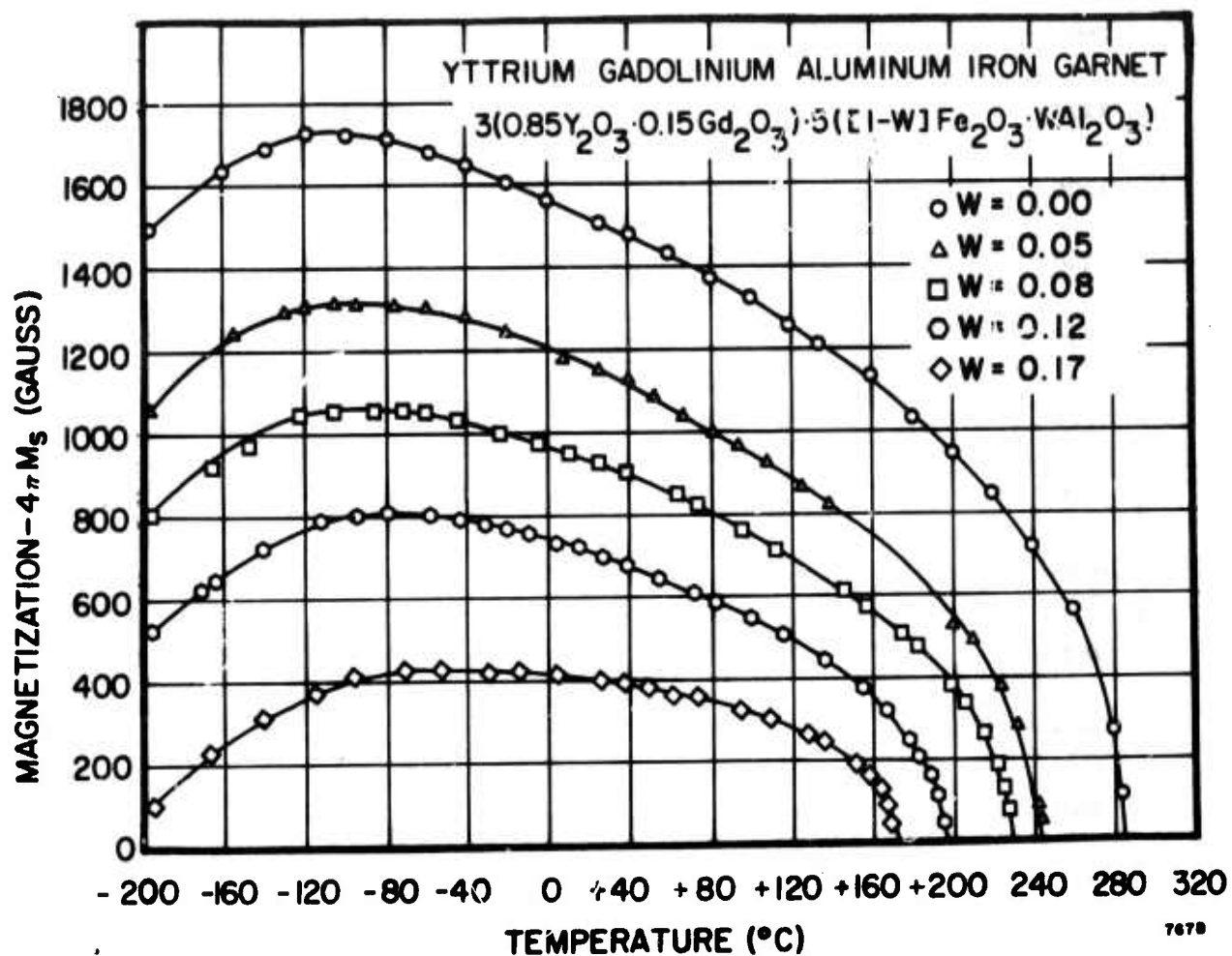
Figure 32. The Variation of Saturation Magnetization with Temperature for
Aluminum Substituted 85% YIG   15% GdIG

4-40
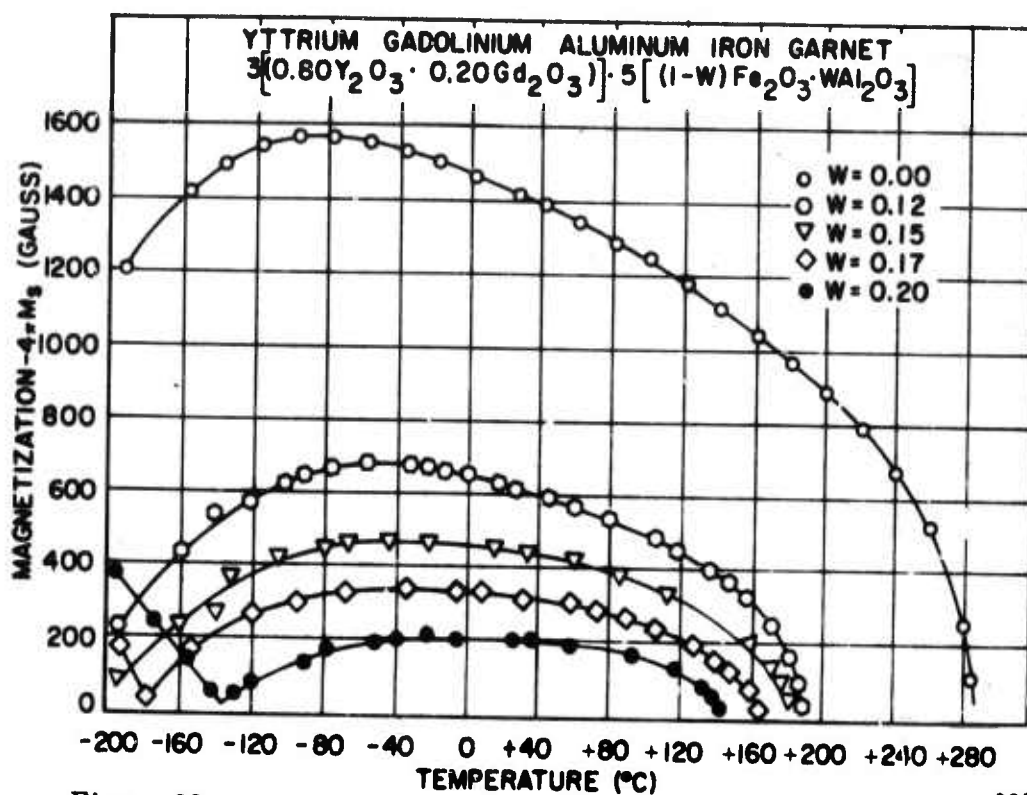
Figure 33. Variation of Saturation Magnetization with Temperature for Aluminum Substituted 80% YIG 20% GdIG
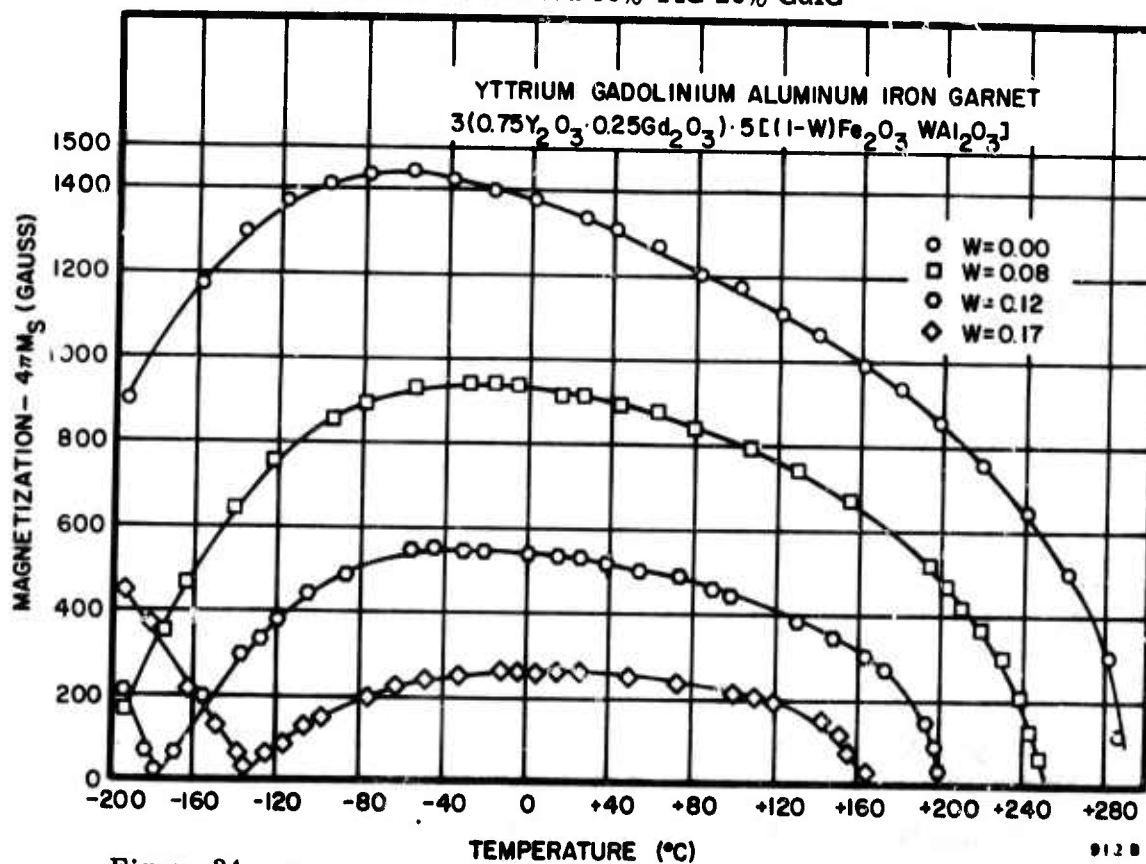
Figure 34. Variation of Saturation Magnetization with Temperature for Aluminum Substituted 75% YIG 25% GdIG
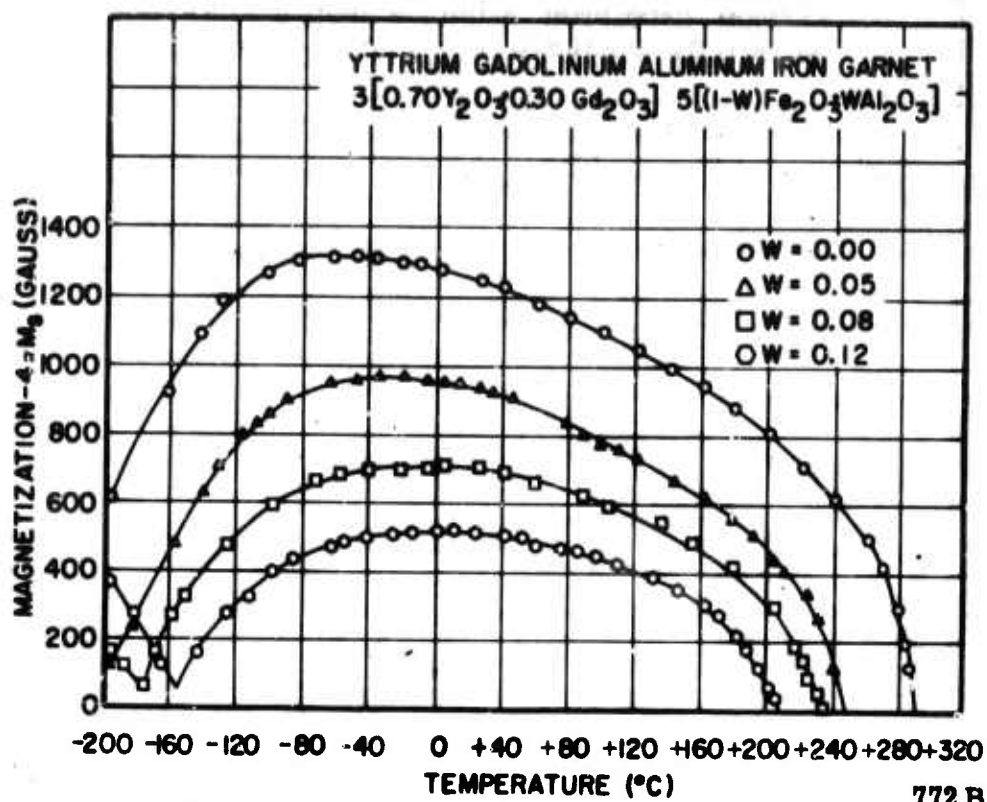
Figure 35. Variation of Saturation Magnetization with Temperature for Aluminum Substituted 70% YIG 30% GdIG
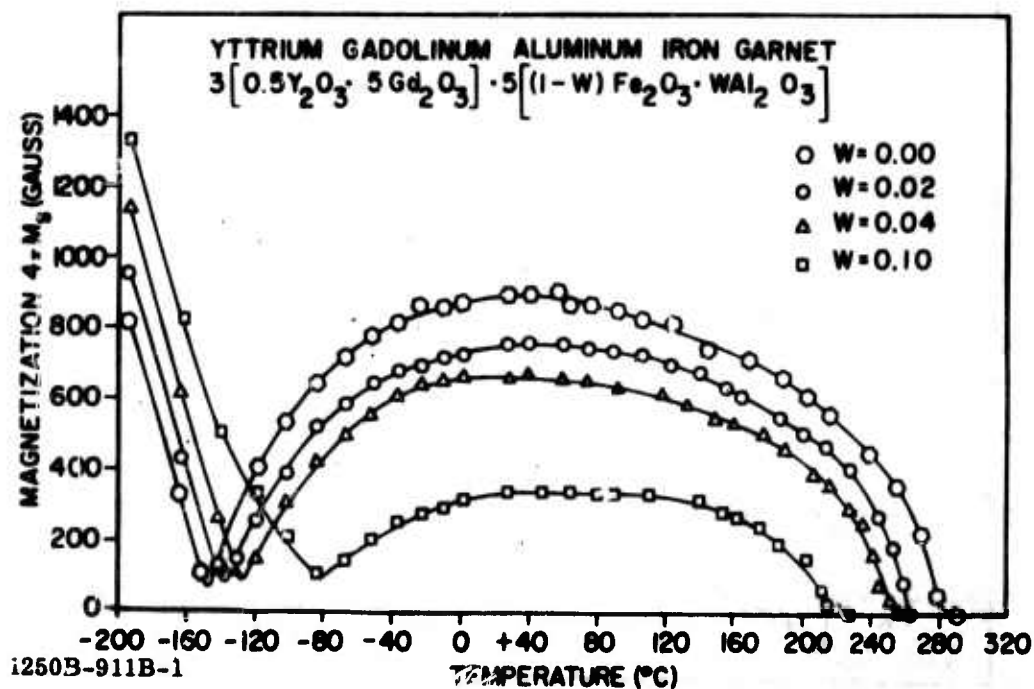
Figure 36. Variation of Saturation Magnetization with Temperature for Aluminum Substituted 50% YIG 50% GdIG

4-42

4.5 EVALUATION OF MATERIALS BY ANALYSIS AND MEASUREMENT OF DEVICE CHARACTERISTICS

Whether or not a given ferrite is satisfactory for a specified phase shifter application must ultimately be decided in the light of the performance characteristics required of the phase shifter. A true correlation of intrinsic ferrite properties with device performance is highly desirable and the ultimate goal of this study has been to achieve the ability to take a device performance specification and accurately predict the required intrinsic material parameters (and, hence, select the appropriate ferrite).

To study the relationship of dimensional and material parameters to the performance characteristics of FDPS a computer-aided analysis of the exact boundary value problem has been carried out for several phase shifter configurations. The solution to each boundary value problem yields the differential phase shift and loss characteristics for the appropriate configuration. This analysis has been supported and guided by an extensive set of experimental measurements on a variety of FDPS configurations and a wide array of material parameters. The propagation constant equation for each configuration was established utilizing the analysis techniques outlined in Section 3.5. The magnetic properties of the ferrite were represented via the "averaged" tensor permeability developed in Section 3.2.1. Numerical computations were carried out on a digital computer.

The correlation obtained between experimental data and calculated values of both magnetic loss and phase shift has permitted the development of a rather complete picture of the mechanisms and phenomena involved in the operation of FDPS. Optimum device configurations have been developed for the materials used. These configurations provide a maximum figure of merit in terms of differential phase shift per unit loss. The ability to calculate meaningful numbers with a high degree of accuracy permits the practical design of a device with a minimum of the cut and try measures usually necessary.

4.5.1 Low Power Characteristics of Waveguide FDPS

The nonreciprocal waveguide FDPS is the device on which both experimental and analytical studies have been concentrated. A cutaway view of a laboratory model phase shifter is shown in Figure 37. The phase shift element is a single ferrite toroid

FERRITE TOROID

DIELECTRIC LOAD

POLYIRON CYLINDER

CHARGING WIRE

TWO-STEP DIELECTRIC
TRANSFORMER

2723B
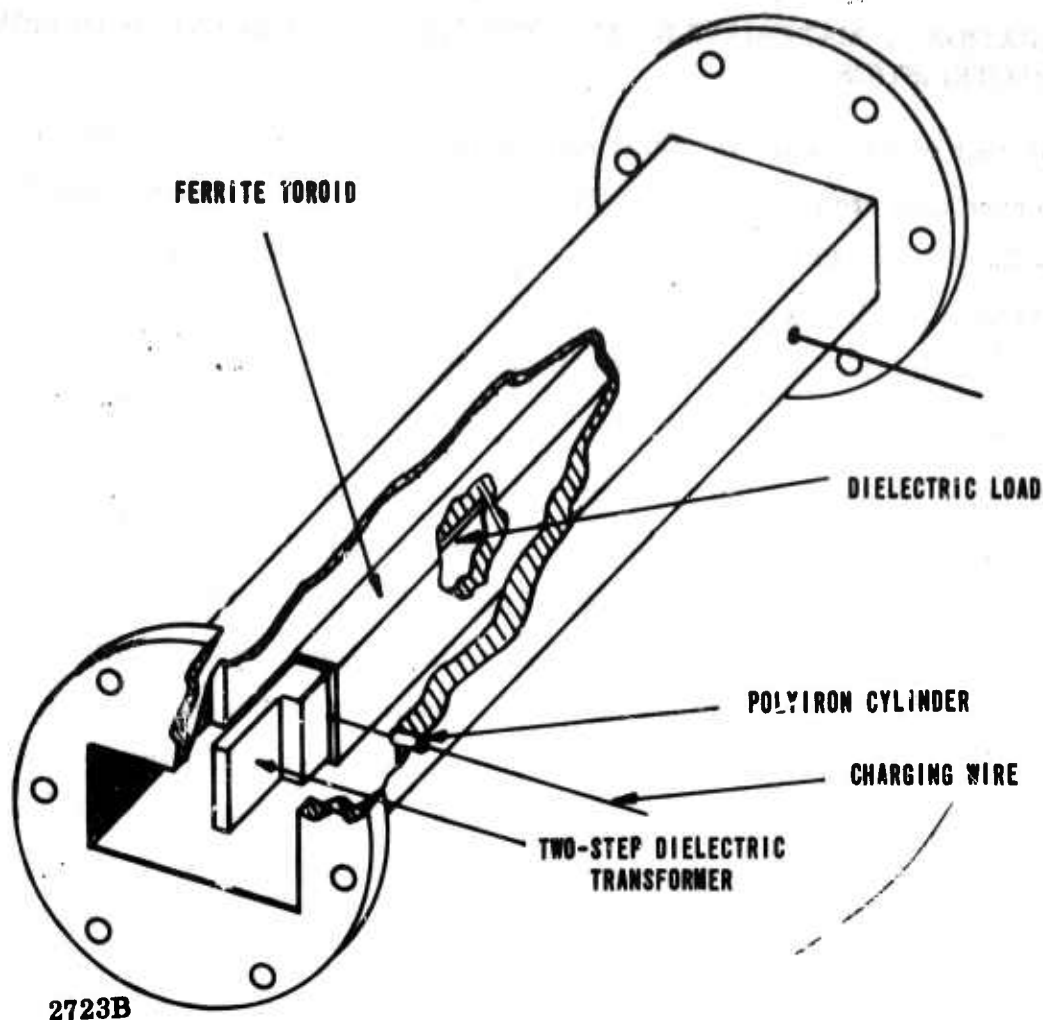
Figure 37. Cutway Illustration of a Typical Nonreciprocal Digital Phase
Shifter Structure

contained wholly within the waveguide. Two-step dielectric transformers were used
for matching into the ferrite-loaded section of waveguide. A single turn of wire
coaxial to the toroid provides a path for the current pulses which magnetize the ferrite
to either of two remanent magnetization states ($+M_r$ or $-M_r$),

A simplified cross-sectional view of the phase shifter of Figure 37 is shown
in Figure 38. As discussed in Section 3.2.3, in the normal operational mode of this
phase shifter (i.e., the fundamental TE mode), the rf magnetic field is entirely in the
plane parallel to the top and bottom of the waveguide. The magnetization in the top
and bottom "crossbars" of the toroid is principally in the direction parallel to the top
and bottom of the waveguide, while in the vertical legs the magnetization tends to be
perpendicular to that direction. To first order, when the incident rf magnetic field
and the direction of magnetization of a sample are mutually parallel, there is no

4-44

interaction between the field and the magnetization. Therefore, the crossbars of the toroid "look" approximately like pieces of dielectric to the incident rf field. In the vertical legs the magnetization is normal to the rf magnetic field and a strong interaction takes place. From these observations, it is apparent that the single toroid latching phase shifter can be represented by the twin slab model shown in Figure 39. When the dielectric core and the ferrite toroid of the practical device have the same dielectric constant, that value is, of course, used for the dielectric constant of the dielectric load of the model. If the dielectric constants of the dielectric core and the ferrite are different, an "effective" dielectric constant is used for the dielectric load of the model. A simple procedure for computing the effective values of dielectric constant and dielectric loss tangent which leads to quite accurate results is to use volume ratios. That is

$$\epsilon'_{\text{effective}} = \epsilon'_f \left(\frac{2W_4}{W_5} \right) + \epsilon'_d \left(\frac{W_5 - 2W_4}{W_5} \right)$$

$$\tan\delta_{\text{effective}} = \tan\delta \left(\frac{2W_4}{W_5} \right) + \tan \left(\frac{W_5 - 2W_4}{W_5} \right)$$

The propagation constant equation for the twin slab model of Figure 39 is given as equation 27 in Section 3.2.1. This equation has been solved numerically with the aid of a digital computer. The numerical solutions for a number of interesting situations are presented below with corroborating experimental data. Both the theoretical and the experimental data are presented in normalized form. Physical dimensions are normalized with respect to the free space wavelength at the center operating frequency. Frequency and the frequency equivalents of static magnetic fields and of remanence and saturation magnetizations are normalized with respect to the center operating frequency. Differential phase shift is given in degrees per GHz-cm. To unnormalize this quantity with respect to frequency, multiply by the center frequency in GHz. Losses are given either as decibels per 360° of differential phase shift or decibels per centimeter.
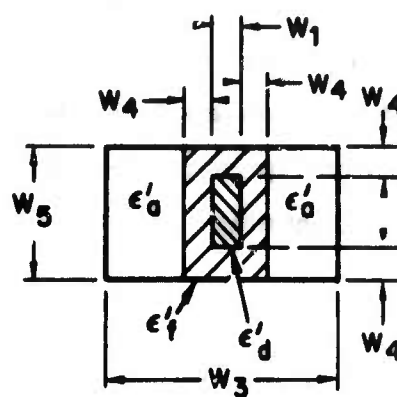
3862B

Figure 38.   An Internal Toroid Latching Phase Shifter
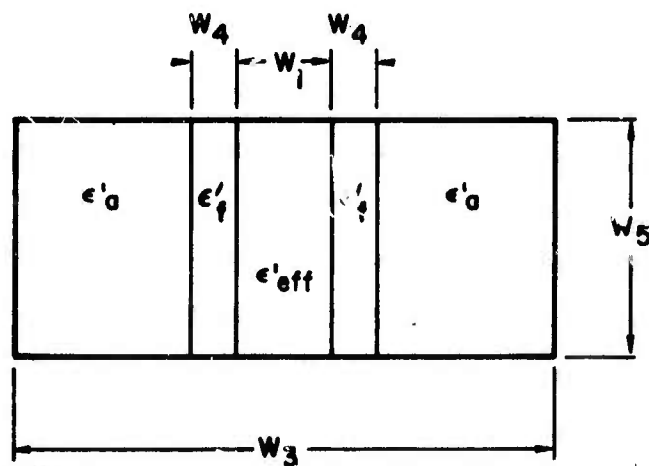
3863B

Figure 39.   Twin Slab Model

The parameters used in the numerical analysis are

$$\omega_c = 2\pi f_c = \text{center frequency}$$

$$\omega = 2\pi f = \text{operating frequency}$$

$$m_s = \frac{\gamma 4\pi M_s}{\omega_c} = \text{normalized saturation magnetization}$$

$$m_r = \frac{\gamma 4\pi M_r}{\omega_c} = \text{normalized remanent magnetization}$$

$$TC = \frac{\gamma \Delta H}{\omega_c} = \text{time constant}$$

$$R_r = \frac{4\pi M_r}{4\pi M_s} = \text{remanence ratio}$$

$$FR = \frac{f}{f_c} = \text{frequency ratio}$$

$$4\pi M_s = \text{saturation magnetization}$$

$$4\pi M_r = \text{remanence magnetization}$$

$$\gamma = \text{gyromagnetic ratio}$$

$$\Delta H = \text{intrinsic linewidth}$$

$$HF = \frac{\gamma H_i}{\omega_c} = \text{normalized effective internal field in major zone of domain}$$

Dielectric constants ϵ'_a, ϵ'_d and ϵ'_f, dielectric loss tangents $\tan \delta_a$, $\tan \delta_d$, and $\tan \delta_f$ apply to the air, dielectric, and ferrite regions, respectively. Normalized dimensions W_1, W_3, W_4 and W_5 apply to the slot width, waveguide width, toroid wall thickness and waveguide height, respectively.

Because the digital phase shifter operates in a remanence state, the effective internal field H_i is determined entirely by the magnetocrystalline anisotropy field and the rf demagnetizing factors of the domain within the toroid. To establish a reasonable value for H_i requires some understanding of the domain structure of the material. For material geometries which lead to an appreciable remanence ratio (0.5 or greater), the domain structure of the ferrite will most likely consist of a few large domains or zones of domains and some smaller domains in "unmagnetized" parts of the material.

Figure 40 is a sketch of such a domain configuration. Most of the toroid volume is effectively saturated and can be treated as a single domain (or zone of domains having nearly parallel magnetizations). These principal zones have shapes closely related to the sample geometry, and for these domains an effective field (H_i) can be assumed based on sample geometry and the anisotropy field of the material. In small unmagnetized volumes of the toroid, the domains take on a variety of shapes. The smaller domains generally will have larger transverse demagnetizing factors and therefore larger effective bias fields. The effective bias field will be largest, approaching $4\pi M_s + H_{anis}$, for those domains with Polder-Smit[17] configurations.

Thus each domain may have different demagnetizing factors and in each domain, the magnetization will exhibit precessional resonance at a characteristic frequency determined by the anisotropy field of the material and the demagnetizing fields. This situation is represented in Figure 41 showing the total absorption of the toroid as made up of resonances in individual domains. The magnetization in each domain experiences different effective bias fields and the position of the peak in total absorption will be determined by the distribution of domains. Thus the peak in total absorption will vary not only with sample shape but also with state of magnetization of any particular sample. An unmagnetized sample will have more Polder-Smit type domains and a resultant higher frequency resonance than a more fully saturated sample. Thus the frequency of the total loss peak and the loss at higher frequencies might be expected to be sensitive to the remanence ratio of the material. The width of the individual domain resonance absorption lines is taken to be the intrinsic linewidth of the material, and interaction with adjacent domains is considered to be only through dipolar forces and their contribution to the effective internal field.

The intrinsic linewidth is that expected on the material in the absence of inhomogeneous broadening mechanism that scatter to degenerate spinwaves. Since, in the normal condition of digital phase shifter operation, there are no long or intermediate wavelength spinwaves degenerate with the operating frequency and, since inhomogeneities are usually too coarse to scatter significantly to very short

---

[17] Ibid
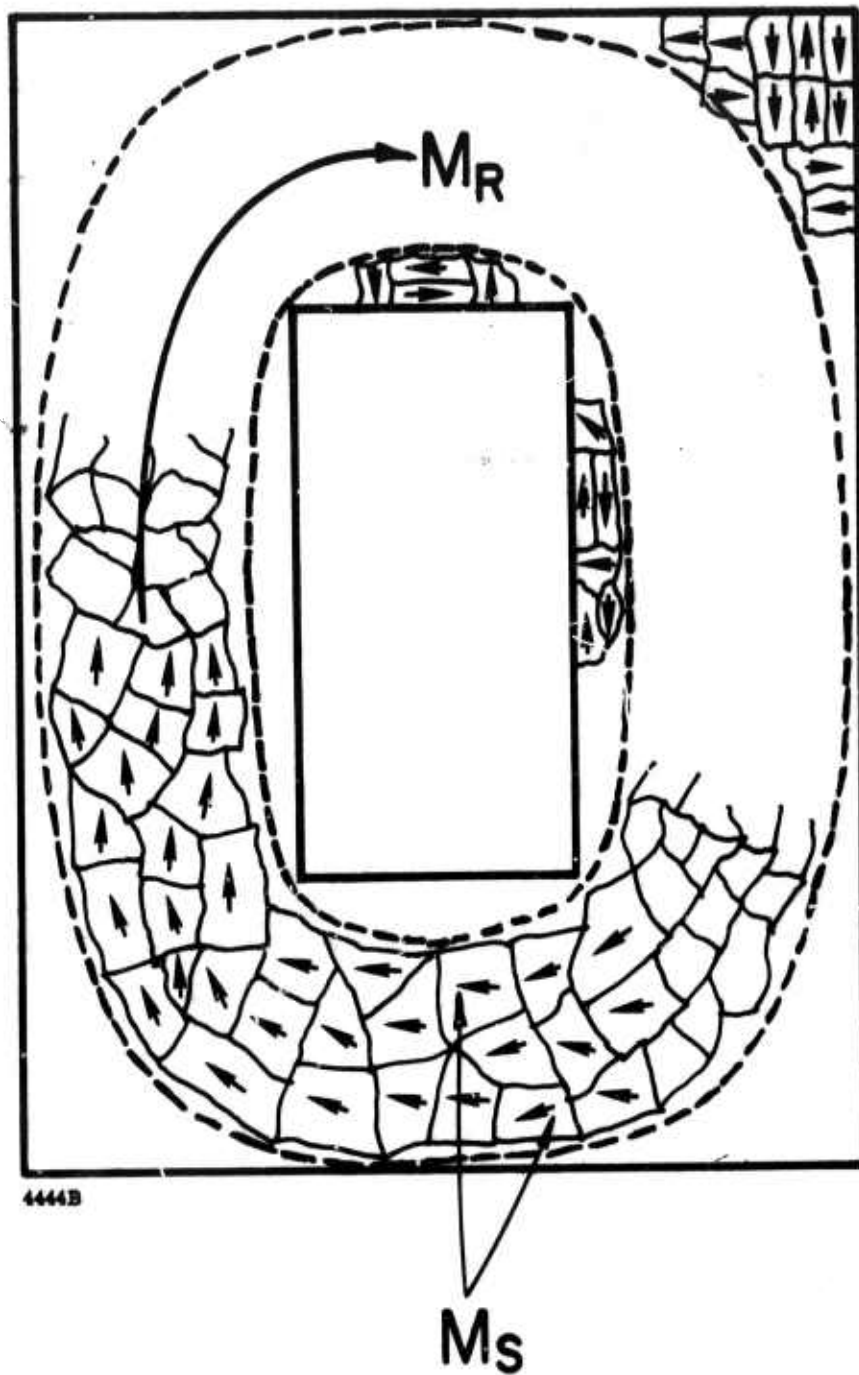
Figure 40. Possible Domain Configurations in Remanent Toroids
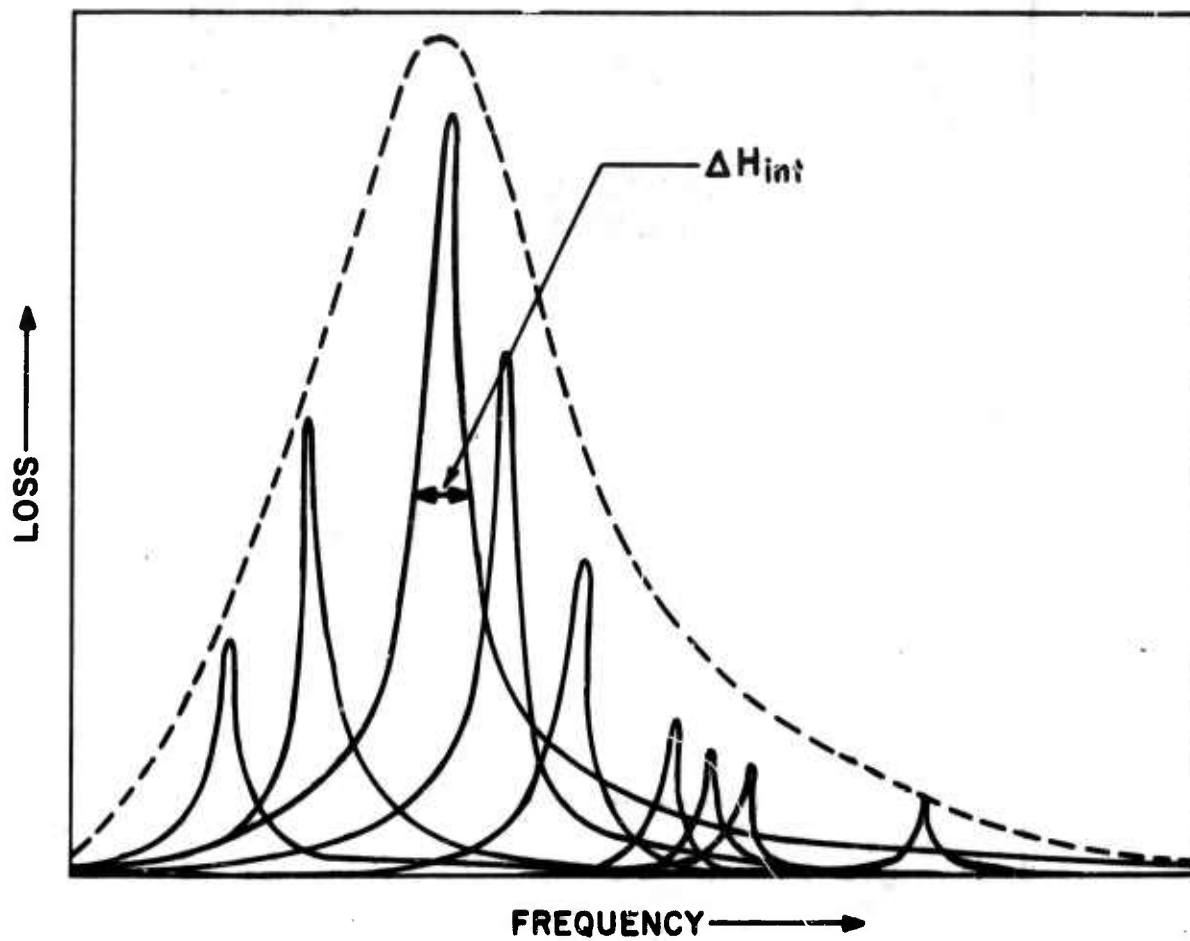
Figure 41. Resonances of Individual Domains Occurring at Different
Frequencies Due to Differing Effective Fields

wavelength spin waves, ($\gamma_k \leq 5 \times 10^{-5}$ cm), it is reasonable to assume that such inhomogeneous broadening mechanisms will not then contribute significantly to magnetic loss. The value of intrinsic linewidth can be obtained from single crystal data on material of equal quality and/or from parallel pump measurements of ΔH_k. In the latter case, the frequency dependence of ΔH_k must be considered in determining the intrinsic linewidth, since the spinwaves of a parallel pump measurement are oscillating at one-half the operating frequency.

It is important to observe that, although the rf demagnetizing factors at the surfaces of the ferrite are accounted for by the applied boundary conditions in the solution of the boundary value problems, the rf demagnetizing factors of the various internal domains are not included by that procedure and must be accounted for in the average effective field H_i. In this model, the major portion of the resonance losses will be determined by the effective field of the largest domains whose magnetizations are oriented orthogonal to the rf magnetic field. The geometry of these major domains should be related to the overall sample dimensions.

Based on this thought, H_i can be estimated using Kittel's equation and the estimated demagnetizing factors of the major domain. Because the applied dc magnetic field is identically zero Kittel's equation can be written as

$$
H_i = \left\{ \left[\left(N_x + N_x{}^a - N_z \right) 4\pi M_s \right] \left[\left(N_y + N_y{}^a - N_z \right) 4\pi M_s \right] \right\}^{1/2}
$$

where $N_x{}^a$, $N_y{}^a$ are the effective demagnetizing factors arising from anisotropy effects and are given by:

$$
N_x{}^a = \frac{K_1}{4\pi M_s{}^2} \left[2 - \sin^2\theta - 3\sin^2 2\theta \right]
$$

$$
N_y{}^a = \frac{2K_1}{4\pi M_s{}^2} \left[1 - 2\sin^2\theta - \frac{3}{8}\sin^2 2\theta \right]
$$

Here θ is the angle the magnetization makes with a $<100>$ direction of the crystallites as measured in a $<110>$ plane. If the magnetization is assumed to lie along the easy direction of a negative anisotropy material, the resonance equation reduces to:

$$H_i = \left\{ \left(\frac{4}{3} \frac{K_1}{M_s} + N_x 4\pi M_s \right) \left(\frac{4}{3} \frac{K_1}{M_s} + N_y 4\pi M_s \right) \right\}^{1/2}$$

where N_z has been set equal to zero in accordance with the toroidal geometry. The parameter K_1 is the first order magnetocrystalline anisotropy constant.

For a typical garnet toroid with $\frac{K_1}{M_s} \approx 60$ oe., $4\pi M_s = 1200$ gauss, and a length to width ratio of 10 to 1 for the toroid legs, the estimated effective field for the major domain is

$$H_i = \sqrt{(80 + 120)(80 + 1080)}$$

$$H_i \approx 480 \text{ oe.}$$

The damping parameter associated with these domain resonances is of the conventional form and is included in the resonance equation in normalized form as a damping time constant

$$TC \sim \frac{\gamma \Delta H}{f_c},$$

where ΔH is the intrinsic linewidth and f_c is the center operating frequency. Since the intrinsic linewidth appears to vary directly with frequency (as will be discussed later), the damping term is in fact a constant independent of frequency, and the calculated results are applicable at any frequency.

4.5.1.1 <u>Effects of Internal Field and Magnetization on Phase Shifter</u>
<u>Performance</u>. The experimental data, used in plotting the various curves which
follow, are present in Tables V, VI, and VII of this report and Tables XII and XIV
of the Final Report on RADC Contract No. AF-30(602)-3490. In Figures 42 and 43
differential phase shift for a latching phase shifter is shown for three different
values of the normalized effective internal field as functions of the width of the
waveguide. In addition, the experimentally observed differential phase shift for
the same structure is given. It is encouraging to note that as the effective field
approaches the value predicted by the simple arguments given above, the predicted
differential phase shift for the structure approaches the observed values more
closely. The theoretical predictions and the experimental results are in fact in
excellent agreement. Figures 43 and 44 illustrate the effect on differential phase
shift and loss of variations in H over a small range of values when all other para-
meters are fixed. It can be seen that loss increases more rapidly than differential
phase shift as H_i increases.

Figure 45 shows theoretical and experimental results for both differential
phase shift and loss/360° of differential phase shift as a function of waveguide width
with toroid slot width as a parameter. For this set of data, the configuration used
is an air cored toroid as indicated.

TABLE V. C, S, AND X BAND DEVICE T
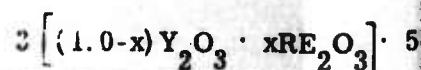
$$3\left[(1.0-x)Y_2O_3 \cdot xRE_2O_3\right]\cdot 5$$

SMEC NO.	COMPOSITION x	w	BATCH SIZE	WAXING TIME (HRS)	FIRING SCHEDULE °C/hr	DENSITY (gm/cm³)	DIELECTRIC LOSS TAN. (X BAND)	DIELECTRIC CONSTANT (X BAND)	G FACTOR	LINE AR X
G-250-5H		0.25	757	16	1500 / 5	4.82	0.0005	14.1	2.03	
G-293-5D		0.15	1412	16	1475 / 5	4.84	0.0005	14.3	2.03	
G-455-C	0.10 Dy	0.12	755	16	1475 / 5	5.14	0.0006	15.4	NM	
G-454-C	0.04 Dy	0.12	757	16	1475 / 5	5.08	0.0006	15.3	NM	
G-292-2D		0.12	1420	16	1475 / 5	4.91	0.0005	14.7	NM	
G-453-D	0.02 Dy	0.12	752	16	1475 / 5	5.07	0.0011	15.5	NM	
G-452-E	0.45 Gd 0.04 Dy		753	16	1475 / 5	5.74	0.0005	16.4	1.94	
G-451-C	0.45 Gd 0.02 Dy		749	16	1475 / 5	5.72	0.0014	16.3	1.99	
G-297-6C	0.45 Gd		745	16	1475 / 5	5.69	0.0008	16.2	NM	
G-291-2D		0.08	1431	16	1475 / 5	5.00	0.0005	15.3	2.02	
G-367-2A	0.30 Gd 0.01 Dy		750	16	1475 / 5	5.45	NM	NM	NM	
G-404-3D		0.05	1440	16	1475 / 5	5.08	0.0005	15.5	2.02	
G-232-73D			1454	24	1475 / 5	5.10	0.0005	16.0	NM	
G-250-5B		0.25	757	16	1500 / 5	4.82	0.0005	14.1	2.03	
G-461-C	0.45 Gd 0.02 Dy	0.06	755	16	1475 / 5	5.64	0.0005	15.9	1.97	
G-459-C	0.10 Dy	0.15	766	16	1475 / 5	5.08	0.0006	14.8	1.80	
G-462-C	0.45 Gd 0.04 Dy	0.06	759	16	1475 / 5	5.69	0.0006	16.1	1.91	
G-460-C	0.45 Gd	0.06	751	16	1475 / 5	5.63	0.0004	16.1	NM	
G-458-C	0.04 Dy	0.15	754	16	1475 / 5	5.00	0.0005	15.1	1.91	
G-293-5E		0.15	1412	16	1475 / 5	4.84	0.0005	14.3	2.03	
G-292-2E		0.12	1420	16	1475 / 5	4.91	0.0006	14.7	NM	
G-291-2E		0.08	1431	16	1475 / 5	5.00	0.0005	15.3	2.02	
G-404-3E		0.05	1440	16	1475 / 5	5.08	0.0007	15.5	2.02	

NM – Not measured

$$3 \cdot xRE_2O_3 \Big] \cdot 5 \Big[(1.0-w)Fe_{1.925}O_3 \cdot wA\ell_{1.925}O_3 \Big]$$

TMIC ANT NO	G FACTOR	LINE WIDTH ΔH (oe) X BAND	$4\pi\mu_s$ (GAUSS)	B_r	COERCIVE FIELD H_c (OE) (60~)	DEVICE TEST RANGE	$\frac{\gamma \& \pi\mu_s}{F_o}$	P_{crit} (kw)	h_{crit}^3 (OE)	LOSS/360° ^{2}	ΔΦ/INCH^2
1	2.03	36	208	0.71	1.11	C Band	0.10	>400	>110	1.42	10
3	2.03	42	676	0.58	1.76	C Band	0.31	>400	>110	0.68	37
4	NM	461	768	0.68	-1.49	C Band	0.38	>400	>110	4.90	33
3	NM	192	815'	0.68	0.85	C Band	0.40	>400	>110	2.50	43
7	NM	47	867	0.58	1.76	C Band	0.41	See Table VI		0.54	41
5	NM	77	860	0.63	0.88	C Band	0.43	100	55.2	1.13	45
4	1.94	275	925	0.42	1.24	C Band	0.46	>400	>110	3.65	49
3	1.99	192	970	0.57	0.99	C Band	0.48	250	87	4.25	51
2	NM	100	980	0.63	1.54	C Band	0.49	25	28	1.45	48
3	2.02	55	1115	0.60	1.18	C Band	0.56	NM		0.50	53
	NM	75'	1250'	0.63	0.60	C Band	0.62	46	48	1.30	68
5	2.02	55	1325	0.55	1.29	C Band	0.66	NM		0.41	78
0	NM	40'	1780'	0.72	0.41	C Band	0.88	NM		0.40	97
1	2.03	36	208	0.58	0.88	S Band	0.16	>300	>63	0.98	14
9	1.97	296	570	0.58	1.73	S Band	0.43	>300	>63	3.35	35
8	1.80	470	572	0.59	1.28	S Band	0.43	>300	>63	5.60	31
1	1.91	412	575	0.38	1.67	S Band	0.44	>300	>63	3.80	47
1	NM	120	600	0.50	1.51	S Band	0.45	110	38	1.55	43
1	1.91	212	625	0.67	1.05	S Band	0.47	>300	>63	3.00	34
3	2.03	42	640	0.43	1.43	S Band	0.48	10	11	0.36	46
7	NM	47	900'	0.38	1.37	S Band	0.68	6	9	0.37	64
3	2.02	55	1115	0.51	0.87	S Band	0.91	3	6	0.44	70
5	2.02	55	1325	0.45	0.93	S Band	1.00	NM		NM	NM

TABLE V. C, S, AND X BAND DEVICE TEST RESUL

$$3\left[(1.0-x)Y_2O_3 \cdot xRE_2O_3\right] \cdot 5$$

SPEC NO.	COMPOSITION x	w	BATCH SIZE (gms)	WAXING TIME (HRS)	FIRING SCHEDULE °C/hr	DENSITY gms .m³	DIELECTRIC LOSS TAN. (X BAND)	DIELECTRIC CONSTANT (X BAND)	g FACTOR	LINE AN X B
G-293-5C		0.15	1412	16	1475 / 5	4.84	<0.0005	14.3	2.03	
G-292-2C		0.12	1420	16	1475 / 5	4.91	<0.0005	14.7	NM	
G-450-C	0.10 Dy	0.08	753	16	1475 / 5	5.23	0.0007	15.7	NM	
G-297-7F	0.45 Gd		745	16	1475 / 5	5.69	0.0008	16.2	NM	
G-287-3C	0.04 Dy	0.08	751	16	1475 / 5	5.13	0.0004	15.7	NM	
G-286-7C	0.02 Dy	0.08	750	16	1475 / 5	5.07	<0.0005	15.4	NM	
G-296-41J	0.30 Gd		3111	24	1475 / 5	5.47	<0.0005	16.1	2.02	
G-404-3C		0.05	1440	16	1475 / 5	5.08	<0.0005	15.5	2.02	
G-232-73C			1454	24	1475 / 5	5.10	<0.0005	16.0	NM	

1 - Estimated Value

2 - Normalized to $R_r = 0.50$

3 - Value calculated by method shown in Appendix A

NM - Not measured

3862B

$$W_1 = 0.060\lambda_c \qquad \epsilon'_1 = 16$$

$$W_3 = 0.382\lambda_c \qquad \epsilon_2 = \epsilon'_F$$

$$W_4 = 0.040\lambda_c \qquad \epsilon_3 = 1$$

$$W_5 = 0.294\lambda_c \qquad m_s = \gamma 4\pi M_s/f_o$$

$$\mu'_1 = 1 \qquad m_p = \gamma 4\pi M_s/f_p$$

$$xRE_2O_3 \cdot 5\left[(1.0-w)Fe_{1.925}O_3 \cdot wAl_{1.925}O_3\right]$$

g FACTOR	LINE WIDTH ΔH (oe) X BAND	$4\pi M_s$ (GAUSS)	R_r	COERCIVE FIELD H_c(oe)(60~)	DEVICE TEST RANGE	$\dfrac{\gamma 4\pi M_s}{f_o}$	P_{crit} (w)	h_{crit} (oe)	LOSS/360° 2	Δφ/inch 2
2.03	42	640	0.48	1.27	X Band	0.19	>150	>113	0.96	39
NM	47	900'	0.38	1.21	X Band	0.27	>150	>113	0.57	57
NM	379	950'	0.65	0.93	X Band	0.29	>150	>113	5.15	45
NM	100	980'	0.60	0.94	X Band	0.31	55	68	1.63	53
NM	163	1120'	0.57	0.79	X Band	0.33	>150	>113	1.98	54
NM	99	1100	0.60	0.61	X Band	0.33	>150	>113	1.35	58
2.02	60'	1240'	0.53	0.90	X Band	0.36	42	60	1.07	68
2.02	55	1325	0.40	0.85	X Band	0.40	5	21	0.48	87
NM	NM	1280	0.64	0.49	X Band	0.53	2	12	0.53	105

$\gamma 4\pi M_s/f_o$

$\gamma 4\pi M_s/f_p$

f_c = the center frequency of the low power test range

= 3.7 GHz, 5.65 GHz and 9.0 GHz at S band, C band and X band respectively

f_p = high power test frequencies

= 3.7 GHz, 5.60 GHz and 9.375 GHz at S band, C band and X band respectively
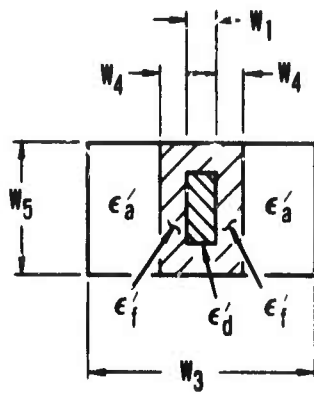
$$m_s = \frac{\gamma 4\pi M_s}{\omega_c} = 0.38 \qquad R_f = 0.5$$

$$f_c = 9 \text{ Gc} \qquad \epsilon'_a = 1.0$$
$$\epsilon'_d = 18.0$$
$$m = \frac{\gamma 4\pi M_r}{\omega_c} = 0.19 \qquad \epsilon'_f = 18.0$$

$$FR = 1.0 \qquad \tan \delta_a = 0$$

$$W_1 = 0.023 \, \lambda_c \qquad \tan \delta_d = 0.0005$$

$$W_3 = \text{VARIABLE} \qquad \tan \delta_f = 0.0007$$

$$W_4 = 0.04 \, \lambda_c \qquad \lambda_c = 3.33 \text{ Cm}$$

$$W_5 = 0.294 \, \lambda_c \qquad HF = \text{PARAMETER}$$
$$\Delta H = 85 \text{ Oe.}$$

Legend:
- △ EXPERIMENTAL
- ● THEORETICAL HF = 0
- ○ THEORETICAL HF = 0.1
- ✕ THEORETICAL HF = 0.2

DIFFERENTIAL PHASE SHIFT (DEGREES/CM - GHz)

NORMALIZED WAVEGUIDE WIDTH $\frac{W_3}{\lambda_c}$
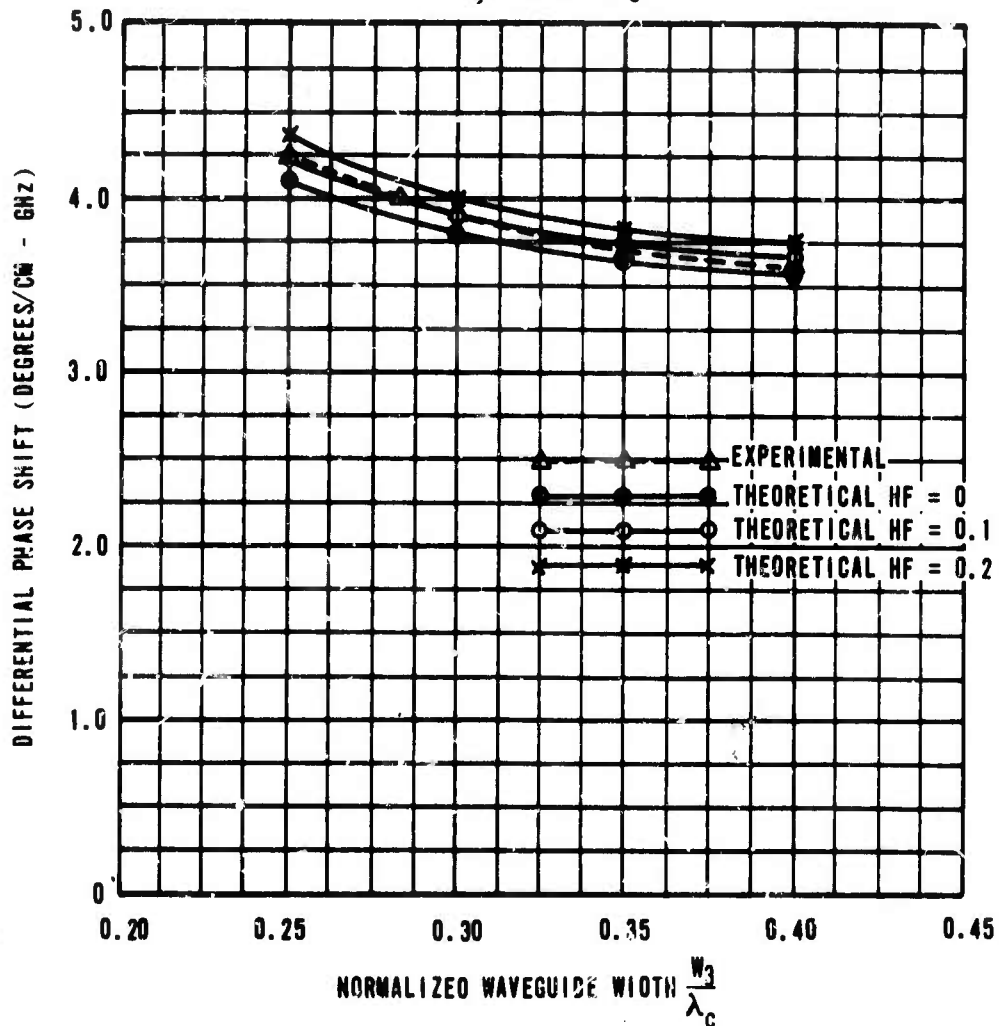
Figure 42. Differential Phase Shift vs Normalized Waveguide
Width For A Latching Phase Shifter With Effective
Internal Field As A Parameter
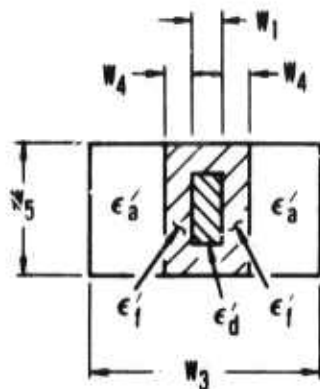
$$m_s = \frac{\gamma 4\pi M_s}{\omega_c} = 0.36 \qquad R_f = 0.5$$

$$f_c = 9 \; Gc \qquad \epsilon_a' = 1.0$$

$$m = \frac{\gamma 4\pi M_f}{\omega_c} = 0.19 \qquad \epsilon_d' = 16.0$$

$$\epsilon_f' = 16.0$$

$$FR = 1.0 \qquad \tan \delta_a = 0$$

$$W_1 = 0.023 \; \lambda_c \qquad \tan \delta_d = 0.0005$$

$$W_3 = 0.3 \; \lambda_c \qquad \tan \delta_f = 0.0007$$

$$W_4 = 0.04 \; \lambda_c \qquad \lambda_c = 3.33 \; Cm$$

$$W_5 = 0.294 \; \lambda_c \qquad HF = VARIABLE$$

$$\Delta H = 65 \; Oe.$$
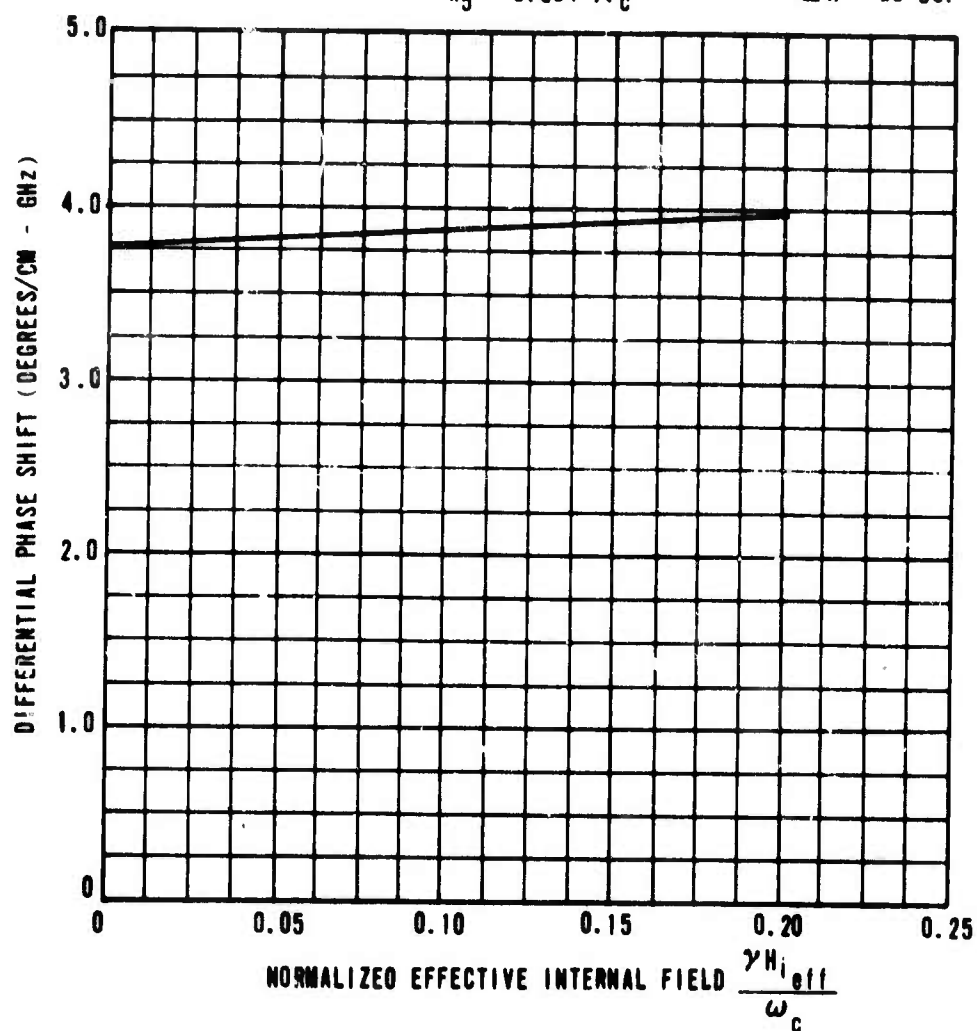
Figure 43. Differential Phase Shift vs Effective Internal
Field For A Latching Phase Shifter
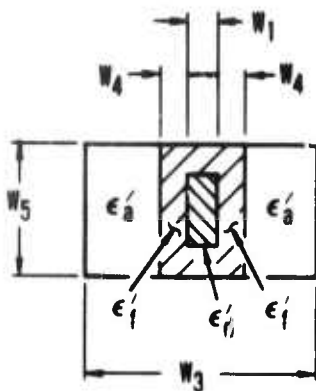
4-60

$$m_s = \frac{\gamma 4\pi M_s}{\omega_c} = 0.38 \qquad R_f = 0.5$$

$$f_c = 9 \text{ Gc} \qquad \epsilon_a' = 1.0$$

$$m = \frac{\gamma 4\pi M_r}{\omega_c} = 0.19 \qquad \epsilon_d' = 16.0$$

$$\epsilon_f' = 16.0$$

$$FR = 1.0 \qquad \tan \delta_a = 0$$

$$W_1 = 0.023 \lambda_c \qquad \tan \delta_d = 0.0005$$

$$W_3 = 0.3 \lambda_c \qquad \tan \delta_f = 0.0007$$

$$W_4 = 0.04 \lambda_c \qquad \lambda_c = 3.33 \text{ Cm}$$

$$W_5 = 0.294 \lambda_c \qquad HF = \text{VARIABLE}$$

$$\Delta H = 85 \text{ Oe.}$$

Figure 44. Loss Per 360° Of Differential Phase Shift vs Effective Internal Field For A Latching Phase Shifter
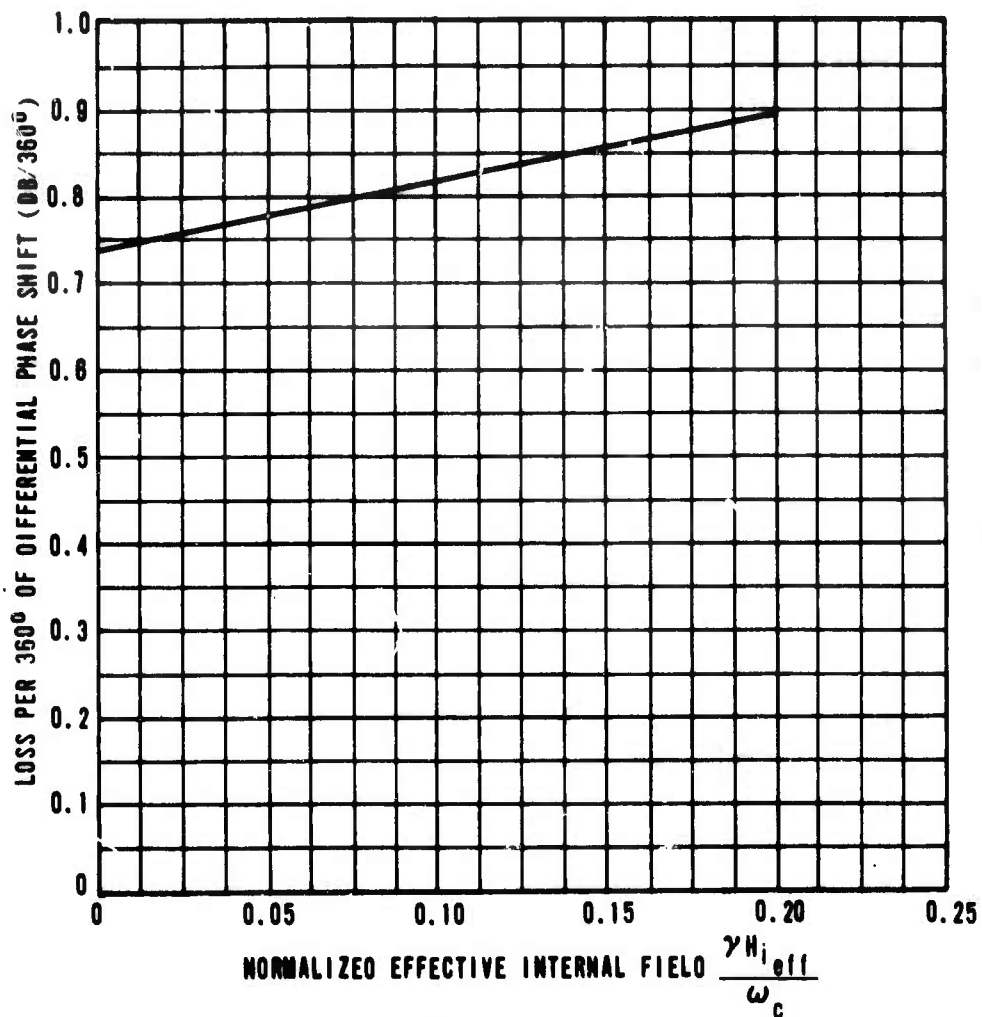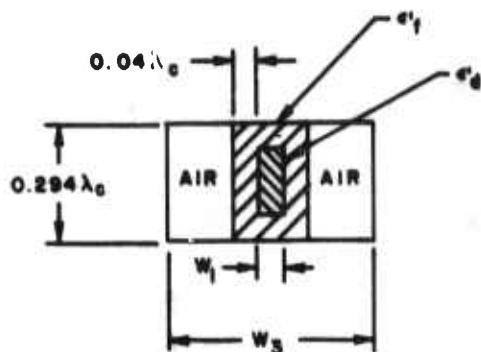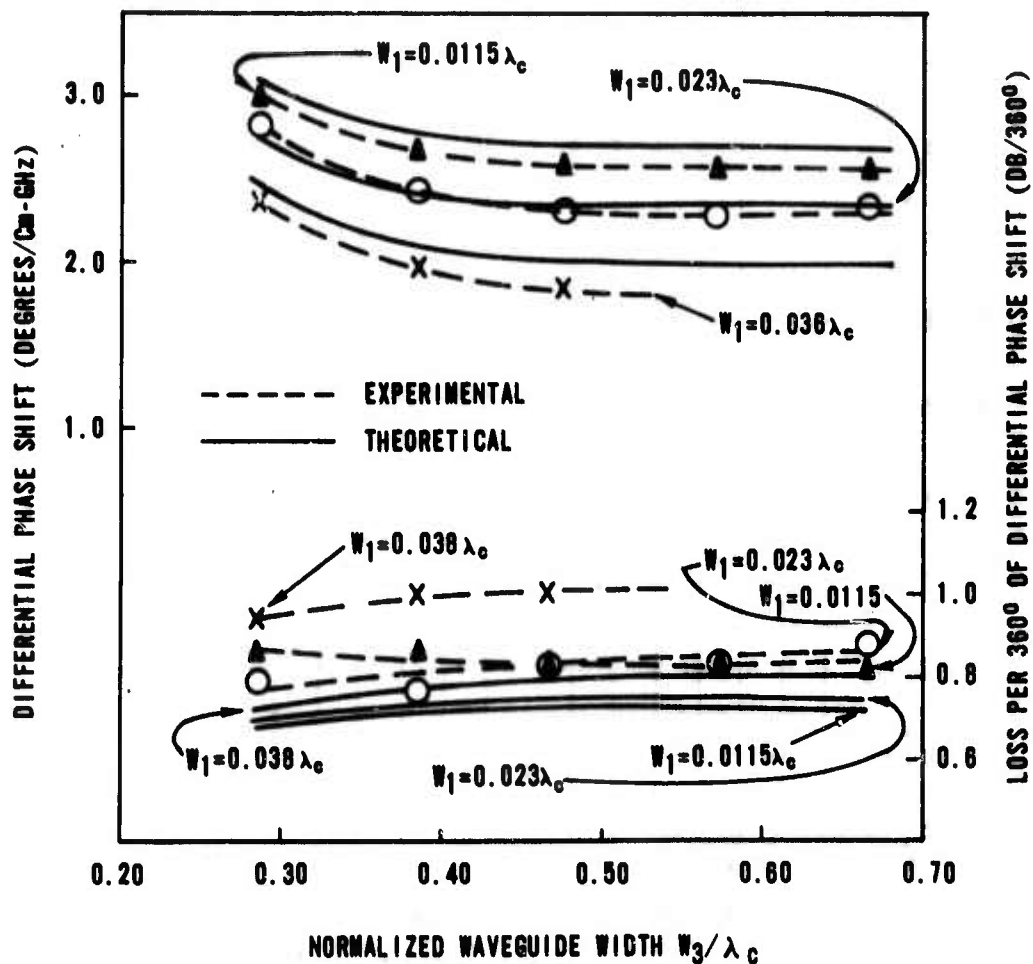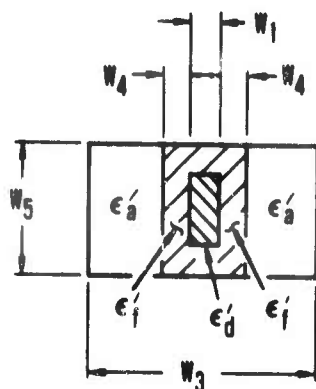
Figure 45. Differential Phase Shift and Loss/360° of Differential Phase Shift vs Normalized Waveguide Width with Toroid Slot Width as a Parameter

While it appears from the results shown in Figures 42 and 45 that to obtain the smallest loss per 360° of differential phase shift one would prefer a waveguide width of less than $0.25\lambda_c$, it will be shown later that for such small waveguide widths it is difficult to obtain a flat response of differential phase shift with frequency.

Figure 46 shows the calculated contributions to the total loss for three different sources -- waveguide wall losses or copper losses, dielectric losses, and theoretical magnetic losses. These add up to a total theoretical loss of approximately 0.68 db per 360° differential phase shift. This compares with approximately 0.73 db per 360° of phase shift as shown in the experimental curve for a thirty percent gadolinium substituted YIG. It is seen that the theoretical waveguide losses are approximately 0.06 db, the dielectric losses are approximately 0.22 db, and the theoretical magnetic losses are approximately 0.40 db. The ability to predict accurately these various losses separately enables us not only to predict what the total loss will be but also to study the influence of the different parameters on the separate loss mechanisms. For this particular set of parameters, it would indicate that reducing the magnetic loss should be the primary goal. This would be accomplished by reducing linewidth or improving other contributors to the magnetic losses.

Figure 47 presents both calculated and measured values of loss per 360° of differential phase shift for a typical configuration as a function of the normalized saturation magnetization. The anisotropy field of the material is a parameter in this figure. These computed curves indicate that for large values of normalized saturation magnetization the loss for 360° of phase shift increases rapidly as we approach ferromagnetic resonance in the material. The proximity to ferromagnetic resonance is influenced by the value of the effective internal field and hence anisotropy field of the material. This dependence on anisotropy field is quite marked as evidenced by the variation of loss with this parameter seen in the curves of Figure 47. At low values of normalized saturation magnetization, loss per 360° also increases rapidly. This increase is due to the fact that the differential phase shift per unit length obtained for small values of m_s is low (proportional to $R_r m_s$), while the insertion loss per unit length is relatively constant, since, for low m_s values, the loss is primarily determined by dielectric and copper losses. Thus, at low m_s values, the

$m_s = \dfrac{\gamma 4\pi M_s}{\omega_c} = 0.38$ $R_f = 0.5$

$f_c = 9 \text{ Gc}$ $\epsilon'_a = 1.0$
  $\epsilon'_d = 16.0$
$m = \dfrac{\gamma 4\pi M_f}{\omega_c} = 0.19$ $\epsilon'_f = 16.0$

  $\tan \delta_a = 0$
FR = 1.0 $\tan \delta_d = 0.0005$
  $\tan \delta_f = 0.0007$
$W_1 = 0.023\,\lambda_c$
$W_3 = \text{VARIABLE}$ $\lambda_c = 3.33 \text{ Cm}$
$W_4 = 0.04\,\lambda_c$ HF = 0.1
$W_5 = 0.294\,\lambda_c$ $\Delta H_i = 40 \text{ Oe.}$

EXPERIMENTAL

TOTAL THEORETICAL LOSSES

THEORETICAL MAGNETIC LOSSES

THEORETICAL DIELECTRIC LOSSES

THEORETICAL WAVEGUIDE LOSSES

LOSS PER 360° OF DIFFERENTIAL PHASE SHIFT (DB/360°)

NORMALIZED WAVEGUIDE WIDTH W_3/λ_c
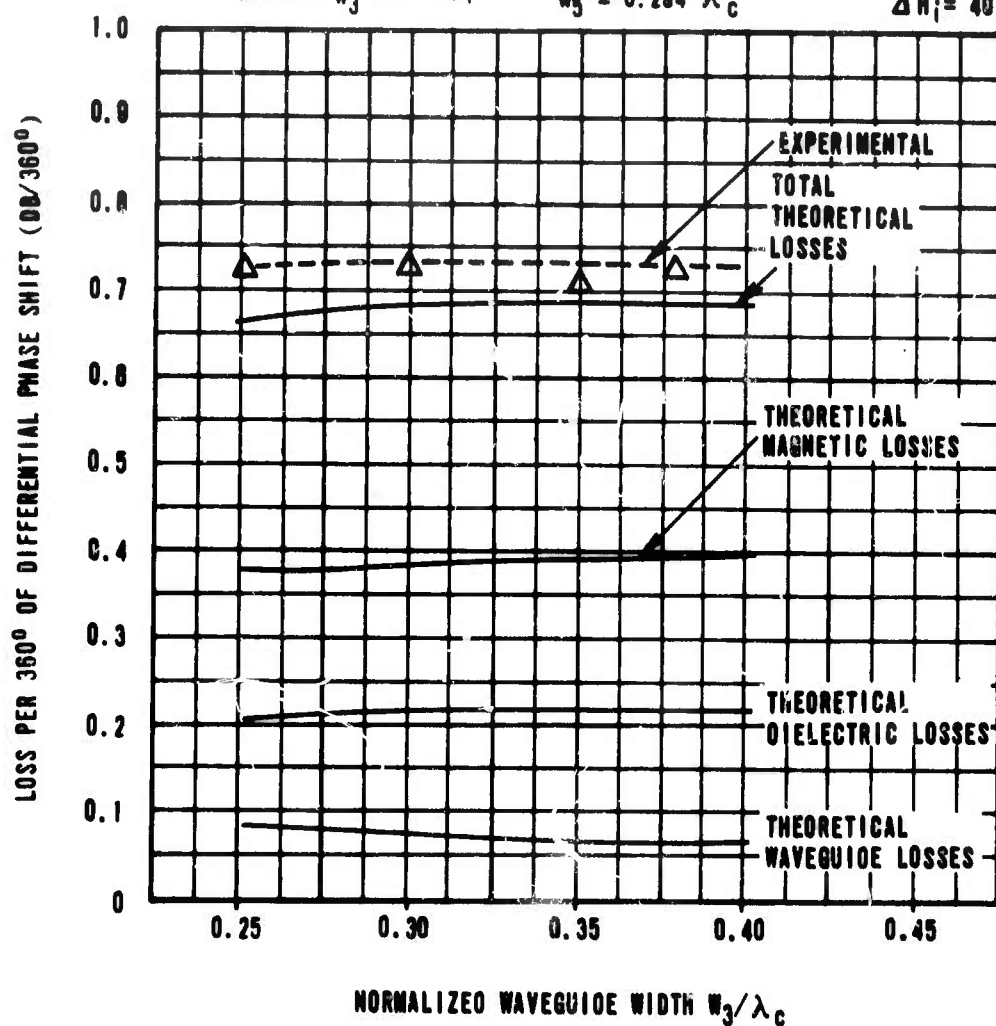
Figure 46. Separation of Losses in a Latching Phase Shifter
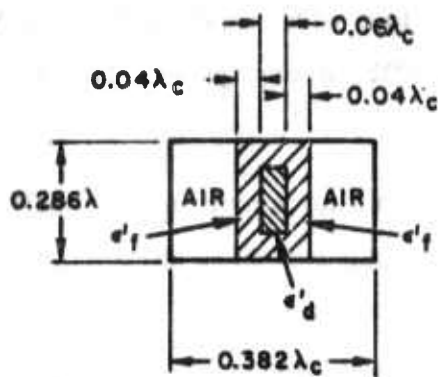
loss per 360° of phase shift vary true approximately as $m_s^{...}$. The agreement between theory and experiment in the case of the a-X-band data with 570 normally used
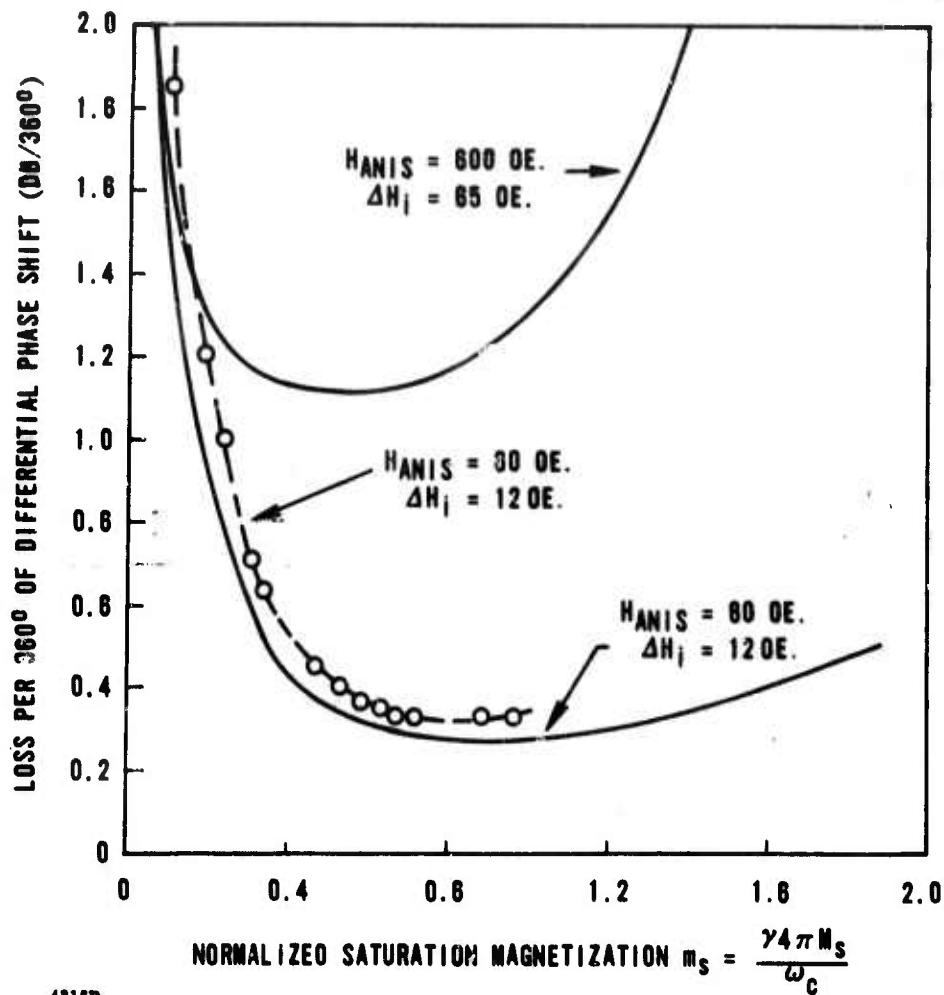
Figure 47. Loss/360° As a Function of Normalized Saturation Magnetization with Material Characteristics as a Parameter

loss per 360° of phase shift varies approximately as $1/m_s$. The agreement between theory and experiment in the case of these X band data with YIG is quite good.

Figure 48 illustrates the variation of loss with frequency in C and X bands for a magnesium manganese ferrite having a $4\pi M_s$ of 2064 guass. The sharp rise of loss with decreasing frequency in C band is due to the proximity of resonance.

These data are replotted in Figure 49 in a form more nearly equivalent to that of Figure 47. The similarity between the shapes of these curves is obvious. The more gradual upturn in the curves of Figure 47 is probably due to the vastly different scale of loss and the smaller intrinsic linewidth of the magnesium manganese ferrite ($\Delta H_i \sim 12$ oe). This magnesium manganese ferrite has an anisotropy field of about 600 oersteds, and therefore the peak resonance absorption should occur at the same m_s value, though the wings seen in these curves would differ because of the difference in linewidth.

The variation of differential phase shift (for a typical configuration) as a function of normalized saturation magnetization for a remanence ratio of 0.5 and an anisotropy field of 100 oersteds is shown in Figure 50.

4.5.1.2 Effects of Linewidth On Loss. Figures 51, 52, and 54 highlight the results of a study of magnetic loss as a function of resonance linewidth. The results of this study have shown that magnetic loss in a remanent state ferrite is directly related to the intrinsic linewidth of the materials. In Figure 51 both calculated and experimental results are presented showing the X band loss for each of the two remanent states as a function of intrinsic linewidth ΔH. The loss for both states is seen to increase linearly with linewidth. The differential loss between remanent states also increases with increasing ΔH. For ΔH greater than about 100 oersteds the differential loss in this configuration is large enough to be bothersome in phase shifter applications. The materials used to obtain the experimental data are also shown in Figure 51.
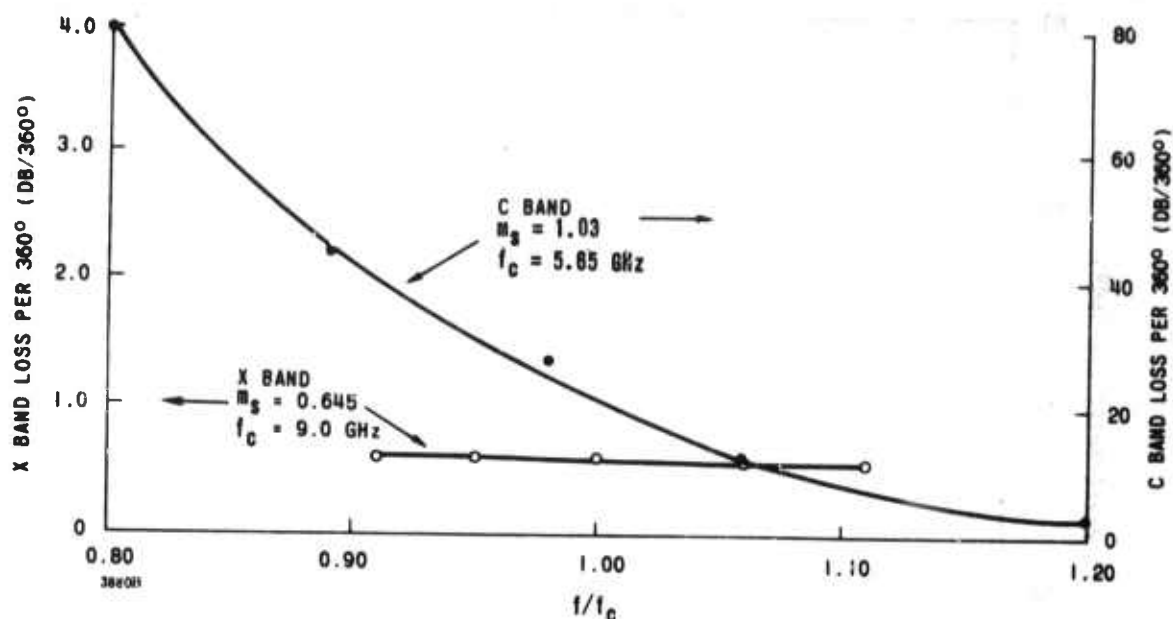
Figure 48. Loss/360° Versus Frequency for Ferrite 83-8 in X Band and C Band Phase Shift Structures. Structure Shown in Table VI

Figure 51 are tabulated on the illustration together with their intrinisic and poly-crystalline linewidth. The data points have been normalized to correspond to a remanence ratio of one-half. For these materials excellent correlation is obtained between experimental losses and those calculated using the intrinsic resonance line-width. However, the linewidth normally measured for polycrystalline materials is the inhomogeneously broadened linewidth, not the intrinsic linewidth per se. What then is the relationship of the <u>intrinsic</u> linewidth to the <u>polycrystalline</u> linewidth?

The linewdith observed on polycrystalline ferrimagnetic materials arises from several different sources. The various line broadening mechanism can be categorized as intrinsic damping, porosity broadening, and anisotropy broadening. Obviously, all damping mechanisms are line broadening mechanisms since, in the absence of damping, the resonance line is infinitely narrow.
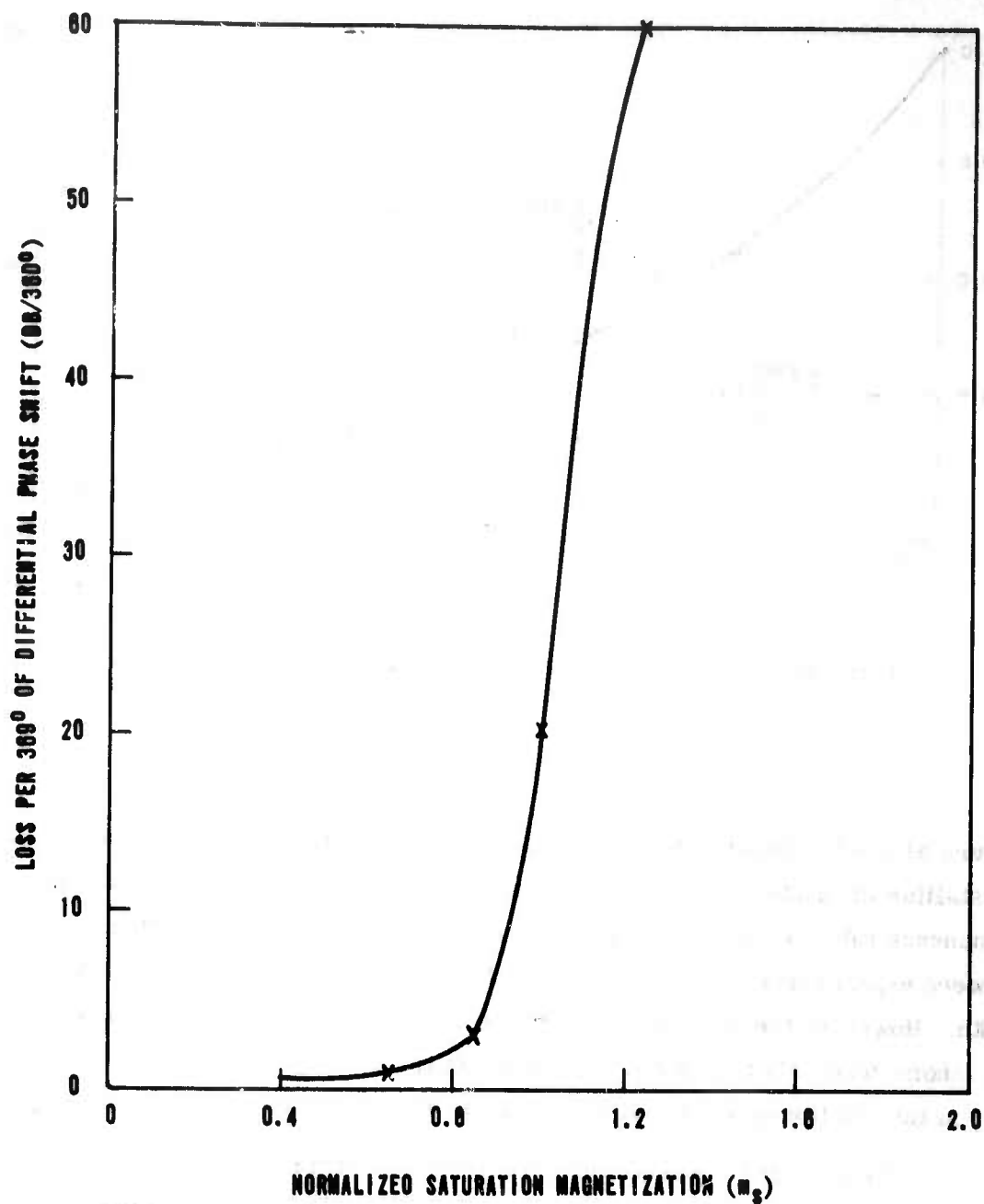
Figure 49. Loss Per 360° Versus Magnetization for Ferrite 83-8 Configuration Shown in Table VI

3672B

M_s = VARIABLE

f_c = 9 Gc

λ_c = 3.33 Cm

$M = \dfrac{\gamma 4\pi M_r}{\omega_c} = R_r M_s$
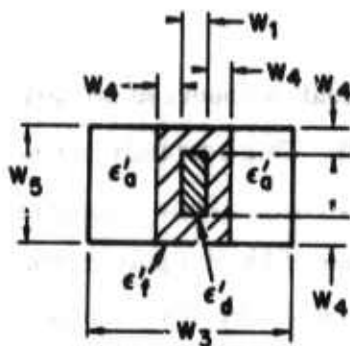
NF = FUNCTION OF M_s & H_{anis}

ΔH = 65 OERSTEOS

FR = 1.0

W_1 = 0.023 λ_c

W_3 = 0.35 λ_c

W_4 = 0.04 λ_c

W_5 = 0.294 λ_c

H_{anis} = 100 OERSTEDS

R_r = 0.5

ϵ_d' = 16.0

ϵ_f' = 16.0

ϵ_a' = 1.0

tan δ_d = 0.0005

tan δ_f = 0.0007

tan δ_a = 0

N_x = 0.9

N_y = 0.1

$M_s = \gamma 4\pi M_s / \omega_c$ = NORMALIZED SATURATION MAGNETIZATION
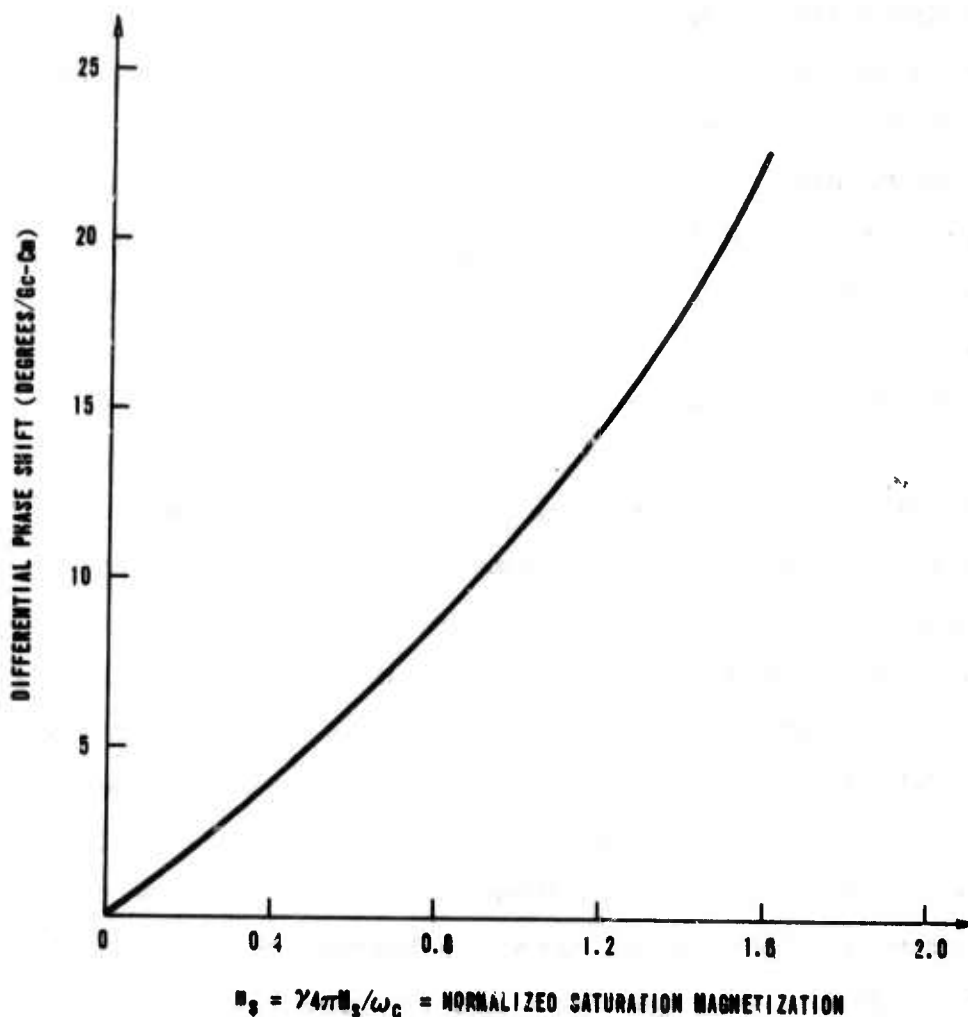
38793

Figure 50. Variation of Differential Phase Shift as a Function of Normalized Saturation Magnetization

4-69

Intrinsic damping contributes to the linewidth that is observed on pure single crystals, free from surface effects and so forth. This certainly represents a lower limit on polycrystalline linewidth, as all other effects will broaden this intrinsic resonance linewidth. The intrinsic linewidth of a polycrystalline sample is the same as the intrinsic linewidth of a single crystal sample of the same material and of equal purity. The equal purity should be kept in mind since lower purity oxides (99.9) are normally used in polycrystalline materials than are used in single crystal work (99.9999). Intrinsic linewidth is rather intimately related to the spin wave linewidth, ΔH_K. In fact, as a good approximation, one can take ΔH_K to be equal to the intrinsic ΔH at the same frequency. A frequency dependence of intrinsic linewidth has been observed on many single crystal samples and some polycrystals. The observed shape of the loss curve and the frequency dependence of linewidth for losses due to intrinsic damping are in excellent agreement with the predictions of the Landau-Lifshitz loss formulation.

Intrinsic linewidths vary widely. Prime examples are found in the garnet family. For example, pure yttrium iron garnet single crystals may have linewidths of a few tenths of an oersted, while the yttrium dysprosium iron garnets may have linewidths of several thousands of oersteds. In fact in the rare earth garnets, intrinsic linewidths are so broad that the single and polycrystalline samples exhibit essentially the same linewidth --- all other contributing factors being almost negligible. This dominance of the intrinsic damping also manifests itself in the observed frequency dependence of the polycrystalline linewidth of rare earth and even of rare earth doped garnets. Thus, the linewidth of a heavily dysprosium doped yttrium iron garnet shows a marked frequency dependence. When intrinsic damping is dominant, X band linewidths may actually be several times larger than L or S band linewidths.

Corruption or porosity broadening occurs in all polycrystalline samples to some extent. The more porous or less dense a polycrystalline sample is, the broader will be its resonance linewidth. Porosity broadening will contribute

a line broadening proportional to the percent porosity and to the saturation magnetization. Porosity broadening seems to be independent of frequency.

Anisotropy broadening has long been recognized as a source of linewidth in polycrystalline materials. Since each grain or crystallite may have its crystallographic axes aligned different from its neighbor, the effective anisotropy field varies from one grain to the next. Thus, each grain will resonate at slightly different field values, and this spread in effective field values gives rise to a spreading out of the resonance loss. This type of line broadening is independent of frequency and is the dominant mechanism in many common ferrites and garnets.

In summary, polycrystalline linewidth of many ferrites and garnets is determined by inhomogeneous broadening mechanisms that scatter energy to degenerate spinwaves. This may be predominately anisotropy broadening and is rather independent of frequency. In very porous samples, porosity broadening may be the dominant mechanism. It, too, is independent of frequency. In some rare earth doped garnets (or single crystals of other materials), intrinsic damping may be the dominant mechanism, and this linewidth will vary almost linearly with frequency. The appropriate linewidth to use in calculating magnetic losses far from resonance appears to be the intrinsic linewidth. As pointed out above, for some materials, such as the rare earth doped garnets, the polycrystalline linewidth is almost identical to the intrinsic linewidth. In particular, this is true for the dysprosium and gadolinium doped garnets whose test results are compared in Figure 51, i.e., $\Delta H_{polycrystalline} \simeq \Delta H_{intrinsic}$ for these materials. The two materials which have no rare earth doping, YIG and MgMn ferrite, have polycrystalline linewidths of 35 and 510 oersteds, respectively, and intrinsic linewidths of 10 to 12 oersteds. With such large differences between the two types of linewidth, the correlation obtained with intrinsic linewidth is striking.

Dielectric and waveguide copper losses are included in the calculated values but not losses due to reflections, charging wire, glue, etc. Obviously, the computation based on intrinsic linewidth again is in very good agreement with measured

results, while the computation based on polycrystalline linewidth would lead to losses much higher than those measured. Thus, the conclusion is that magnetic loss in remanent state ferrimagnetic materials is directly related to intrinsic linewidth and can be accurately predicted from that and other material parameters utilizing the models and analysis techniques presented in Section 3.

The data shown in Table V and plotted in Figures 52 and 53 show the dependence of loss on linewidth for several materials as measured in C and S bands, respectively. These results can be compared with the data shown in Figure 51. Again, in every case, an approximate linear dependence of loss on linewidth is observed. These materials are all garnets and in the broad linewidth cases have considerable dysprosium doping. In the intermediate linewidth range they contain both small dysprosium and gadolinium dopings. It is interesting to note that these curves are very nearly the same for the three frequency bands. The linewidth axis in Figures 52 and 53 is the X band measured polycrystalline linewidth. Since the damping parameter used in the computation is of the form $\dfrac{\Delta H_i}{\omega}$, a linear dependence of ΔH_i on frequency would lead to a constant damping parameter and an almost universal curve of loss versus ΔH_i. This is essentially corroborated by the data at X, C, and S bands where experimentally measured loss agrees very closely with this "universal" loss curve.

4.5.1.3 <u>Effects of Dimensional Changes and Dielectric Loading</u>. For a given set of intrinsic ferrite parameters, the other parameters of a phase shifter structure can be selected to optimize performance in terms of maximum phase shift per unit loss, maximum phase shift per unit length, minimum change in phase shift with frequency, etc. The following figures illustrate how the configurational parameters affect performance characteristics. Both calculated and measured data are given where available. Excellent correlation of experimental and analytical results is obtained.

Figure 54 presents the variation of differential phase shift with dielectric core thickness for several values of core dielectric constant. It can be seen that by proper choice of core width and dielectric constant it is possible to maximize the differential

DATA POINT	COMPOSITION	APPROXIMATE ΔH_k (OE.) (X BAND)	ΔH_{poly} (OE)
1	YIG	10 - 12	35
2	Mg Mn	10 - 12	510
3	15% Gd	20 - 24	45
4	30% Gd	30 - 36	65
5	2% Dy	85	100
6	4% Dy	155	165
7	10% Dy	380	380
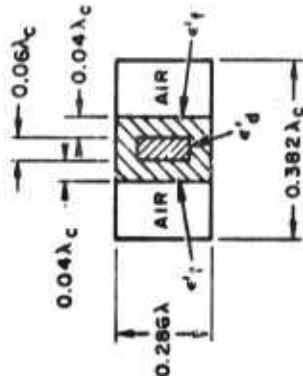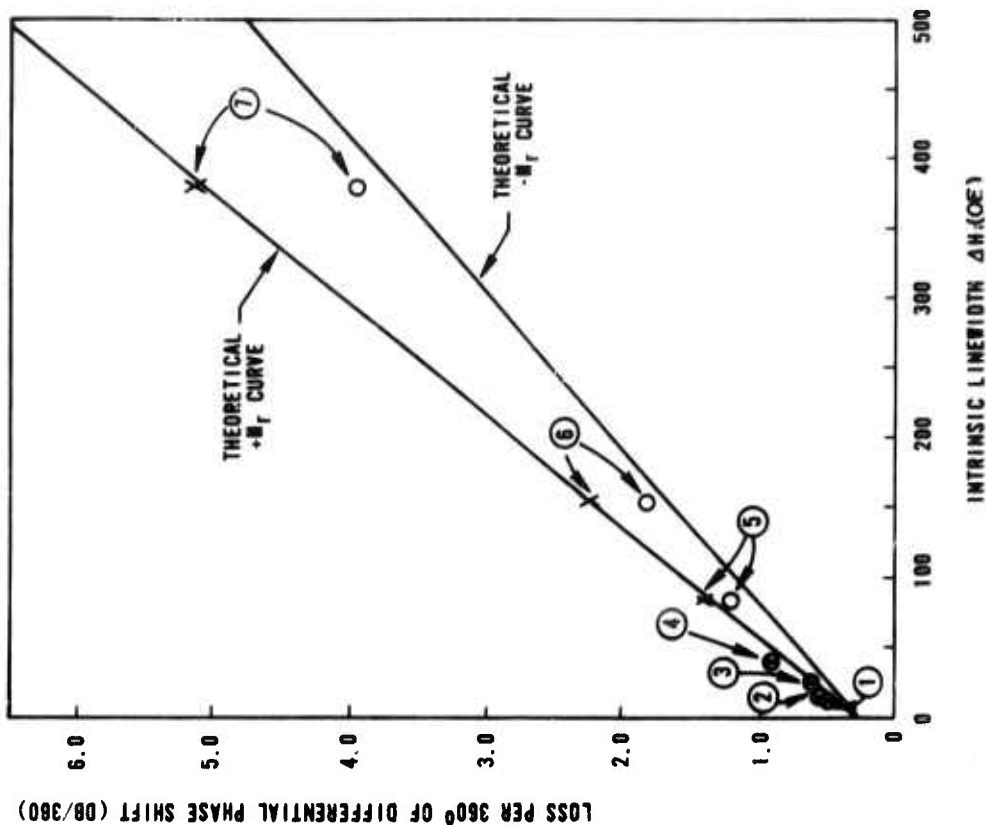
$\epsilon'_d = 16$
$\epsilon'_f = 16$
$\tan \delta_d = 0.0005$
$\tan \delta_f = 0.0007$
f_c = CENTER FREQUENCY = 9 GHz

$R_r = 0.5$
$HF = \dfrac{\gamma H_i}{\omega_c} = 0.14$
ΔH_i = VARIABLE

0.06λ_c
0.04λ_c
AIR
ϵ'_f
0.382λ_c
ϵ'_d
AIR
ϵ'_i
0.04λ_c
0.286λ

THEORETICAL $-M_r$ CURVE

THEORETICAL $+M_r$ CURVE

LOSS PER 360° OF DIFFERENTIAL PHASE SHIFT (DB/360)

INTRINSIC LINEWIDTH ΔH_k(OE)

Figure 51. X Band Loss/360° Versus X Band Intrinsic Linewidth.
Experimental data obtained in the configurations shown
in Table V.
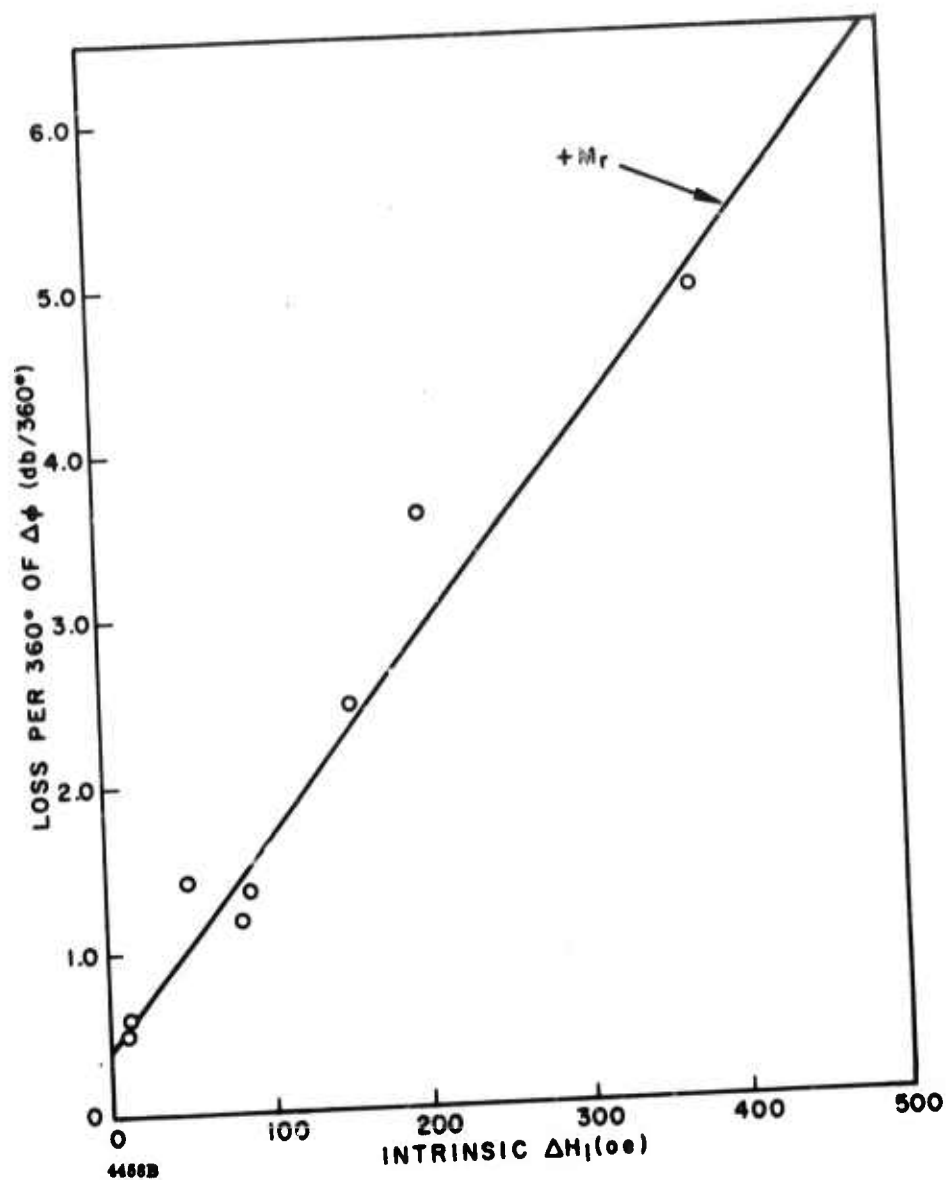
Figure 52. C Band Loss/360° Versus X Band Intrinsic Linewidth. Experimental data obtained in the configuration shown in Table V.

4-74
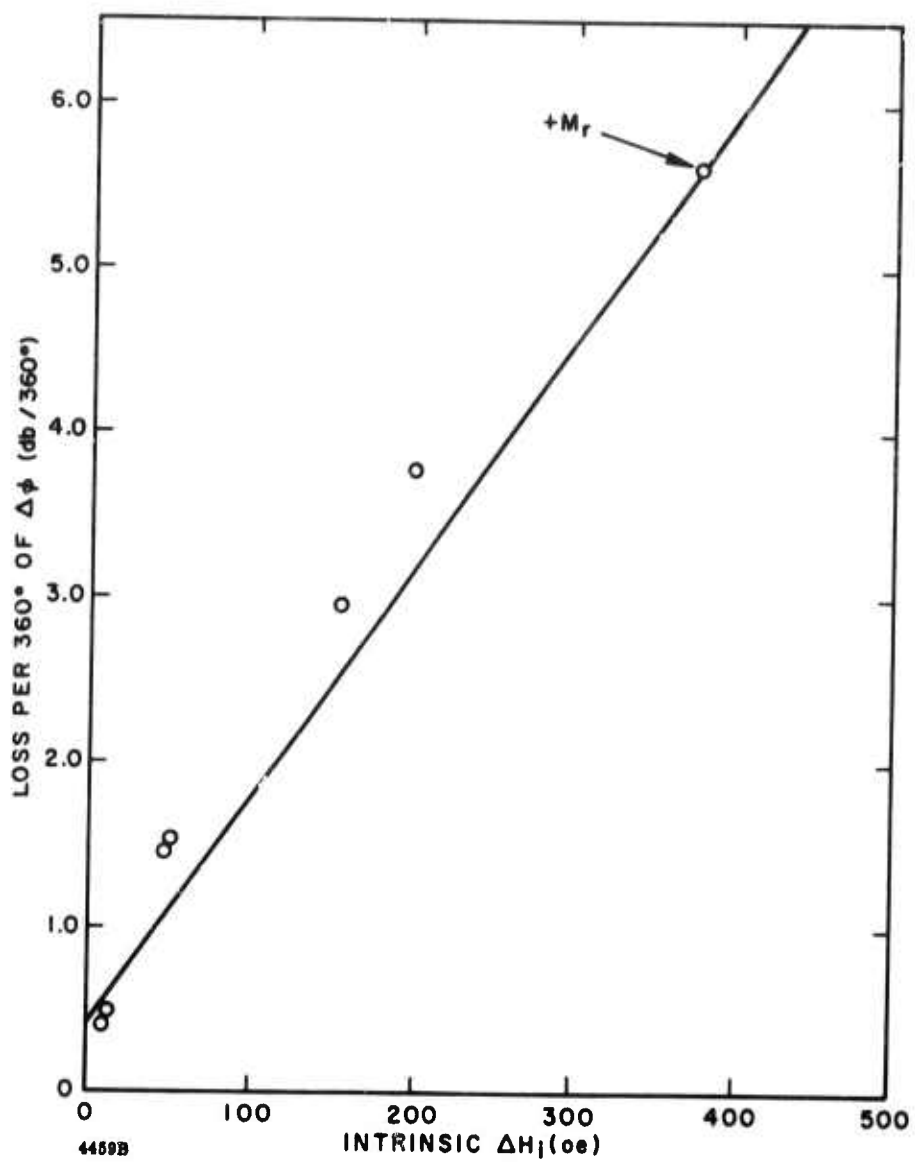
Figure 53. S Band Loss/360° Versus X Band Intrinsic Linewidth.
Experimental data obtained in the configuration shown
in Table V.

$$m_s = \frac{\gamma 4\pi M_s}{\omega_c} = 0.366$$
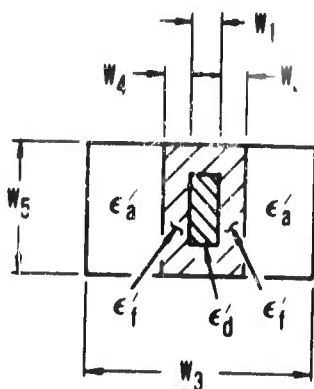
$$f_c = 8 \text{ Gc}$$

$$m = \frac{\gamma 4\pi M_r}{\omega_c} = 0.193$$

FR = 1.0

W_1 = VARIABLE

$W_3 = 0.362 \ \lambda_c$

$W_4 = 0.04 \ \lambda_c$

$W_5 = 0.294 \ \lambda_c$

$R_f = 0.5$

$\epsilon'_a = 1.0$

ϵ'_d = PARAMETER

$\epsilon'_f = 16.0$

$\tan \delta_a = 0.0007$

$\tan \delta_d = 0$

$\tan \delta_f = 0.0005$

$\lambda_c = 3.33 \text{ Cm}$

HF = 0.1

$\Delta H = 65 \text{ Oe.}$
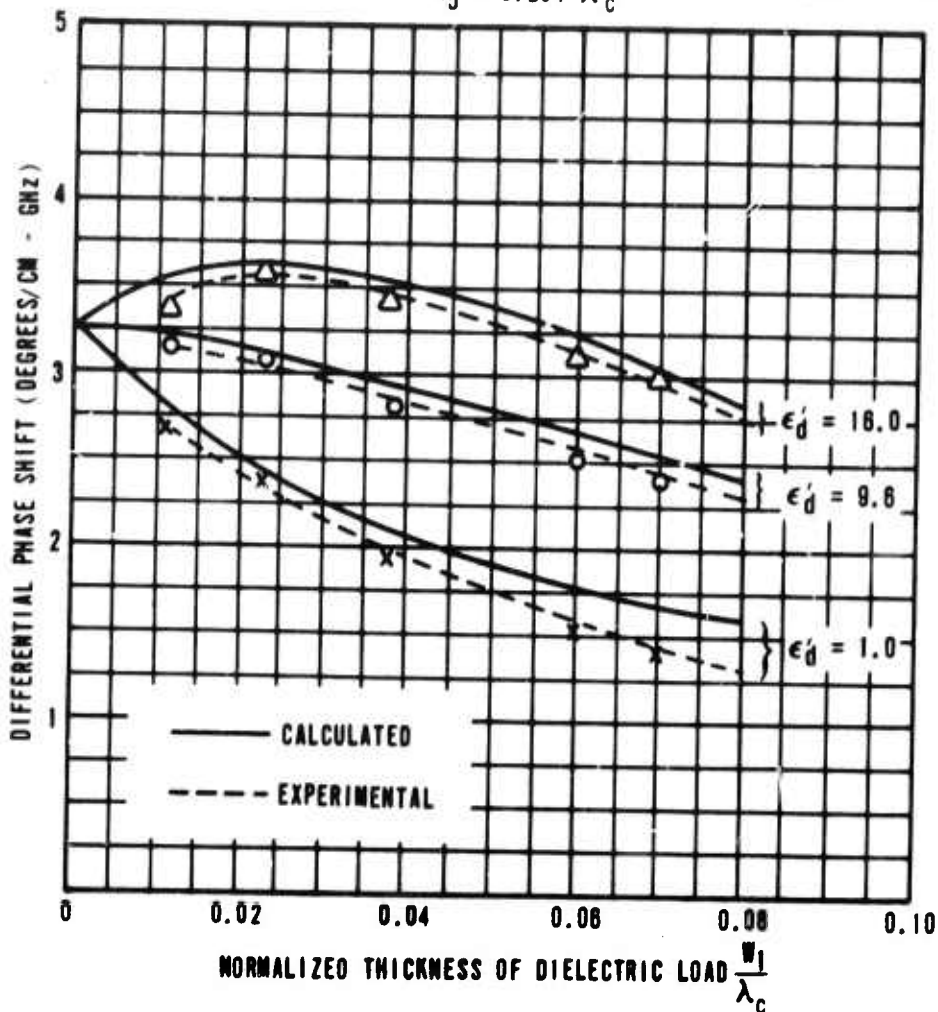
Figure 54. Differential Phase Shift vs Normalized Thickness
Of Dielectric Load With Load Dielectric Constant
As A Parameter
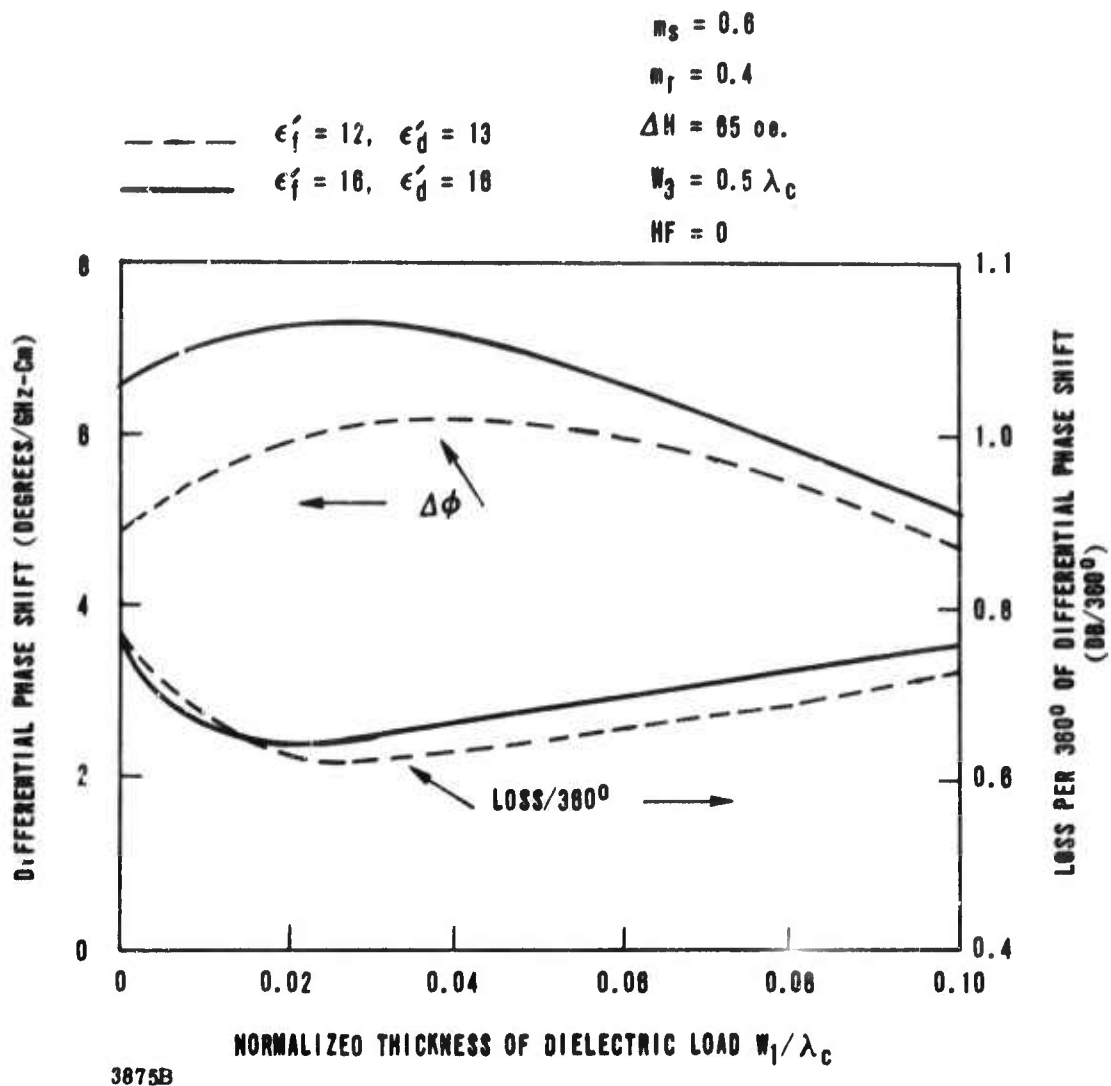
Figure 55. Comparison of Performance of a Typical Ferrite and
a Typical Garnet in a FDPS

phase shift per unit length. For the example shown, this maximum occurs with a dielectric constant of 16 and a normalized core width of $0.025\lambda_c$.

Figure 55 compares a typical ferrite material to a typical garnet material. The dielectric constant of the load is 13 for the ferrite case and 16 for the garnet case. Differential phase shift and loss per 360° are plotted as a function of slot width W_1 with waveguide width $W_3 = 0.5\lambda_c$. It is seen that, although the garnet material produces more differential phase shift, its loss per 360° is also slightly more than in the case of the ferrite. It is also seen that differential phase shift in the garnet material peaks

out at a value of $W_1 = 0.025 \lambda_c$, while $W_1 = 0.04 \lambda_c$ gives maximum phase shift in the case of the ferrite. However, minimum loss per 360° is achieved with a value of $W_1 = 0.020 \lambda_c$ in both the garnet and the ferrite, which yields 0.64 db for the garnet and 0.62 db for the ferrite.

The variation of differential phase shift with frequency can be controlled to some extent by proper selection of waveguide width and dielectric load thickness. Figures 56 and 57 show the frequency variation of differential phase shift for several values of waveguide width and of dielectric load thickness, respectively. It can be seen that in either case there are values of W_3 and W_1 that yield a differential phase shift which is essentially independent of frequency over a wide band of frequencies. For example, from Figure 56 a waveguide width of $0.3 \lambda_c$ and core thickness of $0.023 \lambda_c$ leads to a flat phase shift with frequency when the other parameters of the structure are as shown.

The slope of the phase shift curve is quite important in many applications. Phase slope is defined as the change in differential phase shift over a 0.1 increment in normalized frequency centered at the operating frequency. Figures 58 and 59 show phase slope as a function of waveguide width with core thickness as a parameter. Comparing the two figures, it can be seen that other factors remaining constant, increasing the dielectric constant of the core means that smaller waveguide widths must be used to obtain zero phase slope. For example, if the core dielectric constant is 1.0, then a waveguide width of $0.41 \lambda_c$ and a core thickness of $0.038 \lambda_c$ will yield flat phase with frequency. If the core dielectric constant is increased to 16.0 and the core thickness is maintained at $0.038 \lambda_c$, then the waveguide width must be reduced to $0.32 \lambda_c$ to obtain zero phase slope.

From the data contained in the above figures it is possible to derive a configuration which will have a maximum phase shift per unit loss with the added constraint that the phase slope be zero. For a typical garnet material having a dielectric constant of 16, this optimum configuration would be:

$$\text{Waveguide width } W_3 = 0.365 \lambda_c$$
$$\text{Dielectric core thickness } W_1 = 0.025 \lambda_c$$
$$\text{Toroid wall thickness } W_4 = 0.045 \lambda_c$$
$$\text{Core dielectric constant } \epsilon_d = 16$$

This basic configuration is the one now used in the experimental evaluation of materials.
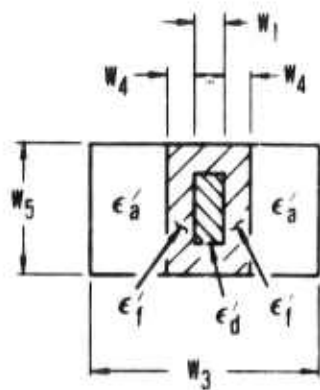
4-78
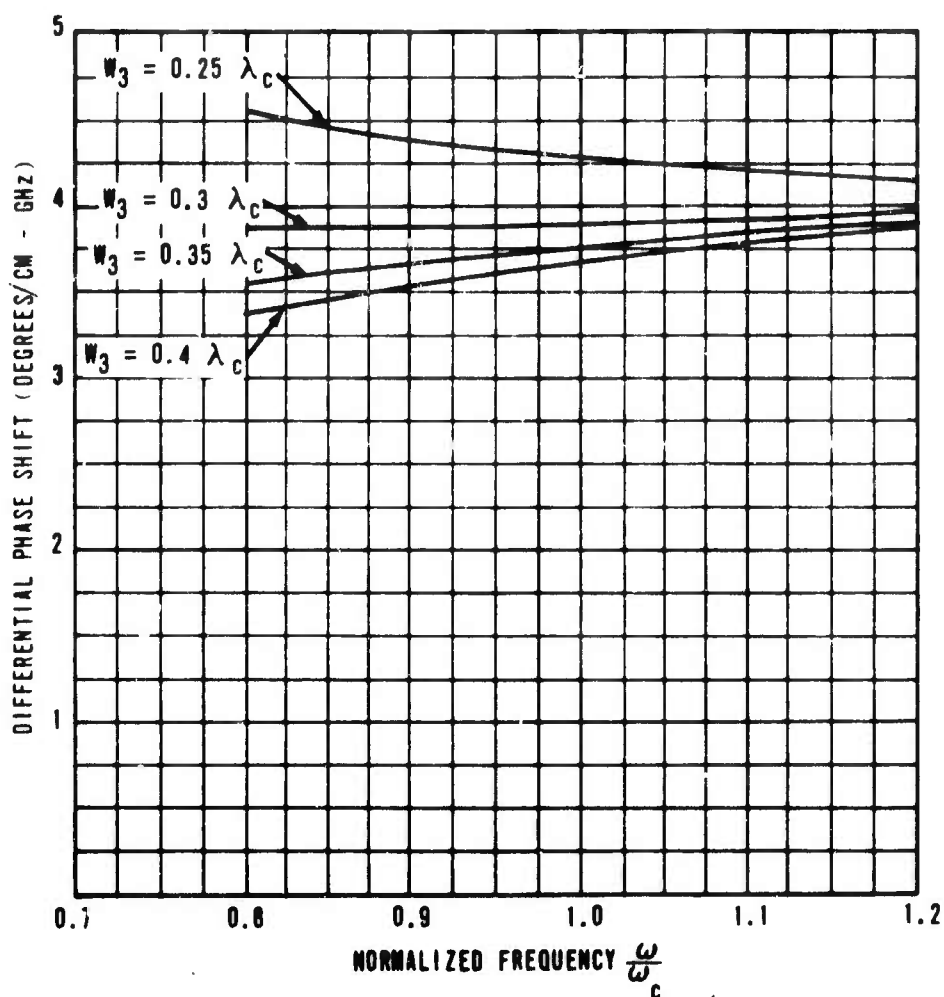
Figure 56. Differential Phase Shift vs Normalized Frequency
With Waveguide Width As A Parameter
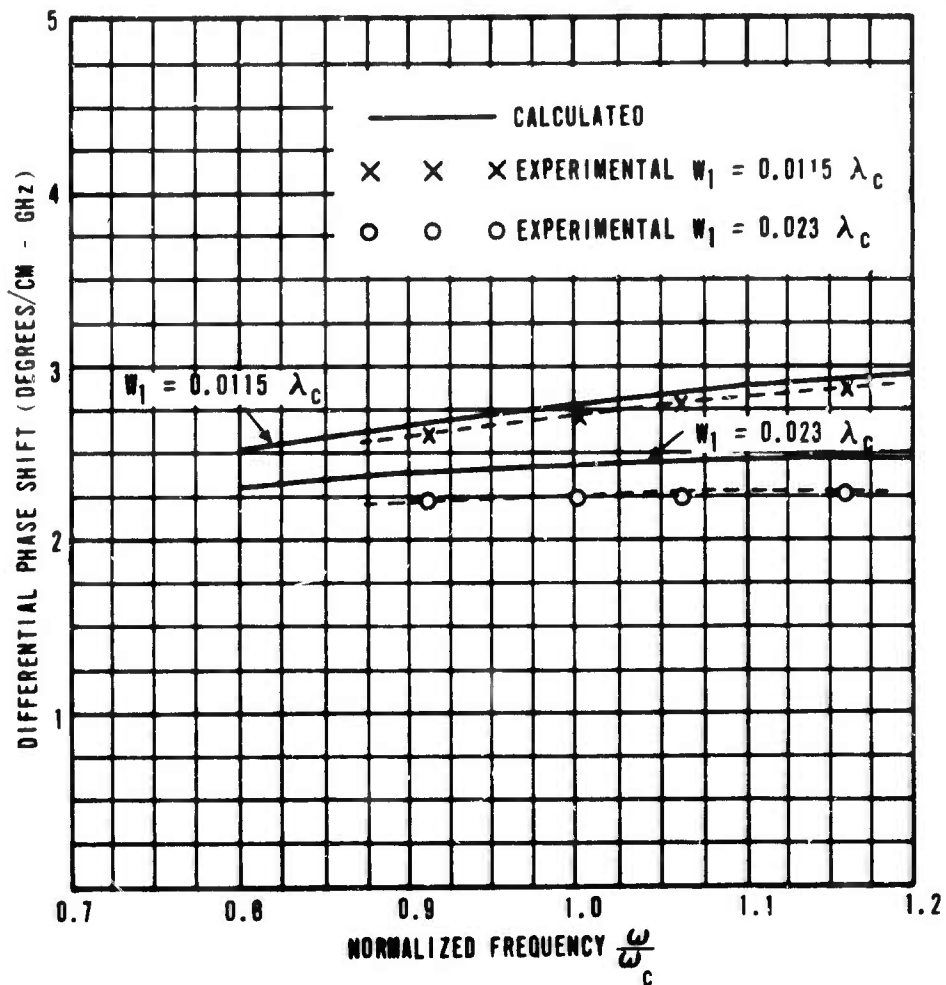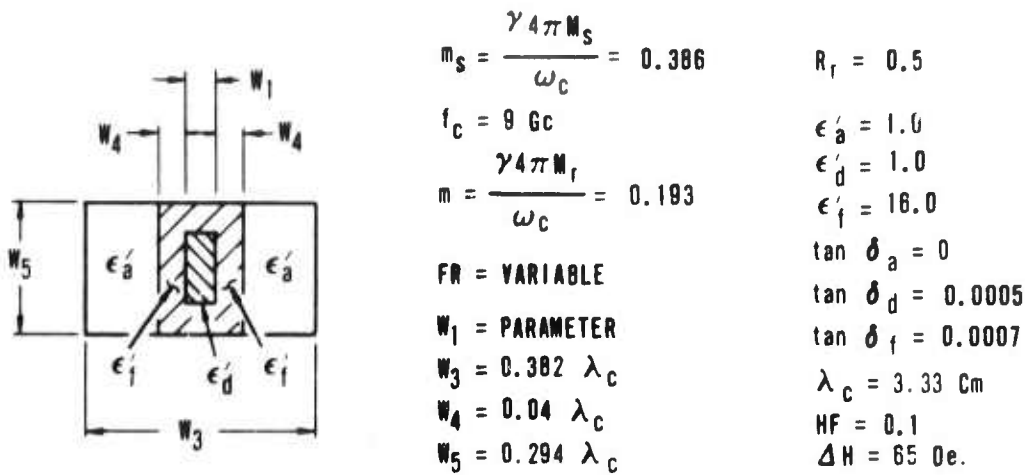
Figure 57. Differential Phase Shift vs Normalized Frequency
With Dielectric Load Thickness As A Parameter
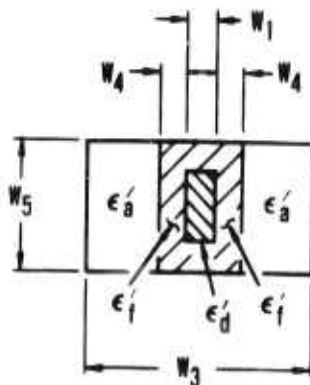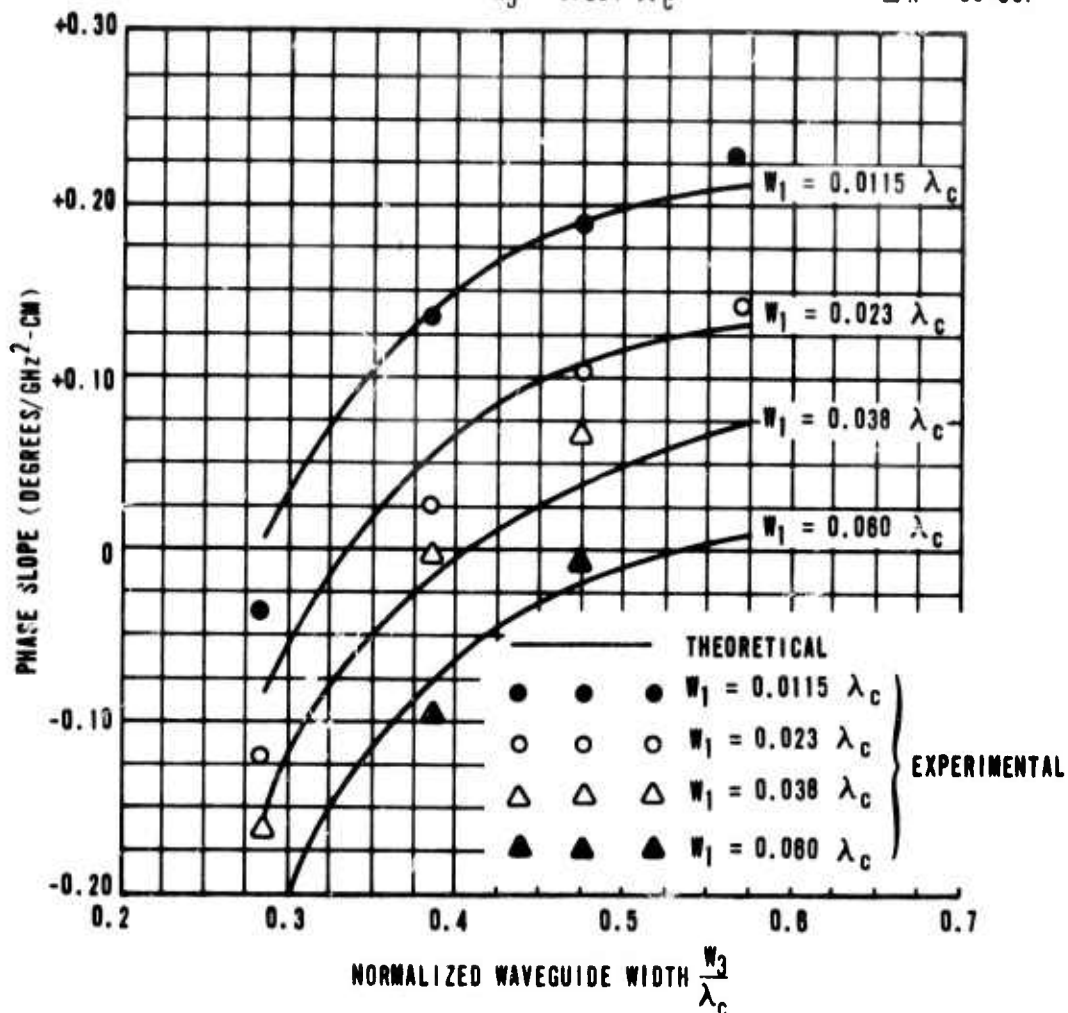
Figure 58. Phase Slope vs Normalized Waveguide Width With Dielectric Load Thickness As A Parameter
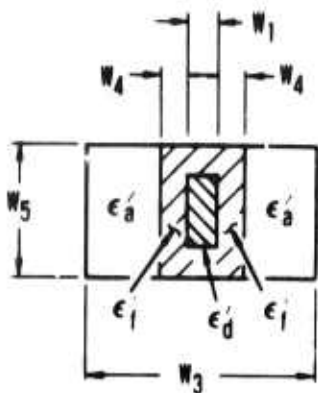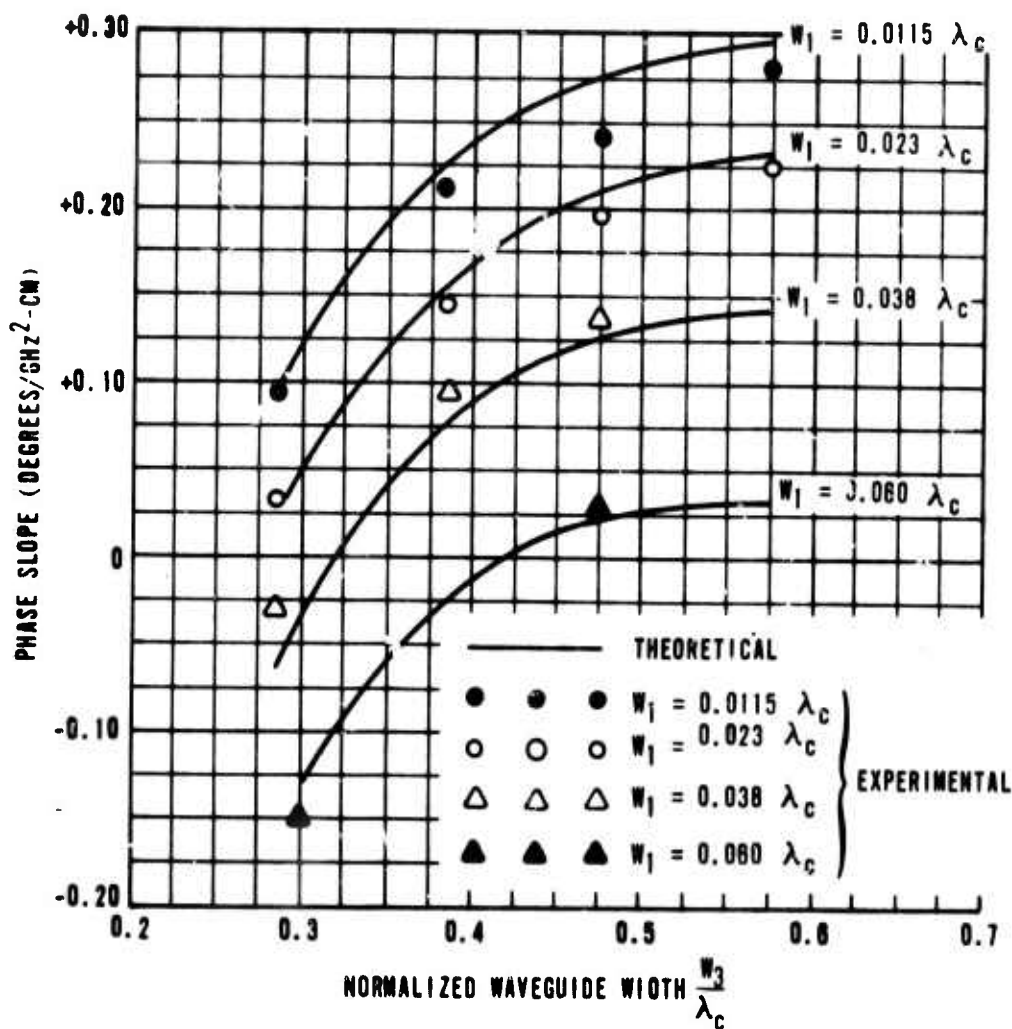
Figure 59. Phase Slope vs Normalized Waveguide Width With
Dielectric Load Thickness As A Parameter

4.5.2 Low Frequency FDPS Characteristics

In this section, measurements of loss and phase shift of low frequency FDPS operating both above and below resonance are reported. The measurements were made in a waveguide FDPS and in a helix line FDPS. Generally, the waveguide FDPS is a low loss, low phase shift per inch structure while the helix FDPS is by contrast a relatively high loss, high phase shift per inch structure.

4.5.2.1 L Band Waveguide Measurements. The principal problem in low frequency rectangular waveguide FDPS is usually the excessive length required to obtain the desired differential phase shift. In this section, measurements of loss and phase shift are reported in six different materials operating above resonance $(f > f_r)$ and three materials operating below resonance $(f < f_r)$. Table VI lists the microwave and square loop properties of the materials tested and shows a cross-sectional view of the geometry of the test configuration. The dimensions of the test structure in wavelengths at the center frequency are seen to be the same as those of the X and C band structures (Figure 77). The toroids for L band were fabricated as 2-piece assemblies. In large toroids such as these, small gaps do not seriously degrade the remanence ratio. The average remanence ratio was about 0.36 which is certainly enough to yield meaningful data. Also listed in Table VI are the loss per inch, phase shift per inch, and the loss per 360° measured on these materials at 1.5 GHz. The measurements were made from 1.0 GHz to 1.8 GHz. No phase shift or loss per 360° data were obtained on the below resonance materials since they were too lossy to permit phase shift measurements to be made.

We consider first just the above resonance $(f > f_r)$ materials. These are the first six materials listed in Table VI. It is seen that the loss per inch depends both on m_s and linewidth. The phase shift data has been normalized to a remanence ratio of 0.50 and varies only with m_s. It is seen that as m_s varies from 0.58 to 1.03, the phase shift varies from 24 degrees/inch to 43 degrees/inch. The loss per 360° varied from a minimum of 0.60 db/360° for aluminum substituted YIG at $m_s = 0.58$ to a maximum of 3.57 db/360° for dysprosium-aluminum substituted material at $m_s = 1.00$. These data are in good agreement with the predicted values shown in Figure 51 and with experimental data at X, C, and S bands. The next to last column in Table VI shows values of P_{crit} which were calculated on the basis of measurements in X and C bands. The calculated value of P_{crit} for G-250 (20% Al + YIG) is 44 kw. Extrapolating to lower values

TABLE VI.   L BAND WAVEGUIDE FDPS T[

SMEC No.	Composition	Firing Schedule (°C/hr)	ρ_m / ρ_x (gm/cm³)	Tanδ / e_f (X Band)	g-Fact (X Ban
G238-6	$3 Y_2O_3 \bullet 5 [0.80 Fe_2O_3 \bullet 0.20 Al_2O_3]$	1500 / 5	4.98 / 5.04	.0024 / 14.9	2.02
G250-6	$3 Y_2O_3 \bullet 5 [0.75 Fe_2O_3 \bullet 0.25 Al_2O_3]$	1500 / 5	4.98 / 5.01	.0019 / 14.2	2.03
G490-1	$3 [0.98 Y_2O_3 \bullet 0.02 Dy_2O_3] \bullet 5 [0.80 Fe_2O_3 \bullet 0.20 Al_2O_3]$	1500 / 5	5.04 / 5.10	.0091 / 15.0	1.96
G491-1	$3 [0.95 Y_2O_3 \bullet 0.50 Dy_2O_3] \bullet 5 [0.80 Fe_2O_3 \bullet 0.20 Al_2O_3]$	1500 / 5	5.07 / 5.16	.0040 / 15.2	1.86
G431-3	$3 [0.85 Y_2O_3 \bullet 0.15 Gd_2O_3] \bullet 5 [0.80 Fe_2O_3 \bullet 0.20 Al_2O_3]$	1500 / 5	5.20 / 5.24	.0016 / 14.5	2.05
G493-:	$3 [0.83 Y_2O_3 \bullet 0.15 Gd_2O_3 \bullet 0.02 Dy_2O_3] \bullet$ $5 [0.80 Fe_2O_3 \bullet 0.20 Al_2O_3]$	1500 / 5	5.19 / 5.31	.0040 / 14.8	1.95
D80A1-108	$3 Y_2O_3 \bullet 5 Fe_2O_3$	1475 / 5	5.08 / 5.17	.0004 / 15.8	2.02
91-3	$Ni_{0.44} Zn_{0.56} Mn_{0.02} Fe_{1.9} O_4$	1250 / 7	5.04 / 5.35	.0016 / 13.7	2.13
83-8	$0.58 MgO \bullet 0.60 MnO \bullet 0.36 Fe_2O_3$	1320 / 7	4.20 / 4.39	.001 / 12.9	2.13
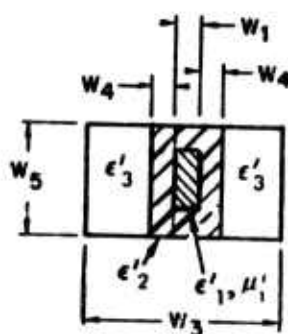
$W_1 = 0.025 \lambda_c$

$W_3 = 0.365 \lambda_c$ except as noted in Last C

$W_4 = 0.045 \lambda_c$

$W_5 = 0.280 \lambda_c$

Note: Toroids were 2-piece structures with joints along W_1 dimensional line as shown.

$\tan\delta/\epsilon_f'$ (X Band)	g-Factor (X Band)	Linewidth (X Band) (oe)	$4\pi M_s$ (Gauss)	R_r	Coercive Field (oe)	m_s (1.5 GHz)	Loss (db/in.)	Phase Shift (°/in.)	Loss/360° (db/360°)	P_{crit}* (kw)	Notes
24/14.9	2.02	35	510	0.41	0.71	1.020	0.21	40	1.98	27	
9/14.2	2.03	38	290	0.33	0.68	0.580	0.04	24	0.60	44	
1/15.0	1.96	123	515	0.33	0.65	1.030	0.24	43	2.03	—	
0/15.2	1.86	274	500	0.23	0.72	1.000	0.44	43	3.57	—	
6/14.5	2.05	110	370	0.29	1.20	0.740	0.11	35	1.18	87	
0/14.8	1.95	230	300	0.30	1.09	0.600	0.14	32	1.60	140	
4/15.8	2.02	47	1730	0.56	0.76	3.460	18.5	NM	NM	—	$W_3 = 0.825\lambda_c$
6/13.7	2.13	115	3770	NM	NM	7.540	16.0	NM	NM	—	$W_3 = 0.825\lambda_c$
/12.9	2.13	512	2065	0.54	2.35	4.130	12.0	NM	NM	—	$W_3 = 0.825\lambda_c$

$\mu_i = 1$

noted in Last Column $\epsilon_1' = 16$

$\epsilon_2' = \epsilon_f'$

$\epsilon_3 = 1$

ece structures
$_1$ dimensional

$m_s = \dfrac{\gamma\, 4\pi M_s}{1.5\,\text{GHz}}$

* P_{crit} values shown are calculated by method shown in Appendix A using data from high power measurements in other bands.

NM - Not measured

of m_s, it can be seen using Figure 47, 78, and 44 that, using aluminum substituted YIG at m_s = 0.25, the loss per 360° would be less than 1.0 db, P_{crit} would be in excess of 1.0 megawatt, and the phase shift would be about 10 degrees per inch. Thus, allowing ten inches for matching transformers, the total length of the unit would be 46 inches.

Figures 60 and 61 show the loss and phase shift data obtained from 20 percent and 25 percent aluminum substituted YIG. The main resonance losses of G-238 (20% Al + YIG) occur below L band. In Figure 60, it is seen that at 1.5 GHz (m_s = 1.02), the loss in this material is still quite high, namely 0.9 db per inch. Phase shift measurements are shown from 1.2 GHz to 1.8 GHz and are seen to be rather erratic, varying from 118° to 144°. (Accurate differential phase shift measurements are difficult to make at these frequencies because of limitations of the available test equipment. Precision phase shifters are not obtainable in L band.) The best straight line drawn through the data points shows a differential phase shift of 131 degrees for four inches of material at 1.5 GHz. Normalizing to R_r = 0.50 yields a phase shift of 40 degrees/inch and a loss per 360° of 1.98 db/360°.

Figure 61 shows the loss and phase shift of G-250 (25% Al + YIG) with m_s = 0.58 at 1.5 GHz. The loss is seen to be much less than in the G-238 material and is quite flat with frequency at about 0.20 db. However, phase shift is also less, varying from 60° to 67° with about 64° at 1.5 GHz. Nevertheless, when the phase shift is normalized to R_r = 0.5 and the proper adjustments are made for transformer losses, the loss per 360° is found to be 0.60 db, or less than one-third that of the previous (G-238) material, while the phase shift is 24 degrees per inch.

The losses in <u>below</u> resonance operation ($f < f_r$) in waveguide were very high. Figure 62 shows the loss of a one-inch long toroid of YIG plotted versus frequency. It appears that when latched in the $-M_r$ state, the toroid reduces the electrical width of the waveguide to the point where severe cutoff type losses show up at the low frequency end of the band, while in the demagnetized (virgin) state and the $+M_r$ state, the losses are considerably less. At 1.0 GHz, the losses are 35 db, 13 db, and 9 db of the $-M_r$ state, virgin state, and $+M_r$ state, respectively. At 1.5 GHz, the losses are 17 db, 19 db, and 11 db, respectively, for these three states.

In an attempt to eliminate the cutoff losses, the waveguide width was increased from W_3 = 0.365λ_c (Figure 62) to W_3 = 0.825λ_c (Figure 63). This substantially reduced
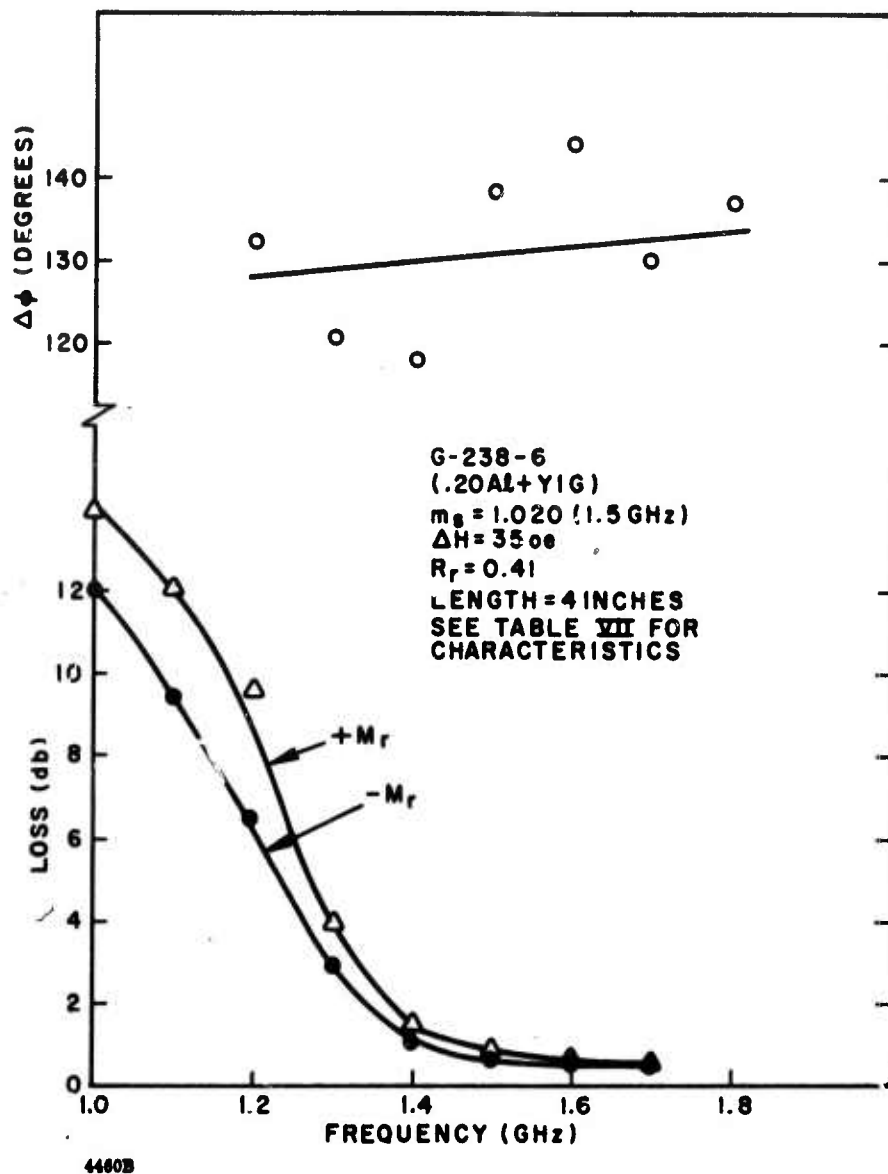
Figure 60. Loss and Phase Shift Variation with Frequency in a 20%
Aluminum Doped YIG in a Waveguide FDPS Structure

G-250-6
$(.25\,\mu\ell + YIG)$
$m_s = 0.58\ (1.5\ GHz)$
$\Delta H = 38\,oe$
$R_f = 0.33$
LENGTH = 4 INCHES
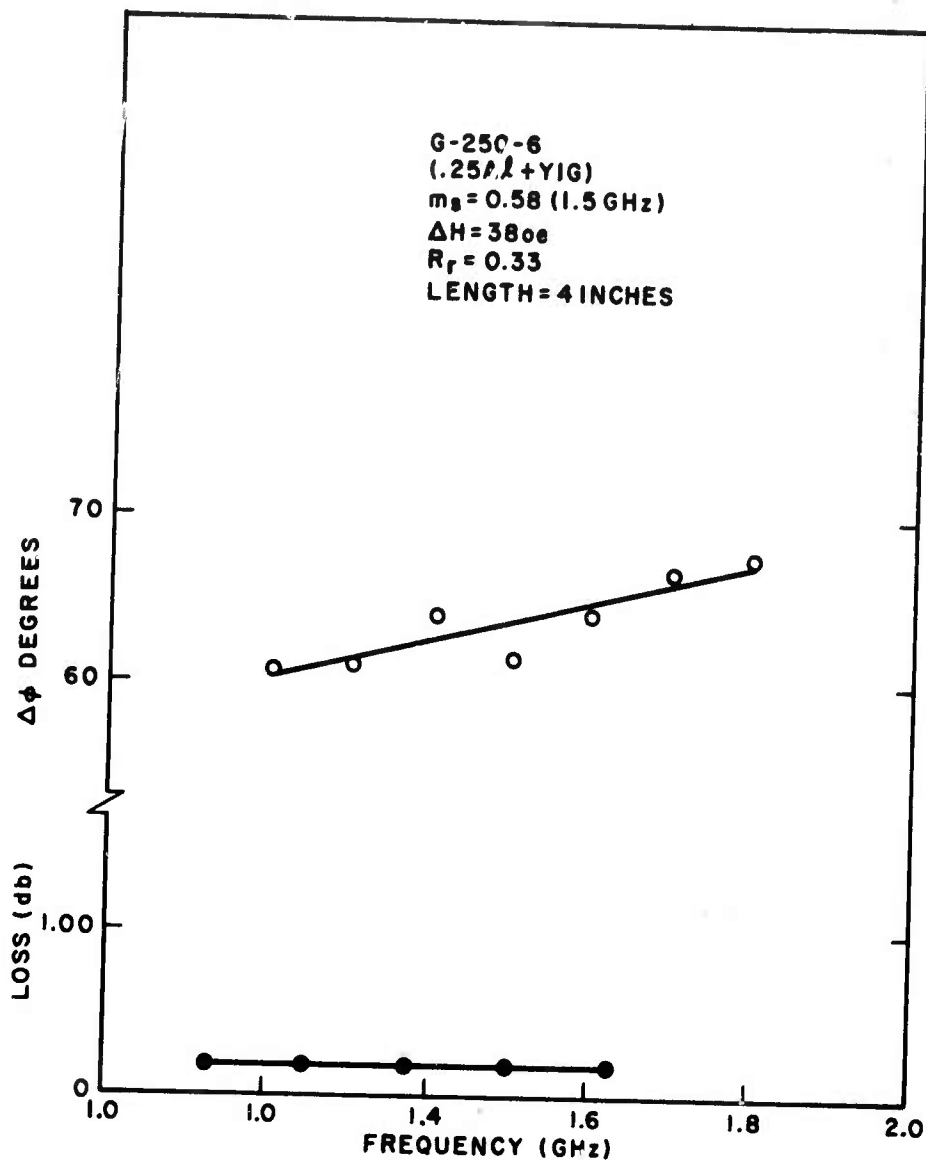
4461B

Figure 61. Loss and Phase Shift Variation with Frequency in a 25%
Aluminum Doped YIG in a Waveguide FDPS Structure
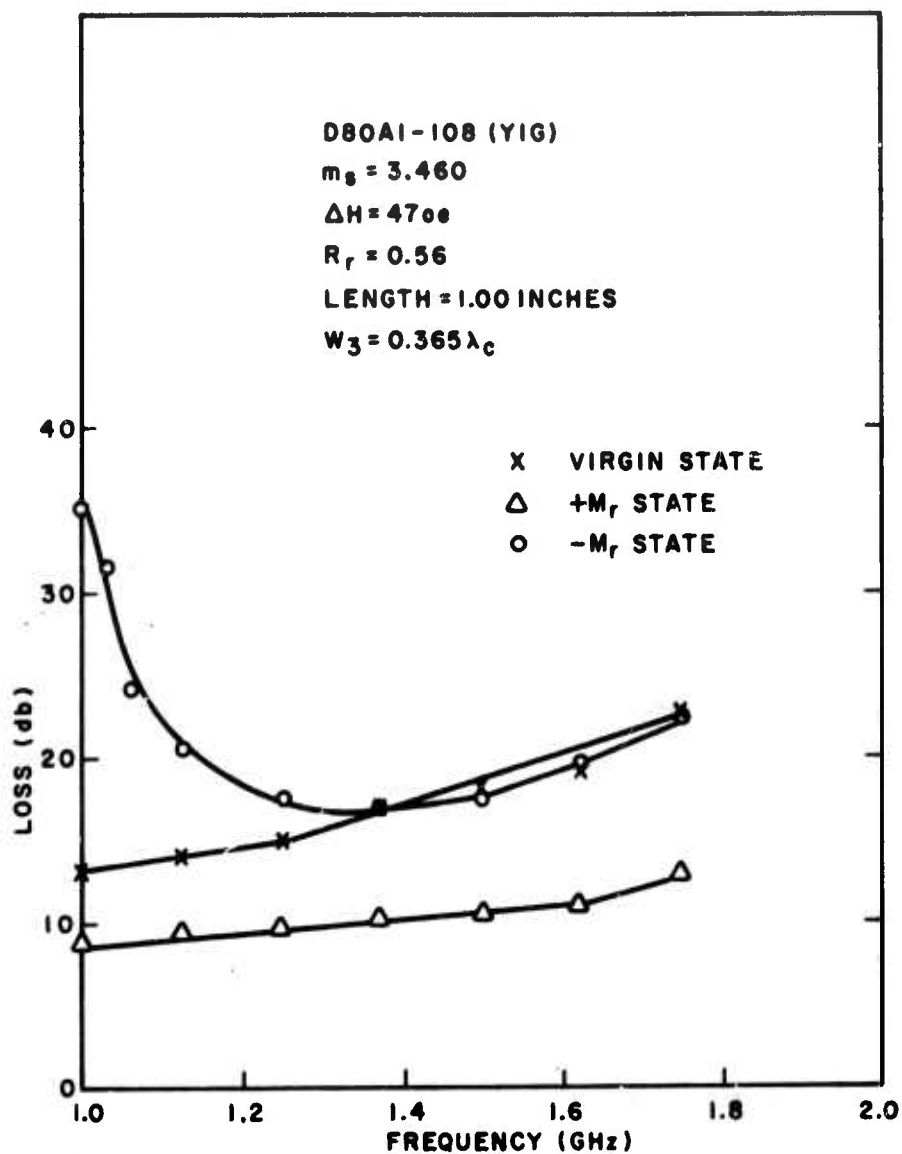
Figure 62. Loss Dependence on Frequency of the Three States of a
1-Inch Long Toroid of YIG Operating Below ($f < f_r$) Resonance.
The waveguide width W_3 is such that cutoff type losses can be
observed in the $-M_r$ state.

DBOAI-108 (YIG)
$m_s = 3.460$
$\Delta H = 47 \, oe$
$R_s = 0.56$
LENGTH = 1.00 INCHES
$W_3 = 0.825 \lambda_c$

△ $+M_r$ STATE
○ $-M_r$ STATE

4463B
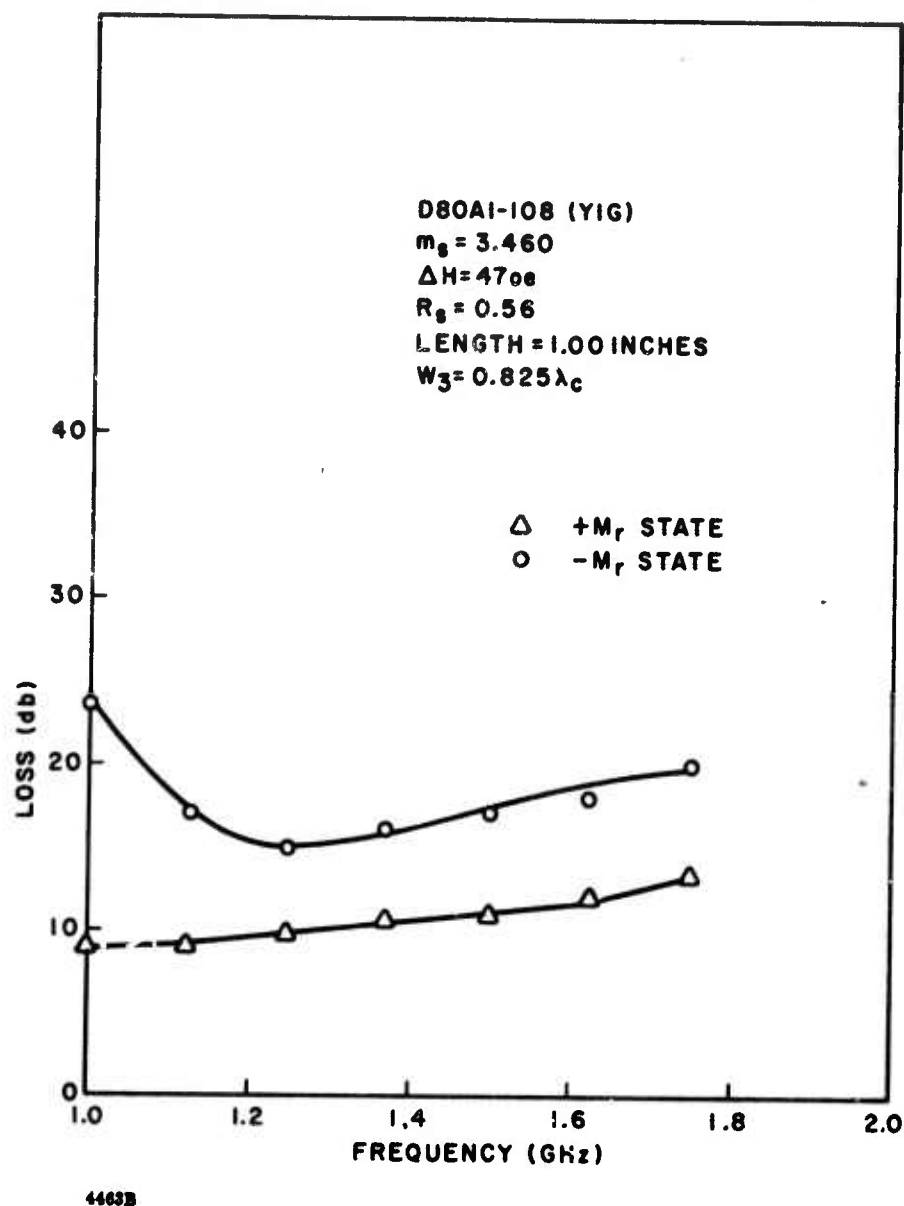
Figure 63.   Loss Dependence on Frequency of Two States of a 1-Inch
Long Toroid of YIG Operating Below ($f < f_r$) Resonance.
Cutoff type losses are still seen in the $-M_r$ state.

the (apparent) cutoff losses but did not eliminate them as was anticipated. Thus, there still existed some question as to the source of the rather large losses at the low frequency end of the band. It is seen that increasing W_3 did not noticeably affect the losses at frequencies above 1.3 GHz in the $-M_r$ state, while no change in the loss versus frequency curve is apparent in the $+M_r$ state. This is exactly what one would expect if the loss in the $-M_r$ state below 1.2 GHz was principally cutoff loss. However, one would also expect them to disappear when W_3 was increased, from 0.365λ to 0.825λ and the fact that they were still observed casts some doubt on the interpretation. The losses were everywhere too high to obtain differential phase shift measurements.

Figure 64 shows the loss of the nickel-zinc ferrite (91-3) material below resonance. The losses at 1.5 GHz ($m_s = 7.540$) are 16 db and 14 db in the $-M_r$ and $+M_r$ states. The cutoff losses in the $-M_r$ state can still be seen at the lower frequencies as well as losses associated with the main resonance at the upper end of the frequency band. Throughout the band, the losses in both states are prohibitively high making it impossible to obtain phase shift measurements.

Lowest below resonance losses were obtained using MgMn ferrite (F-83-8). The measurements are shown in Figure 65. This material, with a small intrinsic linewidth (~12 oe at X band) and an $m_s = 4.13$ (compared to $m_s = 3.46$ for YIG), had measured losses of several db less than YIG. Thus, moving the main resonance to a higher frequency by choosing a material with a larger $4\pi M_s$ reduces the loss. Unfortunately, the differential phase shift would undoubtedly also decrease.

It appears that the main problem in below resonance operation of remanent state phase shifters is the high losses. These losses apparently result from a smearing out of the main resonance in the unsaturated material. If one tries to operate too close to resonance in below resonance latching devices, the losses are too high, while operating too far below resonance would undoubtedly yield little phase shift. In either case, the loss per 360° would be very high. Possibly the below resonance approach could be used if the material were grain-oriented, for then the losses would be confined to a narrower frequency range. This possibility may be explored on another program (Contract No. AF30(603)-4121).

4.5.2.2 Measurements in a Helical Line FDPS. A helical line phase shifter on loan from Mr. D. H. Temme of MIT Lincoln Laboratories, is shown in Figure 66.
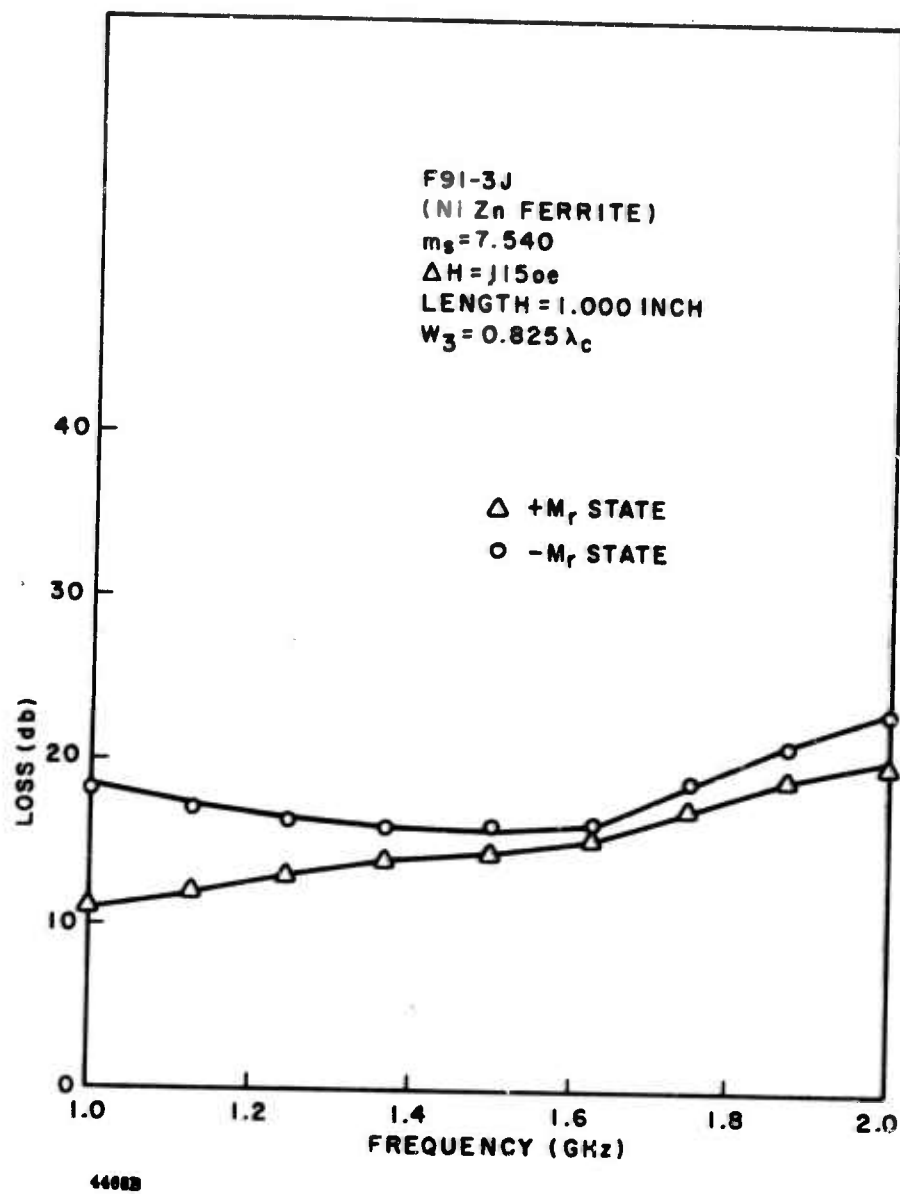
Figure 64. Loss Dependence on Frequency of Two States of a
1-Inch Long Toroid of NiZn Ferrite at $f < f_r$
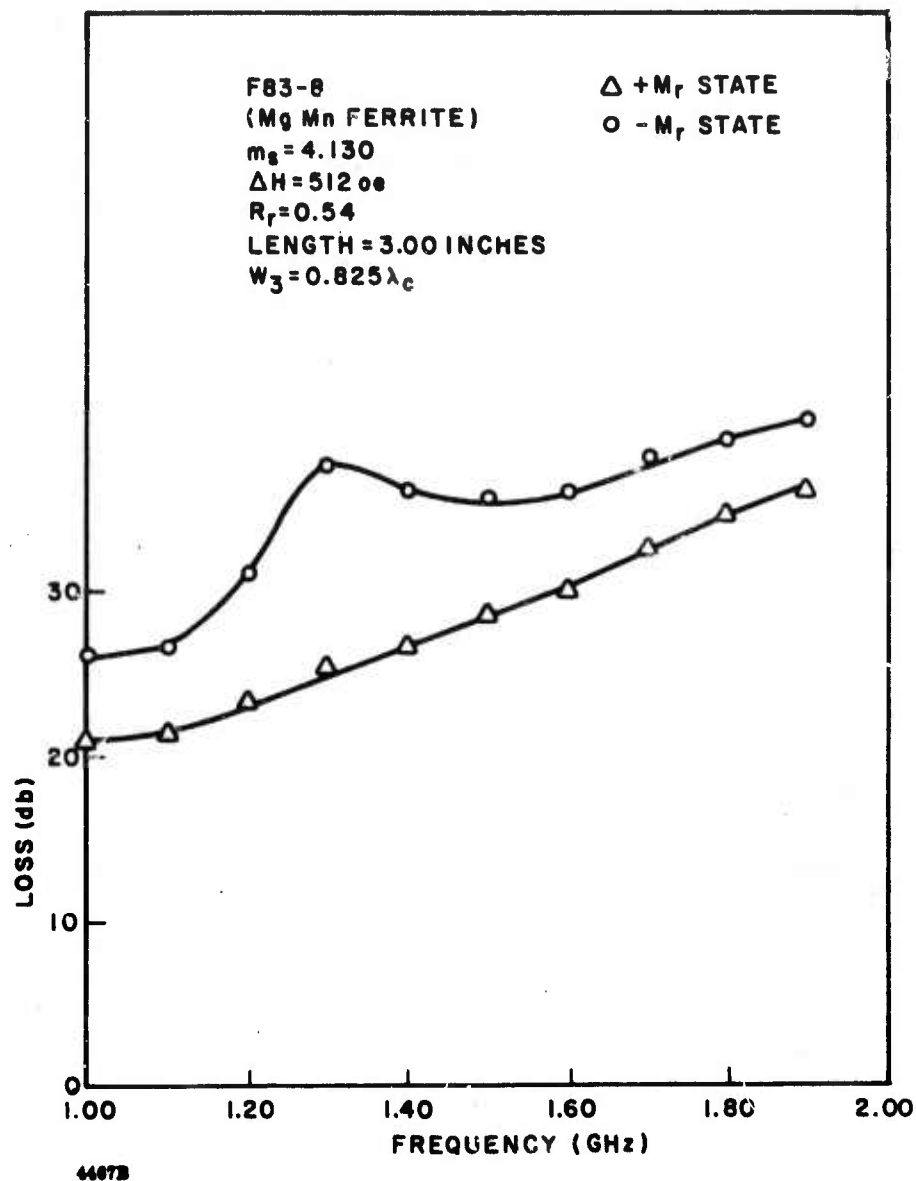
Figure 65. Loss Dependence on Frequency of Two States of a 3-Inch Long Toroid of MgMn Ferrite at $f < f_r$
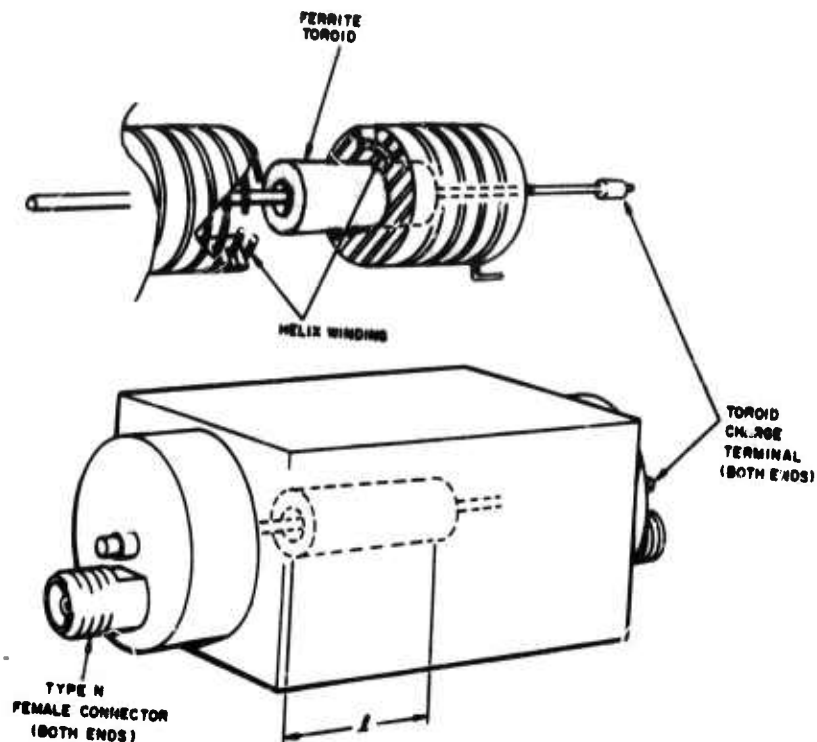
Figure 66. Helical Phase Shifter Structure used for Magnetic Loss
Measurements

A cutaway has been made to show a portion of the circuit including the helix, ferrite toroid, and the toroid charging wire. A more complete description of this device is given elsewhere.[18]   The helix line is essentially a TEM line and thus the "principal mode" experiences no cutoff phenomena such as in waveguide.

---

[18]   Final Report "Development of Helical Phase Shifters", prepared for MIT Lincoln Laboratories on Subcontract No. 250, Prime Contract No. AF19(628)-500, December 1964, Pg. 71.

Nine ferrimagnetic materials were tested in this structure from 1.0 GHz to 3 GHz, three for above resonance and six for below resonance operation. Table VII lists the microwave and square loop properties of these materials, as well as some of the test results.

In order that the relative importance of magnetic losses could be assessed, the loss of the structure, completely filled with a two-inch long dielectric toroid ($\epsilon' = 16$, $\tan \delta \approx 0.0005$), was measured and found to be quite flat with frequency at 0.70 db. Since, typically, the ferrite toroids investigated have similar dielectric properties, any measured excess in loss could be attributed to magnetic loss mechanisms except for differential losses which are due to field displacement. Thus 0.7 db is subtracted from the measured loss of a ferrite toroid to obtain its magnetic loss no matter what its length, since the two inch long structure must be filled with ferrite and/or dielectric whose dielectric (and copper) losses are unchanged. The figures which follow show the losses as they were measured while in the discussion of these figures, other losses are usually subtracted to leave only magnetic loss. In such cases, this adjustment of data is mentioned.

Figure 67 shows the loss and differential phase shift of G-238-6D (20% Al + YIG). Resonance is seen to occur below 1.0 GHz while above 1.5 GHz, the loss is flat and about 1.0 db. Differential phase shift ($\Delta \phi$) varies sinusoidally across the band. Helical lines are cyclic in nonreciprocal differential phase shift with $\Delta \phi$ a minimum at frequencies for which the electrical length, L, of the turns is $2n\lambda/4$, where n is an odd integer, and $\Delta \phi$ a maximum where $L = n\lambda/4$. Thus at 2.8 GHz, the loss is 1.0 db and the normalized phase shift is $\Delta \phi \approx 105^O$ per inch. This compares to a value of 40° per inch in the waveguide structure.

Figure 68 shows loss and phase shift of G-250-6D (25% Al + YIG). At 2.8 GHz, the loss is 0.8 db while the normalized phase shift $\Delta \phi$ is 53° per inch, compared to only 24° per inch in the waveguide.

Figure 69 shows loss and phase shift of F-115-2, a MgMnAl ferrite with a $4\pi M_s$ of 615 gauss. At 2.8 GHz, this material (with $m_s = 0.62$) was measured to have only 0.8 db total loss with a phase shift of 82 degrees per inch. When adjustments are made in the loss for the extraneous dielectric losses, and the phase shift is normalized to a remanence ratio of $R_r = 0.50$, the loss per 360° is calculated to be 1.15 db. On the other hand, the waveguide structure using G-250-6 with $m_s = 0.58$ yielded a loss

TABLE VII. HELICAL FERRITE DIFFERENTL

Sperry No.	Composition	Firing Schedule ($^{\circ}$C/hr)	$\dfrac{\rho_m}{\rho_x}$ (gm/cm^3)	$\dfrac{\text{Tan } \delta}{\epsilon^!_f}$ (X Band)	g-Fac (X Ba
G-289-6J	$3Y_2O_3 \bullet 5Fe_2O_3$	1475/5	$\dfrac{5.09}{5.17}$	$\dfrac{\leqslant 0.0005}{15.8}$	2.02
G-290-R	$3Y_2O_3 \bullet 5[0.97Fe_2O_3 \bullet 0.03Al_2O_3]$	1475/5	$\dfrac{5.10}{5.15}$	$\dfrac{\leqslant 0.0005}{15.7}$	2.01
G-404-J	$3Y_2O_3 \bullet 5[0.95Fe_2O_3 \bullet 0.05Al_2O_3]$	1475/5	$\dfrac{5.08}{5.14}$	NM	NM
G-238-6	$3Y_2O_3 \bullet 5[0.80Fe_2O_3 \bullet 0.20Al_2O_3]$	1500/5	$\dfrac{4.98}{5.04}$	$\dfrac{0.0024}{14.9}$	2.02
G-250-6	$3Y_2O_3 \bullet 5[0.75Fe_2O_3 \bullet 0.25Al_2O_3]$	1500/5	$\dfrac{4.98}{5.01}$	$\dfrac{0.0019}{14.2}$	2.03
115-2	$0.565MgO \bullet 0.063MnCo_3 \bullet 0.112Al_2O_3$	1400/7	$\dfrac{3.95}{4.30}$	$\dfrac{0.001}{11.2}$	2.01
	$0.261Fe_2O_3$				
91-3	$Ni_{0.44}Zn_{0.56}Mn_{0.02}Fe_{1.9}O_4$	1250/7	$\dfrac{5.04}{5.35}$	$\dfrac{0.0016}{13.7}$	2.13
77-3	$Ni_{0.824}Zn_{0.176}Mn_{0.02}Fe_{1.9}O_4$	1275/7	$\dfrac{5.02}{5.35}$	$\dfrac{0.015}{13.2}$	2.27
83-8	$0.58MgO \bullet 0.06MnO \bullet 0.36Fe_2O_3$	1320/7	$\dfrac{4.20}{4.39}$	$\dfrac{0.001}{12.9}$	2.13

NM - Not measured

* See Figure 66 for test configuration

$\frac{\delta}{f}$ (Band)	g-Factor (X Band)	Linewidth (X Band) (oe)	$4\pi M_s$ (gauss)	R_r	Coercive Field (oe)	$\Delta\phi$/Inch (1.2 GHz)	P_{crit} (1.35 GHz) (Watts)
0005 8	2.02	34	1780	0.81	0.40	40	--
0005 7	2.01	30	1600	0.75	0.40	50	--
	NM	NM	1325'	0.84	0.45	55	--
024 9	2.02	35	510	0.44	0.32	--	100
019 2	2.03	38	290	0.38	0.60	--	700
01 2	2.01	176	615	0.29	NM	--	--
016 7	2.13	115	3770	0.43	NM	13	--
15 2	2.27	270	3870	0.45	3.25	10	--
01 9	2.13	512	2065	0.54	2.24	21	--
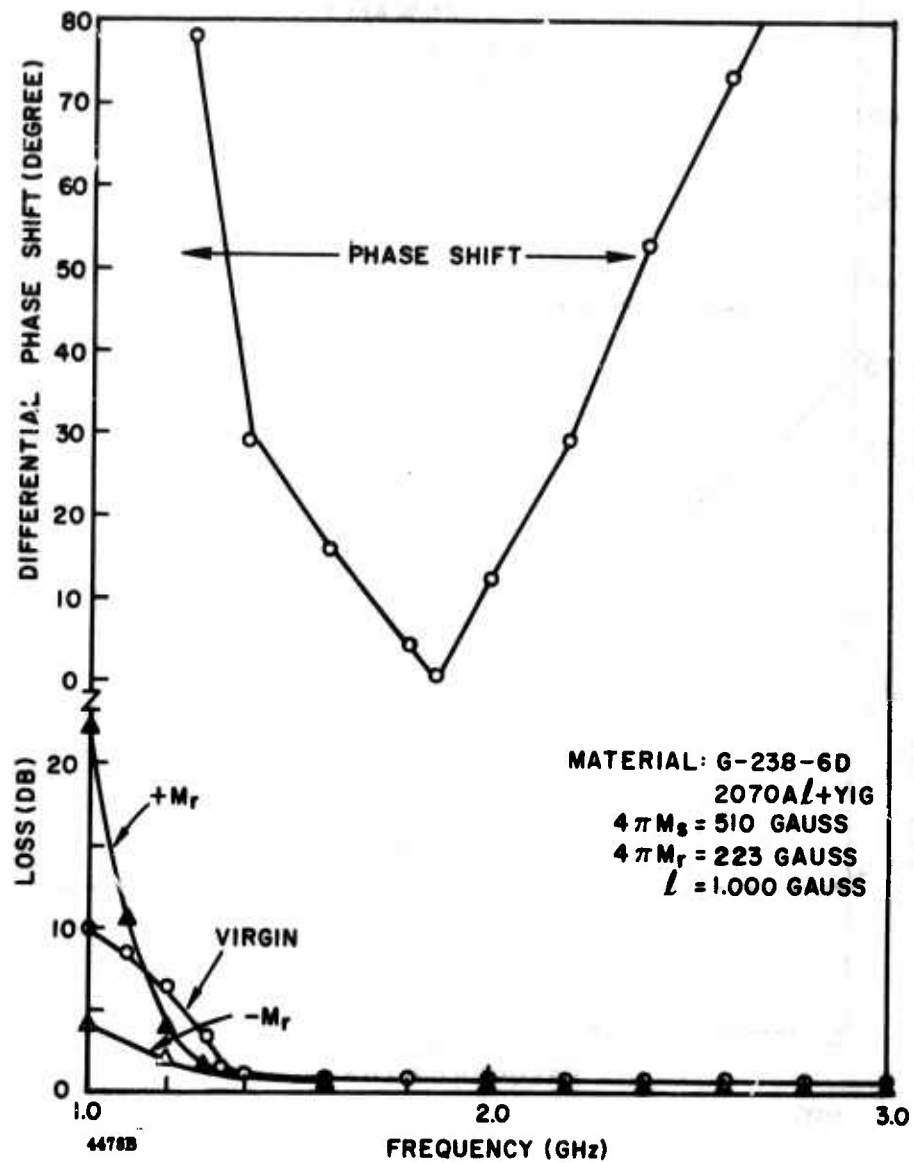
Figure 67. Loss and Differential Phase Shift of G-238-6D in the Helix Structure
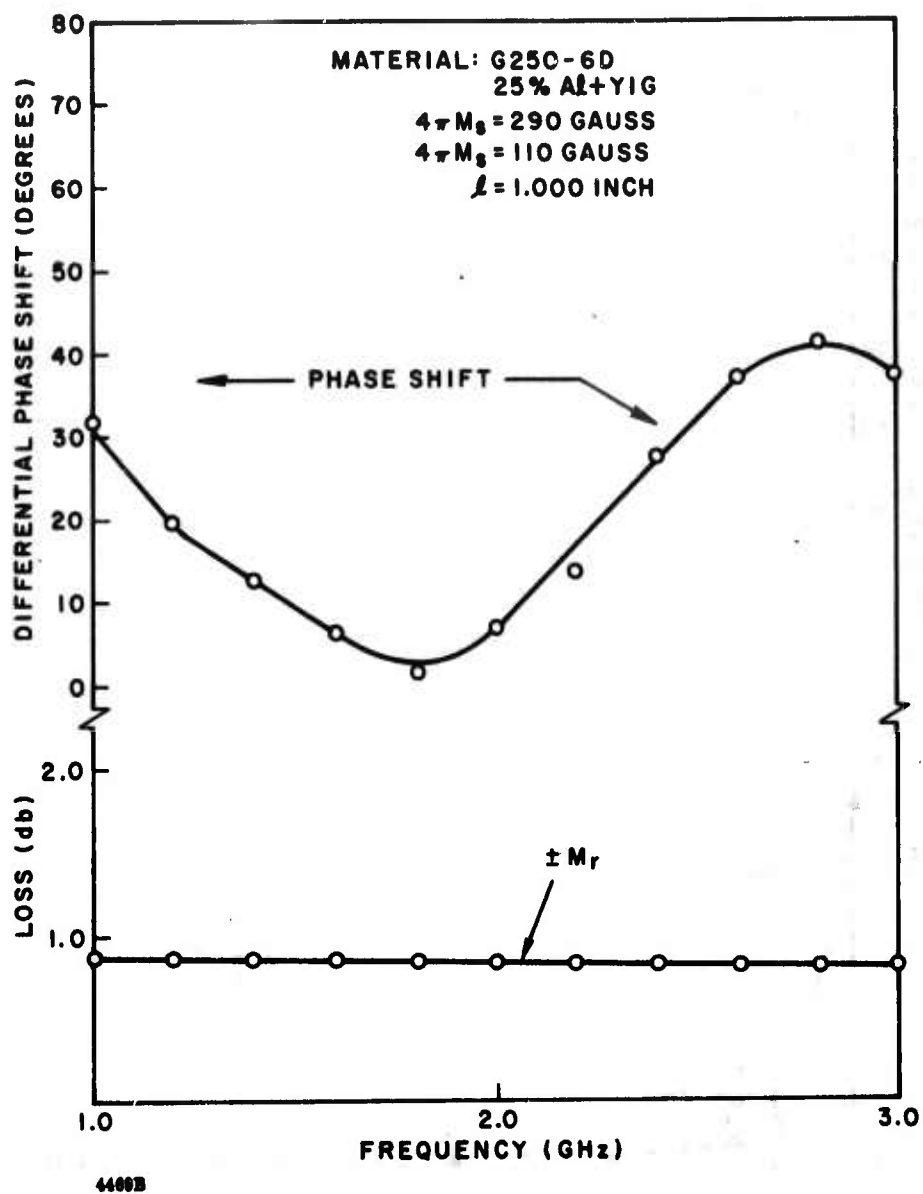
Figure 68. Loss and Differential Phase Shift of G-250-6D in the
Helix Structure
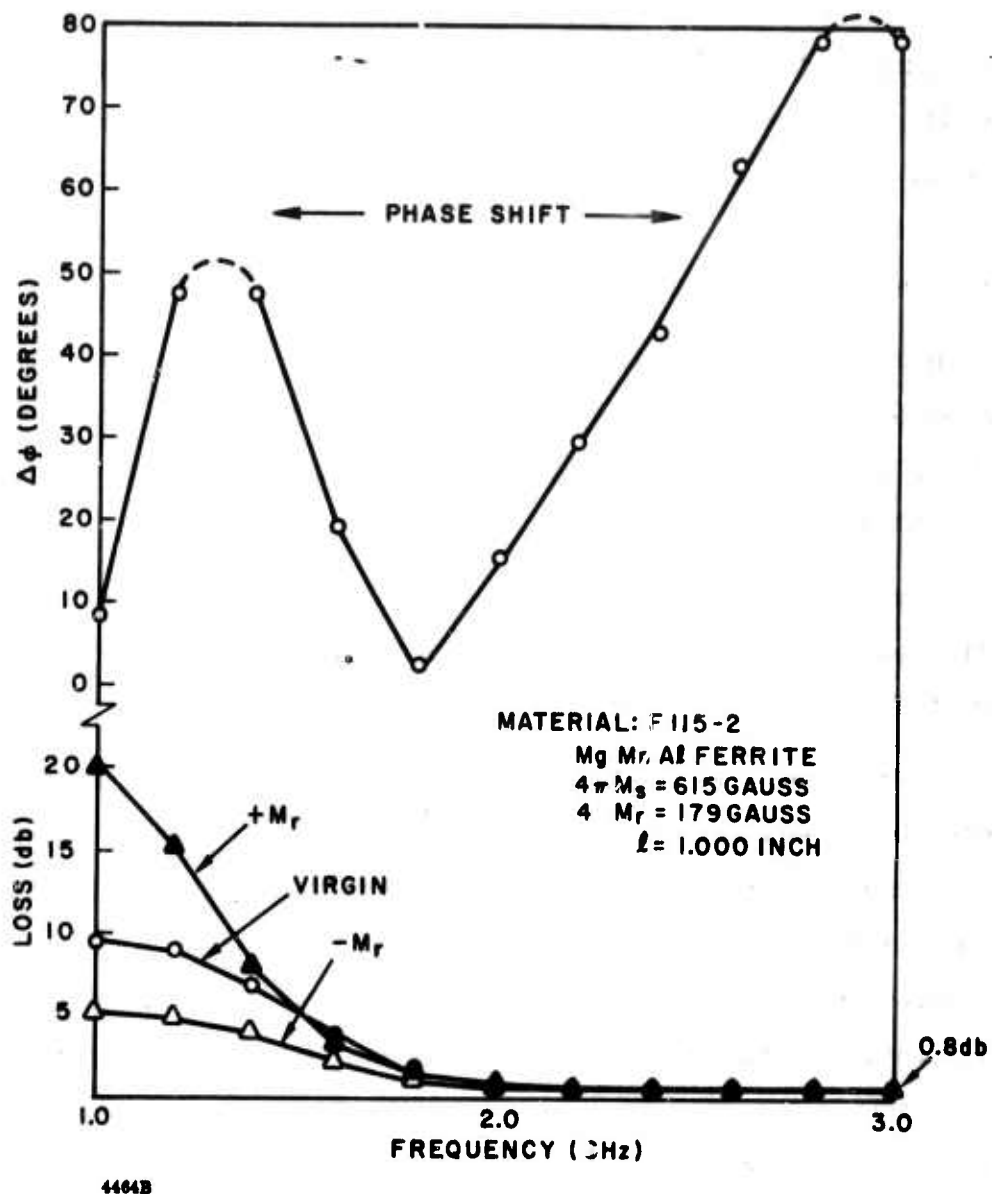
Figure 69.   Loss and Differential Phase Shift of F-115 in the Helix
Structure

per 360° of only 0.60 db. Thus, while the phase shift per inch in the waveguide was only 24°, the losses are much less than in the helix.

The remaining measurements in the helix line at low power were concerned with below resonance operation.

Figure 70 shows the magnetic loss corresponding to the two remanent states $+M_r$ and $-M_r$ in a YIG toroid ($4\pi M_s \approx 1780$ gauss). The toroid length was 0.470 inches. Resonance occurs at about 2400 MHz and 2500 MHz in the two states, respectively. The increases in loss seen at 3800 MHz and the scattering of the data points near resonance cannot be explained at this time but may be due to structural anomalies.

Figure 71 shows the losses corresponding to $+M_r$ and $-M_r$ in a 1-inch long sample of 3 percent aluminum substituted YIG ($4\pi M_s \approx 1600$). The material resonates at '2050 MHz and 2200 MHz respectively in the two states, and the losses decrease smoothly to about 2 db at 3800 MHz.

Figure 72 shows the $+M_r$ and $-M_r$ losses for a 1-inch long toroid made from 5 percent aluminum substituted YIG with a $4\pi M_s \approx 1325$ gauss. The resonance frequencies are 2000 MHz and 1950 MHz respectively.

In both Figures 71 and 72, it is clearly seen that the losses designated $+M_r$ are greater than those designated $-M_r$ at resonance but, at frequencies below resonance, they cross and the $-M_r$ losses are greater than the $+M_r$ losses. The $+M_r$ line is seen to tail out more gradually at the high frequency side of resonance, while the $-M_r$ line tails out more gradually at the low frequency side. This basic difference in the shapes of the resonance lines may be related to the difference in the effective permeability of the two remanent states. The effective permeability corresponding to $+M_r$ and $-M_r$ would be expected to give rise to different degrees of loading in the structure.
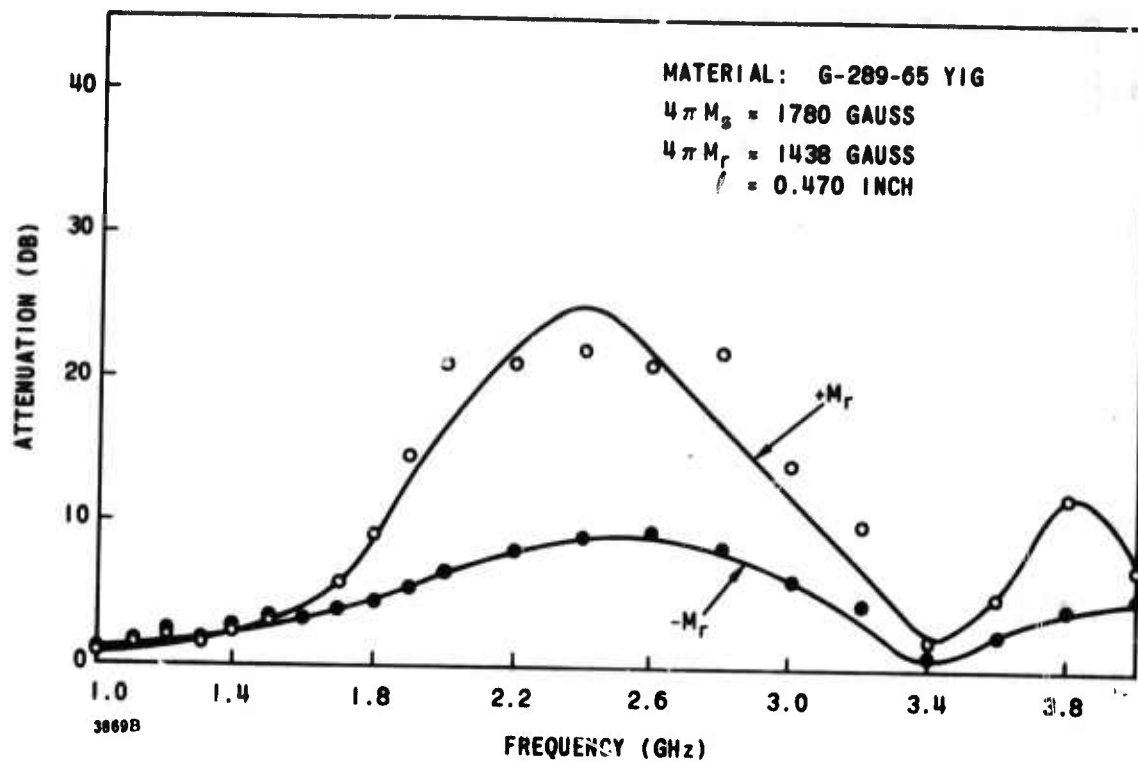
Figure 70. Magnetic Loss Versus Frequency for G-289-6J in the Helix Structure
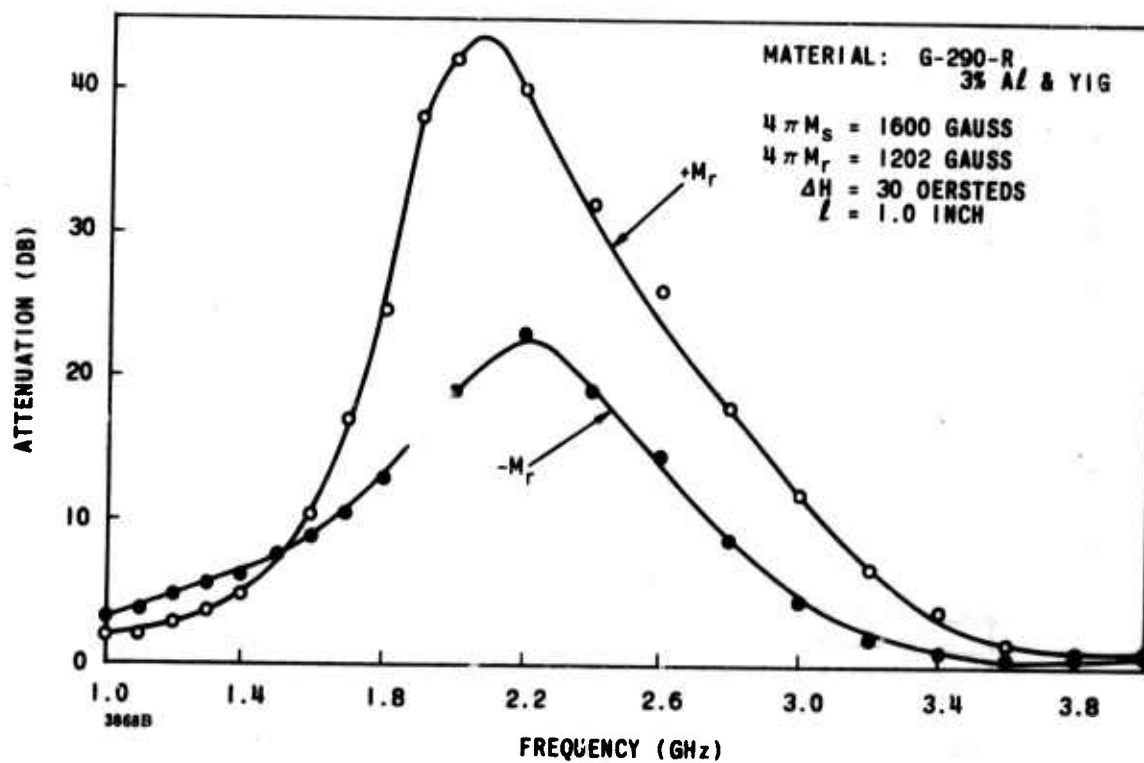
Figure 71. Magnetic Loss Versus Frequency for G-290-R in the Helix Structure

4-103
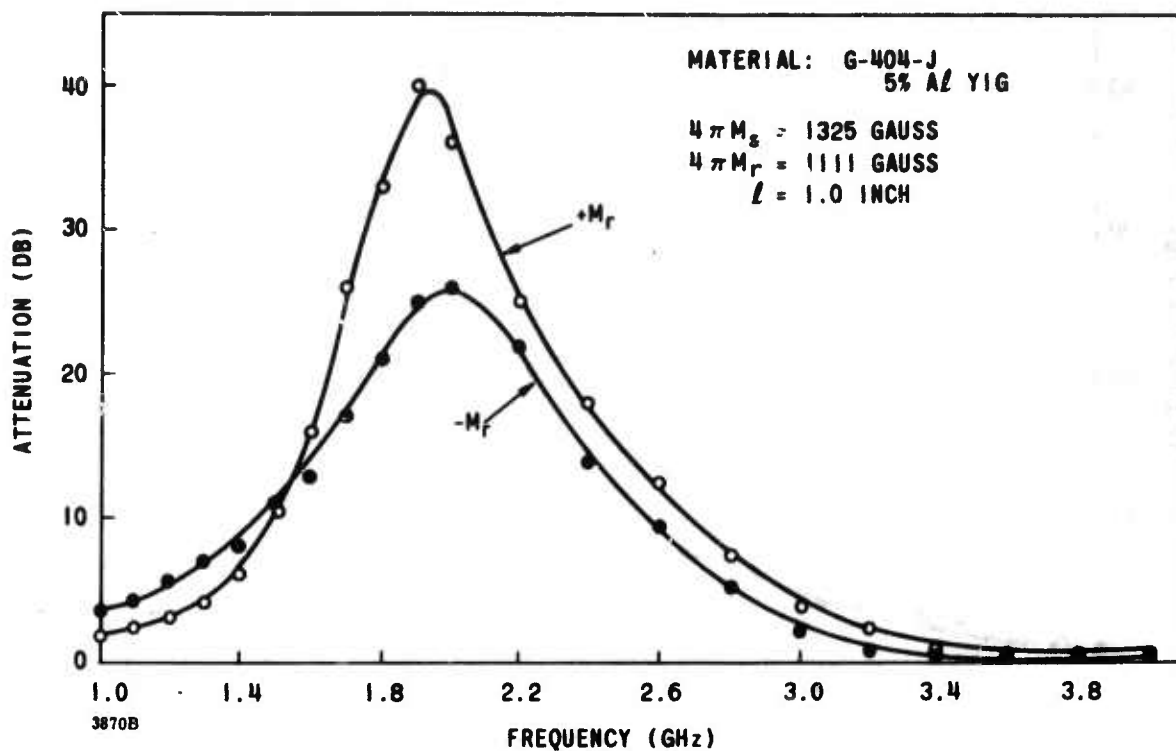
Figure 72. Magnetic Loss Versus Frequency for G-404-J in the Helix Structure
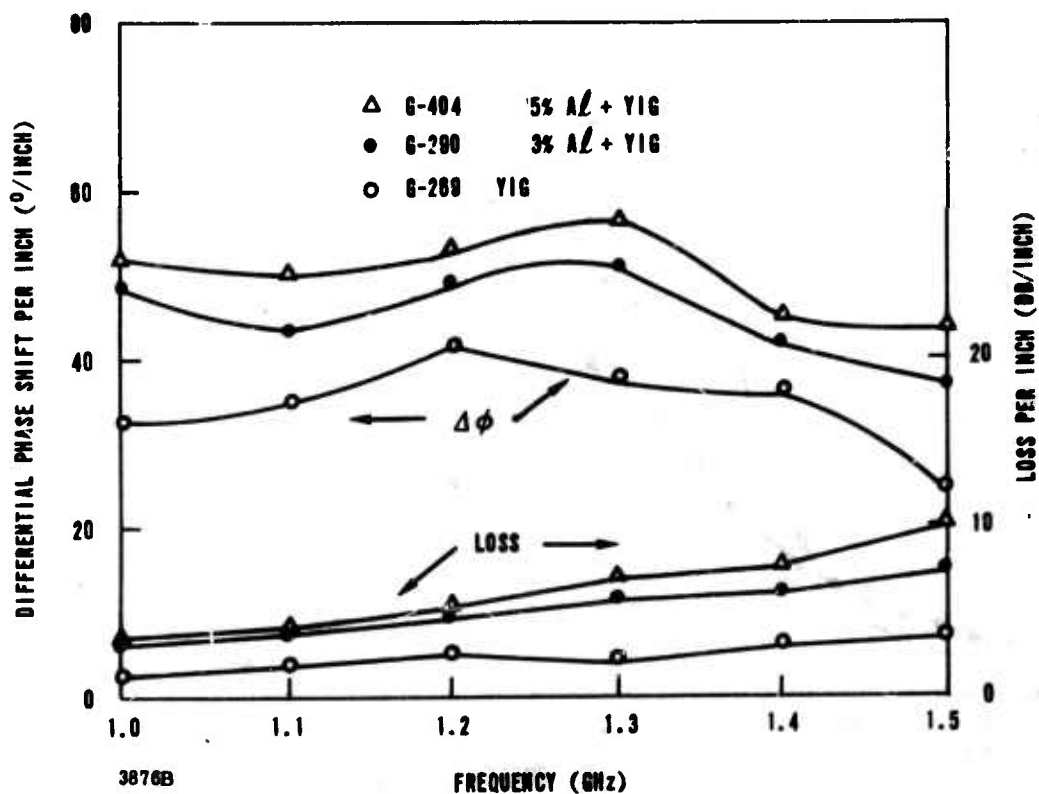
Figure 73. Differential Phase Shift and Loss Versus Frequency in the Helix Structure

Figure 73 shows the below resonance (frequency) nonreciprocal differential phase shift per inch measured on the three materials, YIG, 3 percent aluminum substituted YIG, and 5 percent aluminum substituted YIG (G-239, G-290, and G-404, respectively). The losses shown are those corresponding to the $-M_r$ state which is the maximum loss over this frequency range. The respective phase shifts of these materials are seen to be roughly 40 degrees/inch, 50 degrees/inch, and 55 degrees/ inch. Whether this differential phase shift is due to differences in the field displacements associated with $+M_r$ and $-M_r$, which is the usual cause, or to possible differences in H_1 is not clear at this time. It should also be noted that the measured differential phase shift here decreases with increasing magnetization. This may follow from the fact that differential phase shift in this mode of operation depends on the proximity of the resonance frequency to the operating frequency, and the resonance frequency in turn is a function of $4\pi M_s$.

The observed slight decrease in phase shift with increasing frequency is probably connected with the fact that maximum nonreciprocal phase shift in a helix structure occurs when the length of the helix turns is an odd multiple of $\lambda/4$. Since the length of the helix turns in this case was chosen to be $3\lambda/4$ at 3000 MHz, then maxima in the nonreciprocal phase shift should occur at 1000 MHz, 3000 MHz, 5000 MHz, etc., while minima should occur at 2000 MHz, 4000 MHz, etc. Thus, phase shift due solely to the helix should decrease with frequency from 1000 MHz to 2000 MHz. This decrease is, of course, offset to some extent by the increase that occurs as the resonance in the material is approached. The cyclic variation in phase shift is felt to be due to dimensional effects.

Figures 74, 75, and 76 show loss and phase shift versus frequency of three different ferrite materials in the helix structure. These materials, with generally much higher magnetization than the three garnet materials just reported, exhibited considerably less differential phase shift over the 1.0 to 1.5 GHz range than did the garnets. The last column of Table VII lists the phase shift per inch of the six materials tested. It is seen that $\Delta \phi$ varied from a maximum of 55 degrees per inch for the G-404 material ($4\pi M_s = 1325$ gauss) to a minimum of 10 degrees per inch for the F-77-3 material ($4\pi M_s = 3820$ gauss). No attempt was made to adjust the data to account for variations in remanence ratio or dielectric constant which must somehow affect the results; nevertheless, it seems safe to say that since the phase shift per inch decreased as the $4\pi M_s$ is increased, the differential phase shift below resonance is inversely related to the ratio of $4\pi M_s$ to the operating frequency. One would want then to operate as close to resonance as losses would permit in this below resonance operation. This is, of course, also the case in above resonance operation.

In this mode of operation ($f < f_r$), the differential phase shift apparently decreases much more rapidly than does the loss with separation from the resonance frequency (and also more rapidly than it does above resonance). Thus, well below resonance, where magnetic losses become tolerable, the differential phase shift is insignificant. It appears, therefore, that unless something can be done to permit operating much closer to the main resonance, such as by grain-orienting the material, below resonance operation will probably not be feasible in any latching device whose performance depends on a reasonably large ratio of differential phase shift to loss.

4.5.3 High Power Characteristics of FDPS

4.5.3.1 <u>Waveguide Measurements</u>. The conclusions drawn from the discussion of peak power effects in remanent state ferrites (paragraph 3.2.2) are that the peak power handling capacity of a material at a given frequency can be increased by increasing the spinwave linewidth ΔH_k (perhaps by rare earth doping) or by increasing the saturation magnetization (perhaps by aluminum doping). With these conclusions as a guide, materials have been selected for evaluation which should lead to a good understanding of the material properties required for obtaining high peak power thresholds in L, S, C and X bands. Tables V and VIII provide a list of high power data on a

4-106
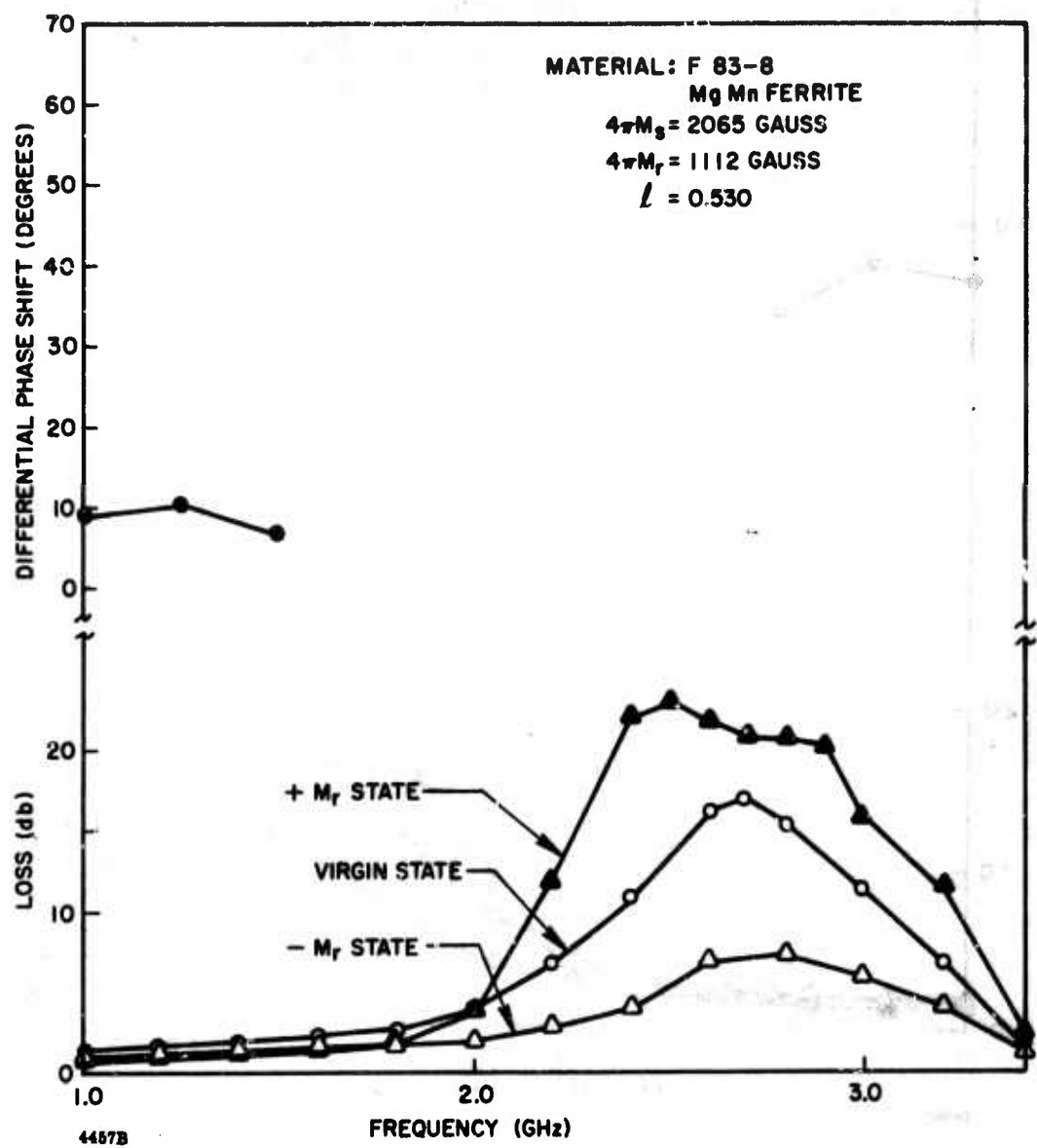
Figure 74.   Loss and Phase Shift Vs Frequency for
F-83-8 in the Helix Structure
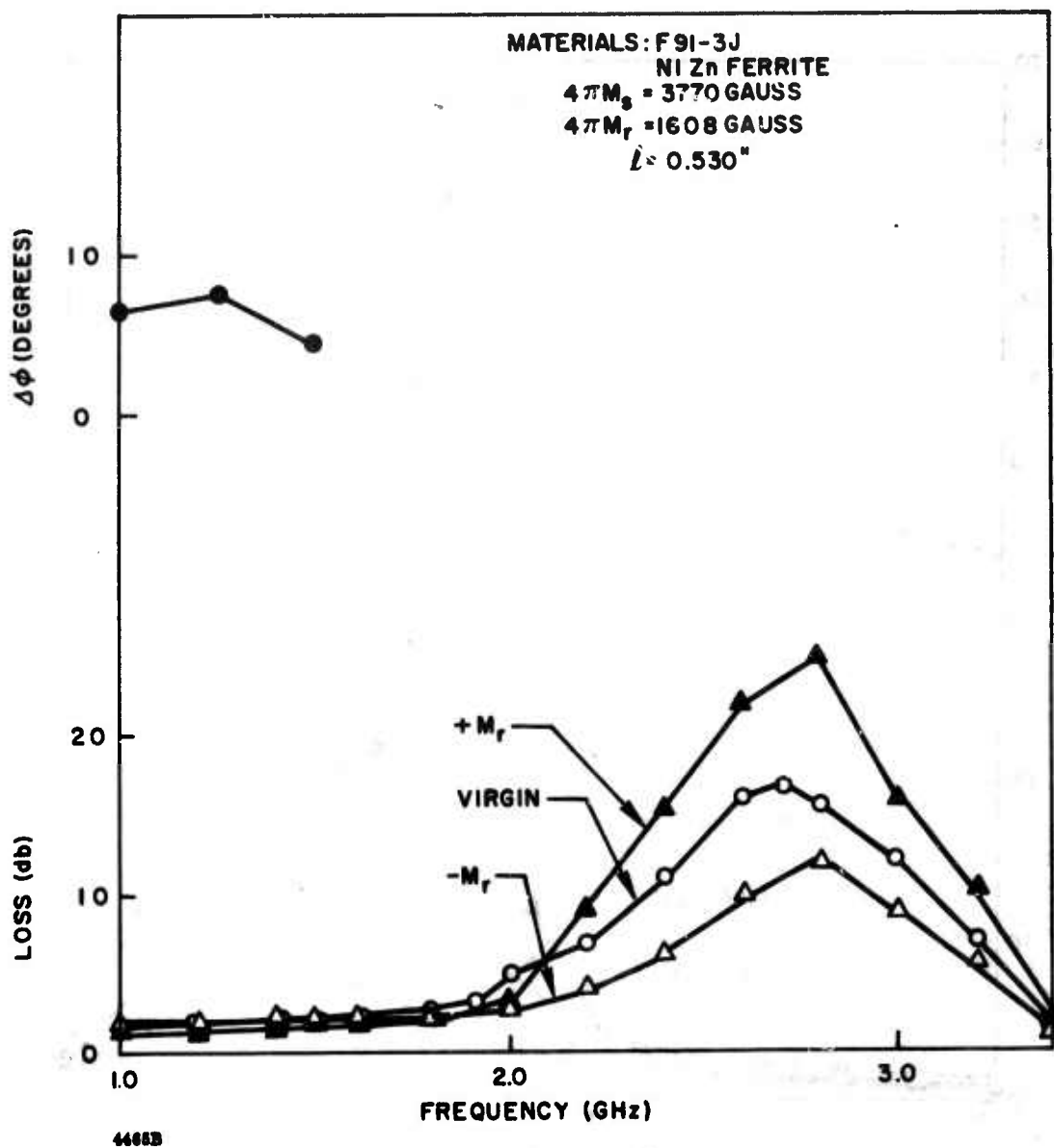
Figure 75.   Loss and Phase Shift Vs Frequency for
             F-91-3J in the Helix Structure
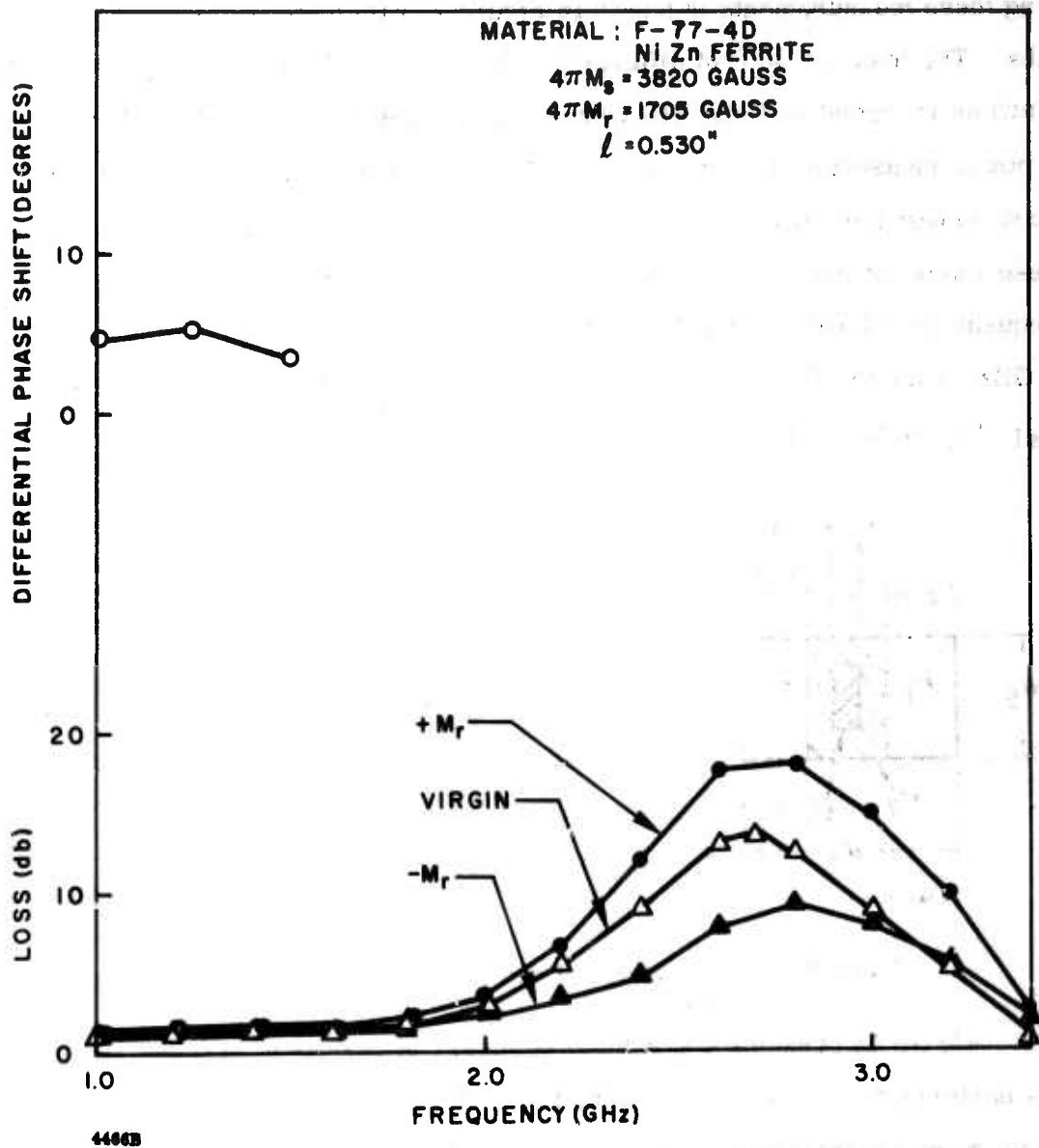
Figure 76. Loss and Phase Shift Vs Frequency of
F-77-4D in the Helix Structure

4468B

number of materials tested in X, C, and S bands. The tables also give microwave and square loop properties of the materials listed and low power phase shifter performance data on the material. The configuration used in the testing is also shown in the tables.

Table VIII contains both X and C band results. The configuration used in making these measurements is shown in Figure 77 with dimensions given in wavelengths. The loss per 360° of differential phase shift and differential phase shift per inch as recorded in Table VIII were measured either at 6.0 GHz or 5.65 GHz. High power measurements were made at three frequencies in each band in some instances to test the frequency dependence of h_{crit} without changing $4\pi M_s$ or structure. In these cases the normalized saturation magnetizations m_{s1}, m_{s2}, and m_{s3} correspond to frequencies 8.5 GHz, 9.0 GHz, and 9.5 GHz, respectively, in X band, and 5.4 GHz, 5.65 GHz, and 5.9 GHz, respectively, in C band. P_{c1} refers to the threshold power level at m_{s1}, P_{c2} at m_{s2}, etc.
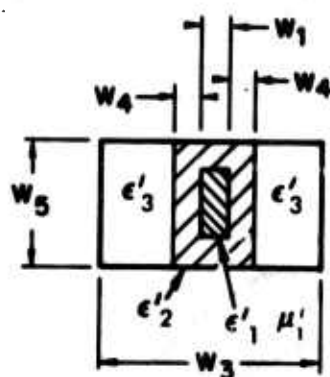
$$W_1 = 0.025\lambda_c \qquad \epsilon_1' = 16$$
$$W_3 = 0.365\lambda_c \qquad \epsilon_2' = \epsilon_f'$$
$$W_4 = 0.045\lambda_c \qquad \epsilon_3' = 1$$
$$W_5 = 0.280\lambda_c \qquad m_s = \gamma 4\pi M_s / f_c$$
$$\mu_1' = 1$$

3862B-1

Figure 77. Configuration Used in Obtaining Experimental Data in Table VIII

Figure 78 presents a graphical summary of results of high power measurements performed on a variety of materials and at X, C, and S bands. The left-hand ordinate gives the threshold values of the rf magnetic field, h_{crit}. These values were calculated from the measured threshold power levels. The two right-hand ordinates specify the corresponding threshold power levels in S and X bands. These threshold power levels are the calculated values of peak power levels required to generate the given rf critical field values in a typical waveguide nonreciprocal phase shifter.

TABLE VIII.   X BAND (8.0 - 10.0 GHz) AND C B...

Sperry No.	Composition	Firing Schedule (°C/hr)	$\frac{\rho_m}{\rho_x}$	$\frac{\tan\delta}{\epsilon'}$ (X Band)	g-Factor (X Band)	Linewidth (X Band) (oe)	$4\pi M_s$ (gauss)	R_r	Co... F... (oe...
16-20	$Ni_{1.0}Mn_{0.02}Fe_{1.9}O_4$	1400/7	$\frac{4.86}{5.35}$	$\frac{0.010}{12.6}$	2.44	520	2815	0.48	4.
78-4	$Ni_{0.97}Zn_{0.03}Mn_{0.02}Fe_{1.9}O_4$	1275/7	$\frac{4.92}{5.35}$	$\frac{0.006}{12.7}$	2.38	485	2965	0.57	6.
77-3	$Ni_{0.824}Zn_{0.176}Mn_{0.02}Fe_{1.9}O_4$	1275/7	$\frac{5.02}{5.35}$	$\frac{0.015}{13.2}$	2.27	270	3820	0.65	3.
91-3	$Ni_{0.44}Zn_{0.56}Mn_{0.02}Fe_{1.9}O_4$	1250/7	$\frac{5.04}{5.35}$	$\frac{0.0016}{13.7}$	2.13	115	3770	0.67	0.
61-4	$Ni_{0.325}Zn_{0.675}Mn_{0.02}Fe_{1.9}O_4$	1250/7	$\frac{5.13}{5.35}$	$\frac{0.001}{14.9}$	2.07	107	2770	0.37	0.
83-8	$0.58MgO\bullet0.06MnO\bullet0.36Fe_2O_3$	1320/7	$\frac{4.20}{4.39}$	$\frac{0.001}{12.9}$	2.13	512	2065	0.67	2.
121-3	$0.87Mg\bullet0.04Mn\bullet0.10Cu\bullet$ $0.03Co\bullet0.27Al\bullet1.48Fe\bullet4O$	1400/7	$\frac{4.29}{4.50}$	$\frac{0.002}{12.7}$	2.05	266	1440	0.35	2.
65-28	$0.516MgO\bullet0.057MnCO_3\bullet$ $0.091Al_2O_3\bullet366Fe_2O_3$	1400/7	$\frac{4.05}{4.40}$	$\frac{0.001}{11.7}$	2.02	140	1190	0.57	1.
115-2	$0.565MgO\bullet0.063MnCO_3\bullet$ $0.112Al_2O_3\bullet0.261Fe_2O_3$	1400/7	$\frac{3.95}{4.30}$	$\frac{0.001}{11.2}$	2.01	176	615	0.28	0.7
18-8	$Ni_{0.975}Co_{0.025}Mn_{0.2}Fe_{1.9}O_4$	1275/7	$\frac{4.80}{5.30}$	$\frac{NM}{NM}$	2.23	375	2865	0.41	11.
50-3	$Ni_{0.965}Co_{0.035}Mn_{0.02}Fe_{1.9}O_4$	1250/7	$\frac{4.86}{5.30}$	$\frac{NM}{NM}$	2.37	349	2970	0.39	10.
147-1	$Ni_{0.950}Co_{0.050}Mn_{0.02}Fe_{1.9}O_4$	1250/7	$\frac{4.87}{5.30}$	$\frac{0.009}{12.5}$	2.35	625	NM	NM	NM
64-4	$Li_{1.0}Fe_5O_8$	1250/7	$\frac{4.34}{4.75}$	$\frac{>0.01}{NM}$	2.23	595	3365	0.71	2.0
D80A1-108	$3Y_2O_3\bullet5Fe_2O_3$	1475/5	$\frac{5.08}{5.17}$	$\frac{0.0004}{15.8}$	2.02	47	1730	0.67	0.8
D80A2-1-14	$3[0.85Y_2O_3\bullet0.15Gd_2O_3]\bullet$ $5Fe_2O_3$	1475/5	$\frac{5.30}{5.38}$	$\frac{0.0005}{16.0}$	2.02	47	1525	0.73	0.85
D80A2-2-10	$3[0.70Y_2O_3\bullet0.30Gd_2O_3]\bullet$ $5Fe_2O_3$	1475/5	$\frac{5.50}{5.56}$	$\frac{0.0005}{16.2}$	2.02	66	1285	0.70	1.05

* See Figure 77 for Test Configuration
** Corrected for xfmrs (loss of xfmrs ≈ 0.10 db)
NM - Not measured

R_r	Coercive Field (oe)(60~)	m_{s_1}	$P_{C_{1 (kw)}}$ / $h_{c_{1(oe)}}$	m_{s_2}	$P_{C_{2 (kw)}}$ / $h_{c_{2 (oe)}}$	m_{s_3}	$P_{C_{3 (kw)}}$ / $h_{c_{3 (oe)}}$	Loss/360° [**] (db/360°)	Δφ/Inch (degrees/inch)	Configuration
0.48	4.75	1.25	NM	1.13	NM	1.11	NM	>10 db 8.0 to 10 GHz		(X Band)
0.57	6.50	1.26	NM	1.14	NM	1.13	NM	>10 db 8.0 to 10 GHz		(X Band)
0.65	3.50	1.52	NM	1.38	NM	1.36	NM	>10 db 8.0 to 10 GHz		(X Band)
0.67	0.55	1.40	NM	1.27	NM	1.25	NM	>30 db 8.0 to 10 GHz		(X Band)
0.37	0.35	0.99	NM	0.89	17 / 37.5	0.88	NM	---	---	(X Band)
0.67	2.25	0.74	NM	0.69	3 / 15.8	0.68	NM	0.45	101	(X Band)
0.35	2.22	0.51	NM	0.46	≥150 / >115	0.46	NM	2.35	85	(X Band)
0.57	1.11	0.43	NM	0.38	33 / 53	0.37	NM	0.52	64	(X Band)
0.28	0.71	0.22	NM	0.20	≥150 / >115	0.20	NM	1.35	43	(X Band)
0.41	11.54	0.12	NM	0.10	NM	0.10	NM	>10 db 8.0 to 10 GHz		(X Band)
0.39	10.3	1.26	NM	1.15	NM	1.13	NM	NM	NM	(X Band)
NM	NM	NM	NM	NM	NM	NM	NM	NM	NM	(X Band)
0.71	2.00	1.35	NM	1.23	NM	1.21	NM	>30 db 8.0 to 10 GHz		(X Band)
0.67	0.80	0.586	NM	0.540	NM	0.535	NM	0.45	80	(X Band)
0.73	0.85	0.515	NM	0.466	6.8 / 23.8	0.461	NM	0.75	78	(X Band)
0.70	1.05	0.432	NM	0.391	32 / 52	0.385	NM	0.85	65	(X Band)

TABLE VIII. X BAND (8.0 - 10.0 GHz) AND C BAND (5.

Sperry No.	Composition	Firing Schedule (°C/hr)	$\frac{\rho_m}{\rho_x}$	$\frac{Tan\,\delta}{\epsilon'}$ (X Band)	g-factor (X Band)	Linewidth (X Band) (oe)	$4\pi M_s$ (gauss)	R_r	Coercive Field (oe)(6
D80A2-3-7	$3[0.55Y_2O_3 \bullet 0.45Gd_2O_3] \bullet 5Fe_2O_3$	1475/5	5.69 / 5.76	0.0001 / 16.5	2.02	69	1025	0.34	1.80
D80A2-4-10	$3[0.40Y_2O_3 \bullet 0.60Gd_2O_3] \bullet 5Fe_2O_3$	1475/5	5.85 / 5.95	0.0006 / 16.3	2.05	220	716	0.30	2.20
G-129-4	$3[0.98Y_2O_3 \bullet 0.02Dy_2O_3] \bullet 5Fe_2O_3$	1475/5	5.14 / 5.20	0.0004 / 16.0	1.99	91	1780	0.73	0.60
G-351-4	$3[0.95Y_2O_3 \bullet 0.05Dy_2O_3] \bullet 5Fe_2O_3$	1475/5	5.18 / 5.32	0.0016 / 16.0	1.96	168	1730	0.70	0.63
G-131-3	$3[0.90Y_2O_3 \bullet 0.10Dy_2O_3] \bullet 5Fe_2O_3$	1475/5	5.26 / 5.25	0.0010 / 16.1	1.88	295	1755	0.61	0.64
G-243-5Y	$3Y_2O_3 \bullet 5[0.90Fe_2O_3 \bullet 0.10Al_2O_3]$	1475/5	5.02 / 5.10	0.0001 / 15.2	2.01	35	960	0.61	0.70
G-291-2F	$3Y_2O_3 \bullet 5[0.92Fe_2O_3 \bullet 0.08Al_2O_3]$	1475/5	5.00 / 5.12	0.0001 / 15.3	2.02	55	1140	0.54	0.87
G-292-2C	$3Y_2O_3 \bullet 5[0.88Fe_2O_3 \bullet 0.12Al_2O_5]$	1475/5	4.91 / 5.09	0.0001 / 14.7	2.01	47	867	0.38	1.21
G-232-73C	$3Y_2O_3 \bullet 5Fe_2O_3$	1475/5	5.10 / 5.17	0.0001 / 16	NM	NM	1780	0.71	0.49
G-404-3C	$3Y_2O_3 \bullet [0.95Fe_2O_3 \bullet 0.05Al_2O_3]$	1475/5	5.08 / 5.14	0.0001 / 15.5	2.02	55	1325	0.42	0.85
16-20	$Ni_{1.0}Mn_{0.02}Fe_{1.9}O_4$	1400/7	4.86 / 5.35	0.010 / 12.6	2.44	520	2815	0.44	5.00
78-4	$Ni_{0.97}Zn_{0.03}Mn_{0.02}Fe_{1.9}O_4$	1275/7	4.92 / 5.35	0.006 / 12.7	2.38	485	2965	0.47	6.85
77-3	$Ni_{0.824}Zn_{0.176}Mn_{0.02}Fe_{1.9}O_4$	1275/7	5.02 / 5.35	0.015 / 13.2	2.27	270	3820	0.54	4.00
91-3	$Ni_{0.44}Zn_{0.56}Mn_{0.02}Fe_{1.9}O_4$	1250/7	5.04 / 5.35	0.0016 / 13.7	2.13	115	3770	0.57	0.70

* See Figure 77 for Test Configuration
** Corrected for xfmrs (loss of xfmrs ≈ 0.10 db)
NM - Not measured

R_r	Coercive Field (oe)(60~)	m_{s_1}	$P_{C_{1(kw)}}$ / $h_{c_{1(oe)}}$	m_{s_2}	$P_{C_{2(kw)}}$ / $h_{c_{2(oe)}}$	m_{s_3}	$P_{C_{3(kw)}}$ / $h_{c_{3(oe)}}$	Loss/360° (db/360°)[**]	Δφ/Inch (degrees/inch)	Configuration
.34	1.80	0.346	NM	0.313	$\frac{110}{96}$	0.309	NM	0.80	80	(X Band)
.30	2.20	0.245	NM	0.222	$\frac{>188}{>125}$	0.219	NM	1.15	52	(X Band)
.73	0.60	0.588	NM	0.533	$\frac{45}{61}$	0.526	NM	1.25	92	(X Band)
.70	0.63	0.573	NM	0.518	$\frac{>150}{>110}$	0.513	NM	2.60	96	(X Band)
.61	0.64	0.546	NM	0.494	NM	0.488	NM	3.70	90	(X Band)
.61	0.70	0.319	$\frac{7.5}{25.5}$	0.288	$\frac{6}{27.5}$	0.285	$\frac{9.0}{28.8}$	---	----	(X Band)
.54	0.87	0.389	$\frac{3.5}{16.2}$	0.366	$\frac{4.8}{19.3}$	0.348	$\frac{5.2}{20.4}$	---	----	(X Band)
.38	1.21	0.298	$\frac{25}{42}$	0.269	$\frac{>150}{>109}$	0.267	NM	---	----	(X Band)
.71	0.49	0.586	NM	0.540	$\frac{1.50}{11.6}$	0.535	NM	---	----	(X Band)
.42	0.85	0.446	---	0.405	$\frac{2.5}{15.0}$	0.399	---	---	----	--- (X Band)
.44	5.00	1.96	NM	1.88	NM	1.80	NM	>30 db 4.5 to	6.5 GHz	(C Band)
.47	6.85	1.83	NM	1.75	NM	1.67	NM	>30 db 4.5 to	6.5 GHz	(C Band)
.54	4.00	2.40	NM	2.29	NM	2.20	NM	>30 db 4.5 to	6.5 GHz	(C Band)
.57	0.70	2.20	NM	2.11	NM	2.03	NM	>30 db 4.5 to	6.5 GHz	(C Band)

TABLE VIII. X BAND (8.0 - 10.0 GHz) AND C BAND

Sperry No.	Composition	Firing Schedule (°C/hr)	$\frac{\rho_m}{\rho_x}$	$\frac{\text{Tan } \delta}{\epsilon'}$ (X Band)	g-Factor (X Band)	Linewidth (X Band) (oe)	$4\pi M_s$ (gauss)	R_r	C (o
61-4	$Ni_{0.325}Zn_{0.675}Mn_{0.02}Fe_{1.9}O_4$	1250/7	$\frac{5.13}{5.35}$	$\frac{0.001}{14.9}$	2.07	107	2770	0.49	0
83-8	$0.58MgO \bullet 0.06MnO \bullet$ $0.36Fe_2O_3$	1320/7	$\frac{4.20}{4.39}$	$\frac{0.001}{12.9}$	2.13	512	2065	0.67	2
121-3	$0.87Mg \bullet 0.04Mn \bullet 0.10Cu \bullet$ $0.03Co \bullet 0.27Al \bullet 1.48Fe \bullet 4O$	1400/7	$\frac{4.29}{4.50}$	$\frac{0.002}{12.7}$	2.05	266	1440	0.34	2
65-28	$0.516MgO \bullet 0.057MnCo_3 \bullet$ $0.091Al_2O_3 \bullet 366Fe_2O_3$	1400/7	$\frac{4.05}{4.40}$	$\frac{0.001}{11.7}$	2.02	140	1190	0.57	1
115-2	$0.565MgO \bullet 0.063MnCo_3 \bullet$ $0.112Al_2O_3 \bullet 0.261Fe_2O_3$	1400/7	$\frac{3.95}{4.30}$	$\frac{0.001}{11.2}$	2.01	176	615	0.27	0.
18-8	$Ni_{0.975}Co_{0.025}Mn_{0.02}Fe_{1.9}O_4$	1275/7	$\frac{4.80}{5.30}$	$\frac{NM}{NM}$	2.23	375	2865	0.22	8.
50-3	$Ni_{0.965}Co_{0.035}Mn_{0.02}Fe_{1.9}O_4$	1250/7	$\frac{4.86}{5.30}$	$\frac{NM}{NM}$	2.37	349	2970	0.16	7.
147-1	$Ni_{0.950}Co_{0.050}Mn_{0.02}Fe_{1.9}O_4$	1250/7	$\frac{4.87}{5.30}$	$\frac{0.009}{12.5}$	2.35	625	NM	NM	NI
64-4	$Li_{1.0}Fe_5O_8$	1250/7	$\frac{4.34}{4.75}$	$\frac{>0.01}{NM}$	2.23	595	3365	0.53	2.
D80A1-108	$3Y_2O_3 \bullet 5Fe_2O_3$	1475/5	$\frac{5.08}{5.17}$	$\frac{0.0004}{15.8}$	2.02	47	1730	0.68	0.
D80A2-1-14	$3[0.85Y_2O_3 \bullet 0.15 Gd_2O_3] \bullet$ $5Fe_2O_3$	1475/5	$\frac{5.30}{5.38}$	$\frac{0.0005}{16.0}$	2.02	47	1525	0.72	0.
D80A2-2-10	$3[0.70Y_2O_3 \bullet 0.30Gd_2O_3] \bullet$ $5Fe_2O_3$	1475/5	$\frac{5.50}{5.56}$	$\frac{0.0005}{16.2}$	2.02	66	1285	0.69	1.0
D80A2-3-7	$3[0.55Y_2O_3 \bullet 0.45Gd_2O_3] \bullet$ $5Fe_2O_3$	1475/5	$\frac{5.69}{5.76}$	$\frac{0.0001}{16.5}$	2.02	69	1025	0.44	1.7
D80A2-4-10	$3[0.40Y_2O_3 \bullet 0.60 Gd_2O_3] \bullet$ $5Fe_2O_3$	1475/5	$\frac{5.85}{5.95}$	$\frac{0.0006}{16.3}$	2.05	220	716	0.31	2.6

* See Figure 77 for Test Configuration
** Corrected for xfmrs (loss of xfmrs $\approx$ 0.10 db)
NM – Not measured

s	R_r	Coercive Field (oe)(60~)	m_{s1}	$\dfrac{P_{C_{1(kw)}}}{h_{c_{1(oe)}}}$	m_{s2}	$\dfrac{P_{C_{2(kw)}}}{h_{c_{2(oe)}}}$	m_{s3}	$\dfrac{P_{C_{3(kw)}}}{h_{c_{3(oe)}}}$	** Loss/360° (db/360°)	Δ¢/Inch (degrees/inch)	Configuration
	0.49	0.61	1.55	NM	1.43	NM	1.42	NM	>30 db 4.5 to	6.5 GHz	(C Band)
	0.67	2.60	1.19	NM	1.14	NM	1.10	NM	20.0	115	Loss/360
	0.34	2.44	0.80	130 / 63.2	0.77	NM	0.74	129 / 65	4.0	85	Loss/360
	0.57	1.10	0.675	13.2 / 20.2	0.645	NM	0.618	14.8 / 22	0.52	64	/(C Band)
	0.27	0.74	0.35	>250 / >87.5	0.33	NM	0.32	NM	0.85	41	(C Band
	0.22	8.66	1.83	NM	1.75	NM	1.68	NM	>40 db 4.5 to	6.5 GHz	(C Band)
	0.16	7.86	1.99	NM	1.90	NM	1.83	NM	>30 db 4.5 to	6.5 GHz	(C Band)
	NM	NM	NM	NM	NM	NM	NM	NM	NM	NM	(C Band)
	0.53	2.43	2.13	NM	2.04	NM	1.95	NM	>30 db 4.5 to	6.5 GHz	(C Band)
	0.68	0.80	0.92	NM	0.88	NM	0.85	NM	0.45	98	(C Band)
	0.72	0.80	0.81	2.0 / 7.85	0.78	NM	0.75	3.7 / 11.0	0.85	91	(C Band)
	0.69	1.00	0.68	8.6 / 16.3	0.65	NM	0.63	9.0 / 17.1	0.90	78	(C Band)
	0.44	1.70	0.545	NM	0.520	NM	0.500	NM	1.40	71	(C Band)
	0.31	2.60	0.389	140 / 65.5	0.372	NM	0.356	185 / 77.5	1.45	55	(C Band)

TABLE VIII. X BAND (8.0 - 10.0 GHz) AND C B...

Sperry No.	Composition	Firing Schedule ($^\circ$C/hr)	$\dfrac{\rho_m}{\rho_x}$	$\dfrac{\text{Tan}\delta}{\epsilon_1}$ (X Band)	g-Factor (X Band)	Linewidth (X Band) (oe,	$4\pi M_s$ (gauss)	R_r
G-129-4	$3\left[0.98Y_2O_3 \bullet 0.02Dy_2O_3\right] \bullet$ $5Fe_2O_3$	1475/5	$\dfrac{5.14}{5.20}$	$\dfrac{0.0004}{16.0}$	1.99	91	1780	0.73
G-351-4	$3\left[0.95Y_2O_3 \bullet 0.05Dy_2O_3\right] \bullet$ $5Fe_2O_3$	1475/5	$\dfrac{5.18}{5.32}$	$\dfrac{0.0016}{16.0}$	1.90	168	1730	0.73
G-131-3	$3\left[0.90Y_2O_3 \bullet 0.10Dy_2O_3\right] \bullet$ $5Fe_2O_3$	1475/5	$\dfrac{5.26}{5.25}$	$\dfrac{0.0010}{16.1}$	1.88	295	1755	0.62
G-292-2D	$3Y_2O_3 \bullet 5\left[0.88Fe_2O_2 \bullet\right.$ $\left.0.12Al_2O_3\right]$	1475/5	$\dfrac{4.91}{5.09}$	$\dfrac{0.0001}{14.7}$	2.02	47	867	0.38

 * See Figure 77 for Test Configuration
** Corrected for xfmrs (loss of xfmrs $\approx$ 0.10 db
NM - Not measured

C BAND (5.0 - 6.5 GHz) DEVICE TEST RESULTS (CONTINUED)[*]

R_r	Coercive Field (oe)(60~)	m_{s_1}	$\dfrac{P_{C_{1(kw)}}}{h_{c_{1(oe)}}}$	m_{s_2}	$\dfrac{P_{C_{2(kw)}}}{h_{c_{2(oe)}}}$	m_{s_3}	$\dfrac{P_{C_{3(kw)}}}{h_{c_{3(oe)}}}$	Loss/360° [**] (db/360°)	$\Delta\phi$/Inch (degrees/inch)	Configuration
0.73	0.61	0.93	$\dfrac{7.5}{15.2}$	0.89	NM	0.85	$\dfrac{12.5}{20.2}$	1.45	103	(C Band)
0.73	0.57	0.90	NM	0.86	NM	0.83	NM	NM	NM	(C Band)
0.62	0.67	0.86	NM	0.82	NM	0.79	NM	NM	NM	(C Band)
0.38	1.21	0.472	$\dfrac{11.5}{18.4}$	0.450	NM	0.430	$\dfrac{12.0}{19.4}$	NM	NM	(C Band)

The data given in Figure 78 is in good agreement with the results expected from predictions based on the domain model for peak power effects presented in paragraph 3.2.2. The threshold field obviously increases with decreasing saturation magnetization. The points represent data collected at fixed frequency and varying $4\pi M_s$ values and at fixed $4\pi M_s$ value and varying frequency. Data taken at a fixed m_s value are consistent and independent of whether that value is achieved by change in $4\pi M_s$ or frequency.

At low values of saturation magnetization, the dependence on m_s $(= \gamma 4\pi M_s/f)$ is clearly much stronger than a simple inverse relation. As pointed out in paragraph 3.2.2, for normalized saturation magnetization values less than 0.3, the relative position of the spinwave manifold is such that (for even the most unfavorable domains) only high k half-frequency spinwaves are available (see Figure 3). Since the spinwave linewidth appears to vary as $\Delta H_k = A + B_k$, the restriction of scattering to high k spin-waves causes an increase in ΔH_k (and h_{crit}) as the normalized magnetization m_s decreases in the vicinity of 0.3.

This increase in h_{crit} is observed to be sharper or more abrupt in the case of the aluminum doped YIG than for the rare earth doped garnets. This difference could be explained in terms of the $\underline{A}$ and $\underline{B}$ coefficients that make up the expression for ΔH_k or ΔH_{int}. For yttrium and aluminum doped garnets, the A term is very small so that the intrinsic linewidth, and hence h_{crit}, is sensitive to changes in the second or Bk term. In the rare earth doped garnets, the A term is considerably larger so that the variation of the Bk term with m_s is essentially negligible. This explanation assumes, of course, that the B coefficient does not vary strongly with rare earth content.

For a fixed value of m_s (e.g., $m_s = 0.6$), the measured value of h_{crit} is seen to vary almost directly with ΔH_k or $\Delta H_{intrinsic}$ as predicted in the discussion of paragraph 3.2.2. Thus, the threshold field varies almost directly with gadolinium (or any rare earth) substitution for all m_s values, and virtually any critical field level could be reached through sufficient rare earth doping. It should be kept in mind that increasing ΔH_k (and therefore, $\Delta H_{intrinsic}$) will also cause an increase in the

PEAK POWER EQUIVALENT (KW)

	ΔH_k	(S BAND)	(X BAND)
O Al DOPED YIG	~10 OE.	1224	180
● 15% Gd DOPED YIG	~20 - 24	850	125
△ 30% Gd DOPED YIG	~30 - 36	544	80
▲ 45% GD DOPED YIG	~40 - 48	306	45

45% Gd DOPED YIG

30% Gd DOPED YIG

15% Gd DOPED YIG

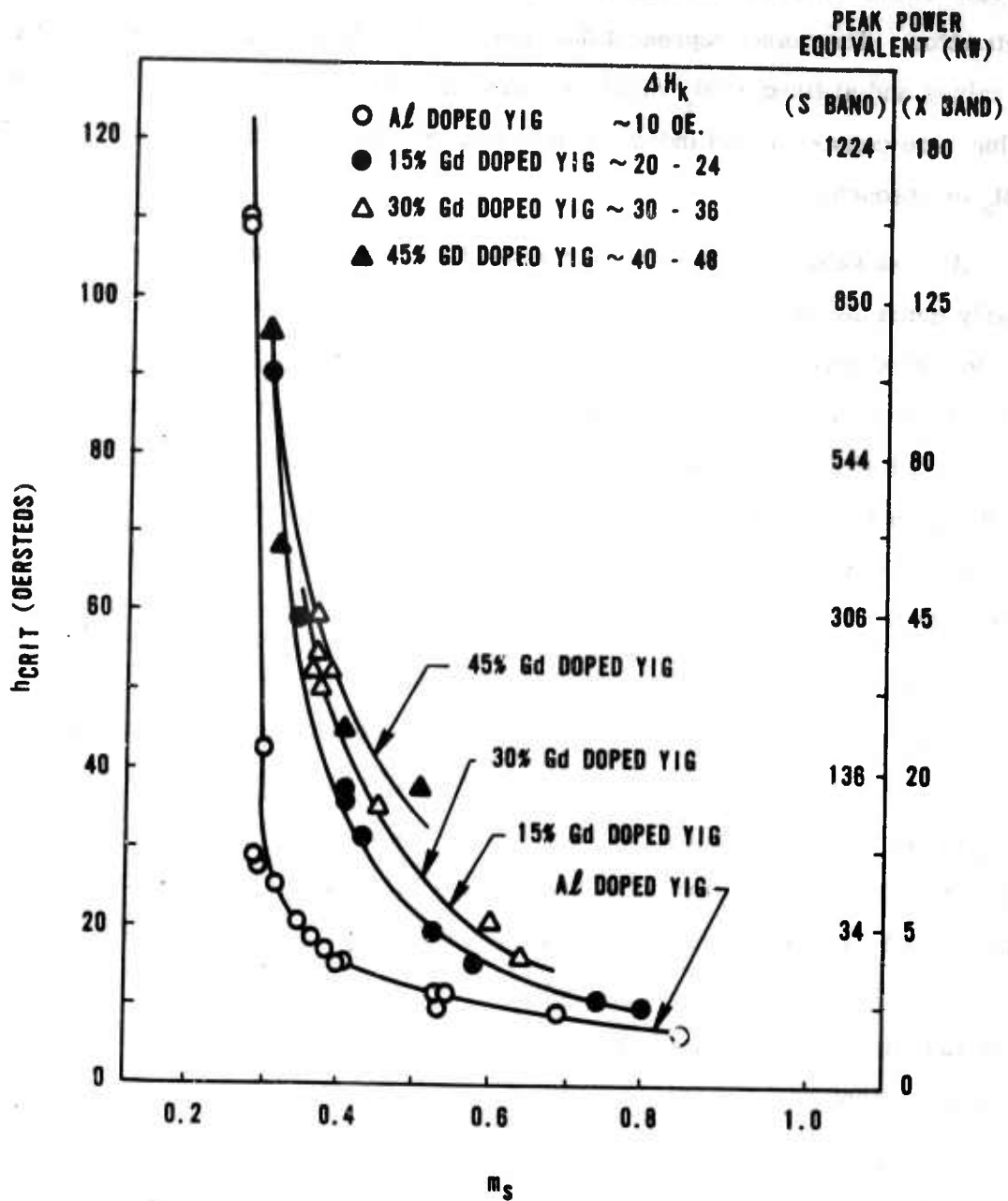Al DOPED YIG

4310B

Figure 78.   Ferrite Critical Field Dependence on the Frequency
             Normalized Saturation Magnetization for Aluminum
             and Gadolinium Substituted YIG. Experimental data
             from Tables V and VIII.

insertion loss. As a result, high peak power levels are often better achieved by going to low m_s values with a smaller sacrifice in terms of loss per 360°.

The basic high power data is recorded as an x-y plot of power output versus power input. Figure 79 shows such a trace taken on 12% Al doped YIG at C band (5.4 GHz). From such curves, insertion loss values can be calculated as indicated in the insert of Figure 79. The critical power level is taken as that input level where an increase in insertion loss is first perceived. The difference in critical power levels for + and - remanent states is felt to arise from field concentration effects. Thus the same critical field level for the two states will show as differing power levels due to the differing dielectric loading of the $+M_r$ and $-M_r$ conditions. Figure 80 shows the same type data recorded on the same Al doped YIG material at a higher frequency when the m_s value is 0.27. This data shows a threshold power level of about 95 kw.

The data shown in Figure 81 were taken on a single dielectrically loaded ferrite slab. The configuration simulates a dielectrically loaded ferrite toroid where the ferrite slab represents one leg of the toroid. These data were taken to indicate the type of dependence of critical power level (P_{crit}) observed as a function of effective bias field.

In the initial region (for applied fields less than about 50 oersteds), the material is essentially unsaturated and as a result certain portions of it (Polder-Smit domains) have high effective bias fields which raise the spinwave manifold so that intermediate and low k spinwaves are degenerate with one-half the operating frequency. As the material is saturated and these Polder-Smit domains are wiped out, P_{crit} increases due to the fact that now the spinwave manifold for all regions of the ferrite has been lowered so that no intermediate or low k spinwaves are degenerate with one-half the operating frequency. This is the same operating region where the low $4\pi M_s$ digital phase shifters operate. As the applied field continues to increase the low k portion of the spinwave manifold is raised until it becomes degenerate with the operating frequency and at that point P_{crit} decreases. As the applied field is still further increased, eventually the point will be reached where the half-frequency point is below the entire spinwave manifold and then a very strong increase in P_{crit} would be observed with
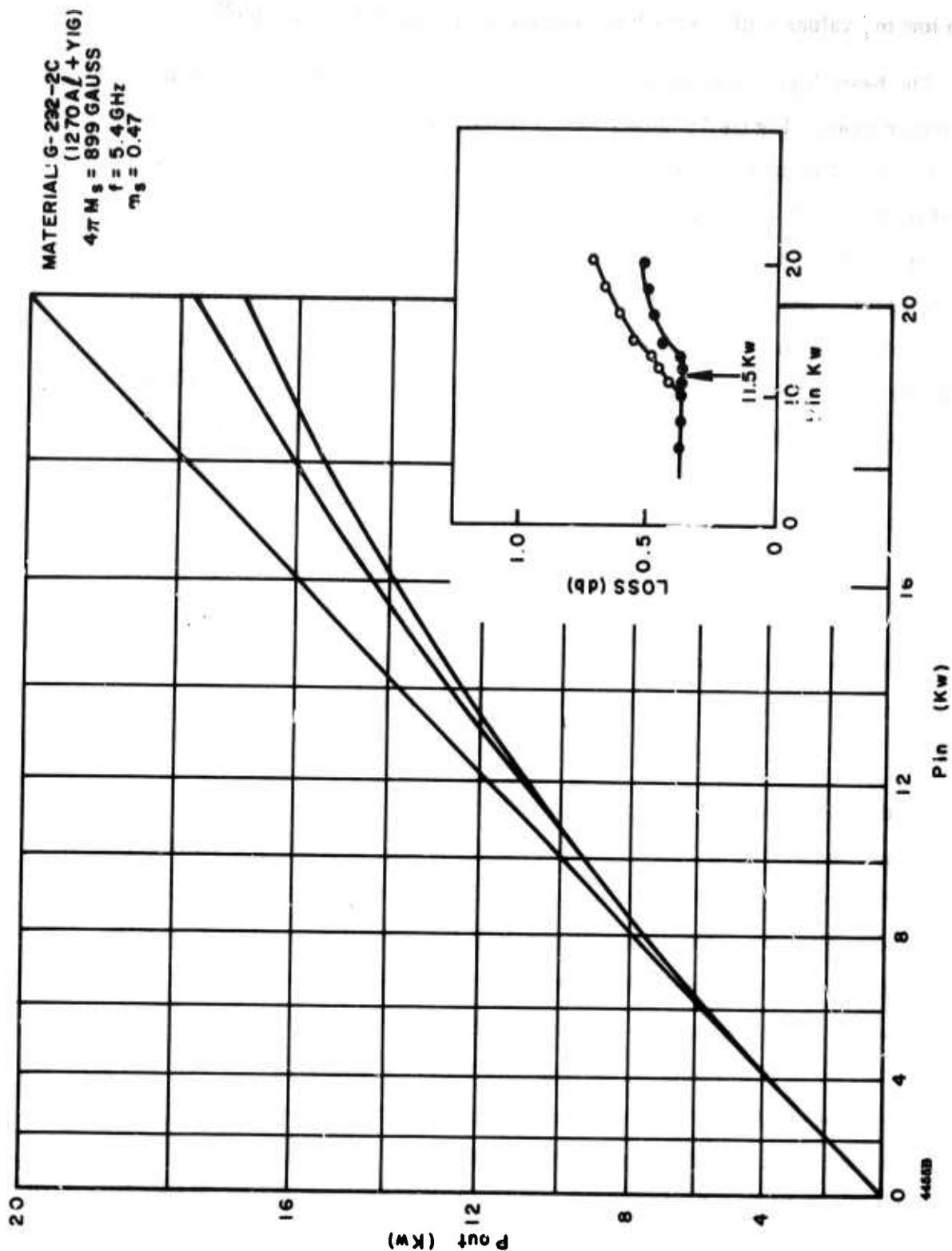
Figure 79. Loss Vs Input Power for Al Doped YIG at 5.4 GHz
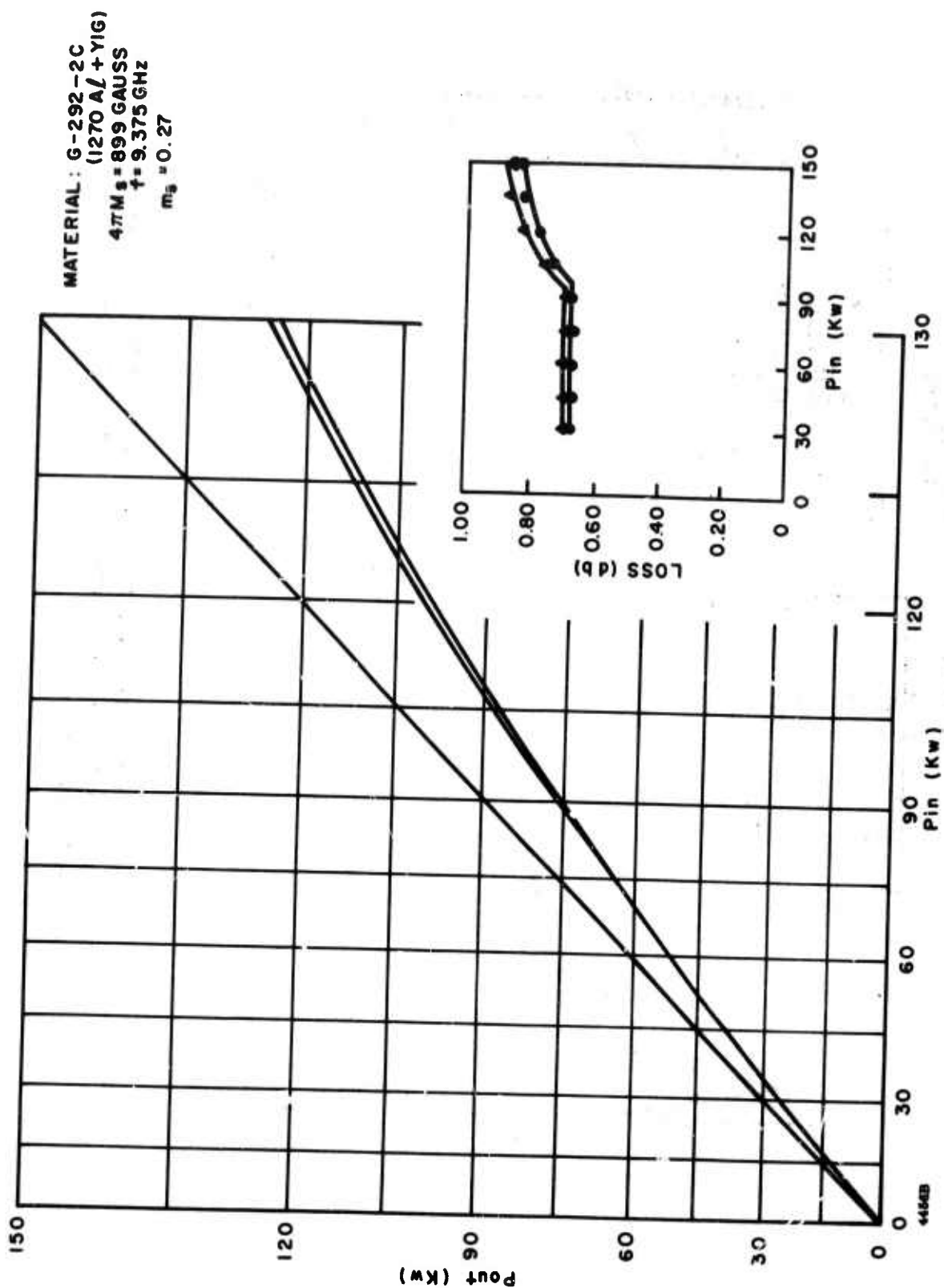
Figure 80. Loss Vs Input Power for Al Doped YIG at 9.375 GHz

MATERIAL: G-292-2C
(1270 Aℓ + YIG)
$4\pi M_S$ = 899 GAUSS
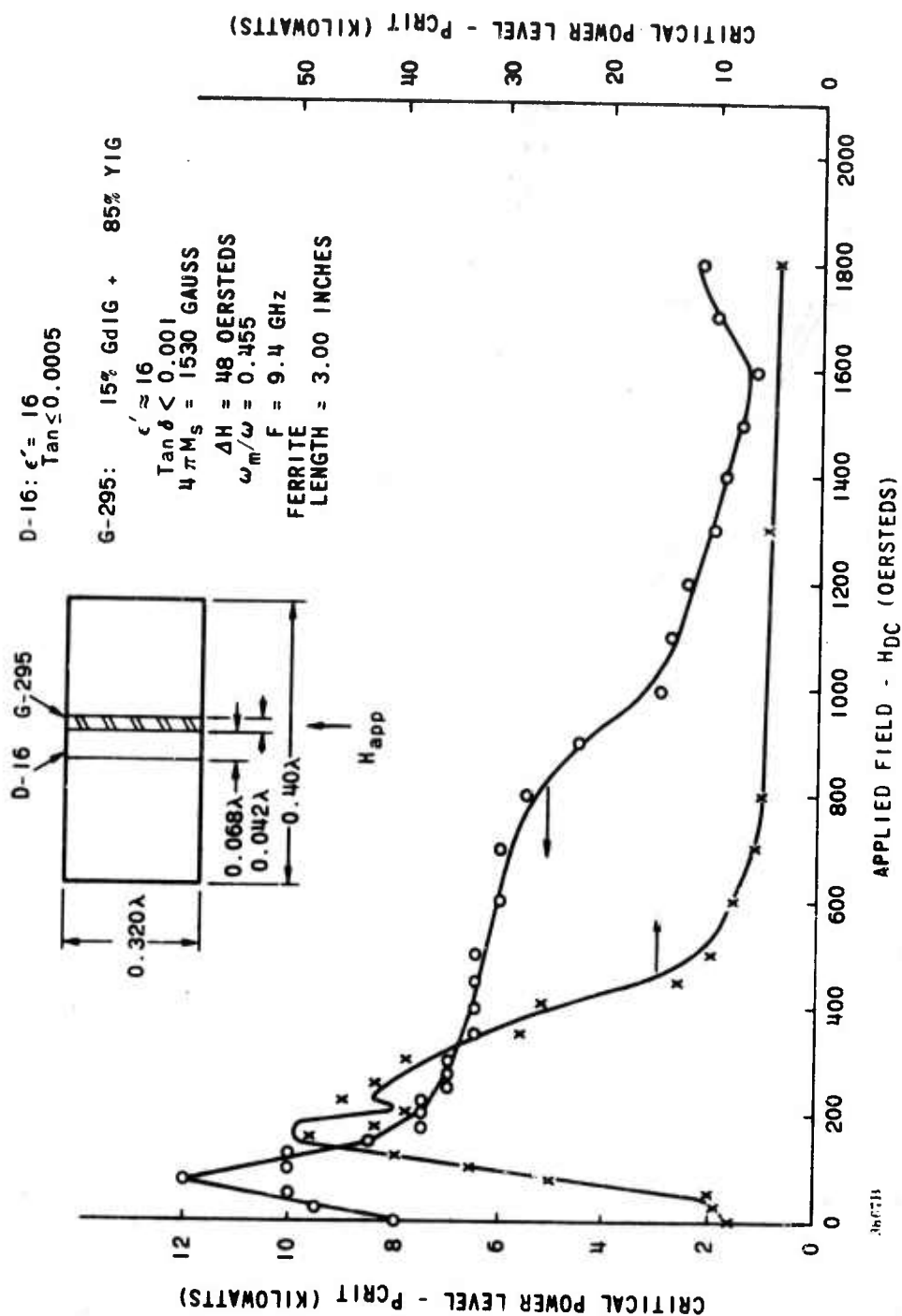f = 9.375 GHz
m_3 = 0.27

Figure 81. Critical Power Level Variation with Applied DC Magnetic Field in a Dielectrically Loaded Ferrite Slab Configuration. Note scale differences for the two curves.

applied field. These measurements do not extend to sufficiently high applied fields to reach this final state.

The variation of P_{crit} with applied field is very nearly the same for the two directions of magnetizations, though the absolute levels are quite different. This difference in absolute level probably arises from field concentration effects. This dielectric loading effect can easily produce differences of a factor of two or more in field equivalent to power differences of four to five. Thus the two curves shown for different magnetization directions very likely represent the same h_{crit} values, but different waveguide power levels due to field concentration effects.

Figure 82 shows the loss and phase shift versus applied field for the same dielectric loaded single slab configuration. It is seen that the differential phase shift, which is the difference in the two phase shift nulls shown, is approximately 150° at about 50 oersteds of applied dc magnetic field. This would be approximately the condition seen by a ferrite toroid in the remanent state. The phase shift is then seen to increase rapidly to a value of approximately 300° at an applied field of approximately 200 oersteds. For further increases in applied field, no appreciable increase in phase shift is seen over the range of dc magnetic field values shown. The loss shown here includes the loss, not only of the phase shifter, but also that due to the unbalance of the bridge used for these measurements. Since the latter loss amounts to approximately 0.40 db, loss of the phase shifter itself is seen to be approximately 0.7 db from approximately 0 to 1400 oersteds of applied dc magnetic field. Thus, this configuration would yield approximately 1.20 db per 360° of phase shift at 50 oersted applied field.

Considerable insight into the adjustment of ferrite material parameters to control peak power effects in digital phase shifters has been provided by the results of the experimental and theoretical studies discussed above. This insight has served as the basis for the synthesis of operational high peak power phase shifters in various frequency bands. For example, operational S band phase shifters have been synthesized having peak power capabilities of the order of 100 kw.

Operational high power phase shifters often have stringent constraints on physical length and low power insertion loss as well as the high power capability
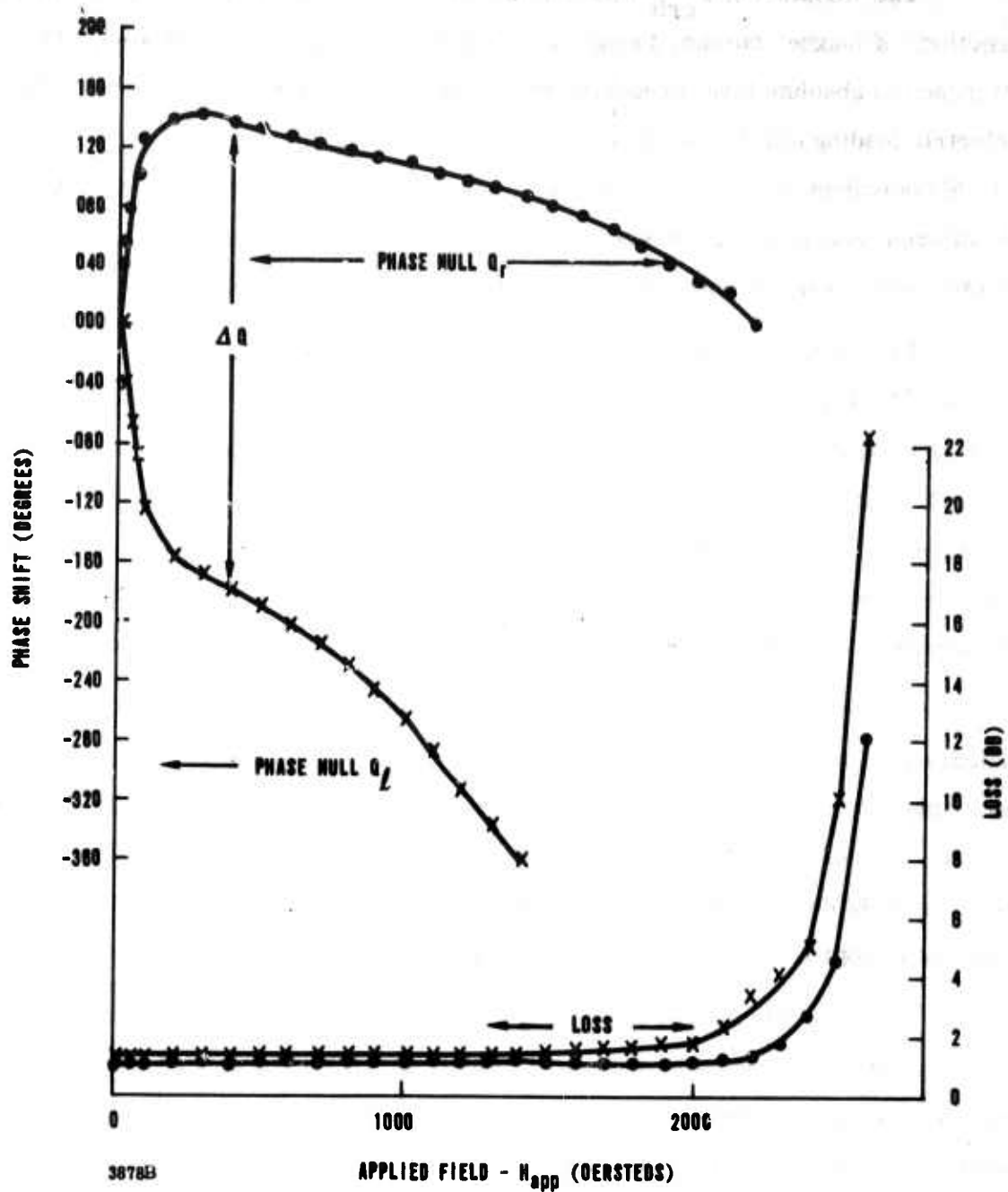
Figure 82. Loss and Phase Shift Versus Applied Field in
the Dielectric-Loaded Ferrite Slab Configuration
Shown in Figure 81

requirement. A price must always be paid to obtain high peak power capability. If the desired peak power threshold is obtained by using a low normalized saturation magnetization, the device will of necessity be longer than if a higher saturation magnetization material could be used, because for a given remanence ratio differential, phase shift is directly proportional to the saturation magnetization. If the saturation magnetization is too low, the insertion loss per 360° of differential phase shift will increase drastically due to dielectric and waveguide copper losses (see Figure 46). On the other hand, if the desired peak power capability is obtained by rare earth doping to increase ΔH_k, the insertion loss will increase in direct proportion to the increase in ΔH_k (see Figure 51). In most operational designs, compromises will obviously be required with the saturation magnetization decreased and ΔH_k increased somewhat. In any case, the data and guide lines presented in this report should permit the selection of material parameters for optimum performance under a known set of constraints. It should also be recognized that for a given input power the rf magnetic field in the ferrite element is a function of the geometry of the structure, the degree of dielectric loading, etc. Therefore, the peak power capability of a phase shifter can also be increased by optimizing the geometry. For example, increasing the height of a TE mode rectangular waveguide phase shifter has little effect on the phase shift or loss but appreciably decreases the rf field intensity in the ferrite and hence, increases the high power capability (it will, of course, ultimately lead to multi-moding difficulties).

In summary, it is felt that the experimental and theoretical results presented here represent a rather complete understanding of the essential features of the high power effects in remanent state ferrites. These results, together with the results of the low power studies, provide a basis for the design of material and structure for optimum high peak power digital phase shifters.

4.5.3.2 <u>High Power Measurements in Helix Line.</u> Two materials from the aluminum substituted YIG family were measured for high power threshold. They are G-250-6D (25% Al + YIG) and G-238-6D (20% Al + YIG). The results are shown in Figures 83 and 84, respectively.
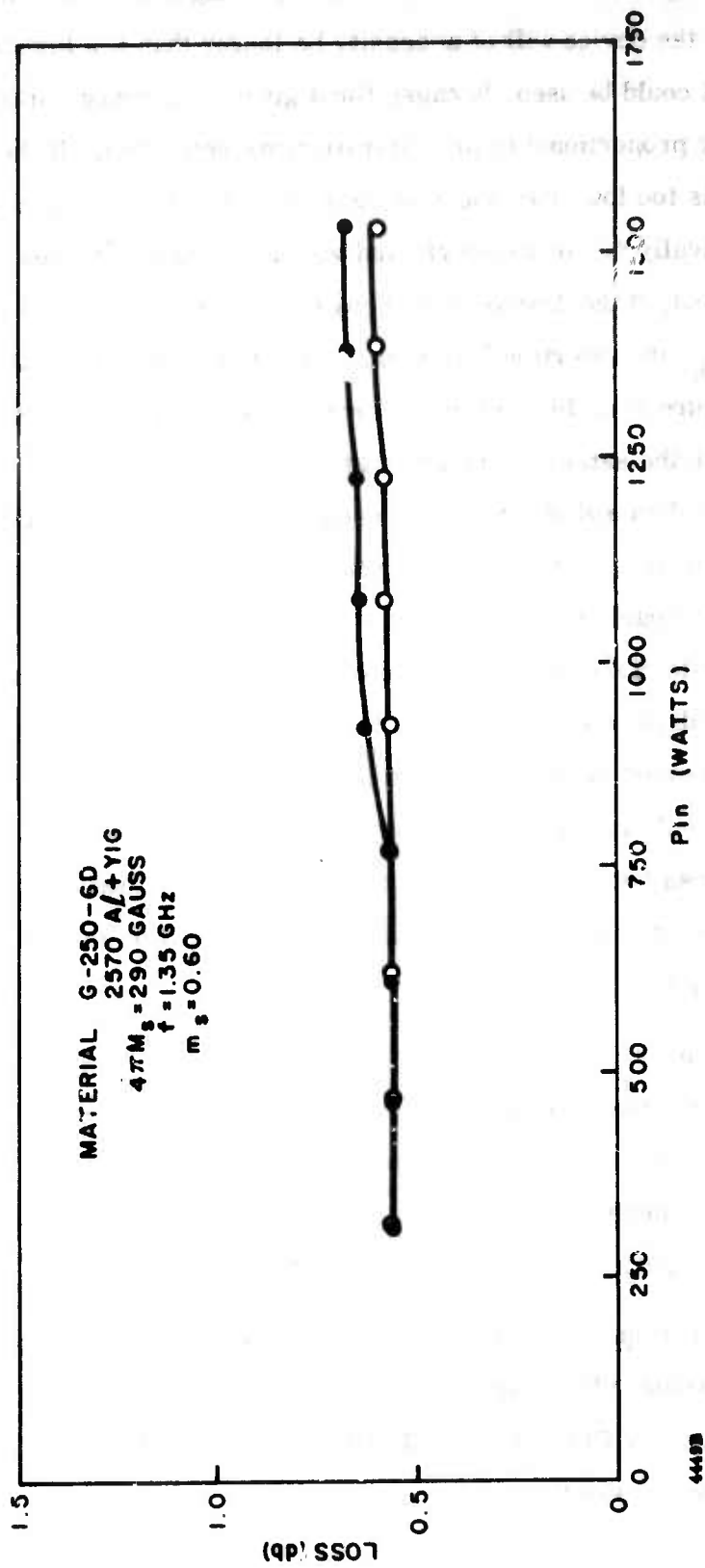
Figure 83. Loss Vs Input Peak Power of G-250-6D in Helix Line
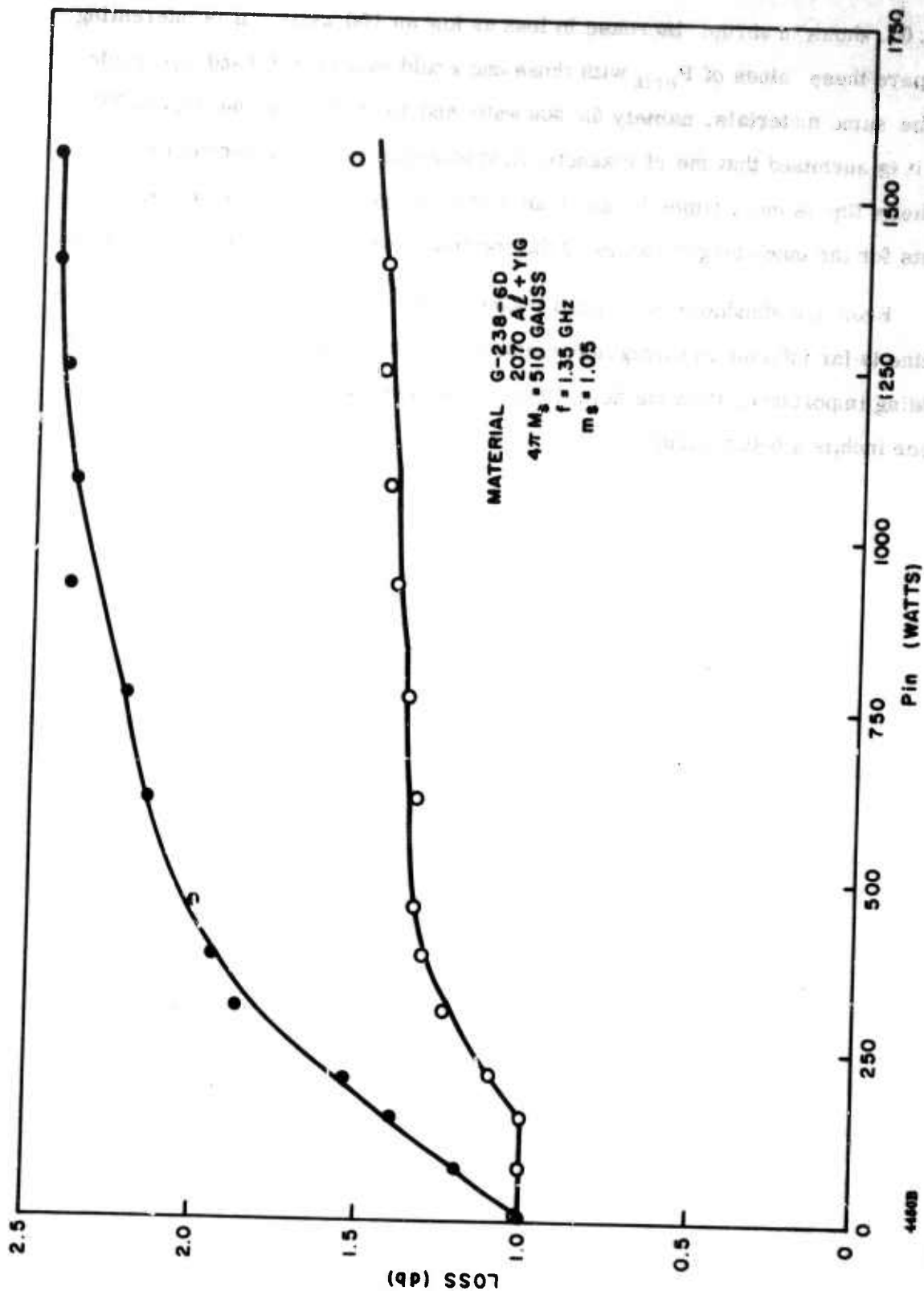
Figure 84. Loss Vs Input Peak Power of G-238-6D in Helix Line

It is seen that a slight increase in the loss of the G-250-6D, with $m_s = \dfrac{\gamma 4\pi M_s}{f} = 0.60$, first occurs at about 700 watts while the G-238-6D, with $m_s = 1.05$, shows an abrupt increase in loss as low as 100 watts. It is interesting to compare these values of P_{crit} with those one would expect in L band waveguide using the same materials, namely 55,000 watts and 14,000 watts (see Figure 78). Thus, it is surmised that the rf magnetic field experienced by the ferrite toroid in the helix line is many times larger than in the waveguide which, of course, accounts for the much larger values of differential phase shift obtained in the helix.

From the standpoint of overall losses as well as high power capability, the helix line is far inferior to waveguide geometries. On the other hand, if size is of overriding importance, then the helix line, with its much greater differential phase shift per inch, is a better structure than waveguide.

5 PUBLICATIONS AND LECTURES

LECTURES

1. D. R. Taft, J. L. Allen, and G. P. Rodrigue, "High Power Performance of Ferrite Digital Phase Shifters", presented at NEREM, Boston, Massachusetts, November 1966.

2. G. P. Rodrigue, J. L. Allen, and D. R. Taft, "Study of Magnetic Loss in Remanent State Toroids", presented at Conference on Magnetism and Magnetic Materials, Washington, D. C., November 1966.

3. J. L. Allen, D. R. Taft, and F. K. Hurd, "Computer-Aided Design of Ferrite Devices Using Intrinsic Material Parameters", presented at the Conference on Magnetism and Magnetic Materials, Washington, D. C., November 1966.

4. J. L. Allen, "Computer-Aided Analysis as a Quantitative Design Tool for Ferrite Phase Shifters and Resonance Isolators", presented at The International Symposium on Microwave Theory and Techniques, Boston, Mass., May 1967.

5. G. P. Rodrigue, J. L. Allen, L. J. Lavedan and D. R. Taft, "Operating Dynamics and Performance Limitations of Ferrite Digital Phase Shifters", presented at The International Symposium on Microwave Theory and Techniques, Boston, Mass., May 1967.

PUBLICATIONS

1. G. P. Rodrigue, J. L. Allen, and D. R. Taft, "Study of Magnetic Loss in Remanent State Toroids", J. A. P., Vol. 38, No. 3, March 1967, p. 1407.

2. J. L. Allen, D. R. Taft, and F. K. Hurd, "Computer-Aided Design of Ferrite Devices Using Intrinsic Material Parameters", J. A. P., Vol. 38, No. 3, March 1967, p. 1399.

3. D. R. Taft and J. L. Allen, "The High Power, Low Loss Conflict in Ferrite Digital Phase Shifters", Electronic Communicator, March/April 1967.

4. G. P. Rodrigue, J. L. Allen, L. J. Lavedan and D. R. Taft, "Operating Dynamics and Performance Limitations of Ferrite Digital Phase Shifters", to be published in IEEE Transactions on Microwave Theory and Techniques.

6 PRINCIPAL CONCLUSIONS

- The correlation obtained between theoretical predictions and measured values of both high and low power characteristics of remanent state devices indicates that ferrimagnetic materials in the remanent state can be accurately represented as an assembly of magnetically saturated regions (domains) whose size and shape depend, among other things, upon the shape of the material sample. Theoretical predictions are based on intrinsic material parameters, saturation magnetization ($4\pi M_s$), effective g-factor (g_{eff}), anisotropy field (H_{anis}), intrinsic linewidth (ΔH_{int}), complex dielectric constant (ϵ^*) and sample shape.

- The analytical approach developed can, with the aid of a digital computer, provide accurate design information as to waveguide geometries providing maximum figure of merit in terms of phase shift/unit loss and maximum flatness of differential phase shift with frequency (zero phase slope). Differential phase shift and loss data can be predicted to well within five percent accuracy. Thus, computer-aided analysis can significantly shorten the cut and try stage of waveguide phase shifter design.

- Insertion loss at low peak power levels is directly proportional to the intrinsic linewidth of the material. The intrinsic linewidth of a material is the linewidth that would be measured on that material in the absence of inhomogeneous broadening, and is approximately equal to ΔH_k at that same frequency (as measured at twice that frequency). The usual polycrystalline linewidth is not generally significant in determining low power loss.

- Phase shifter loss as measured in X, C, S and L frequency bands agrees with computed loss values assuming a direct linear frequency dependence of ΔH_{int}. Thus, a single measurement of ΔH_{int} is capable of providing low power loss information throughout an extremely broad range of microwave frequencies. In addition, this same linewidth data can also be used to accurately predict the high power handling capabilities of the material. The intrinsic linewidth representation offers substantial advantage over the heretofore used magnetic loss tangent representation. The latter quantity is not an intrinsic material parameter and for reasonable accuracy, must be measured at the frequency of use, since this loss tangent depends in turn on intrinsic material parameters like $4\pi M_s$, H_{anis}, and ΔH_{int}.

- The analytical procedure used provides a means of separating and identifying the various sources of loss and thereby serves to guide in the selection of optimum ferrite and dielectric materials and device geometries.

- Loss per 360° of differential phase shift increases rapidly as normalized saturation magnetization ($m_s = \gamma 4\pi M_s/f_c$, where f_c = center frequency) values increase above 1.0 due to the encroachment of resonance loss. Resonance loss can be minimized through the use of materials having lowest ΔH_{int} and lowest anisotropy field (H_{anis}).

- Loss per 360° of differential phase shift increases rapidly for m_s values less than about 0.3 due to the contributions of dielectric and copper losses and the reduced differential phase shift/length.

- Maximum phase shift per unit loss is obtained for m_s values between 0.6 and 0.8, and figures of merit of the order of 1000°/db can be realized.

- Operation of waveguide FDPS in the normal above resonance mode have been demonstrated at operating frequencies as low as L band. At L band frequencies, as in X, C, and S bands, the measured differential phase shift and loss are in very good agreement with the analytical predictions. Figures of merit of the order of 650°/db have been realized. However, the low differential phase shift per inch (10° to 20°) probably means a 360° phaser would be prohibitively long.

- Peak power handling capability of a remanent state phase shifter is directly proportional to the spinwave linewidth ΔH_k of the material and inversely proportional to its normalized saturation magnetization, m_s.

- At a given frequency, ω, peak power capacity can be increased by decreasing $\omega_m = \gamma 4\pi M_s$; e.g., by aluminum doping of garnets. This cannot be done entirely without sacrifice, however, since dielectric and copper losses will increase the loss/360°. Nevertheless, peak powers well in excess of 100 kw can be handled in all bands with less than 1 db insertion loss.

- At a given frequency, , peak power capacity can also be increased by increasing $\Delta H_k = \Delta H_k \big|_{k=0} + Bk$, where the k dependence of ΔH_k is indicated. By increasing $\Delta H_k \big|_{k=0}$, as through rare earth doping of garnets, virtually any peak power level can be attained. However, since ΔH_k is directly related to H_{int}, such rare earth doping causes an immediate increase in low power loss.

- When the relative position of the spinwave manifold and the microwave frequency for a <u>given domain</u> is such that <u>no</u> low k half-frequency spinwaves are available, the Bk term and, consequently, the threshold field of <u>that domain</u> increases. The principal control on the relative

6-2

position of the different spinwave manifolds for the various domains of remanent state material is by variation of m_s through its influence on the effective bias field of each domain. The multidomain model for these materials permits the calculation of the value of m_s at which the increase in ΔH_k, caused by the nonavailability of low k spinwaves, should occur. For domains having the lowest possible threshold field at low $\frac{\omega_m}{\omega}$ values (i.e., Polder-Smit domains), the transition value of m_s is found to be about 0.3. In a given sample, there may not be any domains of this type and as a result, the increase in power handling capacity would occur at a larger value of m_s.

- Best high peak power performance for a given low power insertion loss seems to be obtained by using the low $4\pi M$, low ΔH_{int} (and hence low ΔH_k) materials, and a balance must be reached between high peak power handling ability on the one hand and dielectric, magnetic, and copper loss (as well as unit size and weight) on the other.

- Below resonance (in frequency) operation has been achieved in a helical line digital phase shifter. The shape of the resonance loss curve for the remanent state material is very much like the resonance curve of a saturated sample, only broader. A figure of merit of about 25 degrees/db has been achieved at 1 GHz but further investigation has not indicated that a practical level of performance is feasible.

- High density materials appear to have the best overall properties for use in remanent state phase shifters. Considerable premium should be placed on materials having highest possible density and homogeneity.

- Remanence magnetization appears to vary with temperature in approximately the same manner as the saturation magnetization, indicating that the remanence ratio, R_r, is approximately independent of temperature. Exceptions to this general rule occur in cases where the anisotropy field of the material changes significantly with the temperature, and for sufficient driving fields, increased anisotropy fields produce small increases in remanence ratio.

- Coercive fields, H_c, vary directly with anisotropy fields.

- Table IX lists some possible tradeoffs in FDPS between peak power (P_p), average power (P_{avg}), loss per 360° and phase shift per inch. In each frequency band the first line of values is typical of a low peak, low average power configuration designed to have maximum phase shift per unit length and minimum loss per 360°. The second line of values represents a high peak, low average power configuration in which high peak power capability has been obtained by decreasing the ferrite magnetization. The loss per 360° increases and

the phase shift per inch decreases because of the lower value of m_s. The third line of values represents a high peak, high average power phase shifter configuration. Rare earth doped (gadolinium) garnets would be used to achieve phase shift stability with average power variations and the loss per 360° would increase in proportion to the required doping.

- Note that, in going from the low peak, low average power configuration to the high peak, high average power configuration by rare earth doping, the loss per 360° just about doubles while the phase shift per inch decreases by almost one-third. If it is desired only to increase the peak power capability, aluminum substitution only should be used since the increases in loss associated with this method of increasing the peak power capability are substantially less than with the rare earth doping.

- In the above discussion, the geometries of the ferrite and waveguide were fixed. By making certain adjustments in the ferrite geometry, both the peak and average power capability can be increased by approximately a factor of 10. The corresponding loss per 360° increases about 25 percent while the phase shift per inch decreases to about one-third its previous value. These sacrifices are acceptable in some applications.

TABLE IX.   FERRITE DIGITAL PHASE SHIFTER

Frequency (GHz)	P_p (kw)	P_{avg} (Watts)	$m_s = \gamma 4\pi M_s/f$	$\Delta H_{k}\|_{k=0}$ (X Band) (oe)
9.0	1	1	0.60	12
9.0	100	≲10	0.25	12
9.0	100	100	0.30	25
5.6	1	1	0.90	12
5.6	300	≲30	0.25	12
5.6	300	500	0.30	25
3.7	1	1	0.60	12
3.7	500	≲50	0.25	12
3.7	500	1000	0.30	25
1.5	1	1	0.60	12
1.5	750	≲75	0.25	12
1.5	750	2000	0.30	25

*The values shown are based on the use of dielectrically-loaded ferrit with a remanence ratio of R_r = 0.50.

①Loss/360° values shown are for operational devices at indicated powe

②$\Delta\phi$/inch values shown are for low power, room temperature.

Ⓐ No cooling required.

Ⓑ Boron nitride termal conducting elements and water cooling required.

k = 0 and)	Loss/360° [1] (db/360°)	$\Delta\phi$/Inch [2] (degrees/inch)	Typical Material	Notes
	0.35	150	MgMn Ferrite or YIG	Ⓐ
	0.70	60	Al Doped YIG	Ⓐ
	0.85	60	Gd, Al Doped YIG	Ⓑ
	0.40	100	YIG	Ⓐ
	0.70	40	Al Doped YIG	Ⓐ
	0.75	38	Gd, Al Doped YIG	Ⓑ
	0.50	60	Al Doped YIG	Ⓐ
	0.75	23	Al Doped YIG	Ⓐ
	1.00	20	Gd, Al Doped YIG	Ⓑ
	0.60	30	Al Doped YIG	Ⓐ
	0.80	10	Al Doped YIG	Ⓐ
	1.00	10	Gd, Al Doped YIG	Ⓑ

ded ferrite toroids

ated power levels.

e.

required.

APPENDIX A

APPENDIX A

The following derivation of the mathematical expression for the rf magnetic field intensity applies strictly to a dielectric-slab loaded rectangular waveguide propagating the TE_{10} mode. Figure A1 shows a cross-sectional view of the configuration.
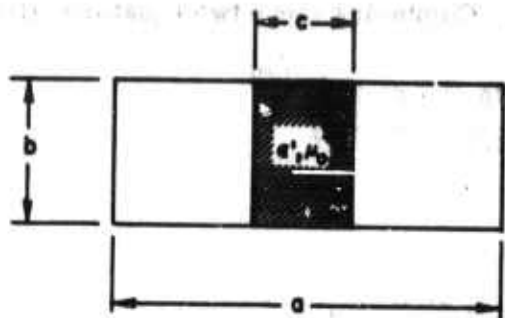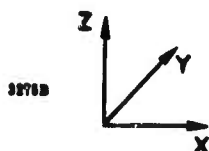

Figure A1. Cross-Sectional View of the Dielectrically-Loaded Rectangular Waveguide

Equation (18) of Vartanian et al[*] is solved to read:

$$E_o^2 = \frac{4 Z_w (1 + r)}{a b R} P_T \tag{1}$$

where $Z_w = \eta \frac{k}{\beta}$ = the wave impedance

η = 377 ohms

$k = 2\pi/\lambda_o$

$\beta = 2\pi/\lambda_g$

$r = \dfrac{C/a}{1 - C/a}$

$R = r \left(1 + \dfrac{\sin 2q}{2q}\right) + \left(\dfrac{\cos q}{\sin p}\right)^2 \left(1 - \dfrac{\sin 2p}{2p}\right)$

$q = C/2a \, (\epsilon' k^2 a^2 - \beta^2 a^2)^{1/2}$

$p = 1/2 \, (1 - C/a) \, (k^2 a^2 - \beta^2 a^2)^{1/2}$

P_T = the threshold power level

E_o = the maximum electric field intensity which occurs at the center of the guide

---

[*]P. H. Vartanian et al, Propagation in Dielectric Slab Loaded Rectangular Waveguide," IRE Trans. of the PGMTT, April 1958.

A-1

The transverse component of rf magnetic field intensity is

$$h_x = \frac{-\beta}{\omega \mu_0} E_z \qquad (2)$$

where, at the center of the waveguide, $E_z = E_0$. Combining these two equations gives

$$h_{ox} = \frac{\beta}{\omega \mu_0} \left(\frac{4 \eta k a / \beta a \,(1+r)\, P_T}{a\,b\,R} \right)^{1/2}$$

and since $\omega \mu_0 = \eta k$ $\left(\eta = \sqrt{\dfrac{\mu_0}{\epsilon_0}} \quad \text{and} \quad k = \omega \sqrt{\mu_0 \epsilon_0} \right)$,

then

$$h_{ox} = \left(\frac{4 \beta a \,(1+r)\, P_T}{\eta \, k a \, R \, a \, b} \right)^{1/2}$$

or

$$h_{ox} \left(\frac{a\,b}{P_T} \right)^{1/2} = \left(\frac{.0106 \beta a \,(1+r)}{R\,k\,a} \right)^{1/2} \quad \text{in MKS units}$$

or

$$h_{ox} \left(\frac{a\,b}{P_T} \right)^{1/2} = \left(\frac{806 \beta a \,(1+r)}{R\,k\,a} \right)^{1/2} \qquad (3)$$

where h_{ox} is in oersteds, P_T in kilowatts and a, b in inches.

Figure A2 shows how $h_{ox} \left(\dfrac{a\,b}{P_T} \right)^{1/2}$ varies with frequency k a and dielectric slab width C/a.

The transverse component of rf magnetic field is maximum at the center of the waveguide $(X = a/2)$ and decreases sinusoidally to the outer dielectric wall. Thus

$$h'_x = h_{ox} \cos \left(\epsilon' k^2 a^2 - \beta^2 a^2 \right)^{1/2} X/a$$

and at the outer dielectric wall $(X = C/2)$

$$h_x = h_{ox} \cos \left(\epsilon' k^2 a^2 - \beta^2 a^2 \right)^{1/2} C/2a \qquad (4)$$

In most digital phase shifter structures the outer toroid wall is a region in which $h_y \approx j h_x$; that is, the rf magnetic field is circularly polarized there and has the magnitude h_x.
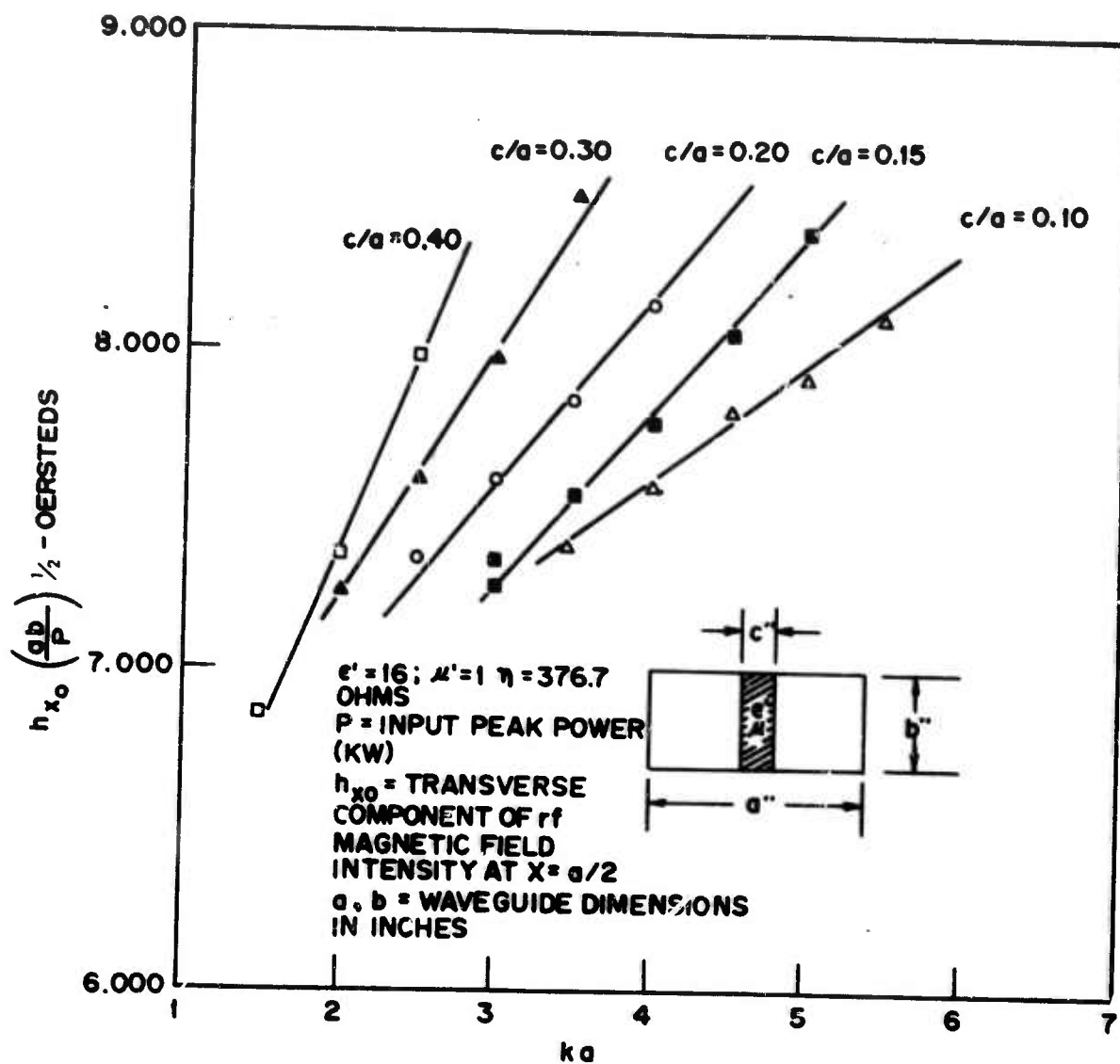
A-2

Figure A2. Transverse Component of rf Magnetic Field at x = a/2 Versus Frequency and Slab Width for the TE$_{10}$ Mode in Rectangular Waveguide

END
7-67

A-3